

SM-43658

✓

Ref. No. _____	_____	
Copy No. _____	of _____	Copies _____

Technical Library, Bellcomm, Inc.

(NASA-CR-129396) HANDOUT FOR SATURN S-4B VEHICLE DYNAMICS AND CONTROL WORKING GROUP MEETING (Douglas Aircraft Co., Inc.) 14 May 1963 221 p	N72-75856
	Unclas 00/99 37773

**HANDOUT FOR SATURN S-IVB VEHICLE  
DYNAMICS & CONTROL WORKING GROUP MEETING**

14 MAY 1963  
DOUGLAS REPORT SM-43658

MISSILE & SPACE SYSTEMS DIVISION  
DOUGLAS AIRCRAFT COMPANY, INC.  
SANTA MONICA/CALIFORNIA

*D. G. Valley*



✓

Ref. No. _____	_____
Copy No. _____	of _____ Copies

SM-43658

Technical Library, Bellcomm, Inc.

(NASA-CR-129396) HANDOUT FOR SATURN S-4B  
 VEHICLE DYNAMICS AND CONTROL WORKING  
 GROUP MEETING (Douglas Aircraft Co.,  
 Inc.) 14 May 1963 221 p

N72-75856

Unclas  
00/99 37773

# HANDOUT FOR SATURN S-IVB VEHICLE DYNAMICS & CONTROL WORKING GROUP MEETING

14 MAY 1963  
DOUGLAS REPORT SM-43658

MISSILE & SPACE SYSTEMS DIVISION  
DOUGLAS AIRCRAFT COMPANY, INC.  
SANTA MONICA/CALIFORNIA

*D. B. Valley*



Ref. No. [REDACTED]  
Copy No. \_\_\_\_\_ of \_\_\_\_\_ Copies

**HANDOUT FOR SATURN S-IVB VEHICLE  
DYNAMICS & CONTROL WORKING GROUP MEETING**

14 MAY 1963  
DOUGLAS REPORT SM-43658

Prepared for:  
National Aeronautics & Space Admins.  
Under NASA Contract No. NAS7-101

***DOUGLAS MISSILE & SPACE SYSTEMS DIVISION***

Ref. No. _____
Copy No. _____ of _____ Copies

ABSTRACT

This report contains copies of the material to be presented at the Saturn S-IVB Stage Vehicle Dynamics and Control Working Group Meeting at the Douglas Aircraft Company, Missile and Space Systems Division, Culver City facility on May 14, 1963.

# HANDOUT MATERIAL

## TABLE OF CONTENTS

<u>Section</u>		<u>Page</u>
1	J-2 Engine Side Loads during Ground Start .....	1
2	Effects of Vehicle Bending, Sloshing and Rigid Body Parameters on Servo Actuator System Requirements .	14
3	Saturn Separation Sequencing S-IVB Stage .....	36
4	Effects of J-2 Engine Gimbal Limits on Post-Separation Attitude Transient .....	49
5	Analytical Approach to the Stability Limits of the Non-Linear Hydraulic Servo .....	74
6	Sloshing and Stability Analysis - S-IVB Stage .....	81
7	Garden Hose Dynamic Coupling Stability Analysis .....	89
8	Roll Torques Generated by Propellant Sloshing .....	105
9	Saturn S-IVB General Protuberance Wind Tunnel Test Preliminary Report .....	113
10	Auxiliary Propulsion System Fairing Wind Tunnel Test ..	141
11	Saturn-IB Propellant Reserve Requirement for a 105 Nautical Mile Circular Orbit Mission .....	166
12	Vent Cycle Perturbations to Earth Waiting Orbit for Apollo Mission .....	172
13	Inflight Venting of the S-IVB/S-II Interstage .....	194
14	External Pressure Time Histories .....	201
15	Servo Actuator Response to Load Inputs .....	206
16	Status Report of Actuation System .....	214

## Section 1

### J-2 ENGINE SIDE LOADS DURING GROUND START

#### SUMMARY:

Ground tests of the Rocketdyne J2 engine thus far have indicated transient starting loads of high magnitude. These loads have been large enough on some runs to cause damage to the test apparatus. Rocketdyne has taken the load data from the firings and has subtracted out induced loads caused by the fixture-engine dynamics. The resulting loads are supposedly the loads due to the gaseous combustion and expansion dynamics only.

The only statement that can be made with authority to date as to the nature of the forcing function is the fact that the loads are caused by sea level exit pressures. No transient loads are expected in a zero pressure condition (outside earth's atmosphere). However, the sea level starting problem will be a problem on the Douglas Aircraft Company static firings of the S-IVB at Sacramento.

To determine the dynamic behavior of the J2 engine on the S-IVB, the load data supplied by Rocketdyne has been imposed on a mathematical model of the S-IVB engine and thrust structure. The extent of the complexity required in the mathematical model was arrived at by determining the overall engine attach structure compliance for a variety of end conditions. The assumption that two degrees of freedom would be required (deflection and rotation at the gimbal point) was modified to one degree of freedom (engine rotation) by the results of the compliance analysis.

The procedure and results of the transient load analysis and the mathematical model justification are contained herein.

## SYMBOLS:

$h$	-	Coordinate describing translation at gimbal point - inches
$\alpha$	-	Coordinate describing engine rotation - radians
$x$	-	Coordinate describing longitudinal engine translation - inches
$I_{HL}$	-	Engine inertia about hinge line - lb.in.sec <sup>2</sup>
$D$	-	Damping of $\alpha$ mode - lb.in.sec
$K$	-	Spring of $\alpha$ mode - lb.in
$S$	-	Laplace operator - 1/sec
$\Omega$	-	Forcing function frequency - rad/sec
$\omega$	-	Natural frequency - rad/sec
$F_n$	-	Natural frequency - cps
$\phi$	-	Influence coefficient
$M$	-	Mass matrix
$F$	-	Dynamical matrix

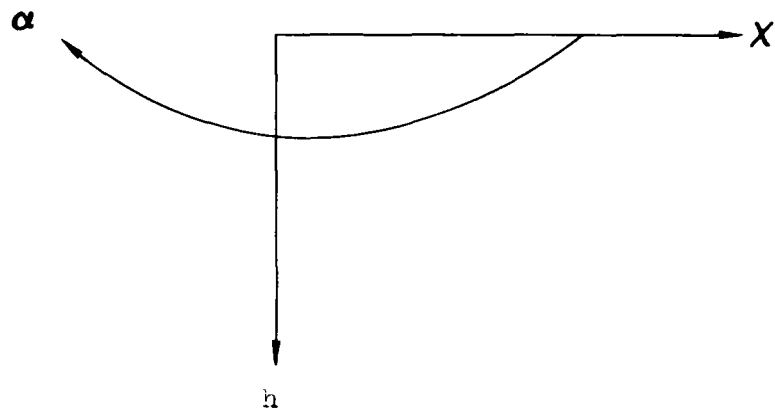
## INTRODUCTION:

The engine mounted on its thrust structure can be completely described by six degrees of freedom (assuming the engine to be rigid and thrust structure mass to be negligible). Two assumptions in addition to the one already offered were then made and are presented without proof:

1. Cross axis coupling is small and single plane motion is all that need be considered. The three remaining degrees of freedom are shown in figure 1.
2. By the geometry of the engine and actuator, much more restraint will be afforded by the longitudinal,  $x$ , degree of freedom than the other two ( $h$  &  $\alpha$ ). Very little dynamic coupling will exist between  $x$  &  $h$  and  $x$  &  $\alpha$ . A compression mode involving the  $x$  degree of freedom will respond to the axial stepped starting transient, but this load will not be transmitted to the actuator. The actuator is the weak link in the engine-thrust structure combination. Therefore, the longitudinal degree of freedom was neglected (figure 2).

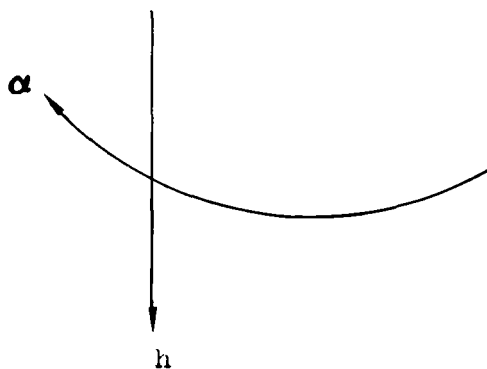
DEGREES OF FREEDOM FOR SINGLE PLANE MOTION

**FIGURE 1**



LATERAL TRANSLATION AND ROTATION      DEGREES OF FREEDOM

**FIGURE 2**



The two remaining degrees of freedom leave some doubt as to their relative worth. The engine rotation degree of freedom certainly must be included in the dynamic model. However, the gimbal point translation degree of freedom must be analyzed to determine its effect on the dynamic coupling between  $h$  &  $\alpha$ .

Beam theory was employed to determine the influence coefficients for  $h$  &  $\alpha$ . Thrust structure and fuselage structure up to the point of tangency of the aft bulkhead (figure 3) was considered. The EI distribution for this structure is shown in figure 4. Notice the gimbal block (the section nearest the gimbal point) has been given a high EI value. Thus, this section will appear to be quite rigid.

Sectional influence coefficients of  $h$  and  $\alpha$  were computed for each section. These values were referred to the beam base (aft dome point of tangency) by matrix transformation methods. The influence coefficients at the gimbal point were then extracted from the resulting set of influence coefficients. The gimbal point influence coefficients are of the form:

$$\begin{bmatrix} \phi_{hh} & \phi_{h\alpha} \\ \phi_{\alpha h} & \phi_{\alpha\alpha} \end{bmatrix} \begin{bmatrix} h \\ \alpha \end{bmatrix} = \begin{bmatrix} \phi \end{bmatrix}$$

A mass matrix was written for the engine:

$$\begin{bmatrix} M_{hh} & M_{h\alpha} \\ M_{\alpha h} & M_{\alpha\alpha} \end{bmatrix} \begin{bmatrix} \ddot{h} \\ \ddot{\alpha} \end{bmatrix} = \begin{bmatrix} M \end{bmatrix}$$

The dynamical matrix was formed:

$$\begin{bmatrix} F \end{bmatrix} = \begin{bmatrix} \phi \end{bmatrix} \begin{bmatrix} M \end{bmatrix}$$

STRUCTURE USED TO OBTAIN INFLUENCE COEFFICIENTS

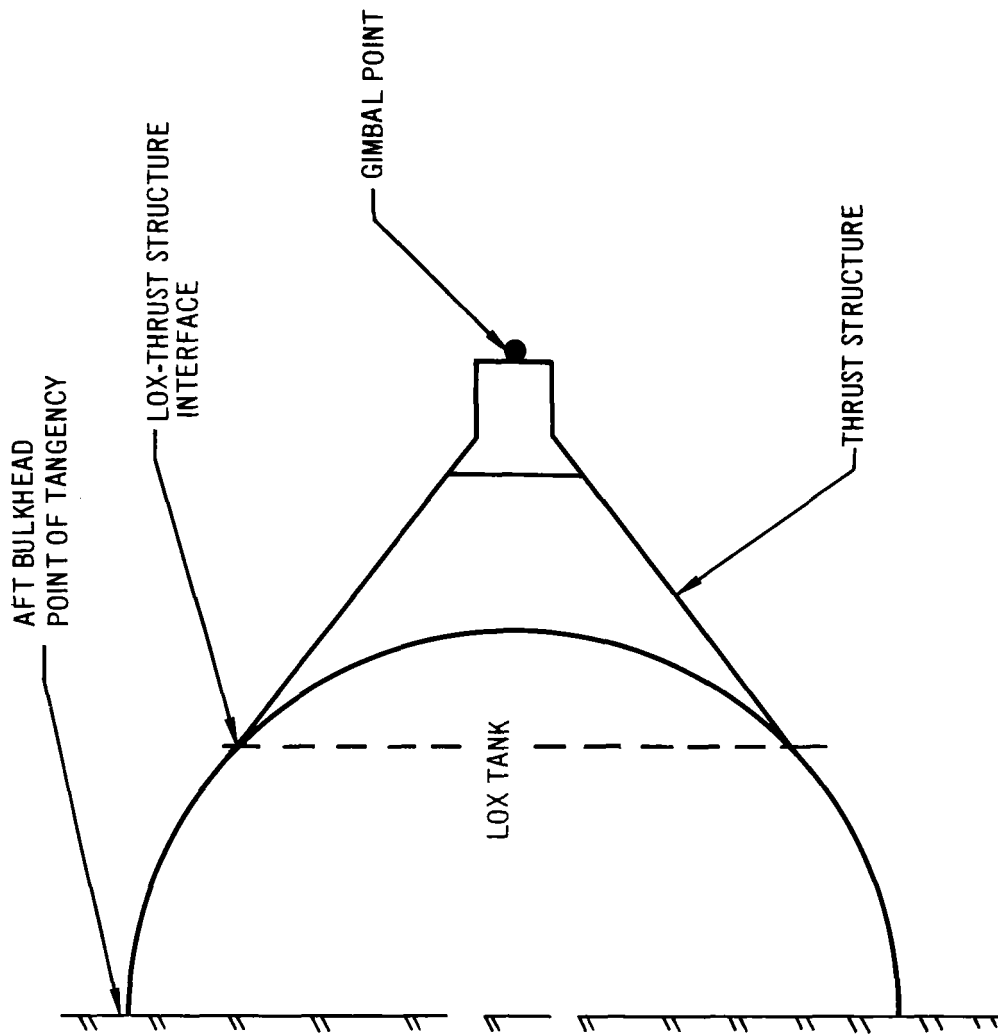


FIGURE 3

# EI DISTRIBUTION

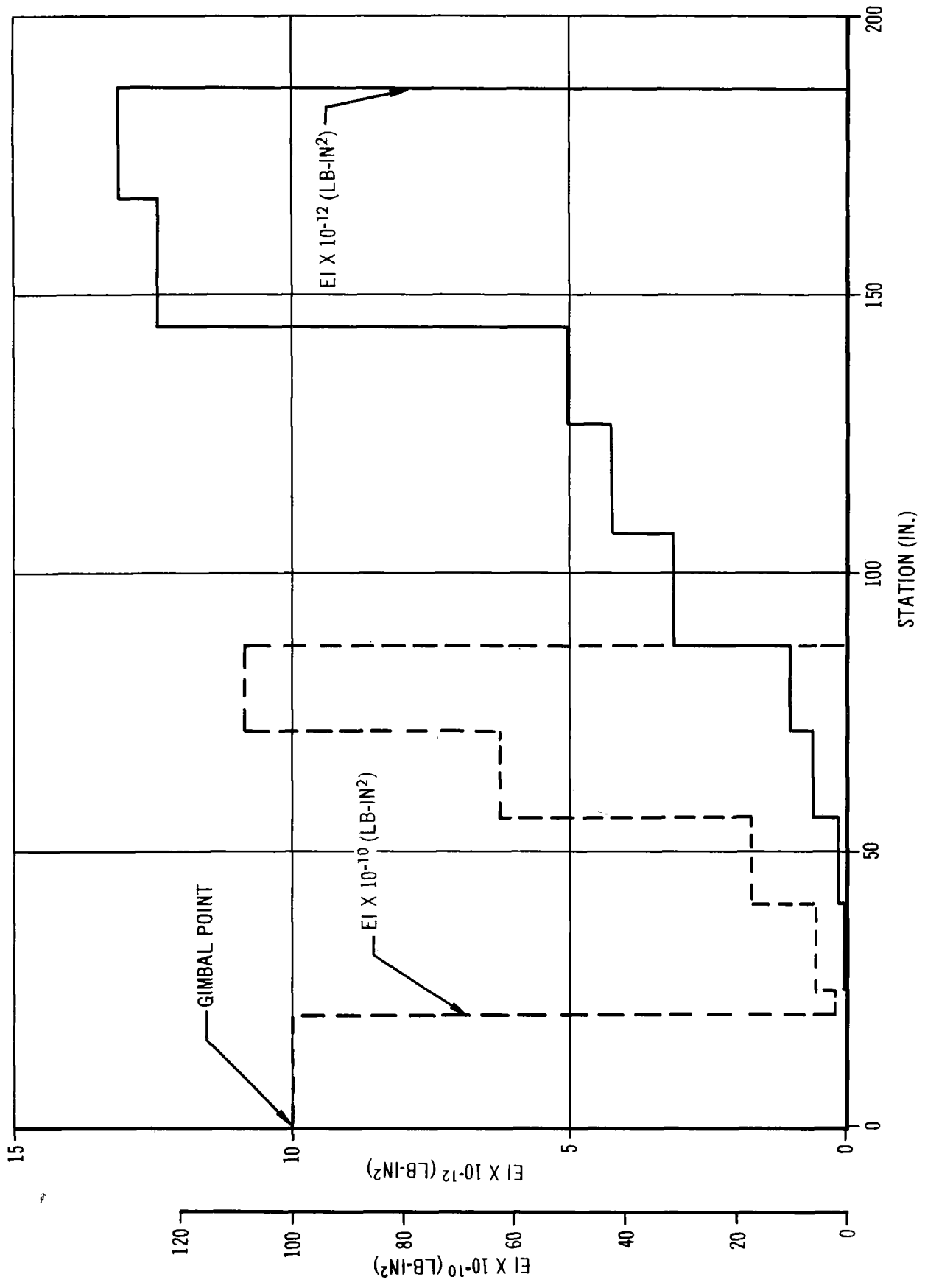


FIGURE 4

The dynamical matrix was iterated to find the dominant root:

$$[F] \begin{vmatrix} q \end{vmatrix} = \lambda \begin{vmatrix} q \end{vmatrix}$$

where  $q$  = eigenvector (mode shape)

$\lambda$  = eigenvalue ( $1/\omega^2$ )

The resulting frequency was 29.8 cps.

The preceding analysis assumed the restraint around the gimbal point to be rigid. However, preliminary data has indicated the flexibility of the actuator attach points and gimbal point will be of such a magnitude to result in an engine natural frequency of about 8 cps. To account for these local flexibilities, the restraint around the gimbal was relaxed by several degrees, and the roots were extracted for each restraint setting.

An approximation to the solution was performed by eliminating the  $h$  degree of freedom. The roots of the resulting single degree of freedom system were extracted for each restraint setting.

The roots by the approximate method and the rigorous method were plotted against one another in figure 5. The accuracy of the approximation is apparent in the 0-10 cps region. The effect of  $h$  on the system can also be evaluated by determining the instantaneous center of rotation from the eigenvectors. This center is plotted as distance removed from the gimbal vs. frequency (fig.6). At 10 cps the center of rotation is only about 2.5" away.

The resulting single degree of freedom system is depicted in figure 7. The engine servo admittance has been approximated for this analysis by a second order function.

The characteristic equation for the system is then:

$$(I_{HL} s^2 + Ds + K) \alpha(s) = 0$$

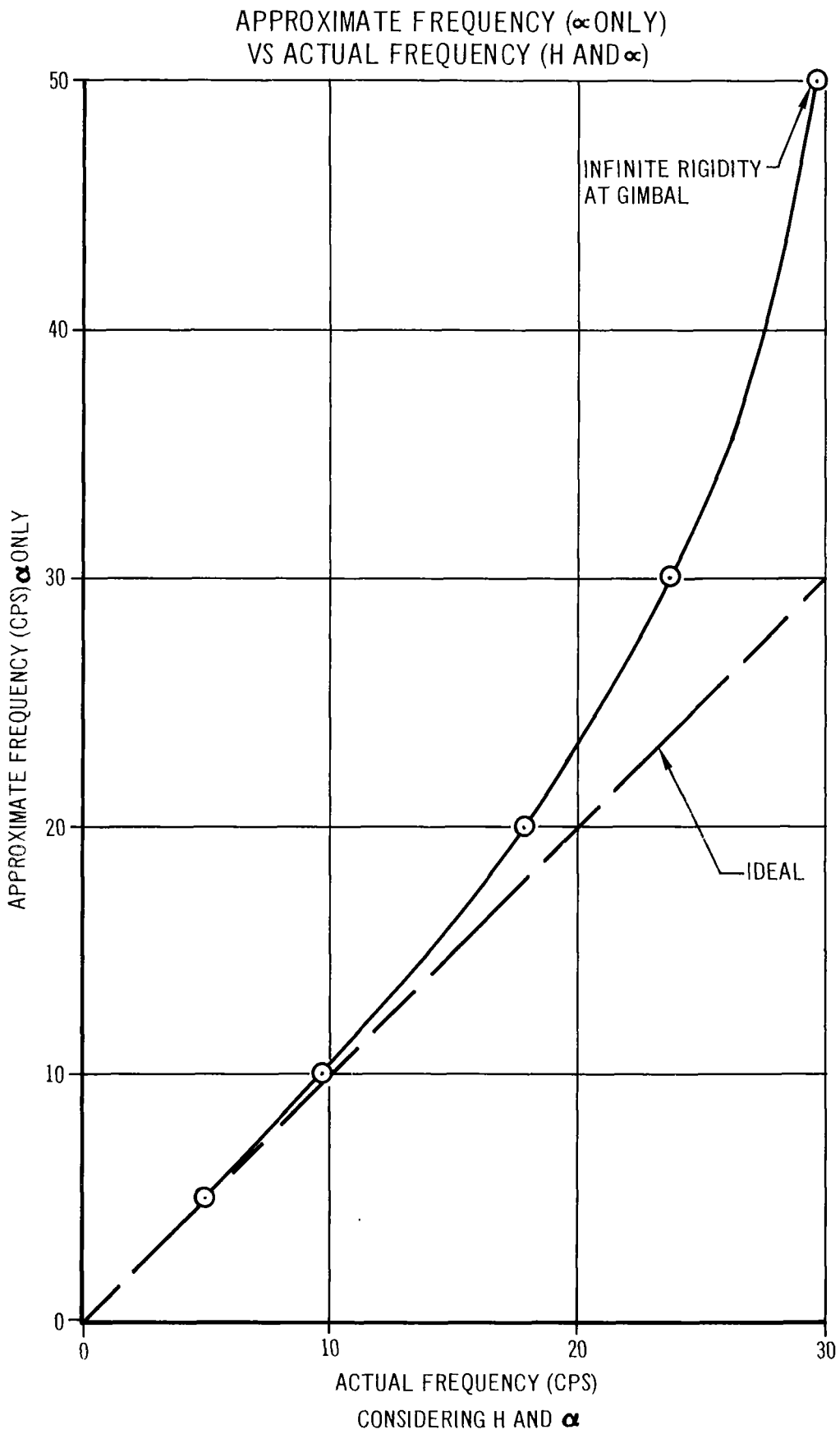
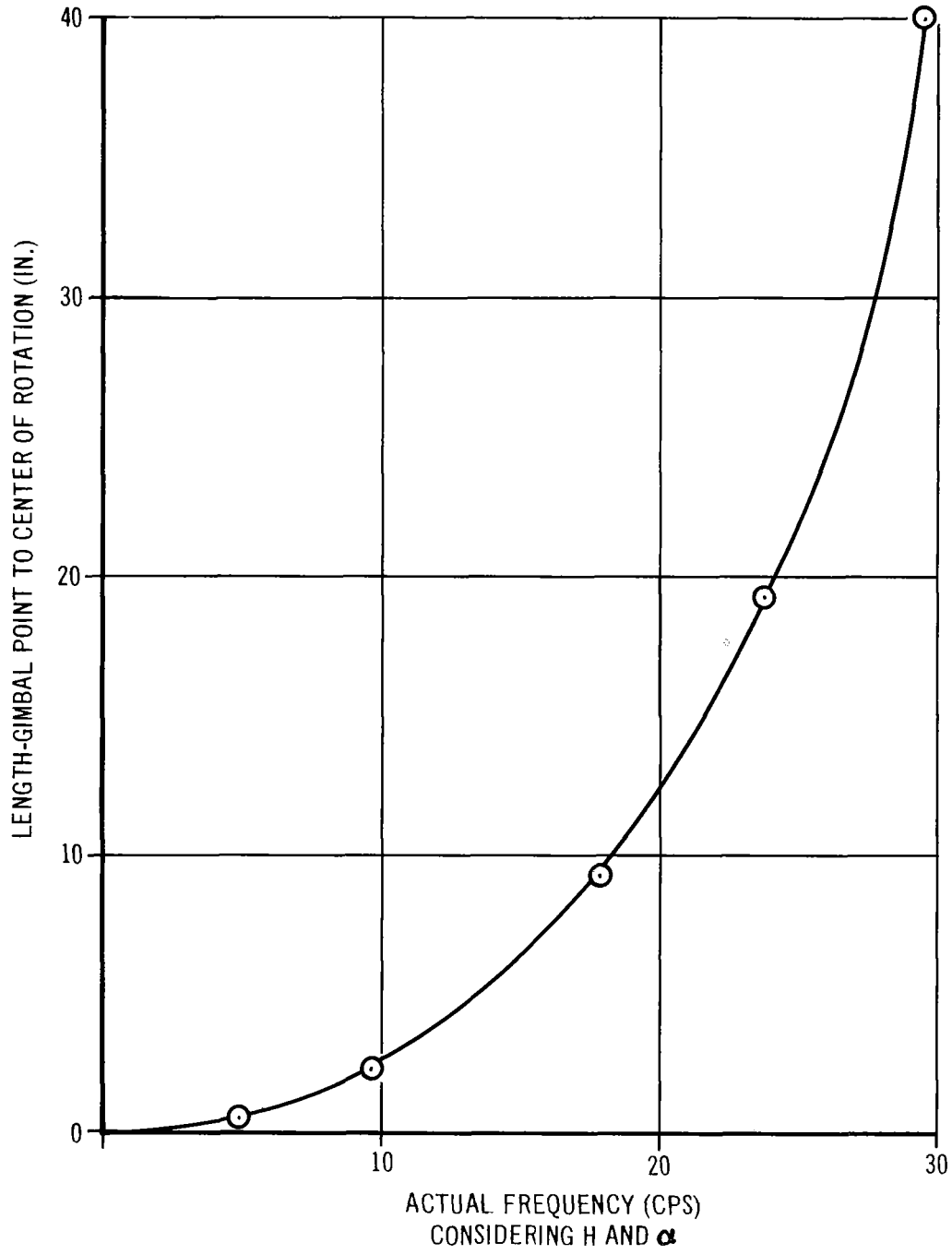


**FIGURE 5**

# CENTER OF ROTATION VS ACTUAL FREQUENCY

**FIGURE 6**



MATHEMATICAL MODEL

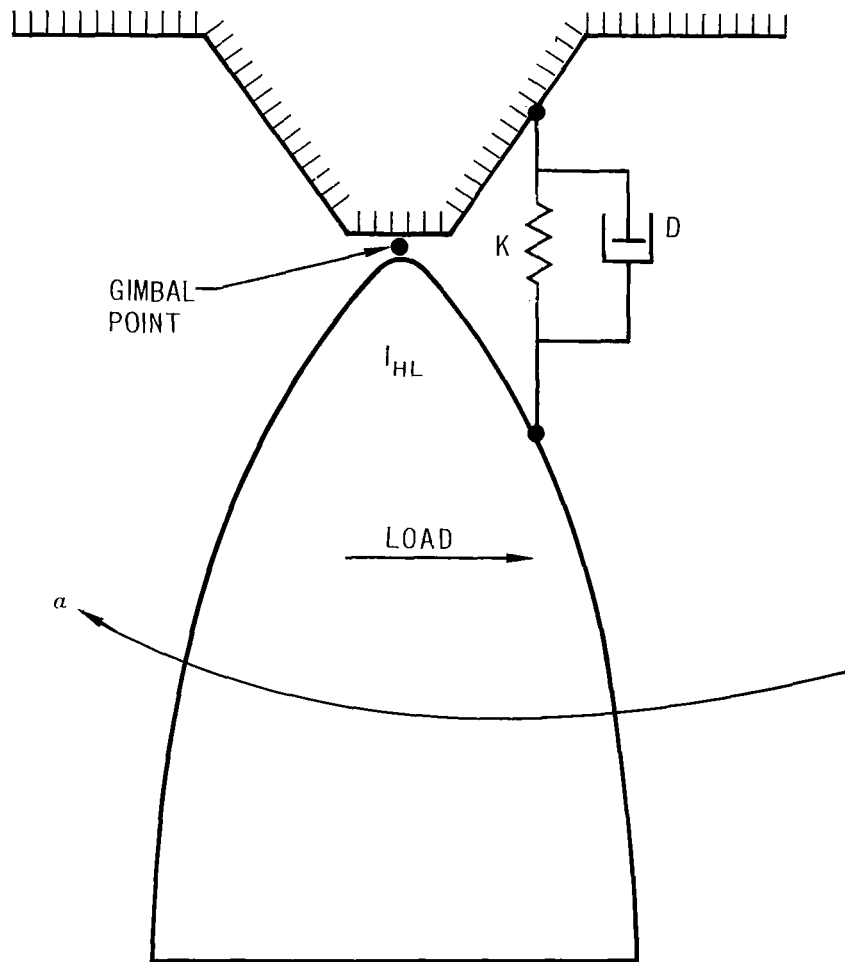


FIGURE 7

The force to be applied to this model was taken from Rocketdyne test #82. The wave form was approximated as a moment of  $4.8 \times 10^5 (1 - \cos \Omega t)$  in lb, for a forcing function frequency of 3 cps. The Laplace transform of the moment is  $4.8 \times 10^5 \frac{\Omega^2}{s(s^2 + \Omega^2)}$ . The system with force imposed is

$$(I_{HL} s^2 + DS + K) \alpha(s) = \frac{4.8 \times 10^5 \Omega^2}{s(s^2 + \Omega^2)}$$

or

$$\alpha(s) = \frac{4.8 \times 10^5 \Omega^2}{s(s^2 + \Omega^2)(I_{HL} s^2 + DS + K)}$$

Two variables (D & K) which are used to represent the servo dynamics are as yet undefined in the S-IVB design, and a single solution of the above was not possible. Thus, time responses were obtained from the above for various values of D and K. Since natural frequency,  $\omega$ , is a function of spring, the data was computed in terms of the frequency ratio,  $\omega/\Omega$ . Damping is equal to  $2 \zeta \omega I_{HL}$  for  $\zeta$  equal to the ratio of damping to critical damping. Therefore,  $\zeta$  was the variable used to describe damping.

The maximum load experienced during a one second time interval of the resulting time response was assumed to be the maximum load the engine will experience. These actuator loads are plotted versus frequency ratio for various damping ratios in figure 8.

For an engine natural frequency of 8 cps, an actuator load between 70,000 and 90,000 pounds resulted. However, if the engine frequency had been 3 cps ( $\omega/\Omega = 1$ ), actuator loads between 100,000 and 390,000 pounds would have resulted.

LOAD ON ACTUATOR VS RATIO OF SYSTEM  
NATURAL FREQUENCY TO FORCING FREQUENCY

$\omega$  = FREQUENCY OF THE SYSTEM

$\Omega$  = FREQUENCY OF THE FORCING FUNCTION - *20/5*

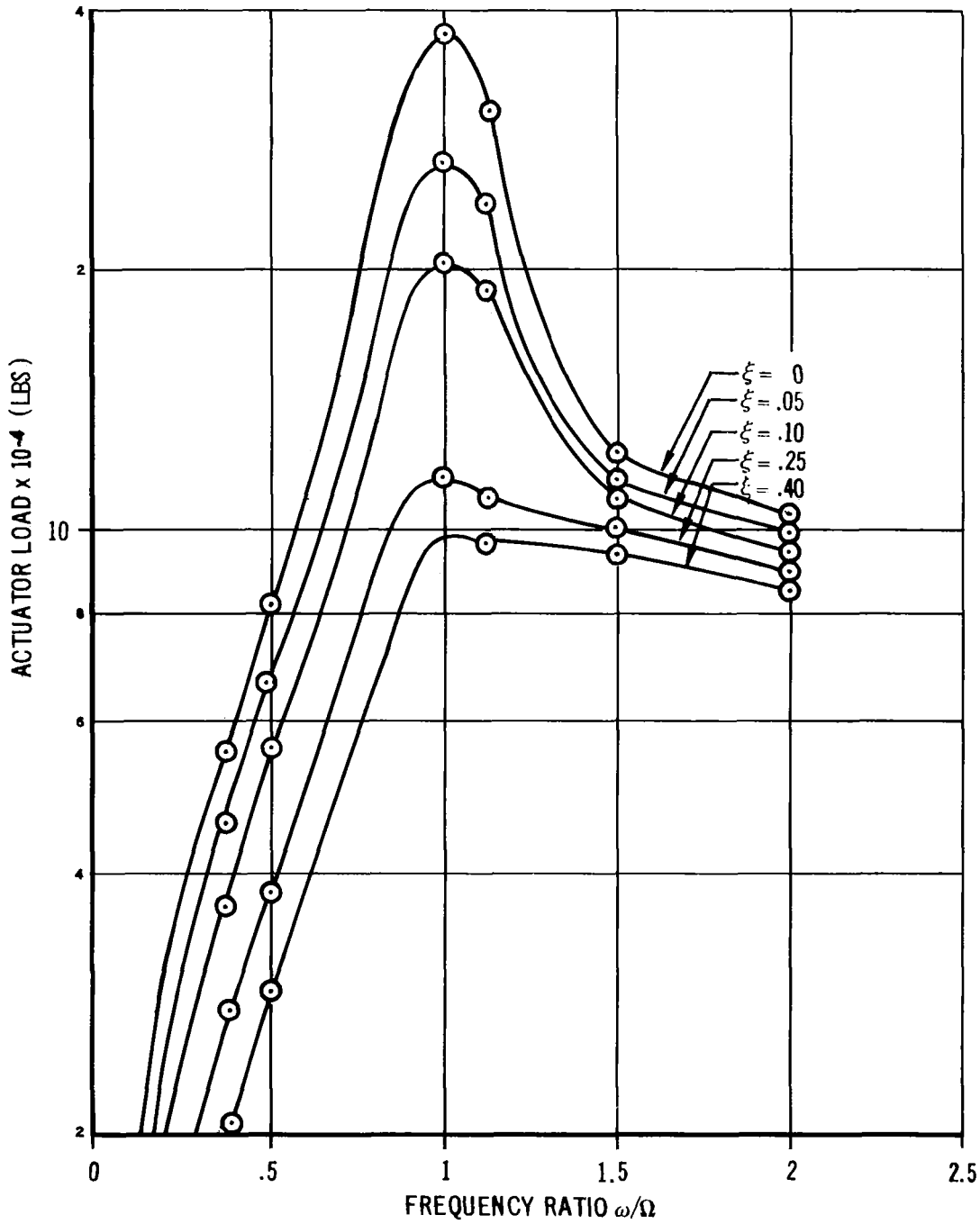


FIGURE 8

### CONCLUSIONS:

✓ For the nominal expected engine boundary conditions ( $F_n = 8$  cps,  $\zeta = .4$ ), the actuator loads exceeded the design condition of 42,000 pounds. Of all of the parameters considered in this study, the only one that might be subject to change for an advantage would be the forcing function. As the magnitude of the force decreases, the resultant actuator load will proportionally decrease. The likelihood of this force lessening is not out of the realm of probability. The Rocketdyne data thus far has been from the Block 1 engine while the Block 2 is expected to render a quicker start and hence decreased starting loads. Also, the assumption that the starting load is independent of engine dynamics might be invalid. If the starting load is a function of engine dynamics, the resultant actuator loads would be less with dynamic pressure feedback than the case for the actuator acting as a straight mechanical link. Whether or not the load is independent will be proved out in subsequent static firings at Rocketdyne.

## Section 2

### EFFECTS OF VEHICLE BENDING, SLOSHING & RIGID BODY PARAMETERS ON SERVO ACTUATOR SYSTEM REQUIREMENTS

In determining the basic requirements of the Saturn S-IVB attitude control system for the hydraulic servo valve, several variables must be considered along with the basic requirements of the attitude control system.

The following requirements have been used for this analysis:

- 1) The rigid body operating frequency should be approximately 0.2 cps throughout flight. Since vehicle inertia varies with burn time, a range of 0.15 cps to 0.35 cps is normally used.
- 2) The gain margin on the servo loop must be at least 12 db at low frequencies and at least 8 db at high frequencies for the servo valve combined with the rigid body.
- 3) The phase margin should be at least  $35^{\circ}$  for all burn time and preferably larger.
- 4) The system should be stable for all frequencies. This requirement cannot be met due to an unstable hydrogen sloshing root. However, the time constant of this instability is very large and the system becomes stable at approximately 20% burn time.

With these requirements as a guide, total loop gain and actuator loop constants were varied to establish an optimum operating area. Although rigid body requirements were primarily considered, body bending resonances were attenuated as much as possible in most analyses. A block diagram of the system used is shown in figure 14. The associated parameters are also given with the values used. Those listed as variable parameters are most important since they represent the adjustment capability for this study. Figures 1 and 2 indicate the effect of  $K_{FB}$  on rigid body operating frequency and low frequency gain margin for 0% and 100% burn times. The

curves are also shown with the necessary lag which is part of derivative rate feedback. This lag corner frequency was held at 2 cps. These figures indicate that a feedback gain of 30 would result in satisfactory rigid body operating characteristics throughout flight. Although this derivative rate lag reduces rigid body gain margin, it stabilizes the otherwise unstable bending modes.

By varying  $K_{\theta}$  (attitude loop gain) along with  $K_{FB}$ , a set of two loop and one loop Nyquist responses were made at both burn out and ignition. A sampling of the most informative responses were plotted (figures 3 thru 8). These responses also indicate that a servo valve feedback value of  $30 \mu\text{a}/\text{deg}$  is optimum if no gain change is to be made. The following additional comments can be made from these Nyquist plots:

1) The rigid body operating frequency will vary from 0.14 cps at 0% BT to 0.34 cps at 100% BT for a  $K_{FB}$  of  $30 \mu\text{a}/\text{deg}$  as seen in figures 1 and 3.

2) The rigid body low frequency gain margin is exceptionally good at both ignition and burn out. To increase this margin would increase the magnitude of the bending modes and decrease the high frequency gain margin which just meets the gain requirement of 8 db.

3) There is no problem on rigid body phase margin when using a  $K_{FB}$  of  $30 \mu\text{a}/\text{deg}$ . In all cases it is greater than 35 degrees as evidenced by figures 3, 4, 5, 6, etc.

4) A notch network will probably be required in order to gain and phase stabilize the bending which increases to unacceptably large values toward the end of flight.

As can be seen from figure 13, which is a frequency response for the closed servo loop, there is over 28 degrees of lag at 1 cps. However, there is less than 5% overshoot.

In an effort to determine the effect of the two constants  $H_0$  and  $\tau$  on the autopilot, figures 9, 10, 11, and 12 were plotted. Figure 9 is an open motor loop Nyquist of the attitude control system and represents a reduced value of  $H_0$  while holding  $\tau$  constant. Figure 10 is the closed motor loop Nyquist of the same system. By comparing figure 9 with 3 it is seen that there is a slight reduction in gain margin and a slight increase in crossover frequency for the lower  $H_0$ . However, as might be expected, the magnitude in the first body bending mode was increased for the lower value of the pressure feedback constant.

A similar study was made on  $\tau$  holding  $H_0$  constant. Figure 10 is the open loop servo and figure 12 the closed loop servo Nyquist for the attitude control system. The effect of  $\tau$  as shown by the comparison of figures 11 and 3 is much greater than that of  $H_0$ . As  $\tau$  is decreased, the high frequency gain margin is markedly decreased. The phase margin is increased and the bending modes are magnified.

From the above study it is seen that by relaxing frequency response overshoot requirements of the servo valve, the overall stability margin of the system is decreased. It therefore appears that the frequency response overshoot should be minimized. Also, the above study was made assuming certain values for the spring rates for the servo valve (see figure 14 and table I).

Since spring rates such as the thrust structural spring constant may change by a factor of 10, the actuator loop constants will be made sufficiently adjustable to provide optimum performance characteristics when the actual flexural environment is known.

To summarize, the following parameter values seem to be optimum at this time:

$$K_{FB} = 30 \mu a/\text{deg} \text{ or } 283 \text{ cis}/\text{deg}$$

$$K_{\theta} = 28.8 \mu a/\text{deg}$$

$$\tau = .1 \text{ sec}$$

$$H_o = .025 \text{ cis}/\text{psi}$$

Derivative rate lag corner frequency = 2 cps

Analyses to date have been concentrated on the C-5 vehicle as it is in general the most critical. One exception is GIB with the escape tower (first 15 seconds of burn time). Stability studies are continuing in this area with emphasis on keeping as many gain parameters as possible common for both configurations. Although the above parameters are analyzed on a total loop basis, they will be reflected in engine actuator loop frequency response characteristics similar to figure 13 for testing purposes.

TITLE: For 0% Burn Time

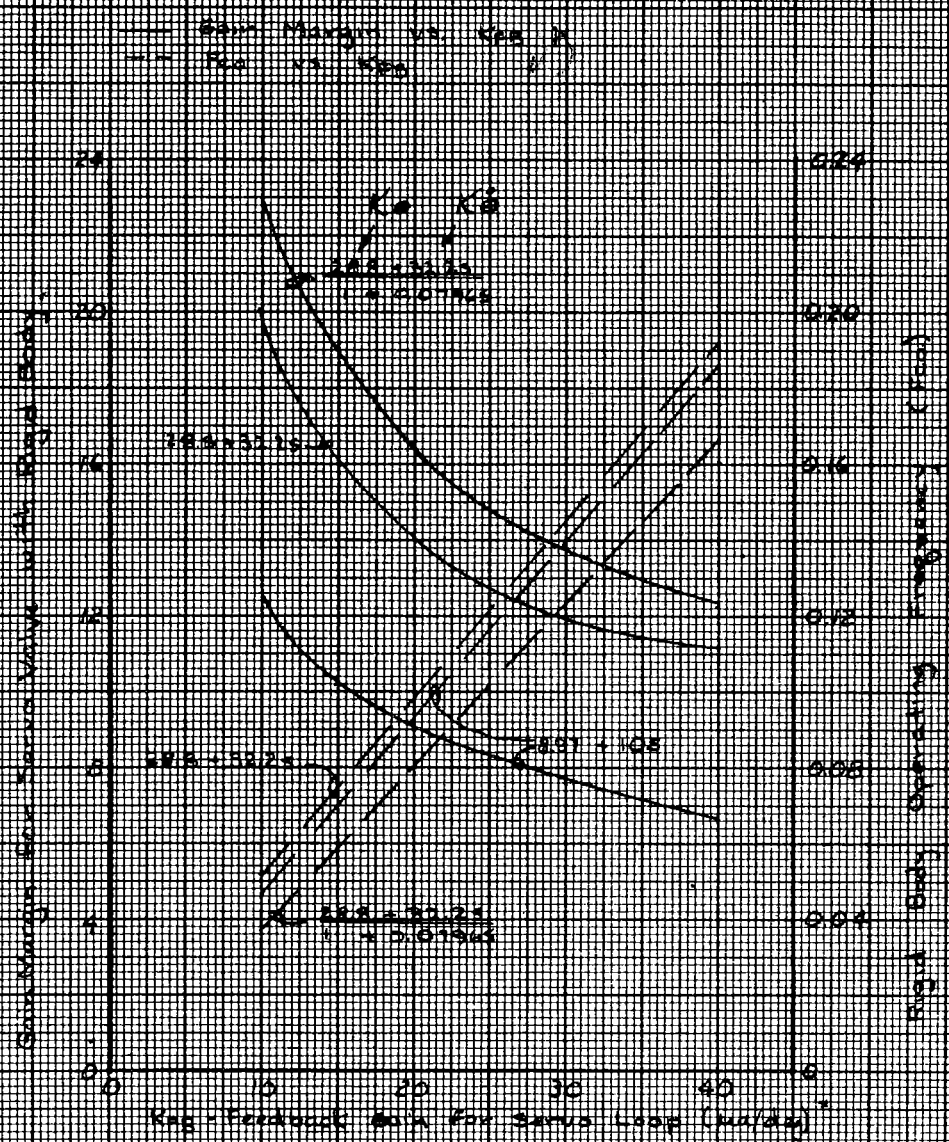


Figure 1.  $K_p$  vs Gain Margin & Crossover Frequency for the Altitude Control System at 0% Burn Time

Note: 1 pole/deg = 0.055 rad/sec



TITLE: For 100% Burn Time

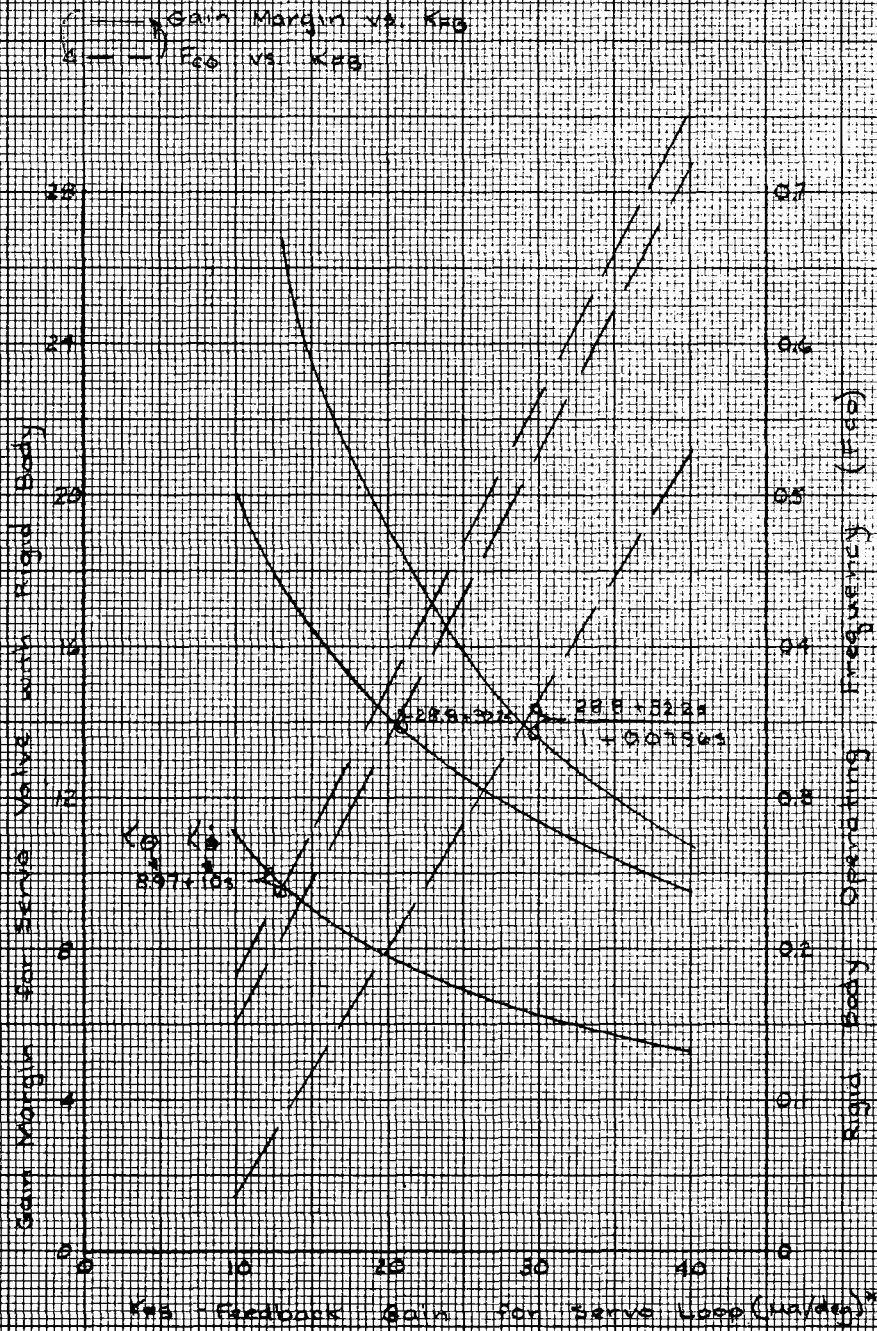
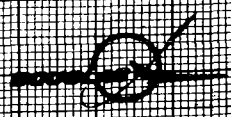


Figure 2  $K_{FB}$  Vs. Gain Margin & Crossover Frequency For the Altitude Control System at 100% Burn Time

\*Note: 1 rad/deg = 0.573 cis/deg



TITLE: 0 % Burn Time, Open Loop Motor loop

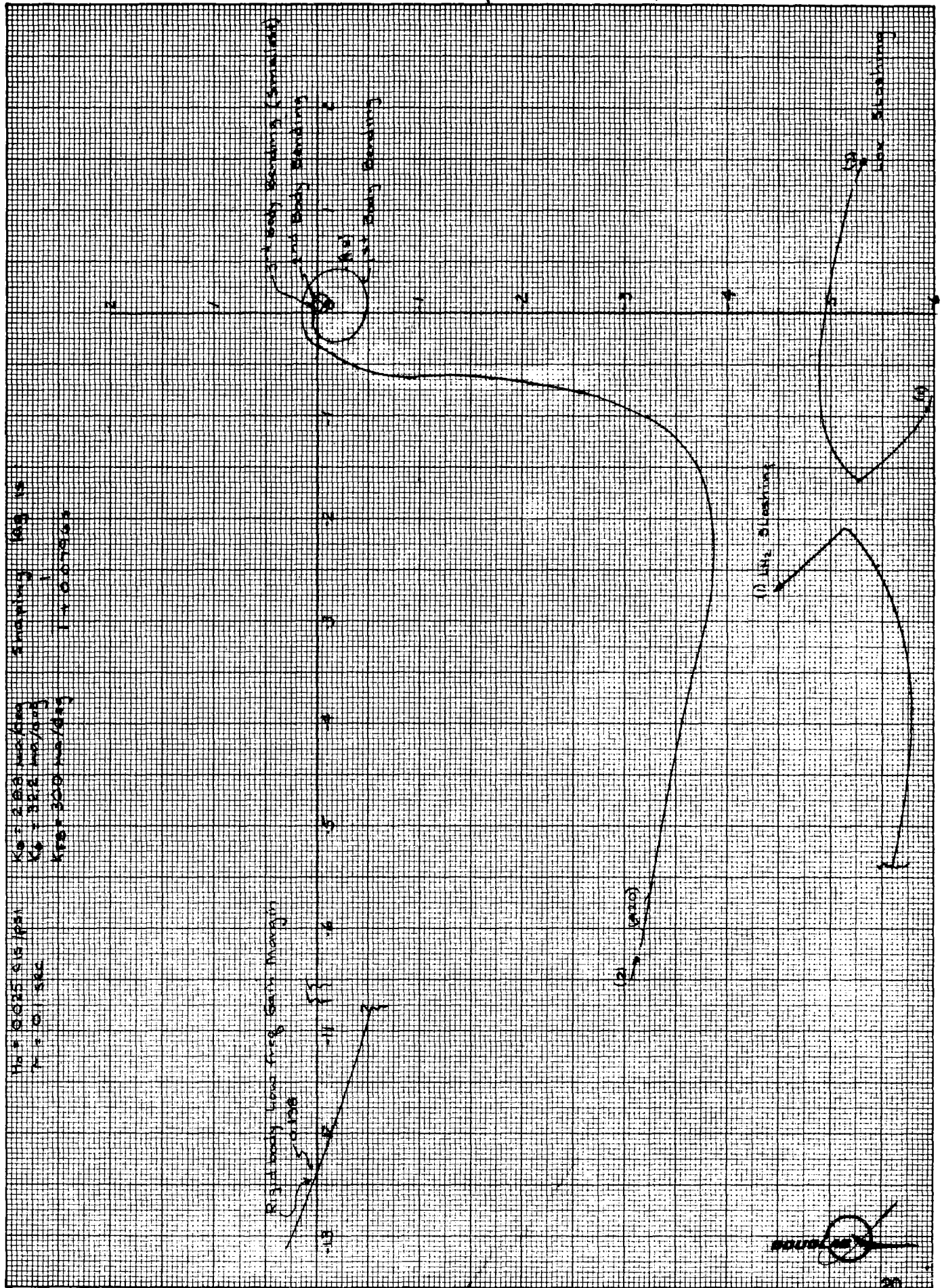


Figure 3

TITLE:  $0\frac{1}{2}$  BT Closed Loop Motor loop

$H_n = 0.025 \text{ in/ps}$   
 $T = 0.1 \text{ sec}$

$K_p = 28.5 \text{ in/deg}$   
 $K_v = 32.2 \text{ in/deg}$   
 $K_{\omega} = 30 \text{ in/deg}$

Shaping Lag  $\tau_s$ :  
 $\tau_s = 0.075 \text{ sec}$

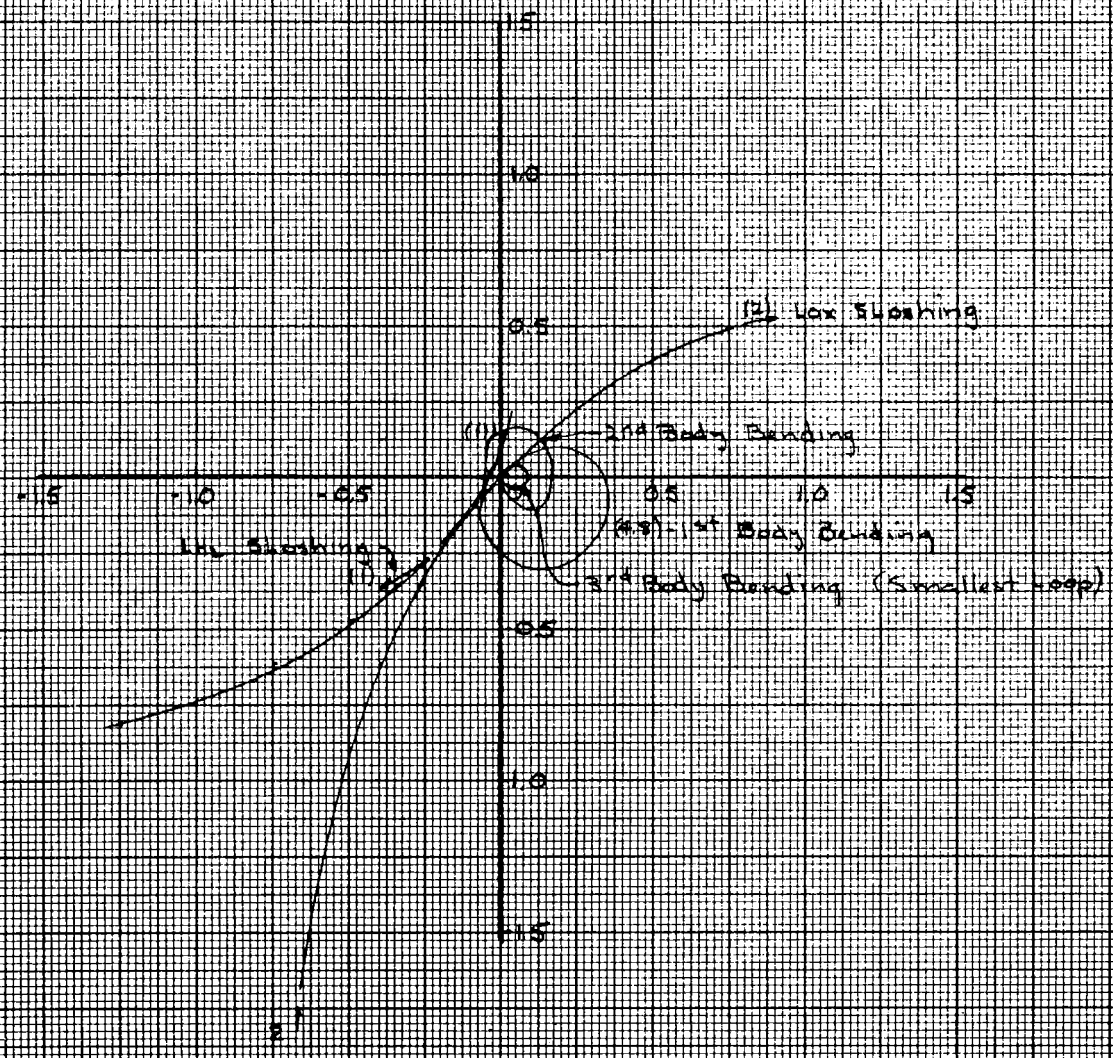
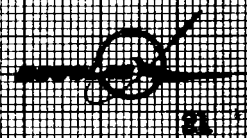


Figure 4







TITLE: 100% Burn Time; Closed Loop Servo Loop

$M_v = 0.025 \text{ cm/deg}$   
 $T = 0.1 \text{ sec}$

$K_p = 299 \text{ rad/deg}$   
 $K_v = 322 \text{ rad/deg}$   
 $K_{ra} = 30 \text{ rad/deg}$

Shaping Lag  $15$   
 $\tau = 0.0796 \text{ sec}$

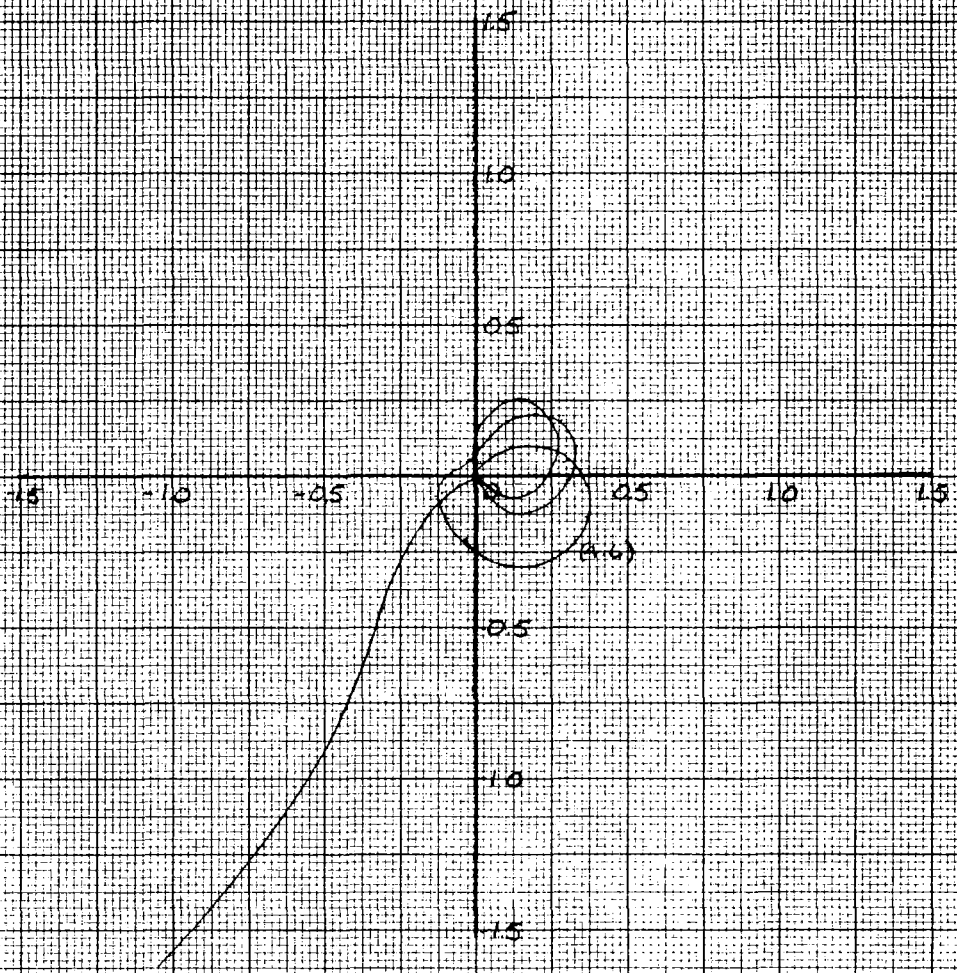


Figure 7









TITLE: 0% Burn Time, Open Loop Motor Loop

$K_p = 0.0250 \text{ s/m}$   
 $K_v = 0.0386$   
 $K_a = 2.819 \text{ Hz/Hz}$   
 $K_b = 32.2 \text{ Hz/Hz}$   
 $K_{fs} = 30 \text{ Hz/deg}$   
 Shipping Lag is  
 $1.400 \text{ s}$

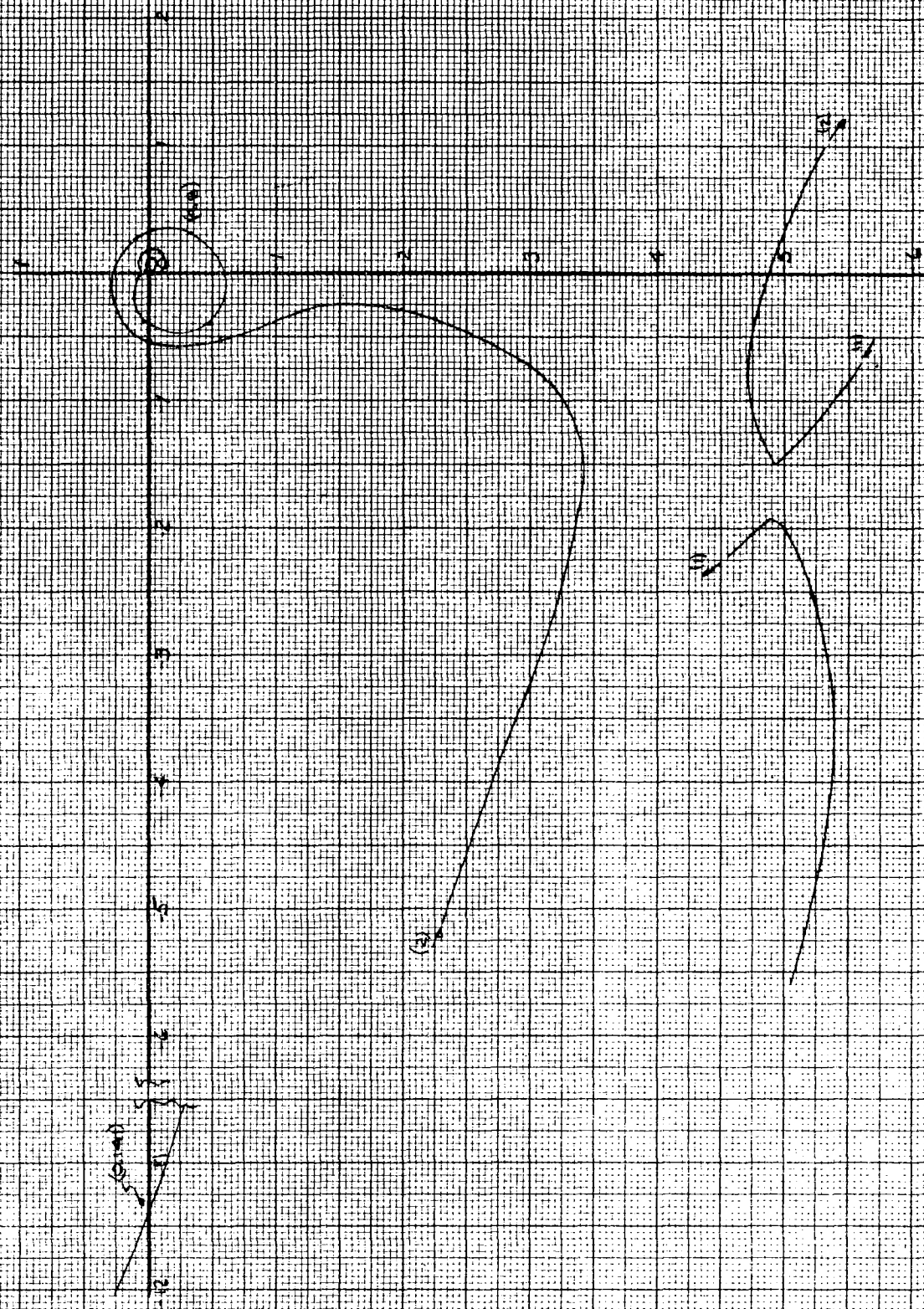


FIGURE 11

TITLE: 0% Burn Time Closed Loop Motor Loop

$K_D = 0.025 \text{ lbs/psi}$   
 $T = 0.05 \text{ sec}$

$K_a = 288 \text{ ma/deg}$   
 $K_e = 32.2 \text{ ma/deg}$   
 $K_{FB} = 30 \text{ ma/deg}$

Shipping Lag =  $\tau$   
 $1 + 0.0796s$

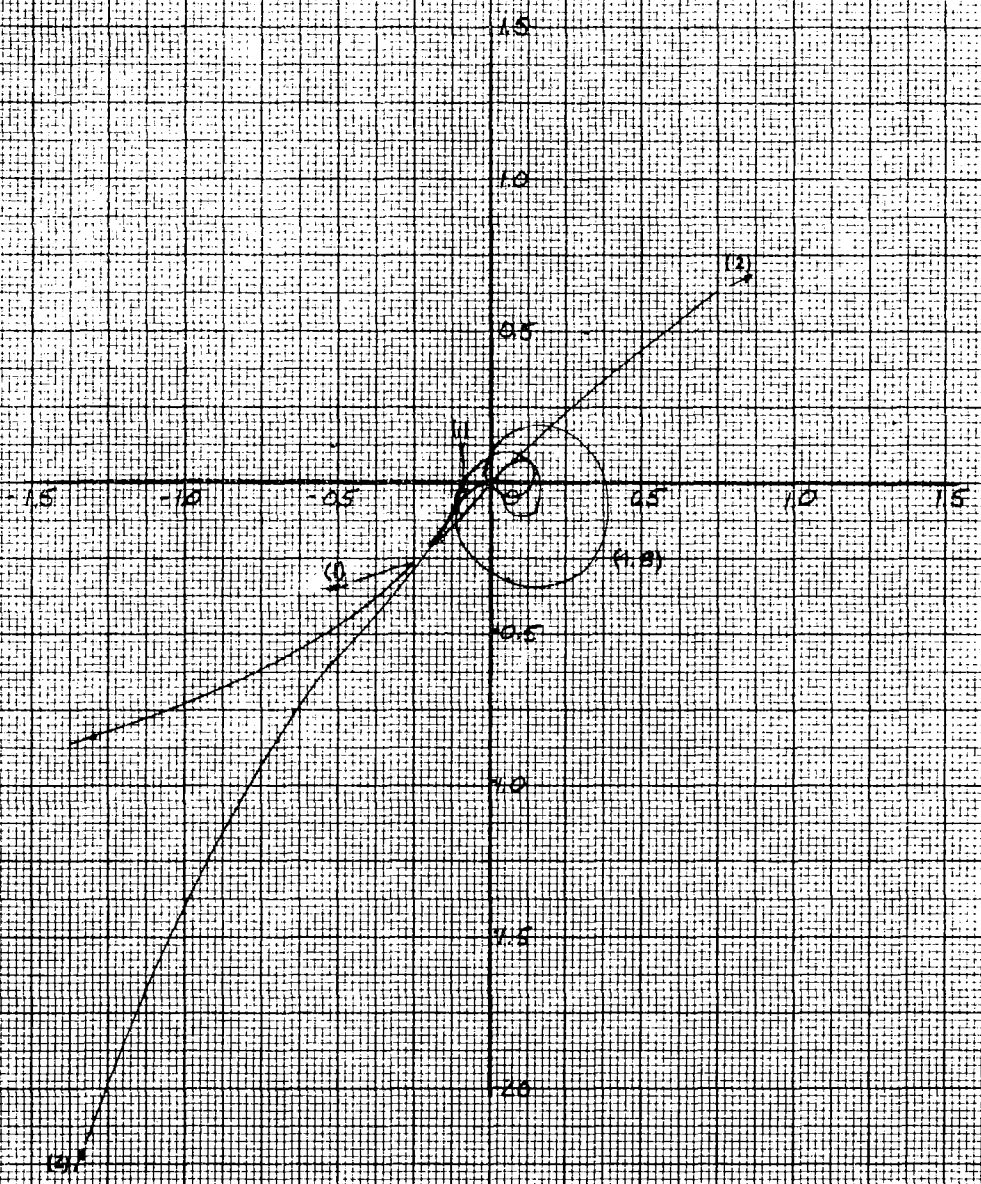
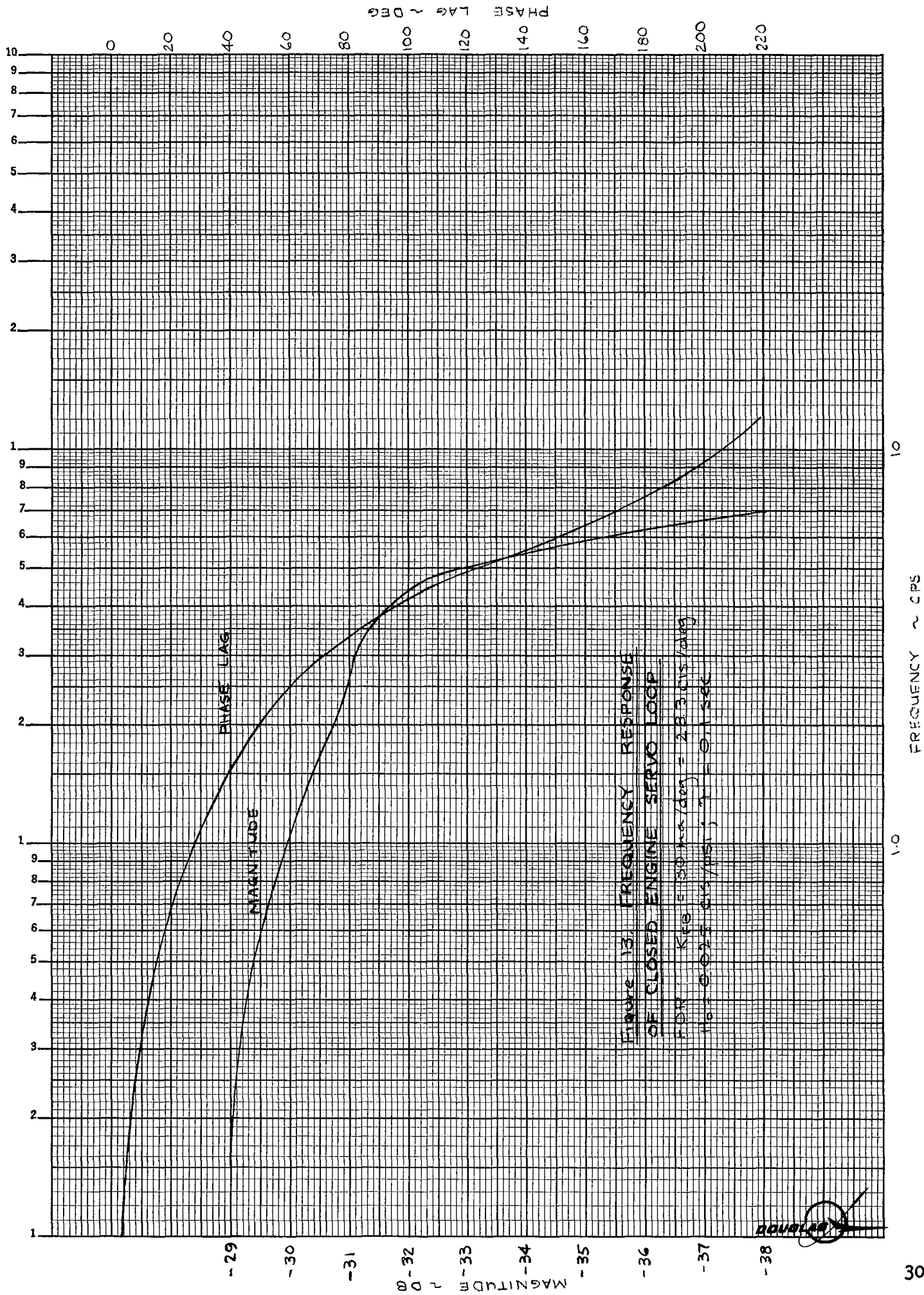


FIGURE 12







FIXED PARAMETERS

T M	Torque Motor
$\mu_a$	Amplifier Gain
$F_a(s)$	Amplifier Dynamics - TBD
$\mu_v$	Valve Flow Gain - $5.8 \text{ in}^3/\text{sec}/\text{ma}$ $\mu_a \mu_v = .944 \text{ in}^3/\text{sec}/\text{ma}$
$l_a$	Actuator Lever Arm - 0.99 ft.
A	Effective Piston Area - $115 \text{ in}^2$
$D_g$	Gimbal Friction Constant - 0 lbs - sec/in
$I_m$	Moment of Inertia about Gimbal Point - $1286 \text{ slug} - \text{ft}^2$
$K_m$	Spring Constant of Engine at Actuator Attach Point - $1.3 \times 10^6 \text{ lb/in}$
$K_n$	Tandem Combination of Hydraulic and Actuator at Attach Point - $0.5 \times 10^6 \text{ lb/in}$
$K_a$	Spring Constant of Structure at Actuator Attach Point - $1.0 \times 10^6 \text{ lb/in}$
$K_g$	Spring Constant of Hose Restraint - 0 lb/in
$K_l$	$= \frac{1}{1/K_m + 1/K_a} ; K_t = \frac{1}{1/K_l + 1/K_h}$
	$= .565 (10)^6 \quad = .266 (10)^6$

VARIABLE PARAMETERS

$H_o$	Dynamic - Pressure Feedback Gain - .0025 & 0.0125 cis/psi
$\tau$	Time Constant of Lag in Pressure Feedback Path - 0.10 and 0.05 sec
$K_{fb}$	Actuator - Position Feedback Gain - See Figures 1 and 2.

FIGURE 14 TABLE 1 - PARAMETERS USED IN ANALYSIS OF ENGINE SERVO LOOP

BENDING PARAMETERS INCLUDED IN VEHICLE DYNAMICS

$\phi_i(x_h)$	Normalized Later Deflection of ith Bending Mode Shape at Gimbal Point
$\phi_i(x_p)$	Slope of ith Bending Mode Shape at Gyro Location
$M_i$	Modal Mass of ith Bending Mode - Slugs
$M_{B_i}$	Structural Mass of ith Bending Mode
$\omega_{B_i}$	Resonant Frequency of ith Bending Mode - rad/sec

SLOSHING PARAMETERS INCLUDED IN VEHICLE DYNAMICS

$$B_i = \frac{M_a (2\zeta_a \omega_a s + \omega_a^2)}{s^2 + 2\zeta_a \omega_a s + \omega_a^2} \& G_1 \ell_i = \frac{a_x M_a \ell_a}{s^2 + 2\zeta_a \omega_a s + \omega_a^2}$$

where:

$M_a$	=	Sloshing mass of a <sup>th</sup> mode - slugs
$\ell_a$	=	Location of a <sup>th</sup> sloshing mass - ft
$\zeta_a$	=	Structural damping ratio of a <sup>th</sup> sloshing mass
$\omega_a$	=	Resonant frequency of a <sup>th</sup> sloshing mode-rad/sec
$a_x$	=	Axial acceleration of missile - ft/sec <sup>2</sup>
$M$	=	Mass of rigid Body - slugs

TAIL-WAGS-DOG PARAMETERS INCLUDED IN VEHICLE DYNAMICS

$T$	=	Thrust at gimbal point from engines-lb/in
$L$	=	Distance from CG of rigid body to gimbal point (ft)
$m$	=	Mass of engine-slugs
$\ell$	=	Distance from CG of engine to gimbal point (ft)
$I$	=	Moment of inertia of rigid body (slug - ft <sup>2</sup> )

VARIABLE ATTITUDE SHAPING DYNAMICS

$$K_{AA} = \frac{K_\theta + K \dot{\theta}_s}{1 + \tau_s s}$$

FIGURE 14 TABLE 2 PARAMETER DESCRIPTIONS

TABLE 2 (continued)

where:

$K_{\theta}$  = Position loop gain - 288  $\mu_a/\text{deg}$  and 8.97  $\mu_a/\text{deg}$ .

$K'_{\theta}$  = Rate loop gain - 32.2  $\mu_a/\text{deg}$  and 10  $\mu_a/\text{deg}$

$\tau_1$  = Lag due to differentiation of  $K_{\theta}$  to  $K'_{\theta}$  (0.0796 sec)

<u>RIGID BODY PARAMETERS</u>		
PARAMETERS	0% Burn Time	100% Burn Time
Rigid Body Mass (slugs)	10,183	3,940
Rigid Body Inertia (slugs-ft <sup>2</sup> ) x 10 <sup>6</sup>	7.995	2.53
Rigid Body Center of Gravity (in)	594.2	952

BODY BENDING PARAMETERS

MODE	$\phi$ (H) (in)	$\phi'$ (P)	Freq (cps)	Mass Slugs
0 percent Burn time (1st)	1.0	-0.00238	5.016	1177
0% B T (2nd)	1.0	0.00402	17.25	404
0% B T (3rd)	1.0	0.00326	21.90	387
100% B T (1st)	1.0	-0.00168	6.13	118
100% B T (2nd)	1.0	0.00141	20.68	236
100% B T (3rd)	1.0	0.00269	35.56	41

TABLE 3 PARAMETER VALUES

TABLE 3 (continued)

SLOSHING PARAMETERS

At 0 percent burn time only

Lox sloshing frequency	-	0.3456 cps
Lox sloshing mass	-	1017.8 slugs
Lox mass location	-	316.1 in
LH <sub>2</sub> sloshing frequency	-	0.2857 cps
LH <sub>2</sub> sloshing mass	-	195.9 slugs
LH <sub>2</sub> mass location	-	573.8 in

Note: Gimbal at Sta 200 in.

## Section 3

### SATURN SEPARATION SEQUENCING - S-IVB STAGE

#### INTRODUCTION

The purpose of this analysis is to define the sequence of events which must be followed to obtain a satisfactory separation of the S-IVB stage from the booster. The separation sequencing will be initiated by the engine shut-down signal of the booster. The subsequent sequence of events must then ignite the retro-rockets on the booster, initiate the S-IVB ullage thrust, separate the two stages, switch control to the S-IVB stage and start the S-IVB engine. To achieve a satisfactory separation, each of the events in the separation sequence, including those listed above, must be timed so that under the most adverse conditions possible within the established design criteria, adequate separation distance is obtained before the S-IVB engine start procedure is initiated and vehicle attitude deviations during the post-separation transient do not exceed the capability of the platform. The separation sequence must also be timed so that the weights of the retro-rockets and ullage rocket fuel are minimized. The separation sequence which has been established to meet these general requirements and numerical values for these parameters will be discussed in this Section.

The separation analysis was conducted to meet the following selected requirements:

1. The separation signal will occur when the booster thrust of the stage preceding the S-IVB decays to 10 percent of the nominal thrust.
2. A clearance of 10 feet between the separation aft interstage and the S-IVB engine bell will be attained before the S-IVB J-2 engine start signal will be given.
3. The separation joint will be under compression when the separation device is ignited.

The S-IVB roll is not critical immediately after separation and hence the S-IVB roll control system can be activated at a time between  $T_0$  and the time the J-2 start tank discharge valve opens.  $T_0$  is the time of the separation signal.

The signal to switch the engine position control from the booster of the stage preceding the S-IVB to the S-IVB actuators will occur at the time of the J-2 mainstage signal. This will permit positioning of the S-IVB engine before the thrust buildup has attained the 90 percent level and will not deplete the accumulator gimbaling capability before the J-2 engine can provide power for gimbaling.

The S-IB booster will have four inboard H-1 engines cut off early to allow their thrust contribution to become negligible at the time the four outboard motors are cut off. In the case of the S-II booster, the center fixed engine is shut down early and allowed to deplete its thrust contribution before the four gimballed engines are cut off. This procedure permits a lower thrust level at separation and allows the retro-rocket thrust to be more effective for separation of the S-IVB and the preceding stage.

*5.0  
Shutdown*

#### SEPARATION AND RETRO-ROCKET SIGNAL SPACING

The signals for separation and retro-rockets are given from an airborne computer in the form of a seven bit binary word which is decoded in a stage switch selector and relayed for various operations. Each stage of the Saturn Vehicle has a switch selector which receives simultaneous signals from the computer. A stage select signal determines which selector will be operative to relay the command signal (see figure 1).

Due to the configuration of the switch selector, the minimum time between adjacent required outputs is 100 milliseconds, thus a .1 second restriction is placed upon the separation sequencing. This restriction is shown in the following breakdown of switch selector operating time.

1. The binary coded signal address to the switch selector will be 28 VDC., should not be less than 25 m.s. and should be

back to zero before the readout or clock pulse is given. This clock pulse enables stage power to drive the addressed output.

2. The clock pulse or read command should not be less than 25 m.s.
3. The output pulse from the switch selector will be a minimum of 20 m.s. and a maximum of 50 m.s. depending on the length of the read command pulse.

Should the necessity arise at a later date to require simultaneous signals from the switch selector, the capability is available to connect another circuit in parallel to the switch selector output, however only one signal can be initiated in the switch selector every 100 m.s.

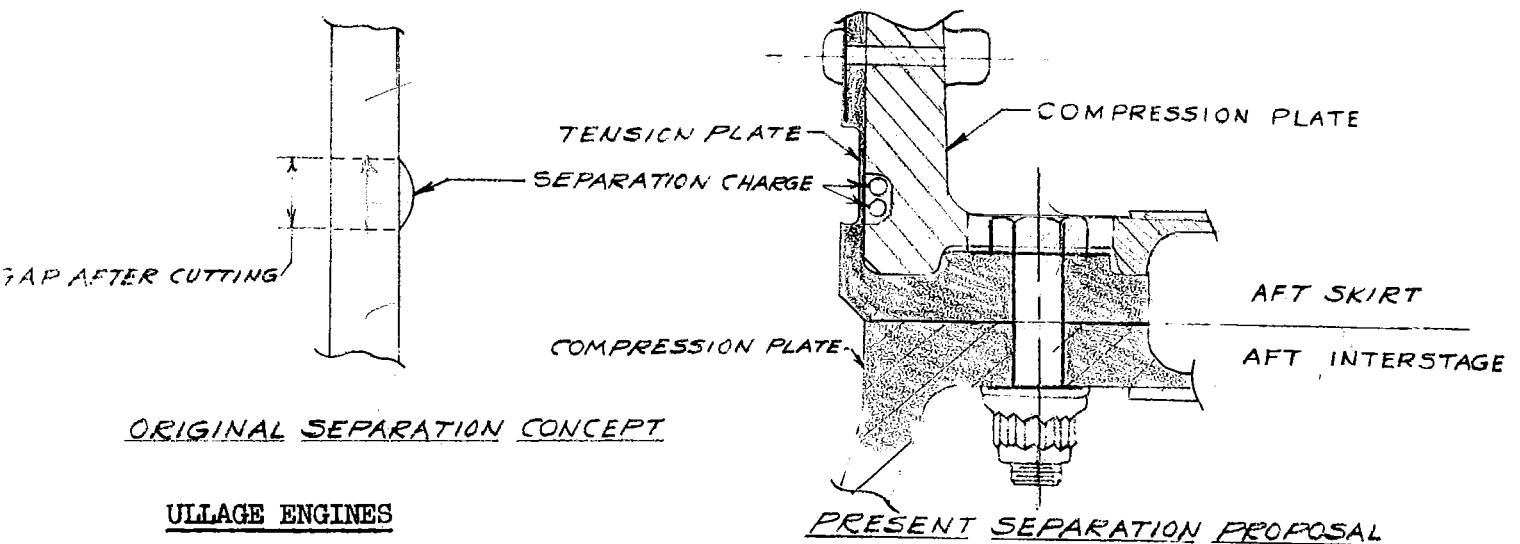
Information on the switch selector was taken from a description of the Saturn switch selector supplied by the Airborne Systems Integration Section, Astrionics Division, Marshall Space Flight Center. Timing signals for events related to separation between the S-IVB and the preceding stage are shown in figures 2 and 3. The timing signals of Saturn IB and Saturn V for ullage, separation and retro rockets are the same, but subsequent commands for the Saturn IB are delayed .6 seconds primarily because of differences between payloads and thrust decay of the S-II and S-IB stages.

#### S-IB AND S-II RETRO-ROCKETS

The S-IB and S-II retro-rockets will be Thiokol Recruits TE-29-1B and will be mounted in the aft interstage of S-IVB. Each retro-rocket develops a thrust of 35,970# @ 70°F., and four of these retro rockets will be used in the S-IVB aft interstage for both the Saturn IB and Saturn V configurations. The nominal burn time of the retro-rocket is 1.55 seconds, and the effective retro thrust as mounted in the S-IVB aft interstage will be 140,000# with four retros and 105,000# with three retros. One retro out capability has been incorporated into the separation sequencing.

## SEPARATION PLANE

It is desirable from the standpoint of separation sequencing to employ the latest proposal for the separation plane between the S-IVB and the preceding stage. This proposal permits the two stages to remain intact under compression loads after the separation explosives sever a tension strap which is bolted to the aft interstage and aft skirt. This type of separation plane eliminates the possibility of collision between stages after the cutting is complete and allows the retro-rockets to be ignited after the separation signal. This separation plane will also allow the use of the slower but more reliable pyrogen igniter rather than the pyro-technic igniter for the retro-rockets. See sketches below for separation planes.



## ULLAGE ENGINES

The S-IVB of the Saturn IB has three TX280 solid rocket motors which serve as ullage engines to seat the S-IVB propellant prior to engine start. Each of these engines has a nominal thrust of 3,390# and a nominal burn time of 3.94 seconds.

The S-IVB of the Saturn V has two 1,750# hypergolic ullage engines which seat the propellant of the S-IVB for J-2 start and restart.

The signal to ignite ullage engines on the S-IVB will be given .1 seconds before the separation signal for both the Saturn IB and Saturn V.

### SEPARATION DISTANCE

Actual physical separation of the stages occurs when the acceleration due to retro thrust plus ullage thrust overcomes the acceleration caused by booster thrust decay. Until this time occurs, the relative velocity, acceleration and distance between the stages is zero.

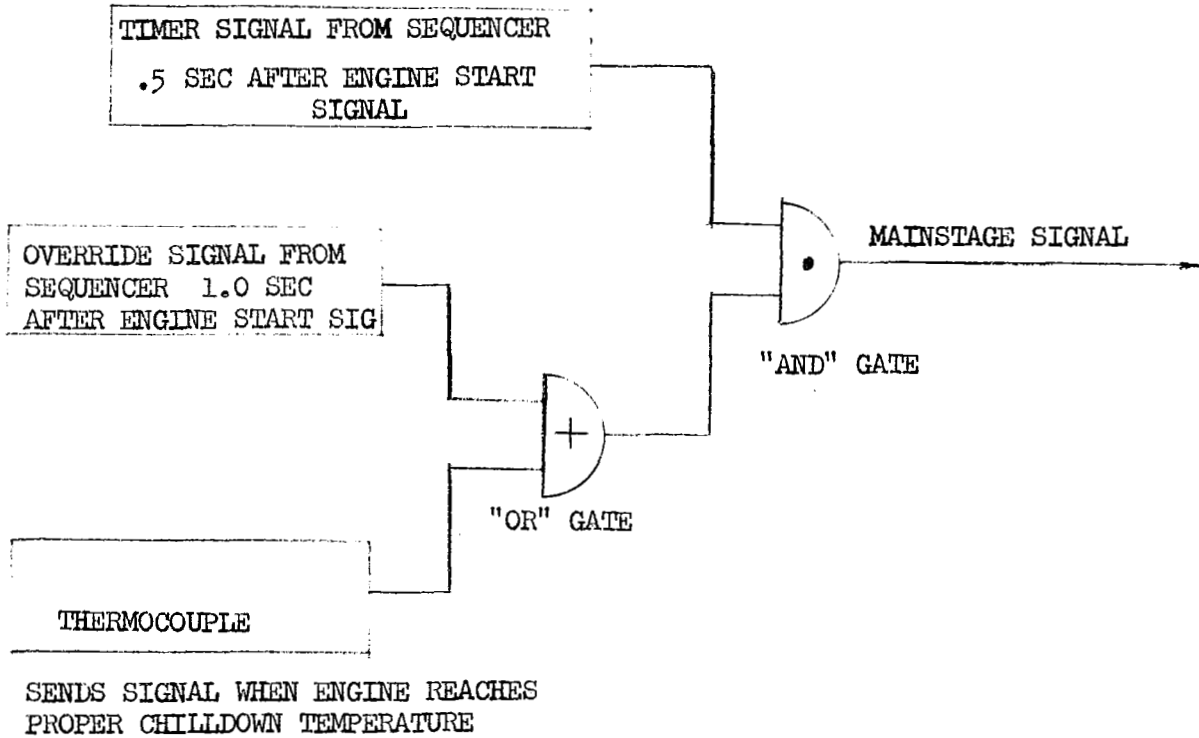
Figure 4 reveals the relationship between the S-IB booster decay thrust and the retro thrust. The tail off of the S-IB booster appears to be excessive, but will be tentatively accepted for separation sequencing until either the thrust decay curve becomes conclusive or a new and more reliable curve is developed. The J-2 engine start signal will be given at a time which will insure a separation distance of approximately 330 inches with a nominal thrust decay and one retro out. The relationship between the S-II booster thrust decay and the retro thrust is shown in figure 5.

Should the high thrust decay prevail at this time, there will only be approximately 4 foot clearance between the S-IVB engine bell and the separated aft interstage when the J-2 engine start signal is given. Figures 4 and 5 show the relationship between time and separation distance between stages. A separation distance of approximately 330 inches between the S-IVB engine bell and the separated aft interstage is sufficient to allow an additional 10 foot clearance after clearance of the engine bell.

### J-2 START SEQUENCE

The J-2 engine start signal initiates a start tank discharge delay timer which allows .5 seconds for J-2 chilldown. At the end of this time, a signal from the timer unit coupled with a signal from a thermocouple operate an "and" gate to produce the mainstage signal after the augmented spark ignition is detected. An override signal has been proposed to prevent termination of mission should the thermocouple have a malfunction and fail to send the signal to operate the "and" gate. This override signal should allow an additional .5 seconds for further chilldown and then supply the "add" gate with the required signal to produce the mainstage signal. See figure below. Figure 6 shows the thrust buildup of the J-2 engine after the start tank discharge valve solenoid is energized. The J-2 engine

attains the slowest 90 percent thrust level approximately 2.8 seconds after the start tank discharge valve solenoid is energized.

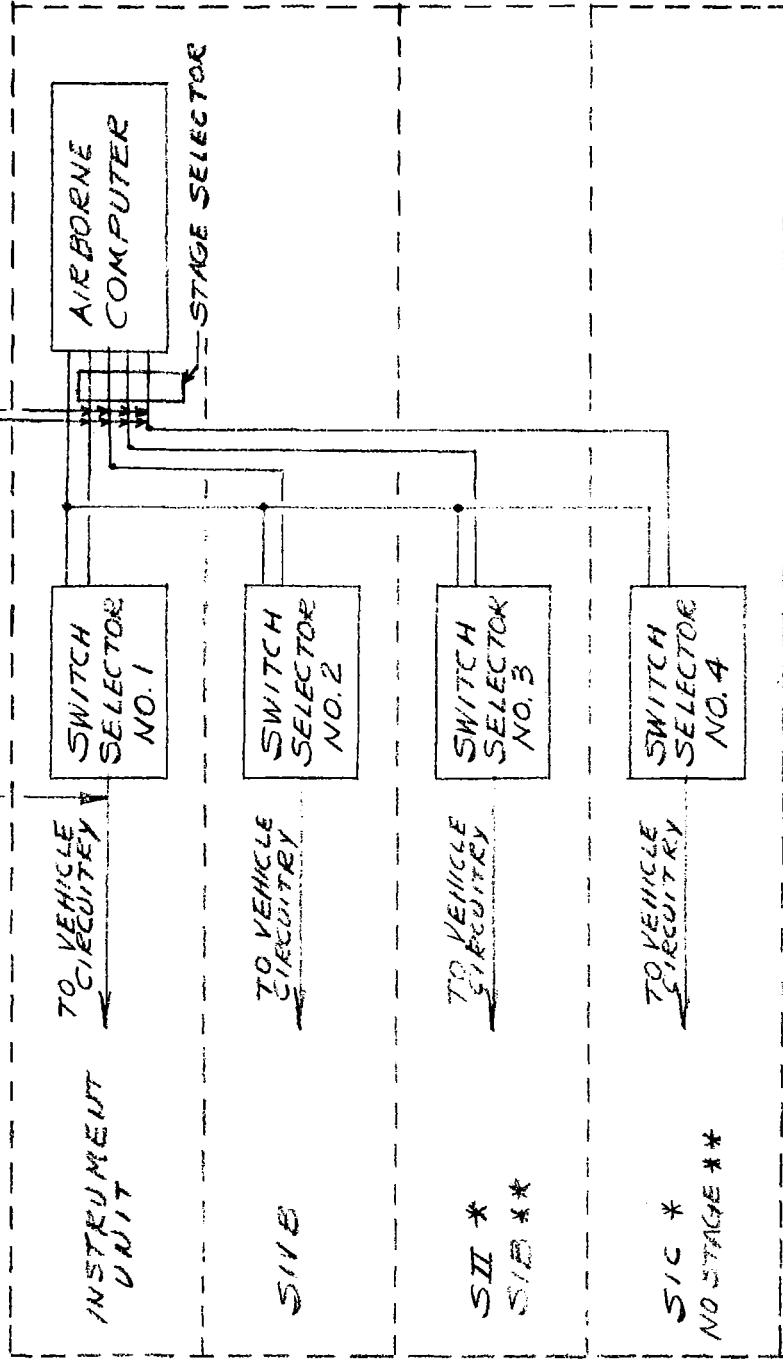


NOTE: The separation sequence analysis is based upon current information on separation component characteristics, and the timing signals for various events will be subject to change should variations in thrust occur.

SWITCH SELECTOR SIGNALS

READ COMMAND AND DELOCK PULSE  
2.5 M.S. MIN. FOLLOWING ADDRESS SIGNAL  
BIT CODED SIGNAL ADDRESS  
2 STAGE SELECT BIT  
MIN. 2.5 M.S.

OUTPUT PULSE  
MIN. 20 M.S.  
MAX. 50 M.S.



INSTRUMENT UNIT

TO VEHICLE CIRCUITRY

S1B

TO VEHICLE CIRCUITRY

S2I \*  
S1B \*\*

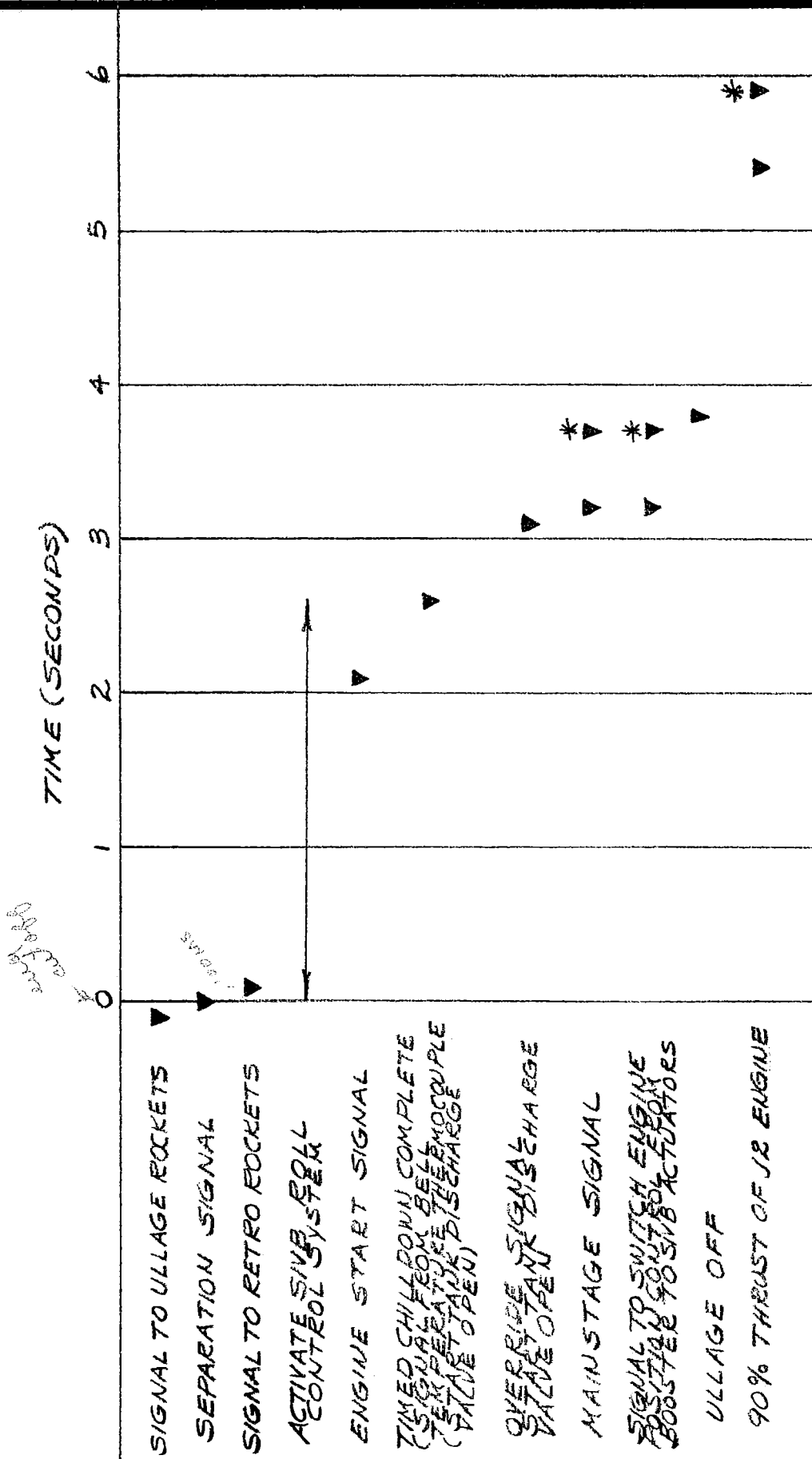
TO VEHICLE CIRCUITRY

S1C \*  
NO STAGE \*\*

TO VEHICLE CIRCUITRY

\* SATURN 5  
\*\* SATURN 1B

SIB/SIB SEPARATION SEQUENCE

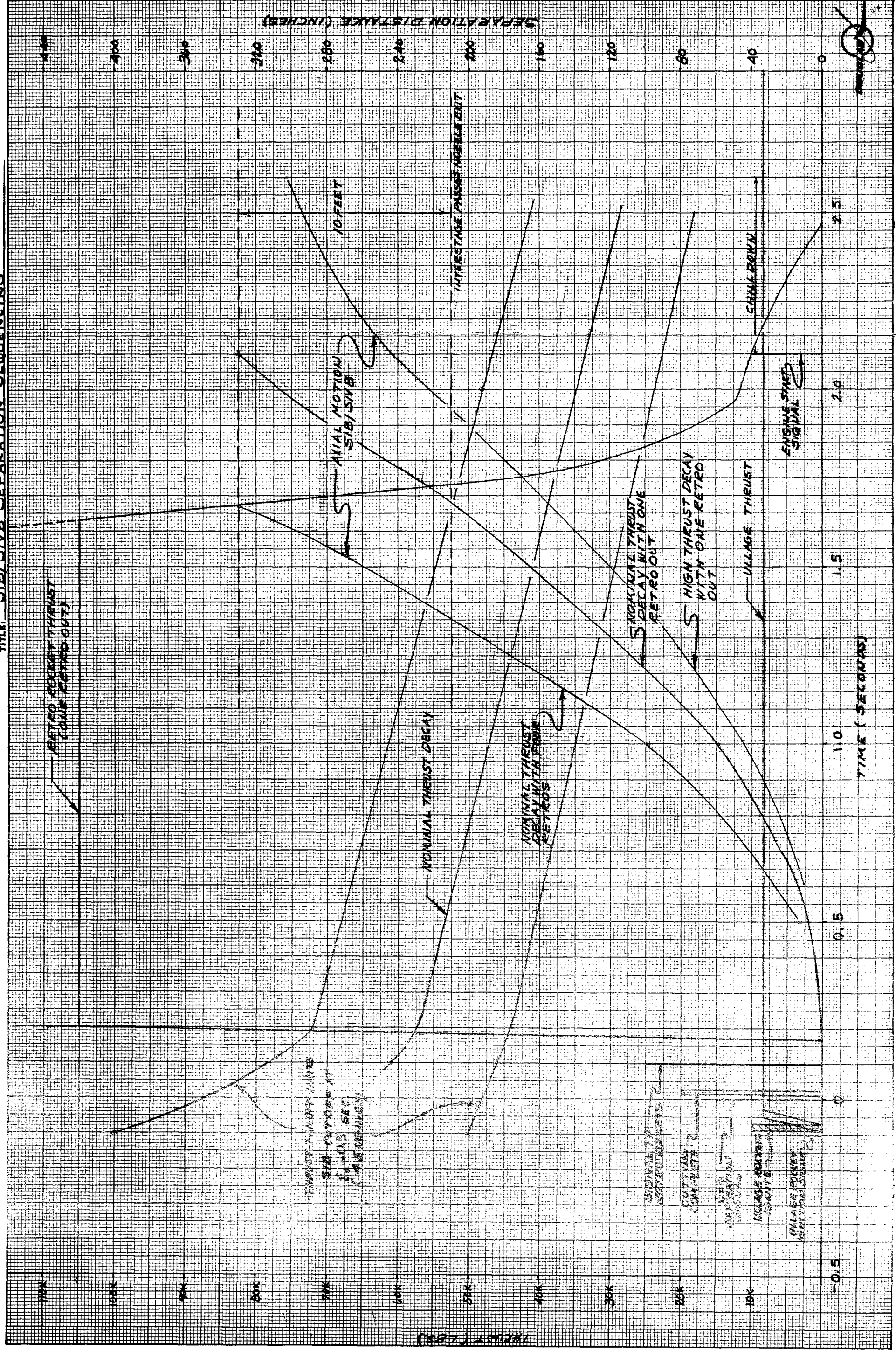


\* DENOTES OCCURRENCE OF EVENT IF OVERRIDE SIGNAL IS REQUIRED TO PRODUCE THE MAINSTAGE SIGNAL



FIGURE 4

TITLE: S1B/S1VA SEPARATION SEQUENCING



TITLE: SII/SIVB SEPARATION SEQUENCING

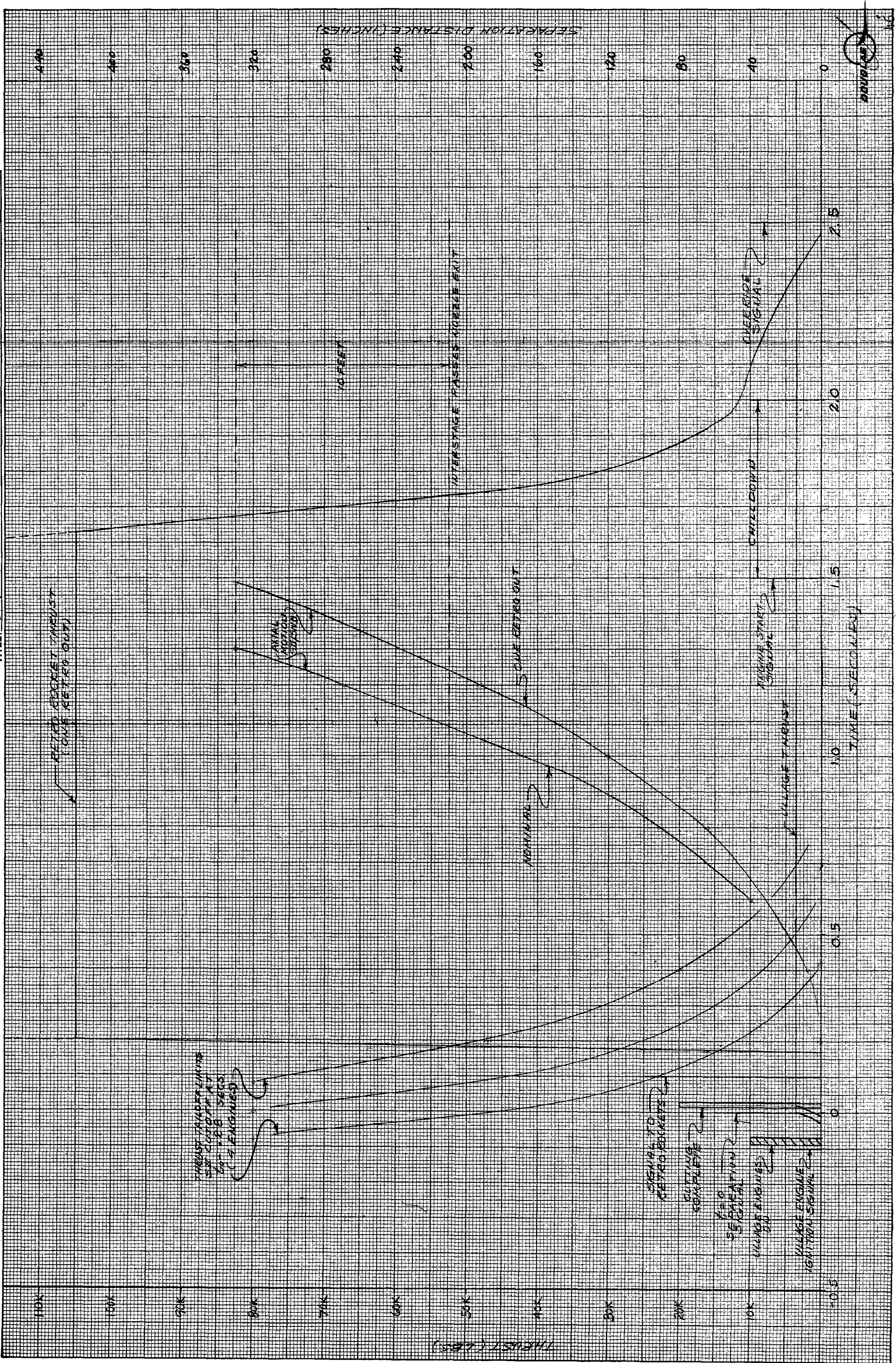


FIGURE 6

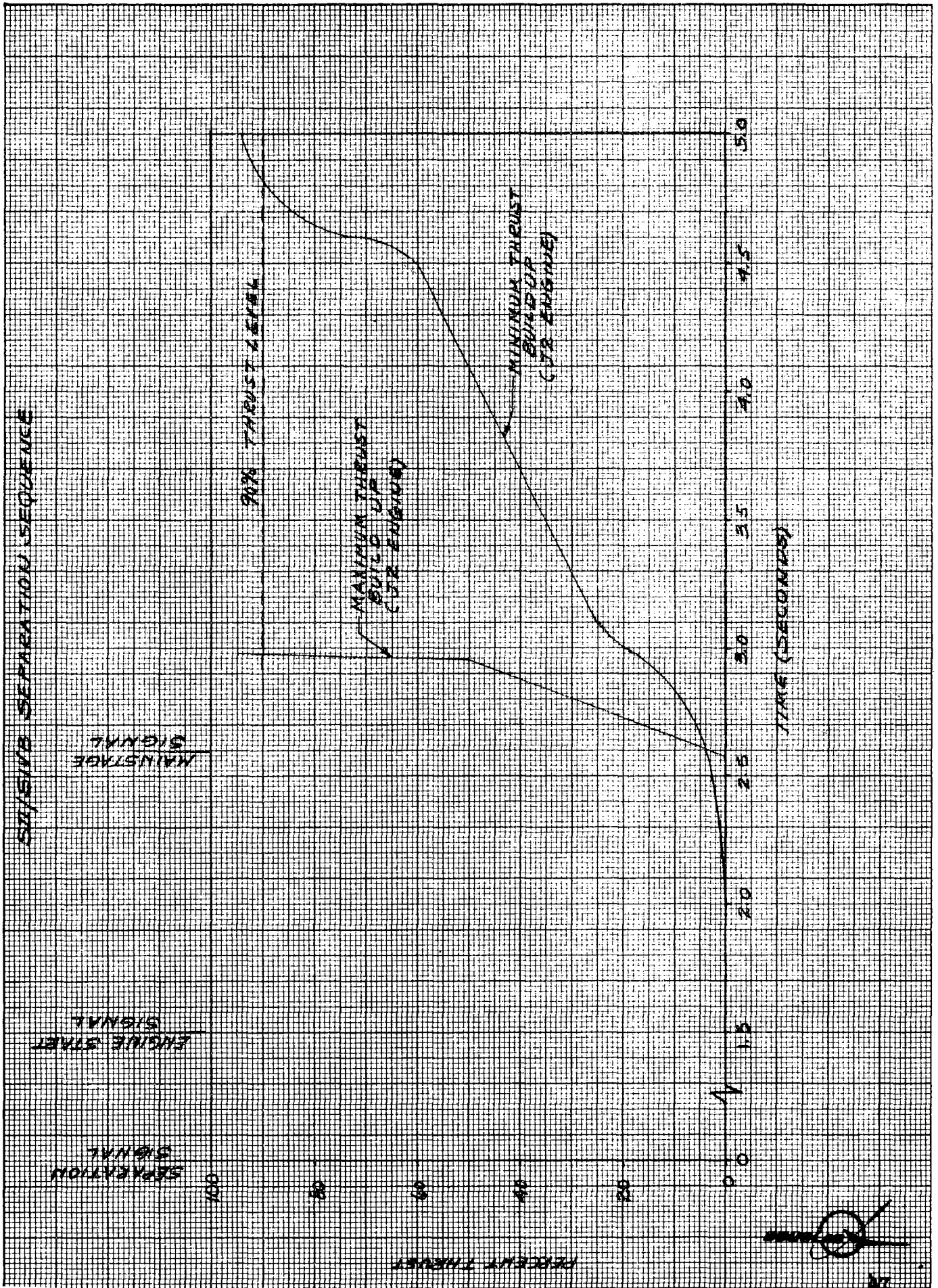
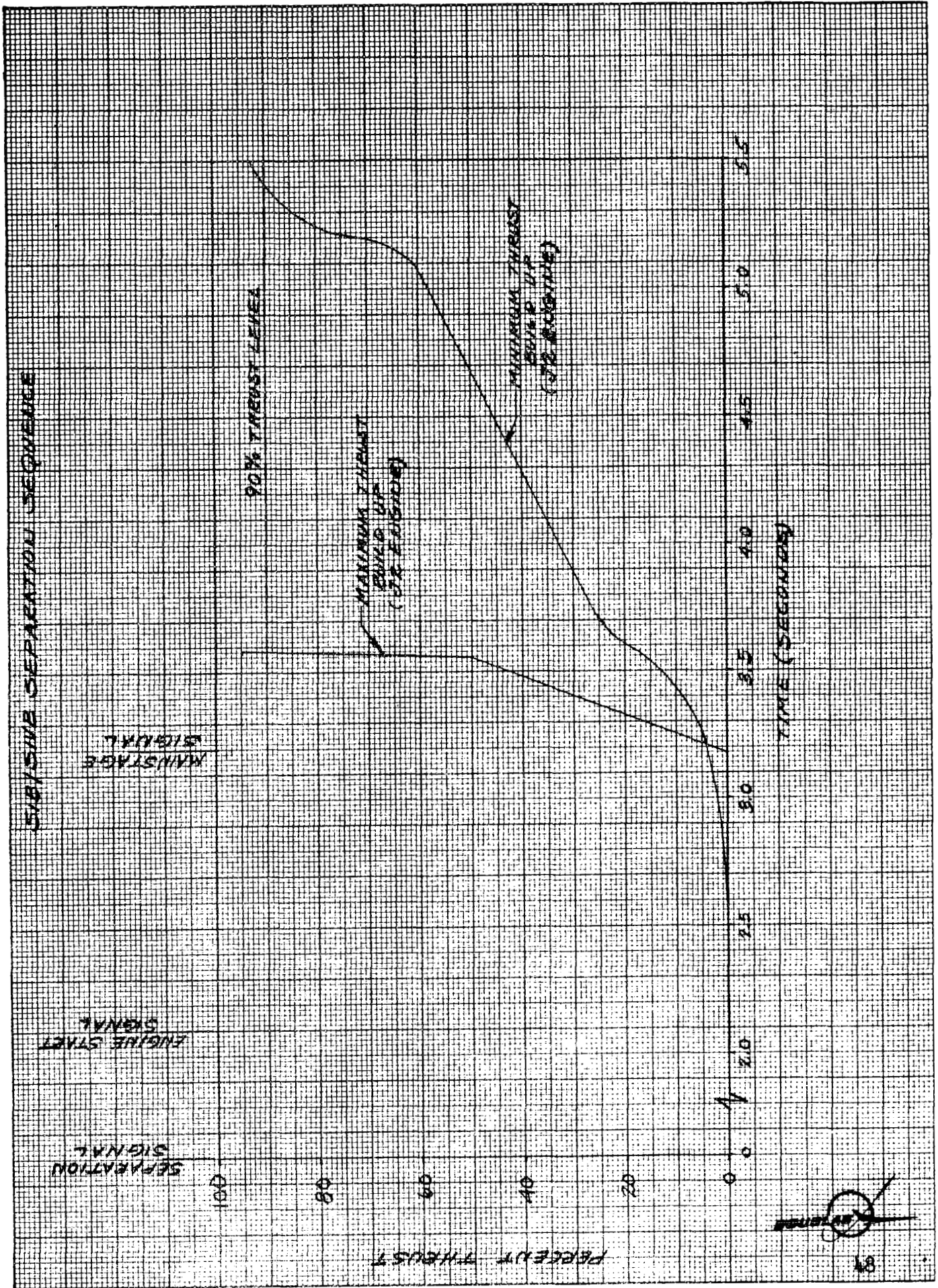


FIGURE 7



## Section 4

### EFFECTS OF J-2 ENGINE GIMBAL LIMITS ON POST-SEPARATION ATTITUDE TRANSIENT

#### INTRODUCTION:

The effects of J-2 engine gimbal limits on controllability of the C-1B after S-I/S-IVB separation has been studied in accordance with action item number 7 of the December 6, 1962 meeting of the S-IVB Vehicle Dynamics and Control Working Group (reference a.). The results of these studies are presented in this memorandum together with a recommendation on required platform mechanical limitations to accommodate separation transients.

The effects of engine gimbal limits on system stability in the presence of engine deflection rate limiting have been studied previously and reported in reference b. This data is included here with an estimate of the effects of the latest control system parameters on these results.

#### DISCUSSION:

##### Separation Controllability

The separation controllability studies were made on an analog computer which was coded to represent the control system block diagram as shown in figure 1. Runs were made to define the maximum attitude deviations of the vehicle during post separation transients. Engine gimbal limit was parameterized to determine the effects of this limit on the attitude deviations which the platform must be capable of handling. In addition, the effects of additional delay in thrust build-up was investigated to determine the sensitivity of the attitude deviations to increased delays in thrust build-up which might result from changes in separation sequence or engine performance.

The initial conditions which were used for the study were those listed in enclosure 3 of the referenced MSFC memorandum. They are listed in table 1 for completeness.

It was found that one ullage engine out had a negligible effect on separation controllability so this condition was not used in the studies.

The vehicle and autopilot data which was used in the study are listed in table II.

presence of engine thrust misalignment and vehicle asymmetries will require the engine to be deflected to a position off the geometrically centered position to achieve a zero net control moment on the vehicle. This will result in less than the nominal engine deflection being available for control during separation. Current estimates of these factors are given in table III. This shows that a maximum of 1 1/2 degrees of effective engine deflection in one direction could be lost from these factors. However, the probability of all of these tolerances being in the same direction is extremely small. If a more probable value is obtained by deriving the root mean square of these tolerances, the result would be considerably smaller than 1 1/2 degrees. In addition to the reduction in engine deflection from these misalignments, some of the engine deflection capability should be reserved for controlling in the presence of moments induced by gusts and sloshing which could occur during separation. If, for these preliminary studies, 1 1/2 degrees of engine deflection is allocated for this purpose, the minimum net engine deflection available for control of separation transients is 3 degrees less than the nominal engine deflection limit. Thus, for a nominal +7 degrees deflection the attitude deviation during the post-separation transient should be based on 4 degrees of engine deflection.

These studies have also shown that a one second additional delay in thrust initiation results in a large increase in the magnitude of the post-separation attitude transient. A similar effect would result from a lower rate of thrust build-up. Because the thrust build-up delay could be increased by changes in separation sequencing, or in engine chill down or performance specifications, and because the attitude deviations of the vehicle are so sensitive to this delay, it seems prudent to allow ample conservatism in setting the platform deflection limits.

The considerations listed above indicate that for nominal engine deflection limits of +7 degrees, and a thrust initiation delay of 2 seconds, the maximum attitude deviations to be expected would be based on gimbal deflection limits of 4 degrees and a separation to thrust initiation time delay of 3 seconds. Figure 18 gives the attitude deviation for these conditions as 25 degrees.

Because of the ease with which this limit can be set in the platform at this early stage in the design, and because of unpredictable changes which inevitably arise as the design and operation of the vehicle progress, it is recommended that an additional margin be allowed for these contingencies.

It is thus recommended that the platform be designed to accept maximum attitude deviations of +35 degrees.

#### REFERENCES:

- a. MSFC memorandum M-AERO-PS-S-4, dated 12-13-62
- b. SM-42083, dated 7-31-62

SATURN CL-B  
S-1/S-IVB STAGE SEPARATION

MAXIMUM ATTITUDE ERROR VS.  
ENGINE DEFLECTION LIMIT

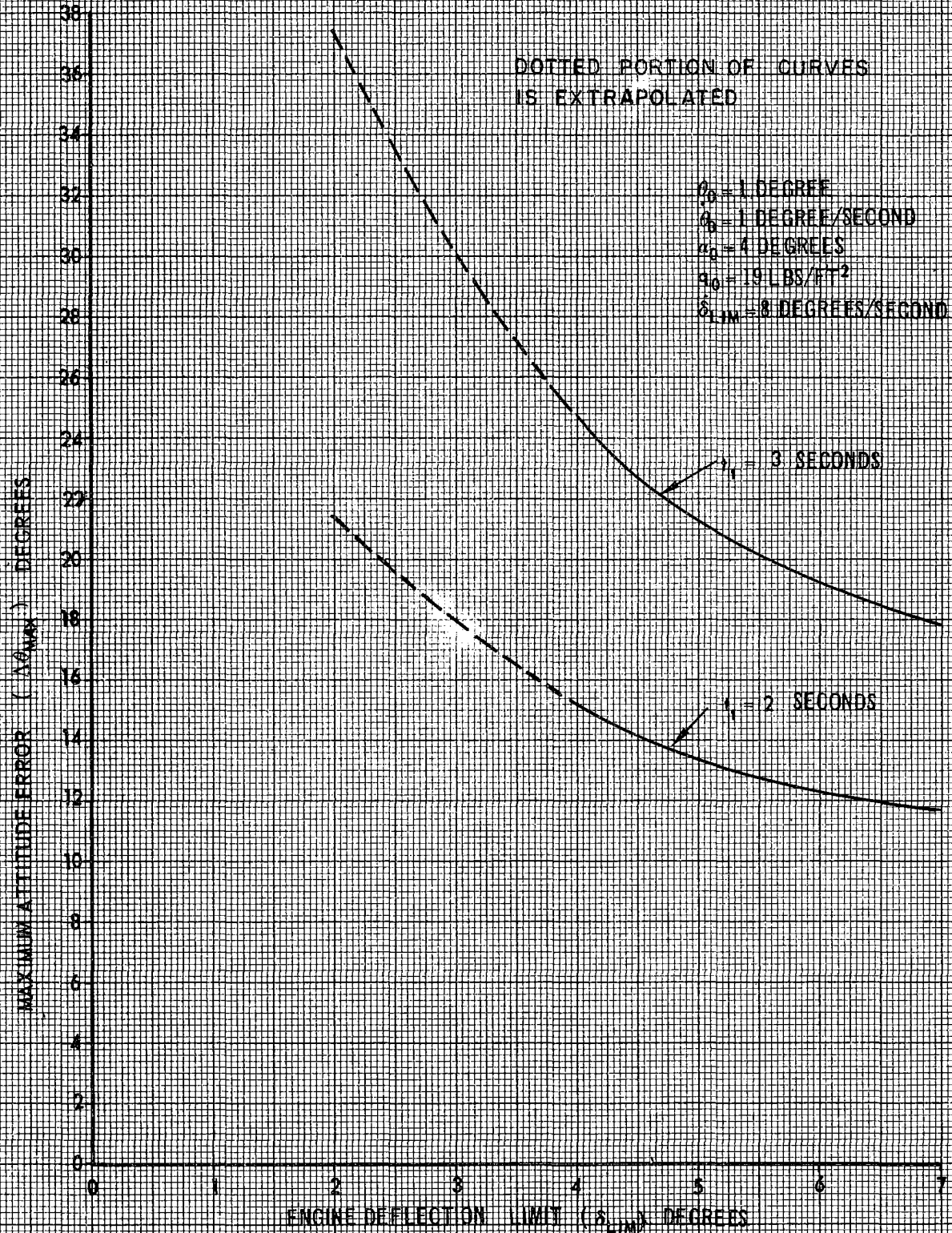


FIGURE 18

ENGINE DEFLECTION AT WHICH LIMIT CYCLING OCCURS FOR VARIOUS VALUES OF RATE LIMIT IN THE SYSTEM OF FIGURE 1.

NOTE:

CURVE "A" WAS GENERATED FOR A SYSTEM USING A LATER AUTOPILOT, A D.P.O. VALVE, AND STRUCTURE DYNAMICS. THE PARAMETERS USED ARE AS FOLLOWS:

$K_D = 1 \text{ RAD}$        $K_I = 2.115 \text{ SEC}$        $H_0 = 0.021 \frac{\text{C.I.S.}}{\text{PSI}}$   
 $K_D = 1.9 \text{ RAD}$        $K_I = 18.4 \text{ RAD}$        $\tau = 0.1 \text{ SEC}$

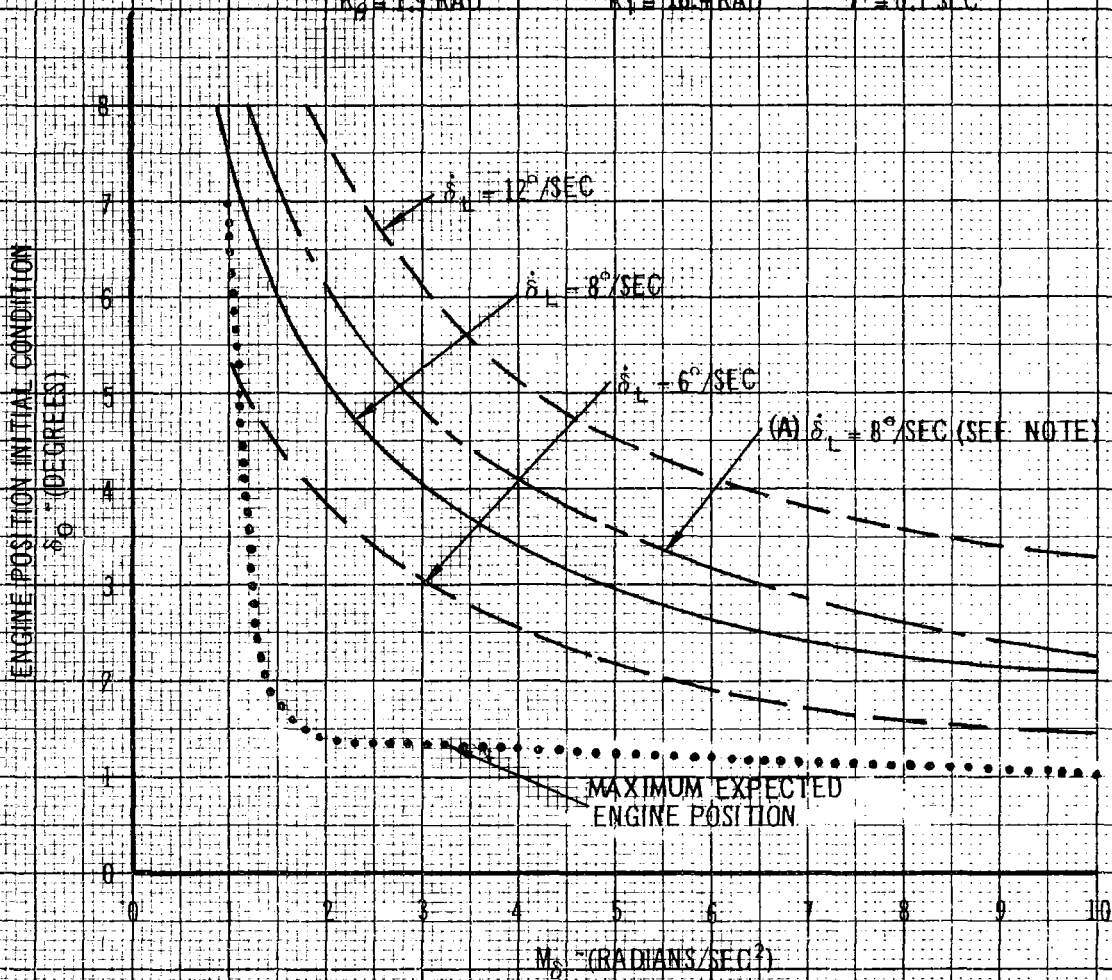


FIGURE 19

## System Stability

Previous studies have shown that the existence of an engine gimbaling rate limit is destabilizing, but that instability will not materialize if the engine deflection is limited. The stable and unstable ranges of engine deflection are shown in figure 19 as a function of control effectiveness  $M_0$  for several values of maximum engine deflection. Later studies have shown that the latest control system parameters will give a larger stability region than shown in figure 9. This data is included in figure 19 for one value of engine gimbaling rate. Also shown in figure 19 is the maximum engine deflection expected during flight. This curve, which is plotted as a function of  $M_0$  shows that the maximum expected engine deflection is within the stability boundary.

### RESULTS:

The results of the study, presented in figures 6 through 17, consist of post-separation attitude transients and engine deflection transients. In these results three parameters were varied, engine gimbaling limits, engine gimbaling rates, and the time between separation and thrust build-up.

Figures 6 through 8 show the vehicle attitude transients and engine deflection histories for the nominal case of a two second delay in thrust initiation and engine gimbaling rates of 8 degrees per second. In these curves the engine deflection limit is parameterized for values of 4, 5, 6 and 7 degrees. The maximum attitude deviation of the vehicle during the post-separation transient varied from 11.6 to 15.2 degrees for engine deflection limits of 7 and 4 degrees respectively.

Figures 9 through 11 show the attitude transients and engine deflection transients for 8 deg/sec gimbaling rates with thrust initiation three seconds after separation. The maximum attitude deviation for this case is 17.8 and 24.9 degrees for engine deflection limits of 7 and 4 degrees respectively. This is nearly a 60 percent increase over the second delay case for the 4 degree gimbaling limit.

Figures 12 through 14 show the attitude transients for an engine deflection rate of 12 deg/sec with a 3 second delay in thrust initiation. These transients show no improvement in the maximum attitude deviation by increasing the engine deflection rate. However, the second overshoot is decreased.

Similar transients have been included for 12 deg/sec gimbaling rates and 2 second thrust initiation delay as figures 15 through 17.

These results are summarized on figure 18 which shows the maximum attitude deviation as a function of the engine deflection limit and the time between separation and engine ignition. Only the curves for 8 deg/sec gimbaling rates are shown as the change to 12 deg/sec resulted in a negligible change to these curves.

Although figure 18 is valid for the assumptions used in this study, several additional factors must be considered when determining the maximum attitude deviation which will be expected during the post-separation transient. The

TABLE I

INITIAL CONDITIONS

a. Angle of attack	$\alpha = 4 \text{ deg}$
b. Attitude rate	$\dot{\theta} = 1 \text{ deg/sec}$
c. Pitch attitude	$\theta = 1 \text{ deg}$
d. Dynamic pressure	$q = 16 \text{ psf} \pm 3 \text{ psf}$ $(80 \text{ Kg/m}^2 \pm 15 \text{ Kg/m}^2)$
e. One ullage engine out	(negligible)
f. Time delay - Separation to thrust initiation	$t_1 = 2 \text{ secs}$ 3 sec also studied
g. Thrust build-up curve from J-2 engine handbook (shown in figure 2). The minimum rate of build-up curve was used.	

TABLE IICI-B, S-I/S-IVB SEPARATION DATA

<u>Symbol</u>	<u>Description</u>	<u>Value</u>
-	Payload	33,740 lb
I	Vehicle Inertia	5,468,000 slug-ft <sup>2</sup>
$l_{cg}$	Control Level Arm	21.9 ft
$l_{cp}$	Aerodynamic Lever Arm	See fig. 5 36.6 ft at $\alpha = 0$
$C_N$	Aerodynamic Force Coefficient	See fig. 3
q	Dynamic Pressure	See fig. 4
A	Aerodynamic Reference Area	360 ft <sup>2</sup>
M	Vehicle Mass = w/g	9,457.7 slugs
$K_1$	Servo Forward Gain	13.56 deg/sec/ua
K	Servo Feedback Gain	1.0 ua/deg
$T_1$	Main Engine Thrust	See fig. 2
$K_\theta$	Attitude Feedback Gain	2.3 ua/deg
$K_{\dot{\theta}}$	Attitude Rate Feedback Gain	2.75 ua/deg/sec
$\omega/2$	Autopilot Natural Frequency	0.25 cps
$\zeta$	Autopilot Damping Ratio	0.7
$M_\delta$	Control Moment Coefficient	$Tl_{cg}/I$ , see fig. 2 0.8 rad/sec <sup>2</sup> /rad max
$\delta_{LIM}$	Max Engine Deflection	<u>+7</u> , <u>+6</u> , <u>+5</u> , <u>+4</u> deg
$\delta_{LIM}$	Max Engine Rate	8, 12 deg/sec



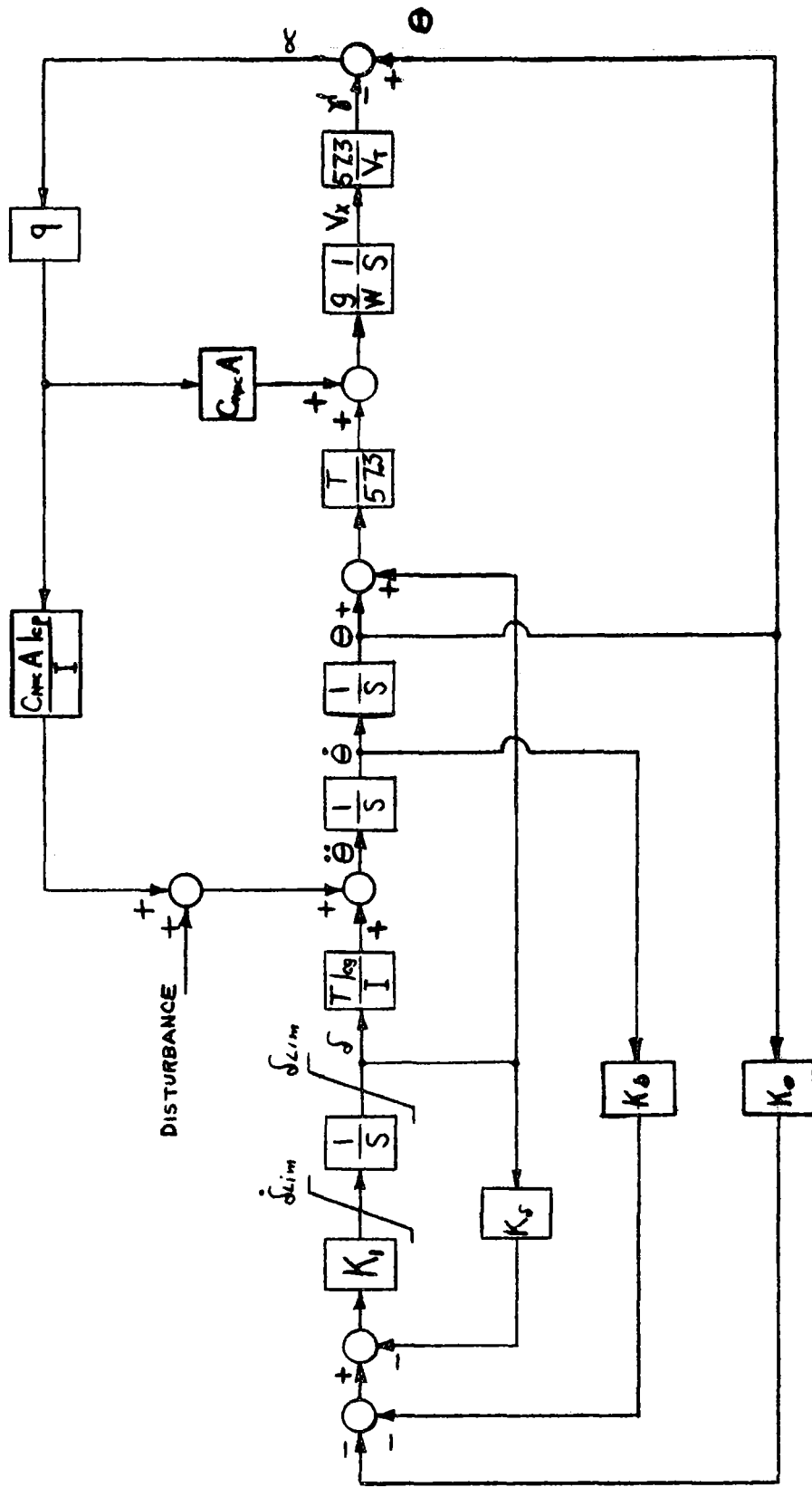


FIGURE 1 SIMPLIFIED CONTROL SYSTEM DIAGRAM

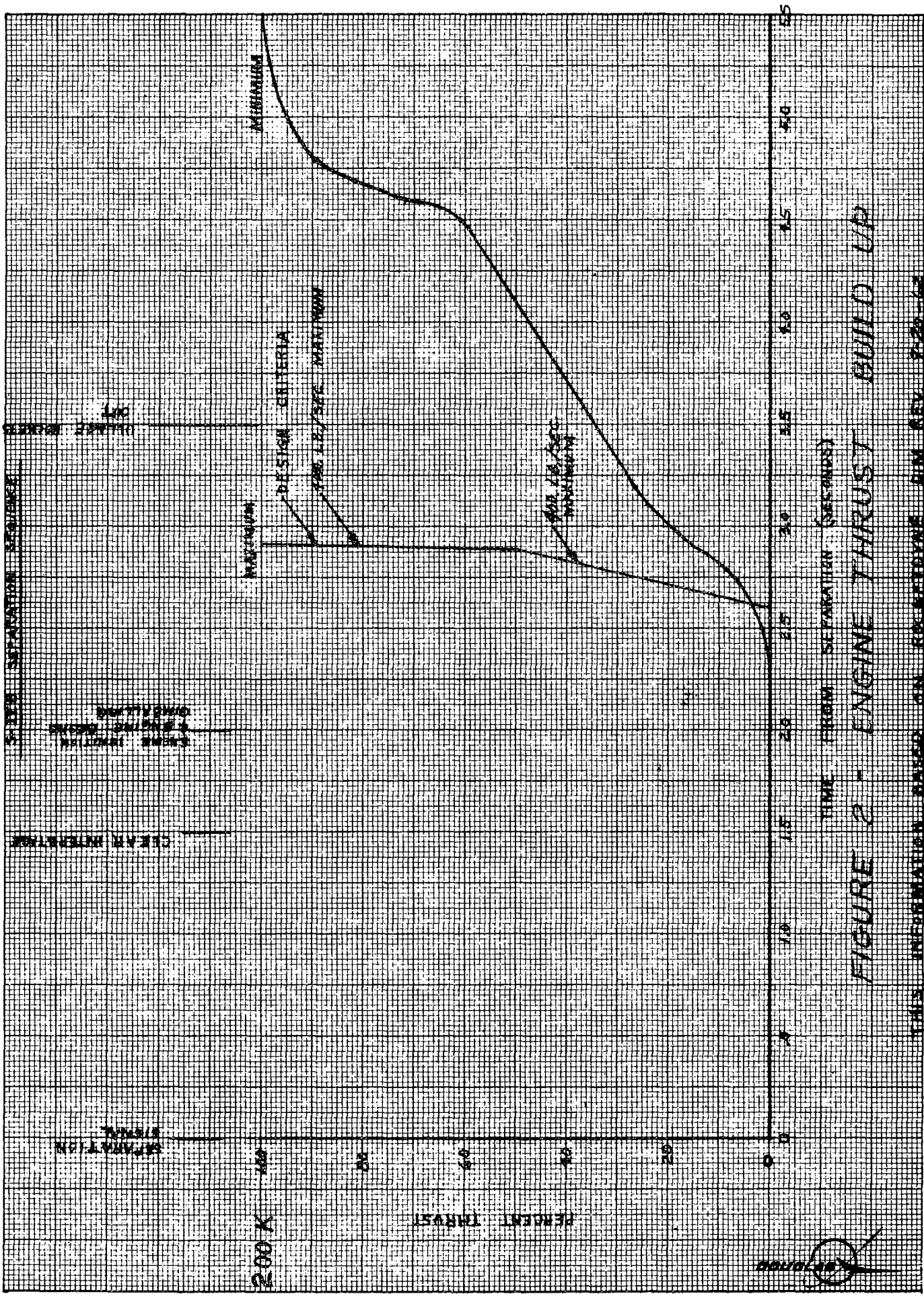


FIGURE 2 - ENGINE THRUST BUILD UP

THIS INFORMATION BASED ON RESEARCHER DIRM REV 7-20-72



SAILOR C-18  
TOTAL NORMAL FORCE COEFFICIENT VS. ANGLE OF ATTACK  
S-BIB PLUS PAYLOAD

N<sub>0</sub> = 5.3

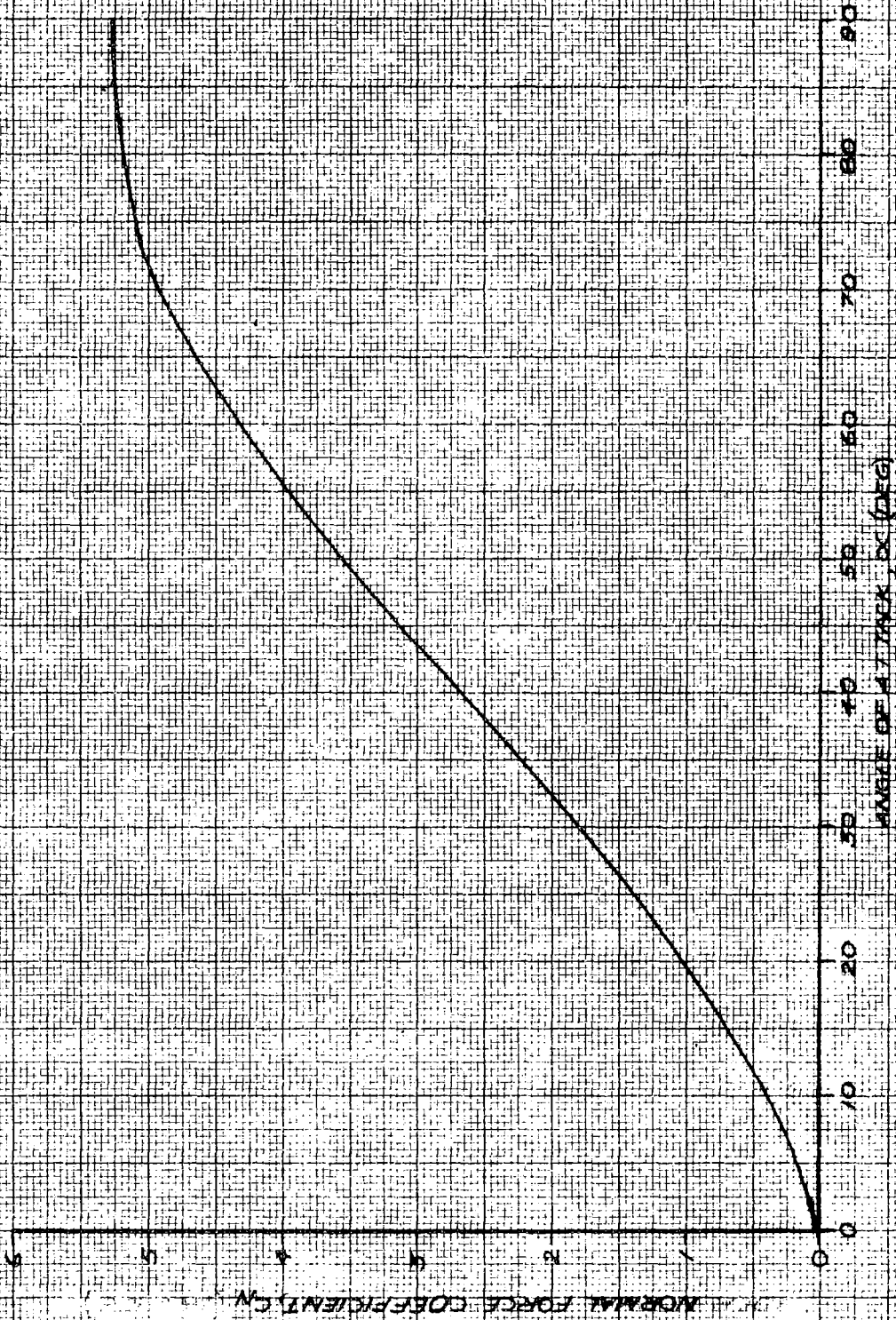


FIGURE 3

FIGURE 3

SEVEN CHS  
SUSPENDED STACK SEPARATION  
15,760 LB PAYLOAD

DYNAMIC PRESSURE DECAY  
FOLLOWING SEPARATION

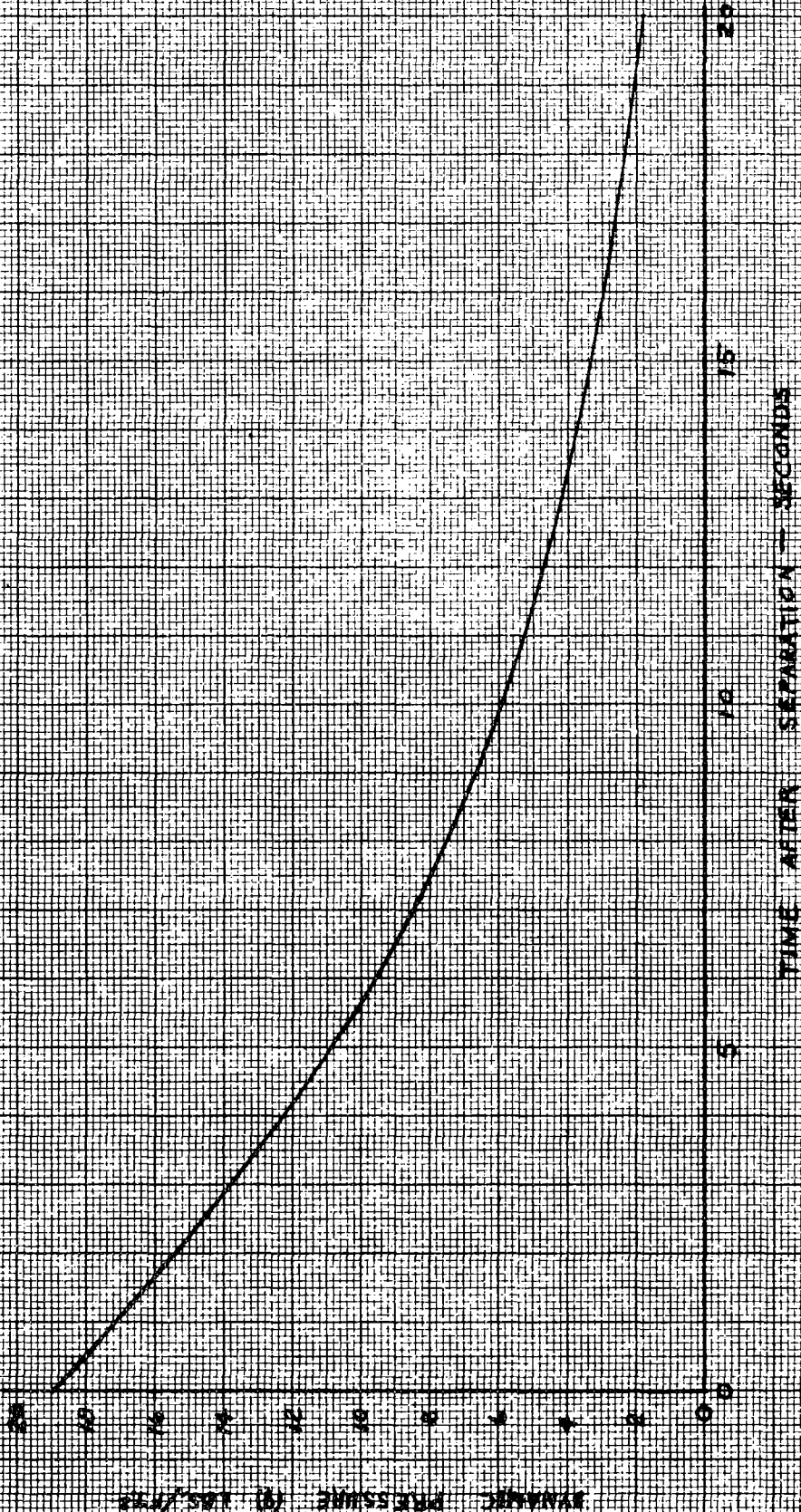


FIGURE 4

*[Handwritten signature]*

SATURDAY C-118  
 CENTER OF PRESSURE VS ANGLE OF ATTACK  
 5.1% PLUS REGION

M:0.3

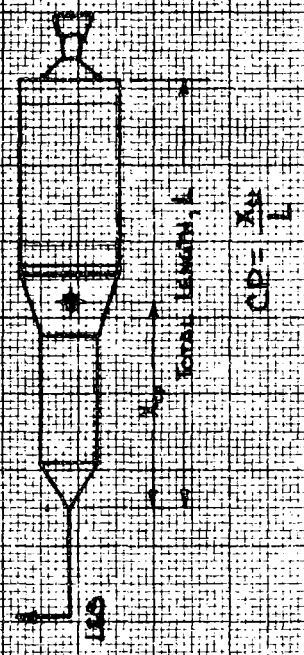
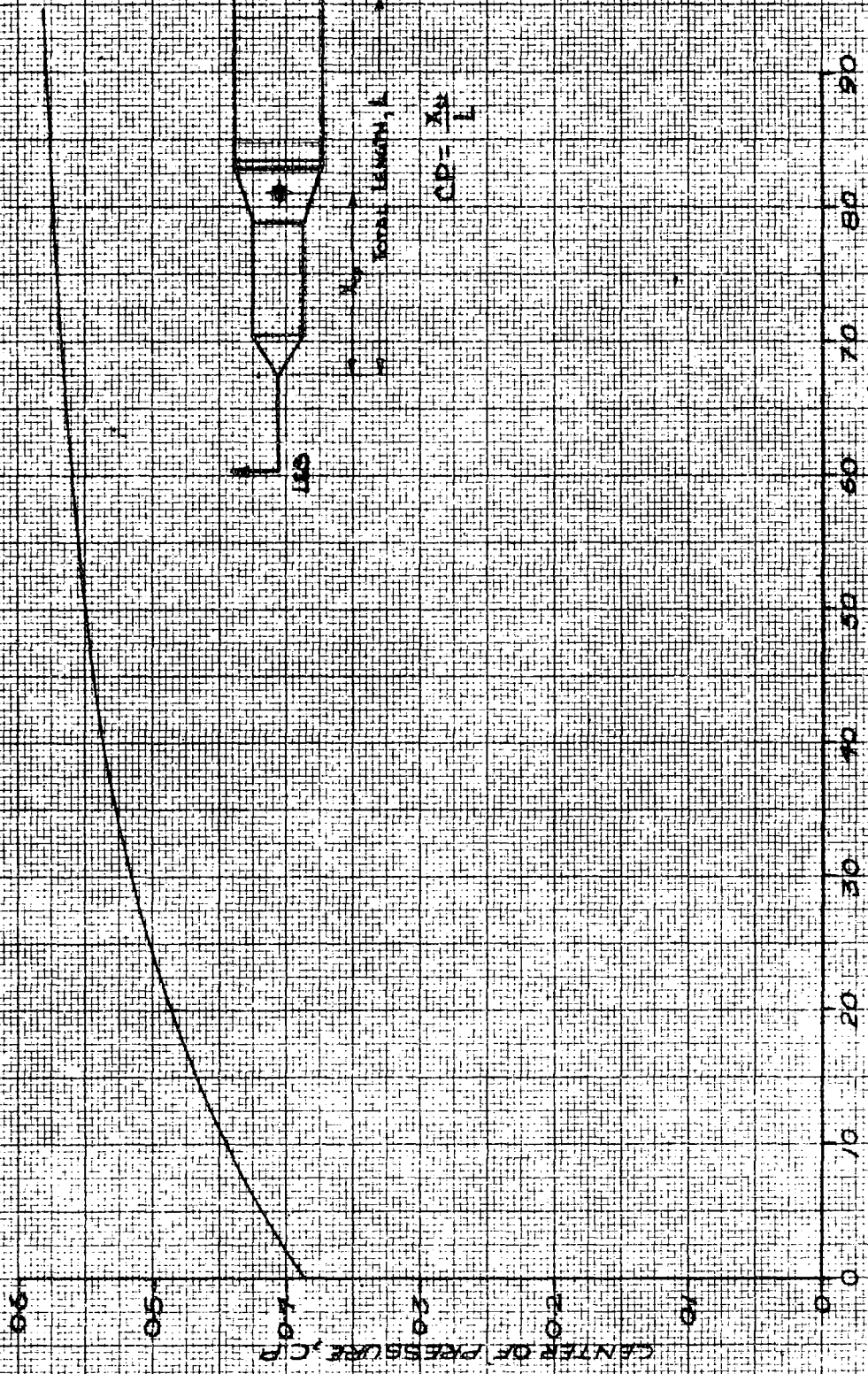


FIGURE 4

FIGURE 5

SATURN C-1/D

5-1/2-1/2 STAGE SEPARATION

ATTITUDE TRANSIENTS FOLLOWING SEPARATION

$\dot{\theta}_0 = 1 \text{ DEGREE}$   
 $\ddot{\theta}_0 = 1 \text{ DEGREE/SECOND}$   
 $\dot{\theta}_0 = 4 \text{ DEGREES}$   
 $\ddot{\theta}_0 = 19 \text{ LGS/FT}^2$   
 $\dot{\theta}_{LIM} = 8 \text{ DEGREES/SECOND}$   
THRUST BUILDUP STARTS AT  
 $t_0 = 2 \text{ SECONDS}$

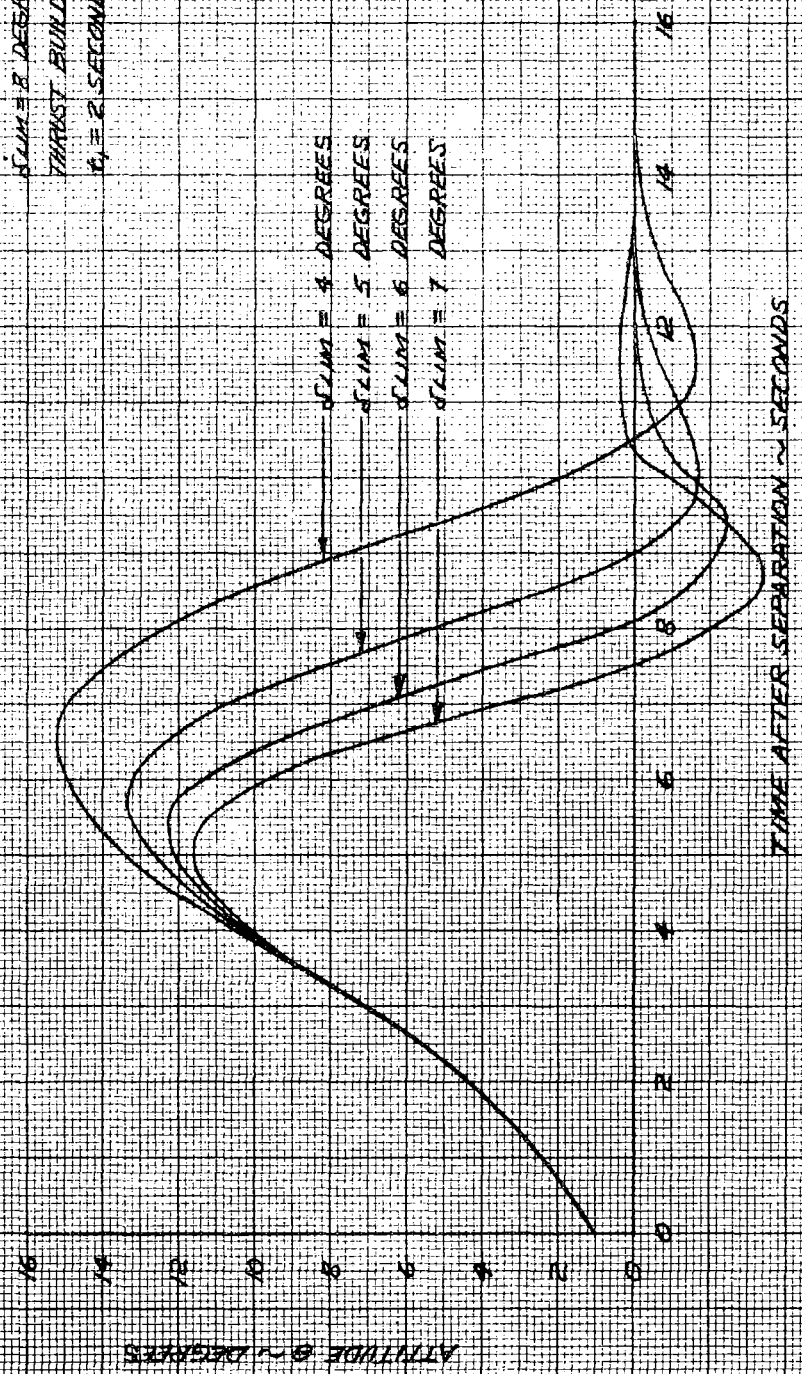


FIGURE 5

*[Handwritten signature]*

SATURN C1-B  
 S-1/S-1VB STAGE SEPARATION  
 33,740 LB PAYLOAD

ENGINE DEFLECTION TRANSIENTS  
 FOLLOWING SEPARATION

$\theta_0 = 1$  DEGREE  
 $\dot{\theta}_0 = 1$  DEGREE/SECOND  
 $\rho_0 = 10$  LBS/FT<sup>2</sup>  
 $\alpha_0 = 4$  DEGREES  
 $\delta_{1,100} = 8$  DEGREES/SECOND

THRUST BUILD UP STARTS  
 AT 2 SECONDS

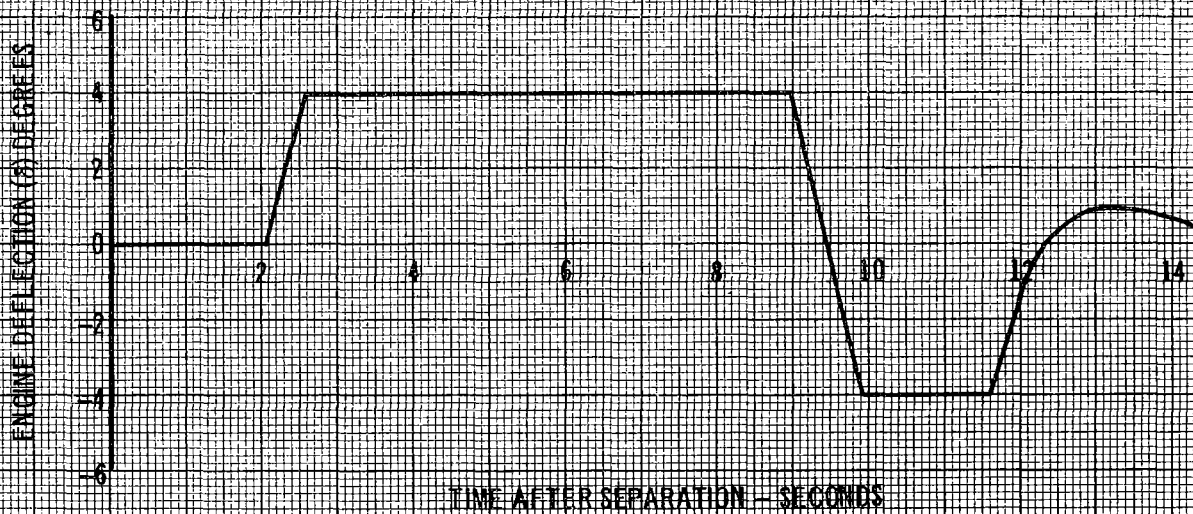
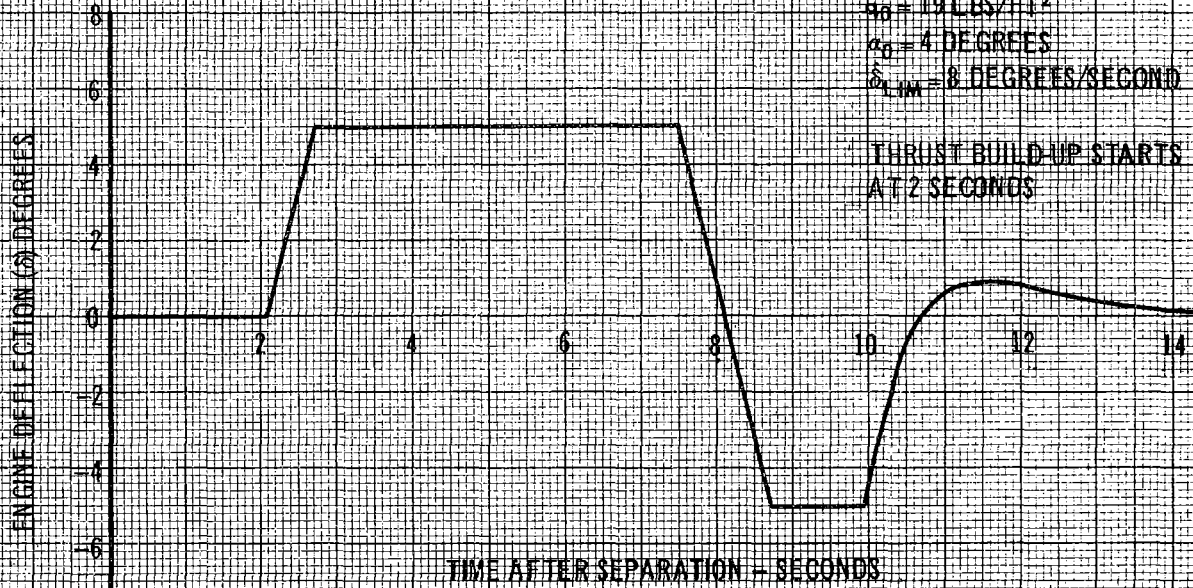


FIGURE 7

SATURN C1B  
 S-1/S-IVB STAGE SEPARATION  
 33,740 LB PAYLOAD

ENGINE DEFLECTION TRANSIENTS  
 FOLLOWING SEPARATION

$\theta_0 = 1$  DEGREE  
 $\dot{\theta}_0 = 1$  DEGREE/SECOND  
 $a_0 = 19$  LBS/FT<sup>2</sup>  
 $\alpha_0 = 4$  DEGREES  
 $\delta_{LIV} = 8$  DEGREES/SECOND  
 THRUST BUILD-UP STARTS  
 AT 2 SECONDS

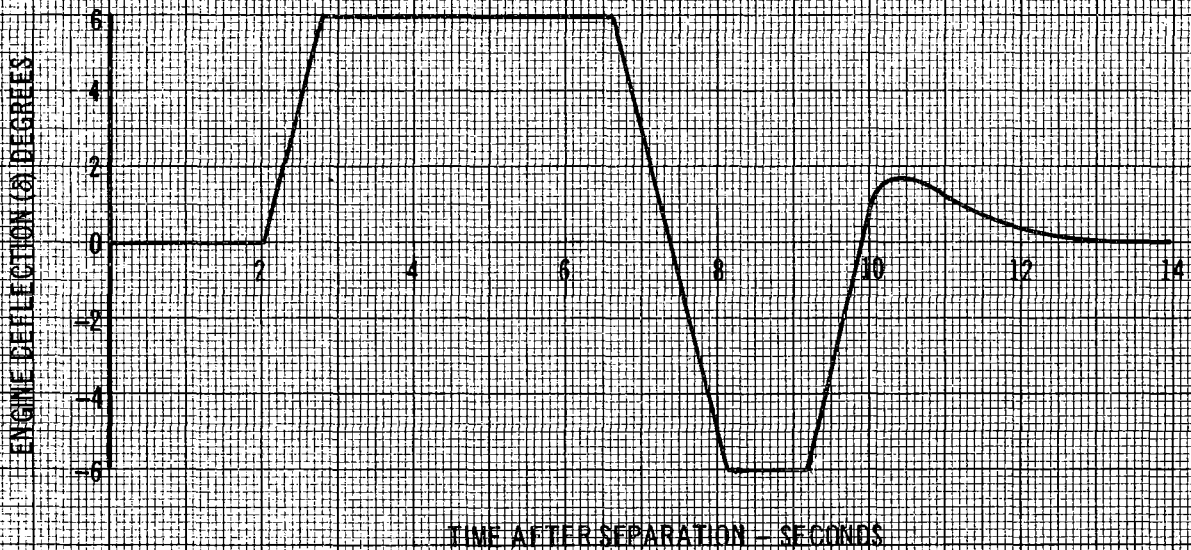
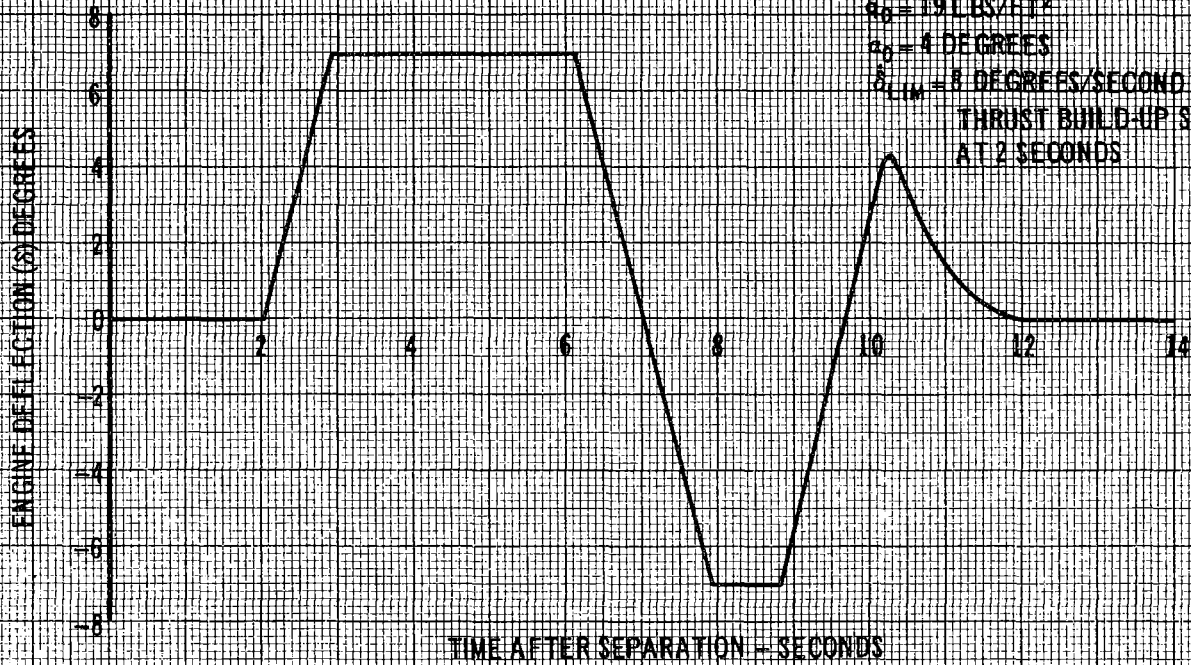


FIGURE 8

SATURN CFB  
 SHOOTING STAGE SEPARATION  
 ATTITUDE TRANSIENTS FOLLOWING SEPARATION

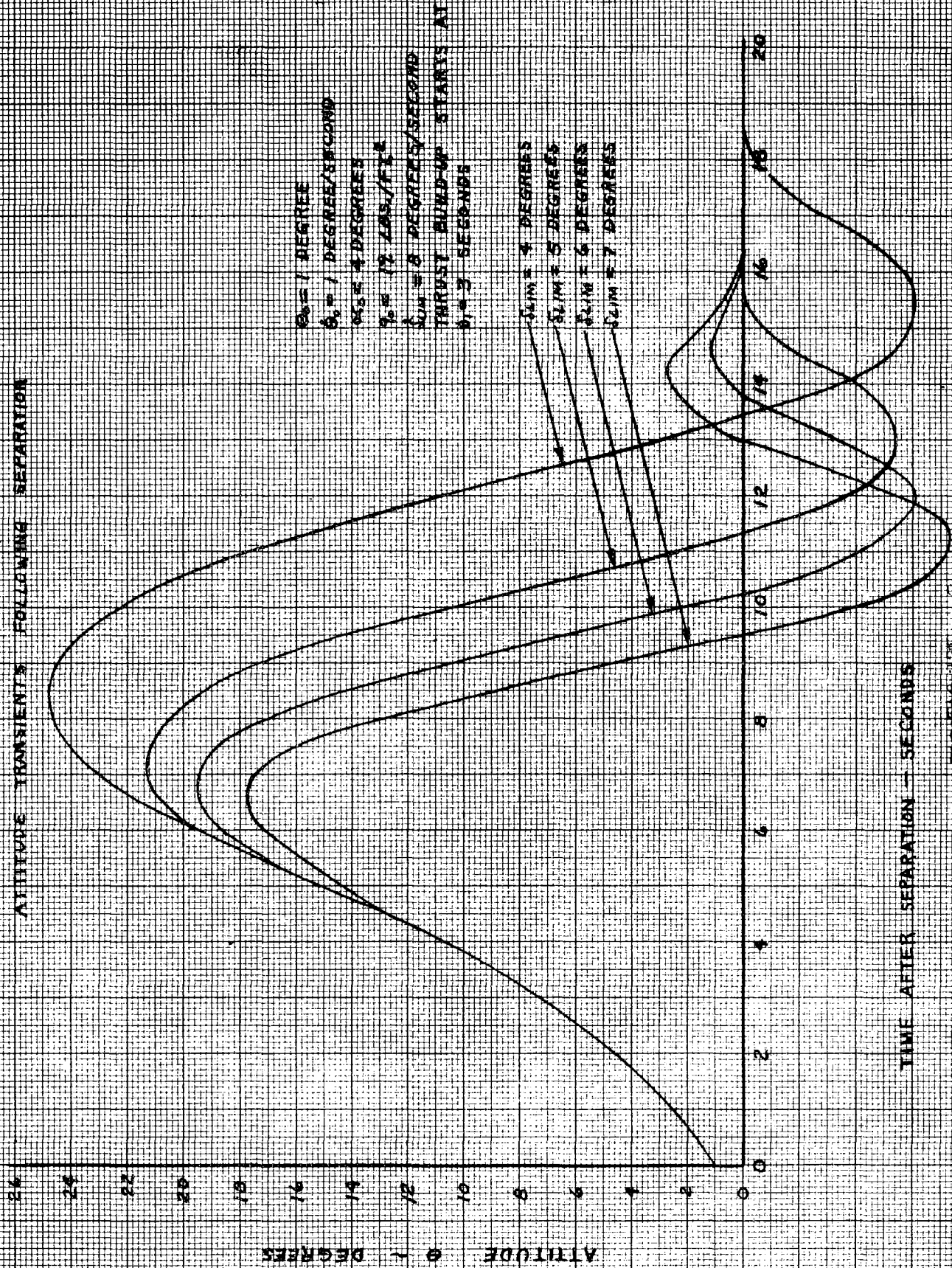


FIGURE 14

SATURN C-1-B  
S-1/S1VB STAGE SEPARATION  
33,740 LB PAYLOAD

ENGINE DEFLECTION TRANSIENTS  
FOLLOWING SEPARATION

- $\theta_0 = 1$  DEGREE
- $\dot{\theta}_0 = 1$  DEGREE/SECOND
- $g_0 = 19$  LBS/FT<sup>2</sup>
- $\sigma_0 = 4$  DEGREES
- $\dot{\sigma}_0 = 8$  DEGREES/SECOND

THRUST BUILD-UP STARTS  
AT 3 SECONDS

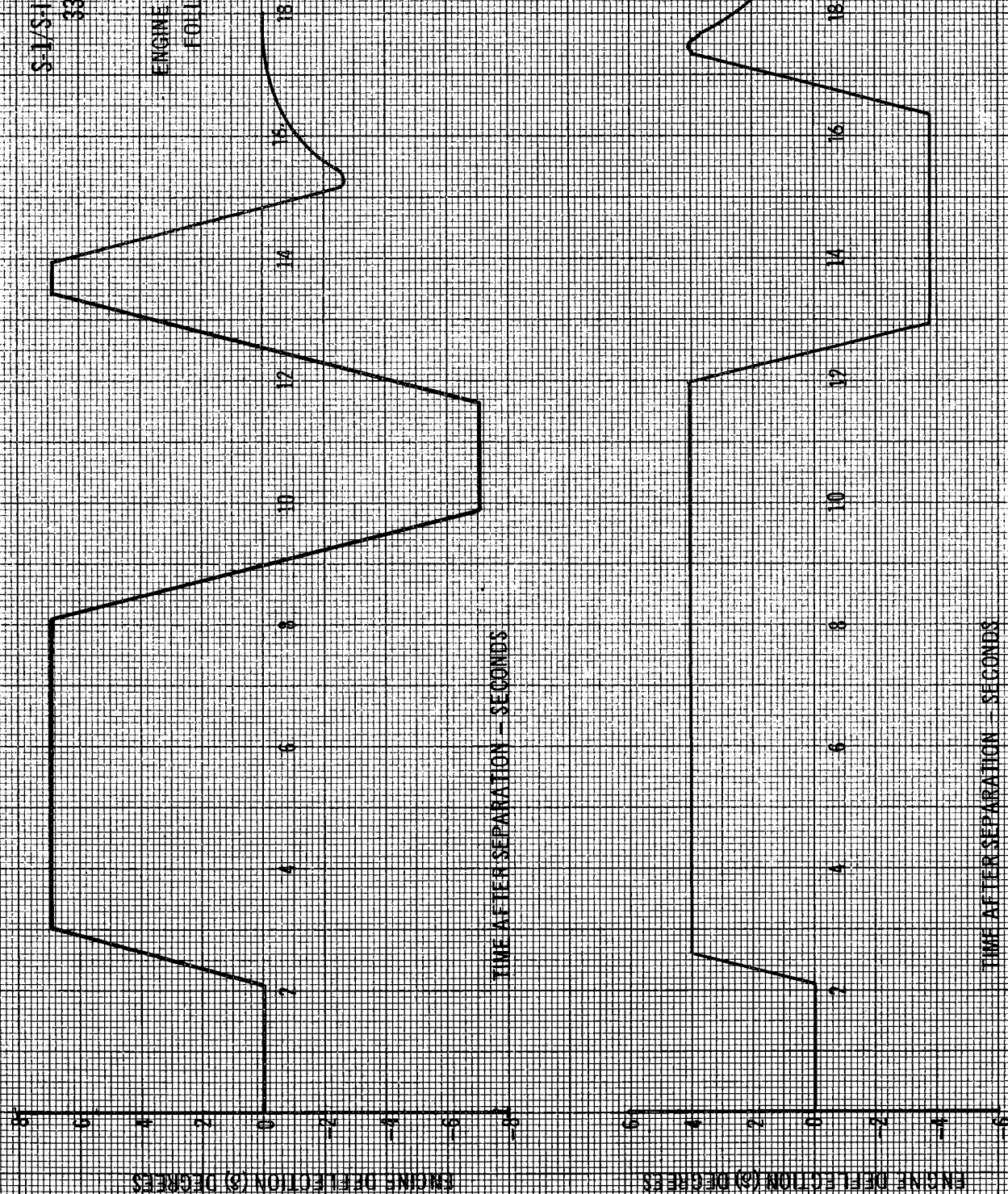


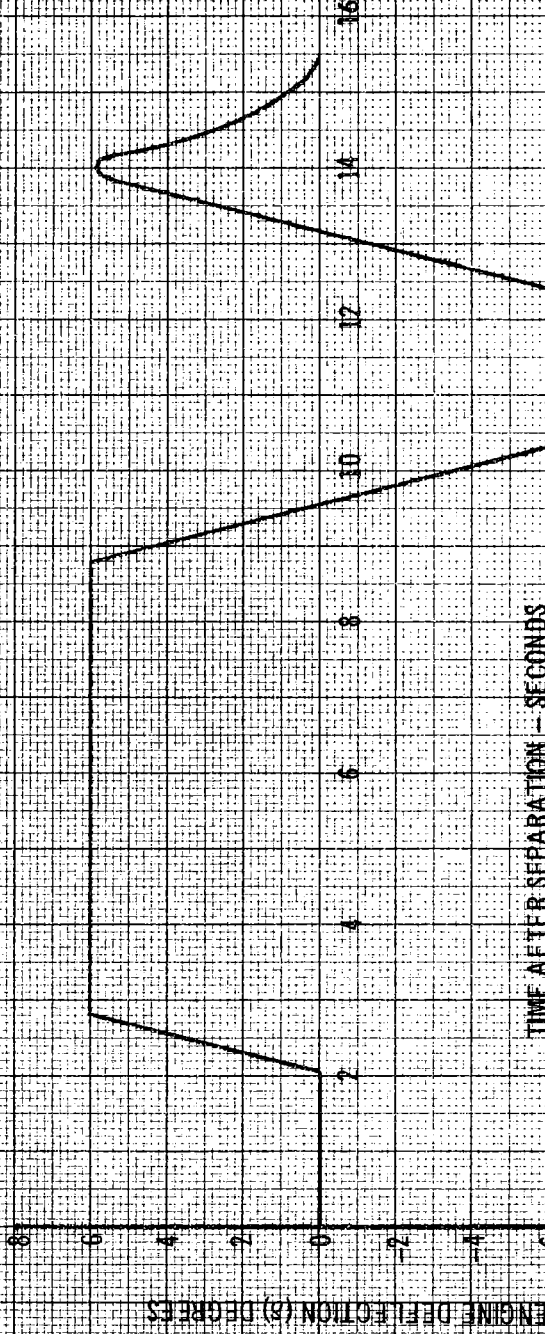
FIGURE 10

SATURN C1-B  
S-1/S-1VB STAGE SEPARATION  
33,740 LB PAYLOAD

ENGINE DEFLECTION TRANSIENTS  
FOLLOWING SEPARATION

- $\phi_0 = 1$  DEGREE
- $\dot{\phi}_0 = 1$  DEGREE/SECOND
- $q_0 = 19$  LBS/FT<sup>2</sup>
- $\dot{q}_0 = 4$  DEGREES
- $\delta_{1,IM} = 8$  DEGREES/SECOND

THRUST BUILD-UP STARTS  
AT 3 SECONDS



TIME AFTER SEPARATION - SECONDS

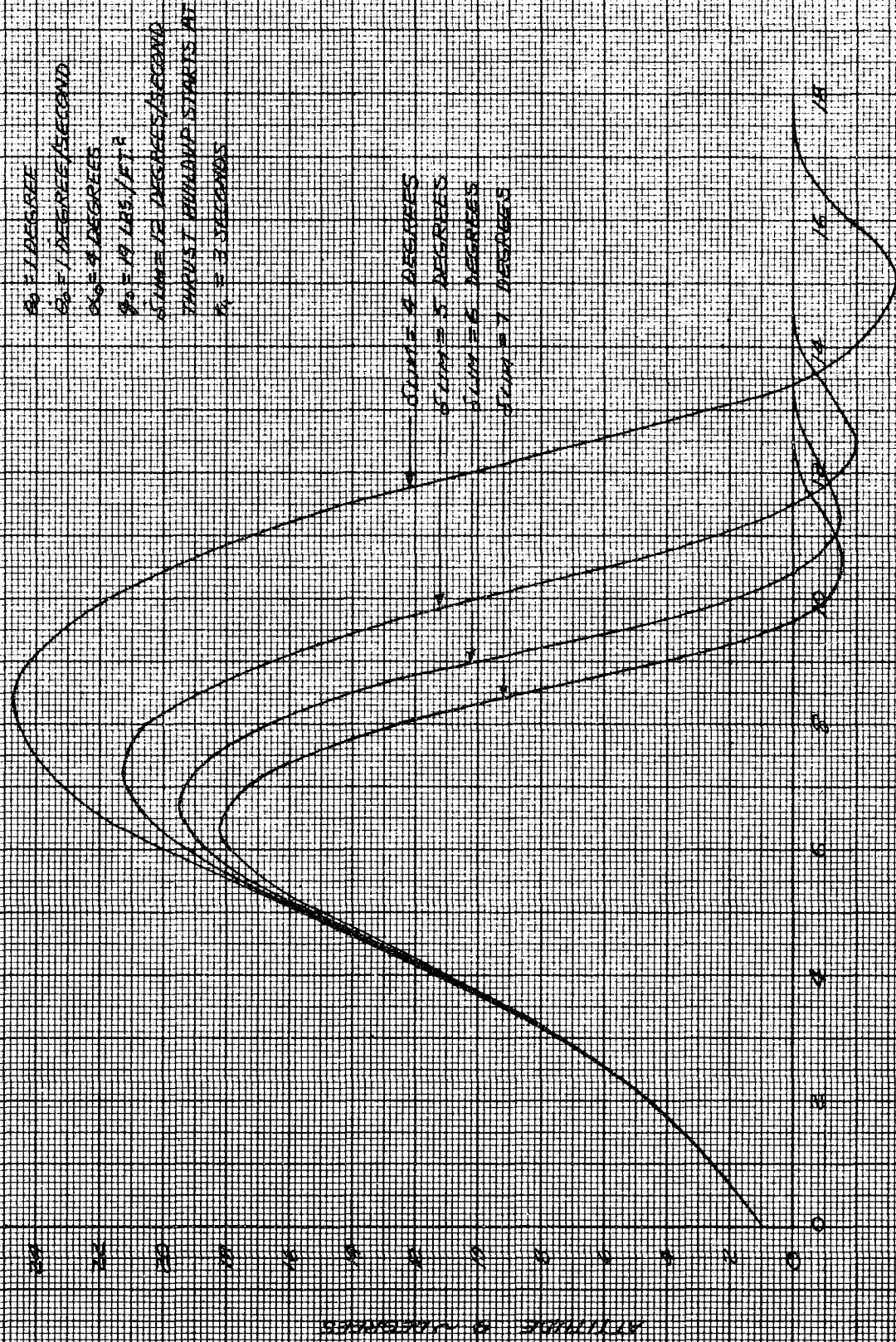
ENGINE DEFLECTION (phi) DEGREES



TIME AFTER SEPARATION - SECONDS

FIGURE 11

SATURN C-1/A  
 35-45 IN EGORE SEPARATION  
 ALTITUDE TRANSIENTS FOLLOWING SEPARATION



TIME AT TEST SEPARATION ~ 10 SECONDS

FIGURE 13



SATURN C/B

S-1/S-IVB STAGE SEPARATION  
33,740 LB PAYLOAD

ENGINE DEFLECTION TRANSIENTS  
FOLLOWING SEPARATION

$\theta_0 = 1 \text{ DEGREE}$

$\dot{\theta}_0 = 1 \text{ DEGREE/SECOND}$

$q_0 = 19 \text{ LBS/FT}^2$

$\alpha_0 = 4 \text{ DEGREES}$

$\delta_{LIM} = 12 \text{ DEGREES/SECOND}$

THRUST BUILD-UP STARTS  
AT 13 SECONDS

ENGINE DEFLECTION (S) DEGREES

TIME AFTER SEPARATION - SECONDS

ENGINE DEFLECTION (S) DEGREES

TIME AFTER SEPARATION - SECONDS

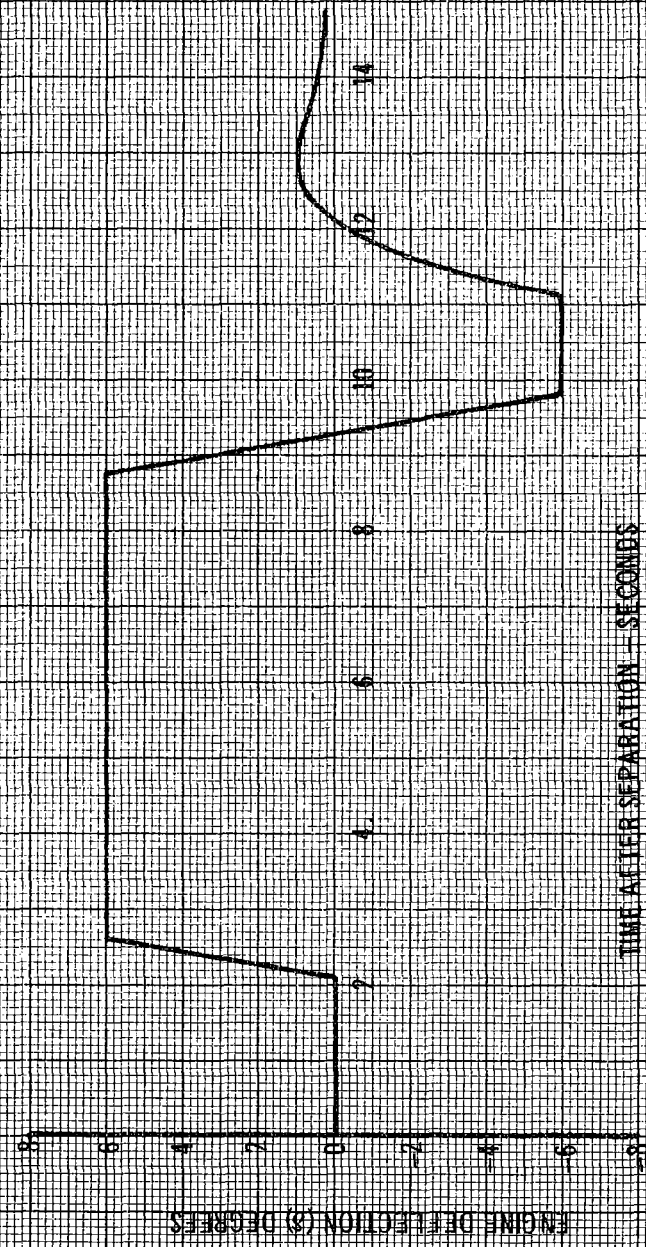
FIGURE 13

SATURN CL-B  
S-1/S-1VB STAGE SEPARATION  
38,740 LB PAYLOAD

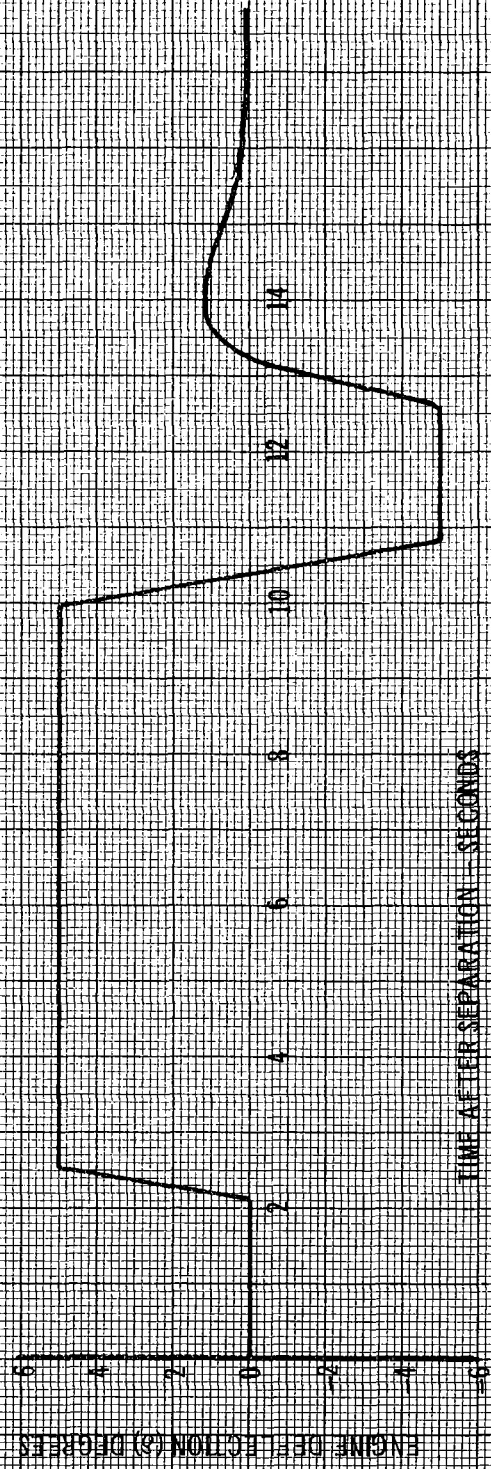
ENGINE DEFLECTION TRANSIENTS  
FOLLOWING SEPARATION

$\theta_0 = 1$  DEGREE  
 $\dot{\theta}_0 = 1$  DEGREE/SECOND  
 $\ddot{\theta}_0 = 10$  LBS/FT<sup>2</sup>  
 $\tau_0 = 4$  DEGREES  
 $\dot{\tau}_{LIM} = 12$  DEGREES/SECOND

THRUST BUILD-UP STARTS  
AT 3 SECONDS



TIME AFTER SEPARATION - SECONDS

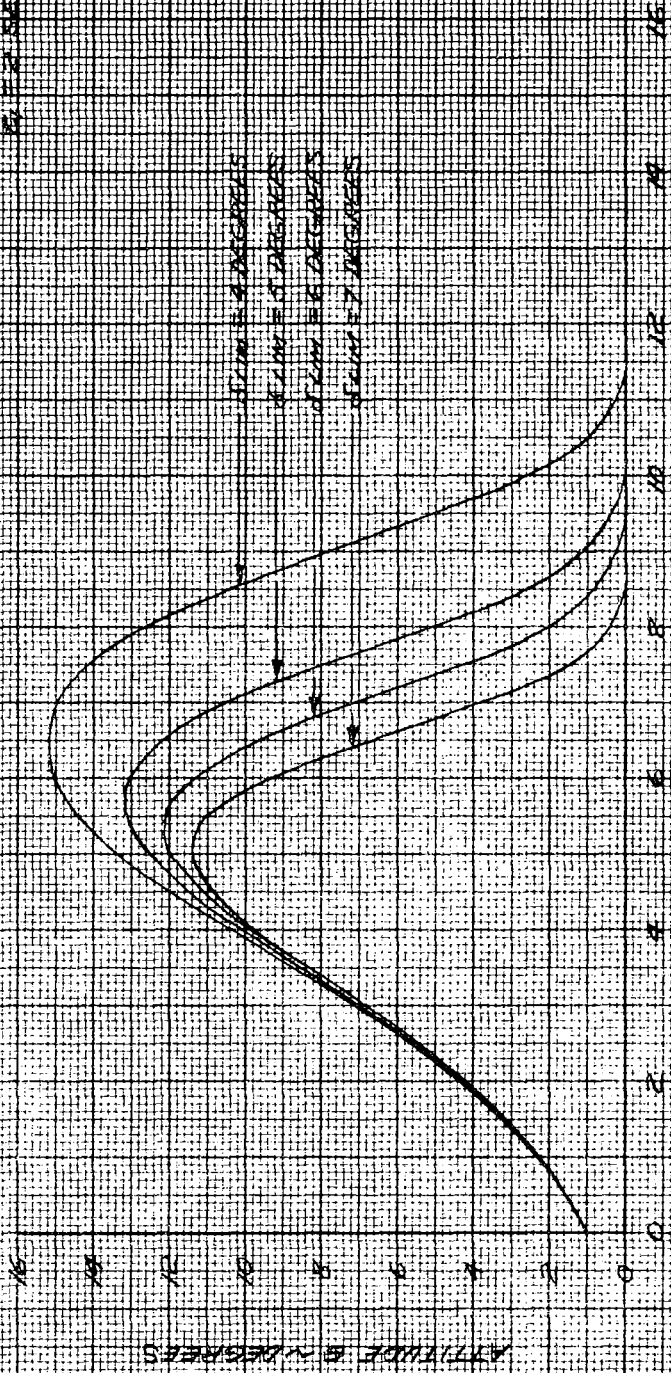


TIME AFTER SEPARATION - SECONDS

FIGURE 14

SATURN C-10  
 15/15-MR STAGE SEPARATION  
 ATTITUDE TRANSIENTS FOLLOWING SEPARATION

0.0 - 1.0 DEGREE  
 0.5 - 1.0 DEGREE / SECOND  
 0.0 - 0.5 DEGREE/S  
 0.0 - 1.0 DEGREE / SEC  
 0.0 - 1.0 DEGREE / SEC  
 0.0 - 1.0 DEGREE / SEC  
 0.0 - 1.0 DEGREE / SEC



0.0 - 1.0 DEGREE  
 0.0 - 1.0 DEGREE / SEC  
 0.0 - 1.0 DEGREE / SEC  
 0.0 - 1.0 DEGREE / SEC

TIME AFTER SEPARATION - SECONDS

FIGURE 15

SATURN C1-B  
 S-L/S-IVB STAGE SEPARATION  
 33,740 LB PAYLOAD

ENGINE DEFLECTION TRANSIENTS  
 FOLLOWING SEPARATION

$\theta_0 = 1$  DEGREE  
 $\dot{\theta}_0 = 1$  DEGREE/SECOND  
 $\rho_p = 19$  LBS/FT<sup>2</sup>  
 $\alpha_0 = 4$  DEGREES  
 $\delta_{LIM} = 12$  DEGREES/SECOND

THRUST BUILD UP STARTS  
 AT 2 SECONDS

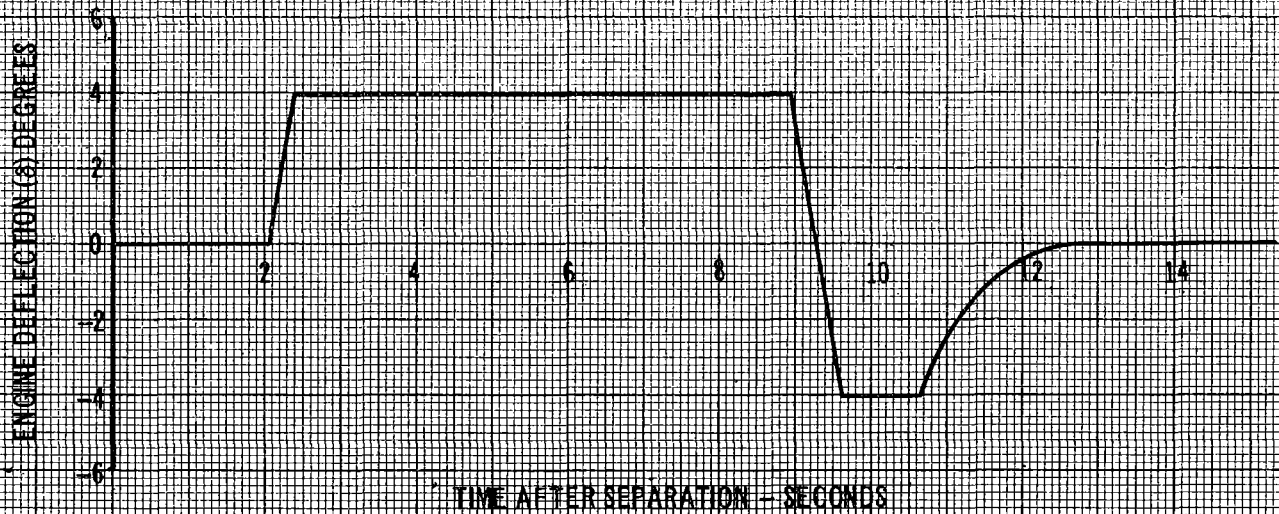
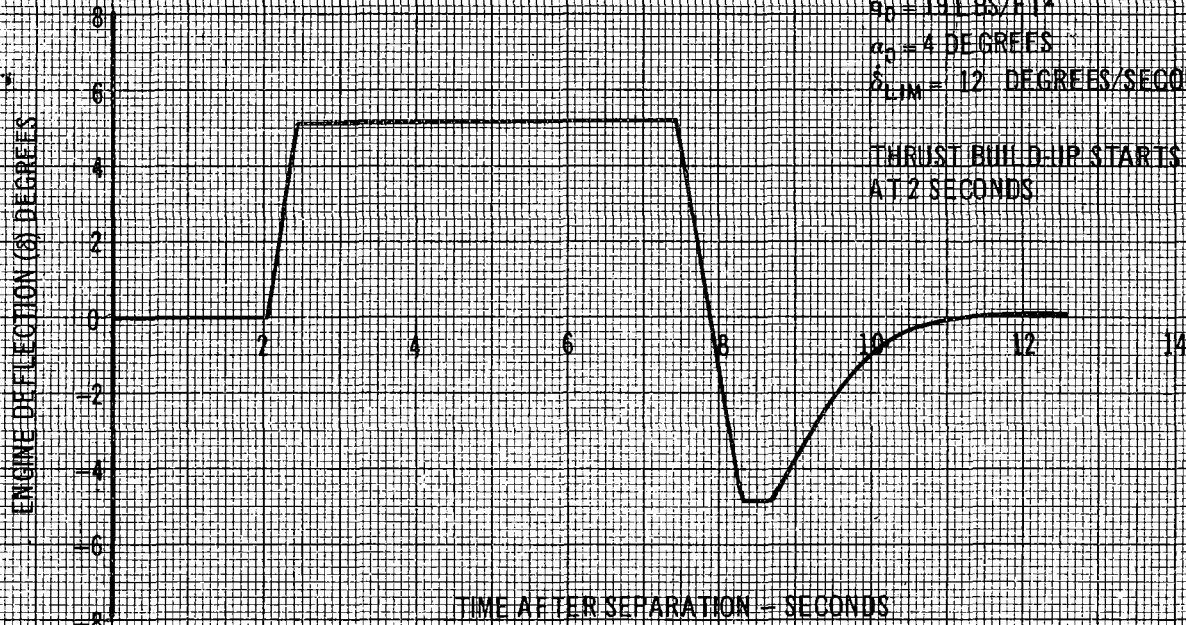


FIGURE 16

SATURN C1/B  
 S-1/S-1VB STAGE SEPARATION  
 33,740 LB PAYLOAD

ENGINE DEFLECTION TRANSIENTS  
 FOLLOWING SEPARATION

$\theta_0 = 1$  DEGREE  
 $\dot{\theta}_0 = 1$  DEGREE/SECOND  
 $\alpha_0 = 19$  LBS/FT<sup>2</sup>  
 $\alpha_0 = 4$  DEGREES  
 $\delta_{LIM} = 12$  DEGREES/SECOND

THRUST BUILD-UP STARTS  
 AT 2 SECONDS

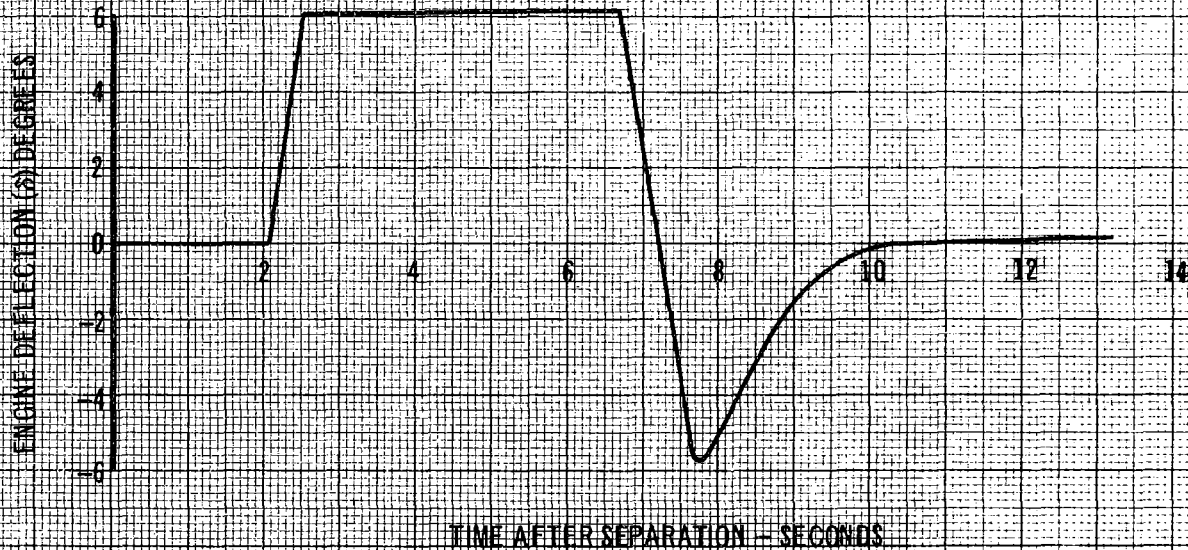
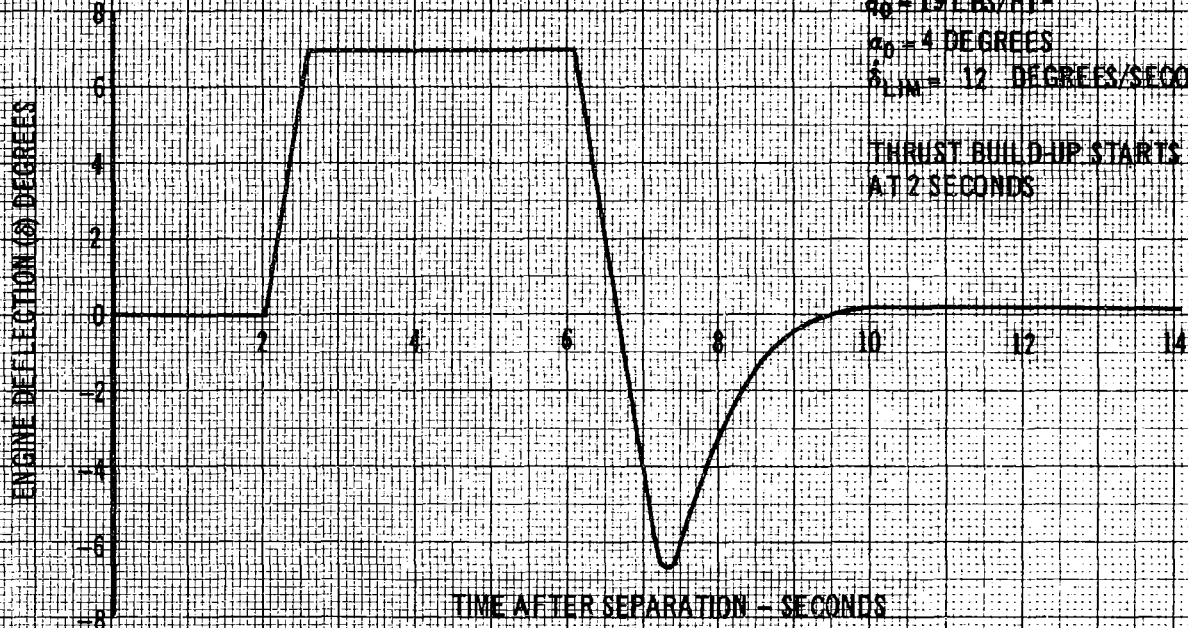


FIGURE 17

## Section 5

### ANALYTICAL APPROACH TO THE STABILITY LIMITS OF THE NON-LINEAR HYDRAULIC SERVO

Once the linear analysis of a servo system has been completed, a question which often arises is the following:

"What effect will the hardware nonlinearities have upon the system stability?"

The search for an answer to this question has prompted the development of a number of analytical techniques, of which the most commonly encountered is a Describing Function Approximation to linearity (DFA). An obsession with generality has relegated a majority of the answers obtained by this technique to a qualitative rather than a quantitative solution. Although it is also based on the DFA, the method presented in this memorandum has sacrificed some generality in order to insure a quantitative answer.

The basic objective of this method is to determine the stability limit, i.e., the magnitude of the input signal at which the system's response exhibits a sustained oscillation, for a system containing a nonlinearity. To determine this stability limit, it is necessary to place several constraints on the form of the input signal; these constraints are derived in detail in the body of the memorandum.

If it is assumed that any system selected for investigation may be represented by the block diagram of figure 1, then a standard mathematical model will be available for the analysis.

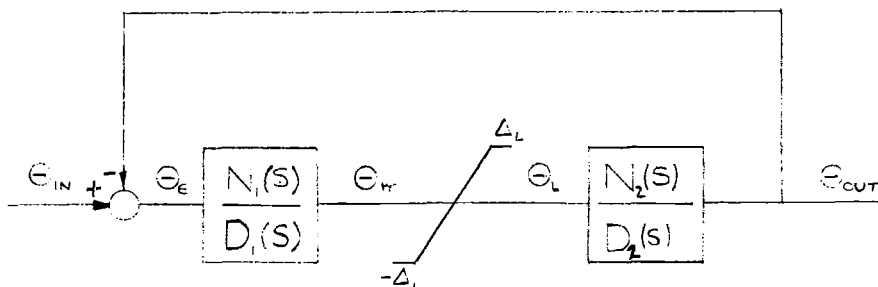


Figure 1. CANONICAL FORM

As it was previously stated this analysis is only concerned with the system when a sustained oscillation or limit cycle is present in the response. Besides giving a well defined criteria for determining the stability limit of a system the assumption of a limit cycle is made necessary by the definition of the describing function. To make use of the DFA, the nonlinearity in the system is replaced by its describing function,  $g$ , which relates the output of the nonlinearity to its input as shown in equation 1. The describing function for a saturation nonlinearity is given by equation 2.

$$\Theta_L(s) = g \Theta_m(s) \quad (1)$$

$$g = \frac{2}{\pi} \left[ \sin^{-1} \frac{\Delta_L}{\frac{A}{2}} + \frac{1}{2} \sin \left( 2 \sin^{-1} \frac{\Delta_L}{\frac{A}{2}} \right) \right] \quad (2)$$

If the analysis is limited to systems with a linear gain margin of at least 6 db (which is not too unreasonable) the following approximations can be made.\*

$$a. \quad \sin^{-1} \frac{\Delta_L}{\frac{A}{2}} \cong \frac{\Delta_L}{\frac{A}{2}}$$

$$b. \quad \frac{1}{2} \sin \left( 2 \sin^{-1} \frac{\Delta_L}{\frac{A}{2}} \right) \cong \frac{\Delta_L}{\frac{A}{2}}$$

and when these approximations are substituted into equation 1 the expression for  $g$  simplifies to:

$$g = \frac{4}{\pi} \cdot \frac{\Delta_L}{A} \quad (3)$$

Once the saturation has been replaced by its describing function gain the characteristic equation of the system in figure 1 may be written as:

$$\frac{\Theta_{out}}{\Theta_e}(s) = 1 + g \frac{N_1(s)N_2(s)}{D_1(s)D_2(s)} = 1 + g \frac{N(s)}{D(s)} \quad (4)$$

---

\* For a system with a linear gain of 6 db, the real axis crossover is at -2 and, therefore, the magnitude of  $g$  necessary to make the system limit cycle is 1/2. If equations 1 and 2 are solved for  $\frac{\Delta_L}{A}$  and the value of 1/2 is used for  $g$ , the error incurred by using equation 3 in place of equation 2 will be only 5.25%.

and if both sides of equation 4 are multiplied by  $D(S)$  the characteristic equation may be rewritten as:

$$\Delta^*(S) = D(S) \frac{\Theta_{out}}{\Theta_i}(S) = D(S) + gN(S) \quad (5)$$

Since both  $N(S)$  and  $D(S)$  are polynomials in  $S$  equation 5 may be written as:

$$\Delta^*(S) = \sum_{i=0}^d a_i S^i + g \sum_{j=0}^n b_j S^j \quad (6)$$

Now if the system is to contain a limit cycle, the characteristic equation,  $\Delta^*(S)$ , must contain a pair of conjugate imaginary roots, in which case  $\Delta^*(S)$  may be written as:

$$\Delta^*(S) = (S^2 + \omega^2) \sum_{k=0}^{d-2} c_k S^k = (S^2 + \omega^2) C(S) \quad (7)$$

Equation 7 may be expanded into:

$$\Delta^*(S) = c_{d-2} S^d + c_{d-3} S^{d-1} + \sum_{k=2}^{d-2} (c_{k-2} + c_k \omega^2) S^k + c_1 \omega^2 S + c_0 \omega^2 \quad (8)$$

It is desirable at this time to equate the  $\Delta^*(S)$  of equation 6 to that of equation 8, to do this equation 6 must be manipulated into the form of equation 8. To facilitate this manipulation a variable  $\sigma(\lambda)$  will be defined as:

$$\sigma(\lambda) \stackrel{\Delta}{=} 1 \quad \lambda \geq 0$$

$$\sigma(\lambda) \stackrel{\Delta}{=} 0 \quad \lambda < 0$$

setting  $\lambda = n-d$  equation 5 may be written as:

$$\Delta^*(S) = [a_d + \sigma(\lambda) g b_d] S^d + [a_{d-1} + \sigma(\lambda+1) g b_{d-1}] S^{d-1} + \sum_{i=2}^{d-2} [a_{d-i} + \sigma(\lambda+i) g b_{d-i}] S^i + [a_1 + \sigma(\lambda-1) g b_1] S + a_0 + g b_0 \quad (9)$$

If the coefficients of like powers of  $S$  are equated between equations 8 and 9, the following equations are derived:

$$c_0 \omega^2 = a_0 + g b_0 \quad (10)$$

$$c_1 \omega^2 = a_1 + g b_1 \quad (11)$$

$$c_{i-2} + \omega^2 c_i = a_i + \sigma(n-i-1)g b_i \quad i = 2, 3, \dots, d-2 \quad (12)$$

$$c_{d-3} = a_{d-1} + \sigma(n-d+1)g b_{d-1} \quad (13)$$

$$c_{d-2} = a_d + \sigma(n-d)g b_d \quad (14)$$

Equation 12 is actually a set of  $d-3$  equations and, therefore, the total number of equations represented by equations 10 through 14 is  $d+1$ . Since there are also  $d+1$  unknowns ( $g, \omega^2, c_0, c_1, \dots, c_{d-2}$ ) each of these variables will be determined uniquely by the system parameters, ( $a_i, b_j : i = 1, 2, \dots, d; j = 1, 2, \dots, n$ ). Two of the solutions of these simultaneous equations will be:

$$g = G(a_i, b_j) \quad (15)$$

$$\omega = \Omega(a_i, b_j) \quad (16)$$

Where equations 15 and 16 represent known functions of the system parameters. Now equations 3 and 15 can be equated.

$$G(a_i, b_j) = \frac{4}{\pi} \cdot \frac{\Delta_L}{Z} \quad (17)$$

and if equation 17 is solved for  $\Delta_L$ :

$$\Delta_L = \frac{\pi}{4} \cdot G(a_i, b_j) \cdot Z \quad (18)$$

The only chore remaining is the determination of an expression for  $Z$ . Since  $Z$  is the magnitude of the system's response to the driving function,  $\theta_{in}(s)$ , the form of the driving function must be known before an expression for  $Z$  can be derived.

The two types of driving function that are most commonly employed in systems analysis are the sinusoidal and polynomial functions of time; therefore, it would be desirable to calculate the stability limit for both of these. In choosing a

$\Theta_{in}(t)$  for the analysis it should be kept in mind that the steady state form of  $\Theta_m(t)$  must be a sinusoid if the DFA is to be used and that it must be a single sinusoid only, i.e., not a sum of two or more, since the inclusion of a non-linearity in the system precludes any application of the superposition law applied so unconsciously in linear systems analysis. With this in mind the expression for  $\Theta_\epsilon(s)$  is written as:

$$\Theta_\epsilon(s) = \frac{D(s)}{\Delta^*(s)} \Theta_{in}(s) \quad (19)$$

using equation 19 and the fact that  $\Theta_m(s) = \frac{N_1(s)}{D_1(s)} \Theta_\epsilon(s)$

$$\Theta_m(s) = \frac{N_1(s)}{D_1(s)} \cdot \frac{D_1(s)D_2(s)}{\Delta^*(s)} \cdot \Theta_{in}(s) \quad (20)$$

or

$$\Theta_m(s) = \frac{N_1(s)D_2(s)\Theta_{in}(s)}{\Delta^*(s)} \quad (21)$$

In view of the previous discussion all of the poles of  $\Theta_m(s)$ , except the two at  $\pm j\omega$ , must be restricted to the left half of the S plane. Unfortunately this restriction automatically removes the sinusoid from the realm of investigation, for if  $\Theta_{in}(s)$  is the transform of a sine wave it will contain a pair of conjugate imaginary poles which would violate the restriction set forth previously. At first glance it would appear that a polynomial function of time would also violate this restriction, however, further investigation will show that there is a way around this seeming road block. Let  $\Theta_{in}(t)$  be a polynomial function of time such that its transform  $\Theta_{in}(s)$  is:

$$\Theta_{in} = \sum_{r=0}^m \frac{r_r}{s^r} = \frac{1}{s^m} \sum_{r=0}^m r_r s^{m-r} \quad (22)$$

(It should be noted that the term  $\frac{r_0}{s^0} = r_0$  in equation 22 is the Dirac delta or impulse function of time.) Now if this expression for  $\Theta_{in}(s)$  is substituted into equation 21:

$$\Theta_m(s) = \frac{N_1(s)D_2(s)}{s^m \Delta^*(s)} \cdot \sum_{r=0}^m r_r s^{m-r} \quad (23)$$

It is now apparent that the  $m^{\text{th}}$  order pole at the origin brought into the equation by  $\Theta_{\text{in}}(s)$  violates the restriction and must be removed. This task is easier than it seems: If one of the roots of  $D_2(s)$  is a factor of the form  $s^p$  then it is only necessary to make certain that  $m \leq p$  to eliminate the  $m^{\text{th}}$  order pole at the origin, in which case equation 23 becomes:

$$\Theta_m(s) = \frac{N_1(s) s^{p-m}}{C(s)(s^2 + \omega^2)} \cdot \left[ \frac{\sum_{i=p}^d a_i s^{i-p}}{D_1(s)} \right] \cdot \sum_{r=0}^m r_r s^{m-r} \quad (24)$$

Now if equation 24 is multiplied and divided by  $\omega$ :

$$\Theta_m(s) = \left\{ \frac{N_1(s) s^{p-m}}{C(s) \omega} \cdot \left[ \frac{D_2(s)}{s^p} \right] \cdot \sum_{r=0}^m r_r s^{m-r} \right\} \cdot \left\{ \frac{\omega}{s^2 + \omega^2} \right\} \quad (25)$$

Since this analysis is only interested in the system response after all the transient terms have died out, the inverse transform of equation 25 may be written as:

$$\Theta_m(t) = z \sin \omega t \quad (26)$$

Where

$$z = \omega^{p-m-1} \left| \frac{N_1(j\omega) [D_2(j\omega)/(j\omega)^p]}{C(j\omega)} \cdot \sum_{r=0}^m r_r (j\omega)^{m-r} \right| \quad (27)$$

Substituting this value of  $\Theta_m$  into equation 18 the final equation is arrived at:

$$\Delta_L = \frac{\pi}{4} G(\alpha_i, b_j) \omega^{p-m-1} \left| \frac{N_1(j\omega) [D_2(j\omega)/(j\omega)^p]}{C(j\omega)} \cdot \sum_{r=0}^m r_r (j\omega)^{m-r} \right| \quad (28)$$

Equation 28 gives the value of  $\Delta_L$  at which the system will limit cycle as a function of the system parameters and the magnitude of the forcing function. The main difficulty in using this method is solving the simultaneous equations 10 through 14, if an attempt is made to apply this method to a complex model it may be necessary to resort to digital computer techniques to solve these equations. It should be emphasized that while this method was derived for a saturation non-linearity it should not be too difficult to apply it to other nonlinearities which do not contribute any phase lag to the system, and it might even be possible to extend the general philosophy to any nonlinearity.

## LIST OF SYMBOLS

$a_i, b_j$	System parameters
$d$	Order of denominator polynomial
$n$	Order of numerator polynomial
$\theta_{in}$	Input signal to the system
$\theta_{out}$	Output of the system
$\theta_e$	Error signal
$\theta_m$	Input to the saturation
$\theta_L$	Output of the saturation
$\Delta_L$	Value at which the signal saturates
$\Delta^*$	Characteristic equation
$g$	Describing function gain
$\omega$	Frequency of the limit cycle
$Z$	Magnitude of the limit cycle oscillation prior to entering the saturation
$\frac{N_1}{D_1}$ and $\frac{N_2}{D_2}$	Transfer functions of the system

## SECTION 6

### SLOSHING & STABILITY ANALYSIS

The purpose of this study was to determine the sloshing effect of LH<sub>2</sub> and LOX on the time response of the C-5 configuration S-IVB autopilot. The rigid body autopilot model shown in Figure 1 on page 2 was used in conjunction with representative equations of sloshing motion. These sloshing motion equations are reproduced on page 9.

The above system equations were programmed on a PACE 231 R analog computer and computer runs were made using the following values of LH<sub>2</sub> and LOX damping coefficients ( $\zeta_1$  and  $\zeta_2$  respectively):

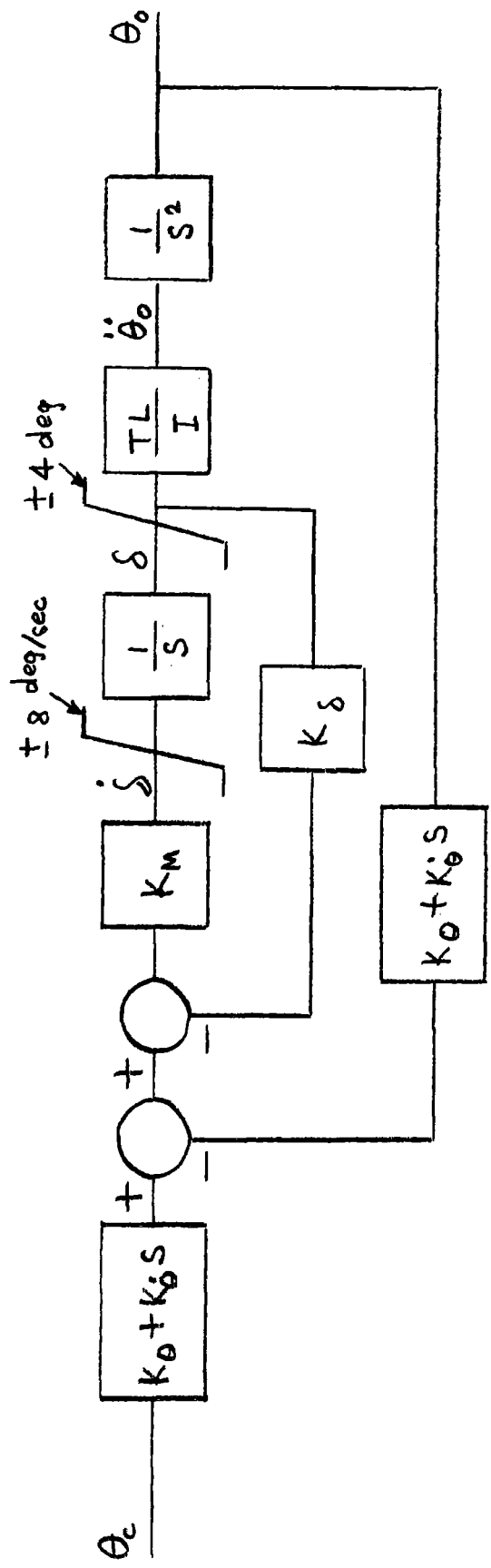
$\zeta_1$	$\zeta_2$
0	0
0.0001	0.001
0.001	.003
0.01	0.01

The initial conditions used in all runs were:

$$\dot{\theta} = 0.5 \text{ deg/sec (rate change of pitch)}$$

$$\theta = 1.0 \text{ deg (pitch)}$$

The results of this investigation are based on peak to peak oscillation values of  $\delta$ ,  $\theta$ ,  $\psi$  about a nominal value of zero. Values at 25, 50, 75, and 100 seconds burning time are presented in tables 1 through 4 on pages 3 through 6. In addition, a plot of peak to peak values of  $\delta$  versus time for a typical run is shown in figures 2 and 3 on pages 7 and 8. After the first 10 seconds burning, the oscillations of  $\delta$ ,  $\theta$ , and  $\psi$  follow similar patterns.



- $K_\theta = 17.05 \text{ deg/deg}$
- $K_{\dot{\theta}} = 19.0 \text{ deg/deg/sec}$
- $K_M = 0.717 \text{ deg/sec/deg}$
- $K_\delta = 8.77 \text{ deg/deg}$

Figure 1. sIV B Autopilot Model.

Peak to peak range of  $\delta$ ,  $\dot{\theta}$ ,  $\theta$  for SIV B  
at 25 secs burning time

$\begin{matrix} \downarrow \\ \downarrow_1 \\ \downarrow_2 \end{matrix}$	0.0	0.0001	0.001	0.01
0.0	0.2 0.07 0.033	0.2 0.07 0.033	0.2 0.07 0.033	0.2 0.07 0.033
0.001	0.21 0.07 0.033	0.2 0.07 0.033	0.2 0.07 0.033	0.2 0.07 0.033
0.003	0.19 0.07 0.033	0.19 0.07 0.033	0.2 0.07 0.033	0.19 0.07 0.033
0.01	0.17 0.05 0.03	0.17 0.05 0.03	0.17 0.05 0.03	0.17 0.05 0.03

$\pm \delta$ : deg
$\pm \dot{\theta}$ : deg/sec
$\pm \theta$ : deg

$\downarrow_1$  - LH<sub>2</sub> damping coeff  
 $\downarrow_2$  - LOX damping coeff

Table 1.

Peak to peak range of  $\delta$ ,  $\dot{\theta}$ ,  $\theta$  for SIV B  
at 50 secs burning time

$\int_2 \backslash \int_1$	0.0	0.0001	0.001	0.01
0.0	0.130 0.06 0.03	0.13 0.06 0.029	0.13 0.063 0.029	0.10 0.044 0.021
0.001	0.132 0.062 0.03	0.131 0.06 0.03	0.132 0.058 0.029	0.085 0.044 0.02
0.003	0.13 0.054 0.028	0.13 0.055 0.027	0.112 0.05 0.025	0.08 0.035 0.018
0.01	0.095 0.043 0.021	0.094 0.04 0.021	0.089 0.037 0.02	0.055 0.025 0.013

$\pm \delta$ : deg
$\pm \dot{\theta}$ : deg/sec
$\pm \theta$ : deg

$\int_1$  - LH<sub>2</sub> damping coeff.  
 $\int_2$  - LOX damping coeff.

Table 2.

Peak to peak range of  $\delta$ ,  $\dot{\theta}$ ,  $\theta$  for SIV B  
at 75 secs burning time

$\zeta_2 \backslash \zeta_1$	0.0	0.0001	0.001	0.01
0.0	0.095 0.04 0.021	0.09 0.042 0.02	0.087 0.04 0.021	0.04 0.018 0.0075
0.001	0.09 0.041 0.02	0.092 0.04 0.021	0.085 0.038 0.02	0.038 0.016 0.0075
0.003	0.085 0.038 0.019	0.085 0.038 0.018	0.08 0.035 0.018	0.033 0.015 0.0075
0.01	0.081 0.035 0.019	0.08 0.035 0.018	0.072 0.031 0.015	0.026 0.013 0.005

$\pm \delta$ : deg
$\pm \dot{\theta}$ : deg/sec
$\pm \theta$ : deg

$\zeta_1$  - LH<sub>2</sub> damping coeff.  
 $\zeta_2$  - LOX damping coeff.

Table 3.

Peak to peak range of  $\delta$ ,  $\dot{\theta}$ ,  $\theta$  for SIV B  
after 100 secs of flight

$\int_2 \backslash \int_1$	0.0	0.0001	0.001	0.01
0.0	0.088	0.085	0.075	0.02
	0.04	0.038	0.032	0.0088
	0.02	0.02	0.018	0.0043
0.001	0.088	0.088	0.075	0.021
	0.04	0.038	0.035	0.009
	0.02	0.02	0.018	0.005
0.003	0.085	0.082	0.073	0.02
	0.038	0.035	0.032	0.008
	0.019	0.019	0.015	0.004
0.01	0.08	0.078	0.07	0.0175
	0.035	0.034	0.03	0.0075
	0.018	0.016	0.015	0.0038

$\pm \delta$ : deg
$\pm \dot{\theta}$ : deg/sec
$\pm \theta$ : deg

$\int_1$  - LH<sub>2</sub> damping coeff.

$\int_2$  - LOX damping coeff.

Table 4.

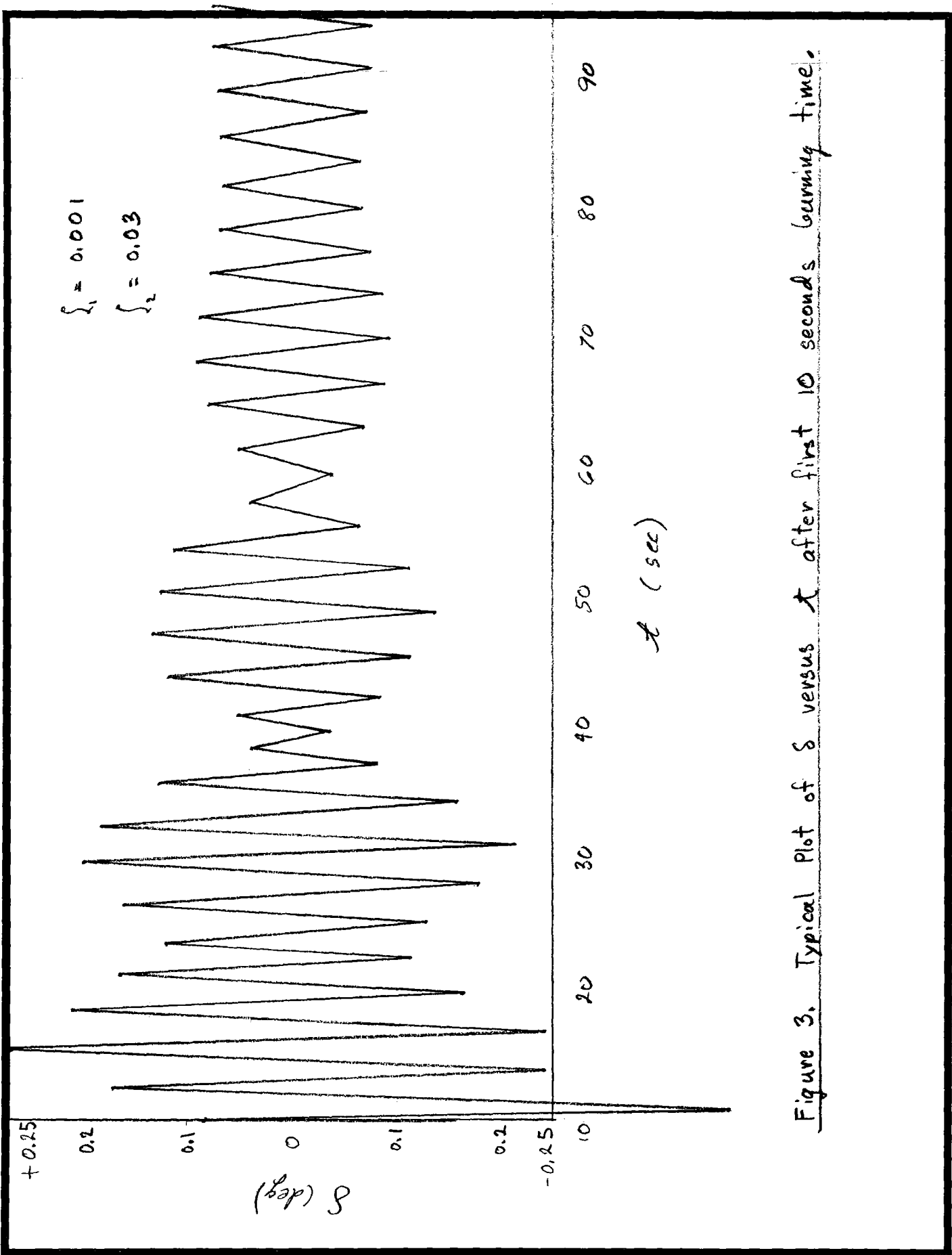


Figure 3. Typical Plot of  $\delta$  versus  $t$  after first 10 seconds ginning time.

## Equations of Sloshing Motion:

$$1. \ddot{\theta} = \frac{TL}{I} \delta + \frac{57.3 m_1}{I} \left[ -l_1 (2\zeta_1 \omega_1 \dot{\xi}_1 + \omega_1^2 \xi_1) + a \xi_1 \right] \\ + \frac{57.3 m_2}{I} \left[ -l_2 (2\zeta_2 \omega_2 \dot{\xi}_2 + \omega_2^2 \xi_2) + a \xi_2 \right]$$

$$2. \ddot{x} = -\frac{T}{57.3 m} \delta + \frac{m_1}{m} (2\zeta_1 \omega_1 \dot{\xi}_1 + \omega_1^2 \xi_1) + \frac{m_2}{m} (2\zeta_2 \omega_2 \dot{\xi}_2 + \omega_2^2 \xi_2)$$

$$3. \dot{\xi}_1 = \frac{l_1}{57.3} \ddot{\theta} - \dot{x} - 2\zeta_1 \omega_1 \dot{\xi}_1 - \omega_1^2 \xi_1$$

$$4. \dot{\xi}_2 = \frac{l_2}{57.3} \ddot{\theta} - \dot{x} - 2\zeta_2 \omega_2 \dot{\xi}_2 - \omega_2^2 \xi_2$$

where:

$\theta$  = vehicle pitch (deg)

$T$  = engine thrust (lb)

$I$  = pitch moment of inertia (slug-ft<sup>2</sup>/sec<sup>2</sup>)

$\delta$  = engine deflection (deg)

$m_1$  = LH<sub>2</sub> sloshing mass (slugs)

$m_2$  = LOX sloshing mass (slugs)

$m$  = total mass of vehicle and fuel (slugs)

$\zeta_1$  = LH<sub>2</sub> damping coefficient (unitless)

$\zeta_2$  = LOX damping coefficient (unitless)

$\omega_1$  = LH<sub>2</sub> sloshing frequency (rad/sec)

$\omega_2$  = LOX sloshing frequency (rad/sec)

$\xi_1$  = lateral motion of LH<sub>2</sub> sloshing mass (ft)

$\xi_2$  = lateral motion of LOX sloshing mass (ft)

$a$  = vehicle acceleration (ft/sec<sup>2</sup>)

$\dot{x}$  = lateral motion of vehicle c.g. (ft)

GARDEN HOSE DYNAMIC COUPLING STABILITY ANALYSIS

SUMMARY:

The main objective of a control system analysis is to seek out any adverse stability effects that may be present. Quite often coined expressions are attached to certain problems which occur more often than others and can be categorized by their nature. Eventually, these terms make their way into the engineering vernacular. Classic examples of this are tail-wags-dog and flutter. The text of this presentation deals with still a third undesirable dynamic affect--garden hose. Impact of this instability on the Saturn IB vehicle is discussed. A mathematical formulation and solution of the garden hose equations presented. Finally, a comparison is made between garden hose and classical flutter, and the mysteries surrounding the exotic name of garden hose are reduced to straightforward engineering terms.

INTRODUCTION:

Garden hose is an instability whose basic ingredients are one free-free body bending mode and one engine rotation mode with thrust. Figure 1 is a schematic of these modes--in this case, a first body bending mode and an engine rotation mode, both acting in the same plane. The fact is to be noted that the system is made up only of masses, springs and dampers. The only external force results from engine thrust. No control system is included, as the instability is not a result of the control system. However, an engine servo included in the system will alter the problem; this feature will be discussed later in the text.

The easiest explanation of the mechanism of garden hose is accomplished by demonstrating the forcing effect a body bending mode has on an engine rotation mode due to mass coupling and the effect an engine rotation mode has on body bending due to the thrust forces. These two interreactions are discussed separately, and the effects are then combined to demonstrate the overall mechanism.

To illustrate the forcing effect body bending imparts to engine rotation, a two degree of freedom system is assumed. This system consists of an engine resiliently mounted about its gimbal and a body bending mode which can be commanded

## SYMBOLS

$\xi$	-	Coordinate describing body bending (inches)
$\delta$	-	Coordinate describing engine rotation (radians)
$M_{\xi}$	-	Body bending modal mass (lb·sec <sup>2</sup> /inch)
$I_{HL}$	-	Inertia of engine about hinge line (lb·inch·sec <sup>2</sup> )
$P_{\xi\delta}$	-	Product of inertia between body and engine (lb·sec <sup>2</sup> )
$D_{\xi}$	-	Modal damping of body (lb·sec/inch)
$D_{\delta}$	-	Damping of engine (lb·inch·sec)
$K_{\xi}$	-	Modal spring of body (lb/inch)
$K_{\delta}$	-	Engine spring (in·lb)
$A_{\delta}$	-	Modal hinge line deflection (non-dimensional)
$A'_{\delta}$	-	Modal hinge line rotation (1/inch)
$T$	-	Thrust (pounds)
$S$	-	Laplace operator (1/sec)
$C_{Z\delta}$	-	Aerodynamic force coefficient of airfoil (non-dimensional)
$q$	-	Dynamic pressure (PSF)
$s$	-	Area of airfoil (ft <sup>2</sup> )

SCHEMATIC OF THE SYSTEM

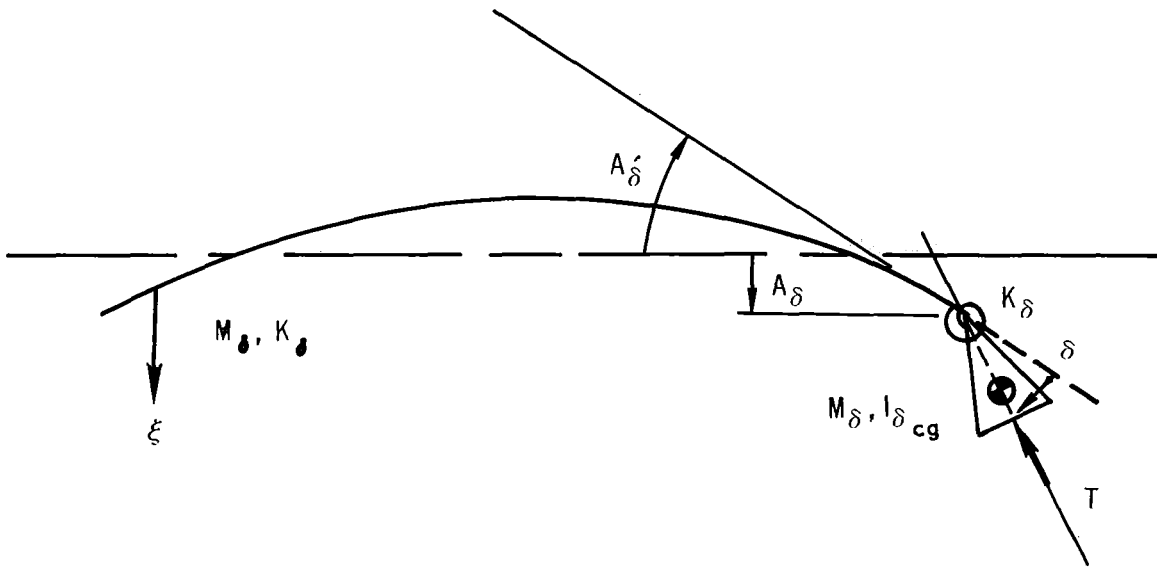


FIGURE 1

to move at the engine open loop natural frequency.<sup>1</sup> The assumed system is pictorially represented in figure 2a with initial conditions of a finite counterclockwise engine deflection but no angular engine rate. The body is initially at a zero deflection but possesses a sinusoidal velocity such that the gimbal point is displacing down with time. Since displacement of the body is zero, instantaneous acceleration at the gimbal is zero and no moment is applied to the overhanging mass of the engine. Time response plots of engine rotation, body deflection and moment on the engine due to gimbal acceleration are presented in figure 2b.

If the system were allowed to move through a phase angle of  $90^\circ$ , the new body and engine positions would be as shown in figure 3a. The body has deflected such that the gimbal point has translated down. Since the body is moving in sinusoidal motion, the acceleration vector at the gimbal will be directed up. This acceleration will result in a clockwise moment to act on the overhanging mass of the engine throughout the  $90^\circ$  of displacement. The engine was assumed initially to be at a counterclockwise angle with no angular rate. This assumption implies the engine reached its maximum excursion and will displace to zero angular deflection in sinusoidal motion  $90^\circ$  later. By plotting this implied engine motion and the moment resulting from gimbal acceleration versus time, the fact that the moment is leading the engine displacement by  $90^\circ$  is apparent. Also, body deflection will lead the engine by  $90^\circ$  since the moment and body displacement are in phase. Therefore, the moment has the proper phase to sustain sinusoidal motion in the engine at the engine natural frequency.

The argument is pursued further in figures 4, 5 and 6 for progressively increasing body phase angles of  $180^\circ$ ,  $270^\circ$  and  $360^\circ$ . The conclusions reached for the first  $90^\circ$  of movement hold up for all of these later periods. Thus, the pictorial representation is valid for the assumed system.

A second system is employed to illustrate engine force on the body. This system consists of a body bending mode with no constraints and an engine rotation mode that can be commanded to move at the body bending natural frequency. The engine will impose a vertical force component on the body which is equal (for small angles) to  $-T X \delta$ .<sup>2</sup> This force will drive body bending at its natural frequency

---

1 A note should be made of the fact such a mechanism cannot exist unless the product of inertia between body and engine were zero.

2 The negative sign results because a positive engine rotation (clockwise) produces a negative force (up) on the body.

BODY/ENGINE PHASE RELATIONSHIP DURING GARDEN HOSE

FIG 2-A

BODY BENDING  
PHASE ANGLE = 0

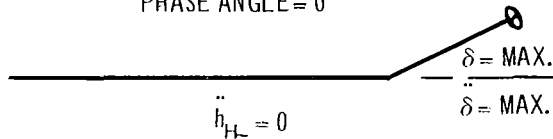


FIG 2-B

FIG 3-A

PHASE ANGLE =  $\frac{\pi}{2}$

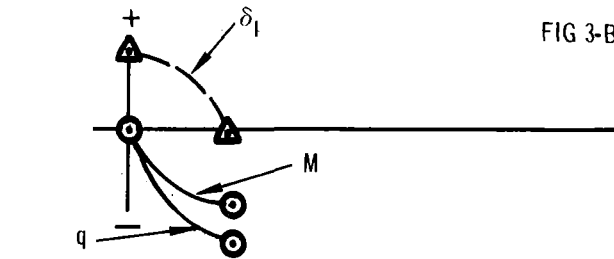
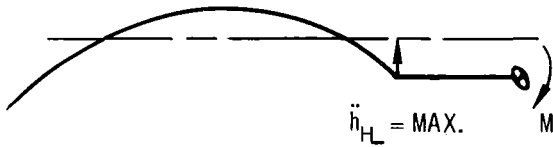


FIG 3-B

FIG 4-A

PHASE ANGLE =  $\pi$

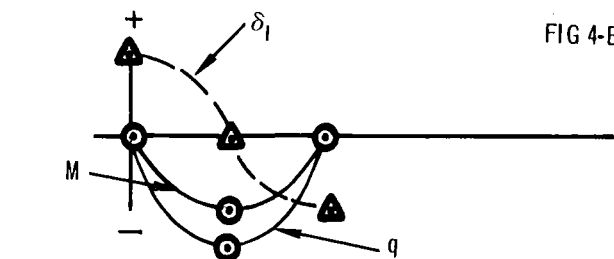
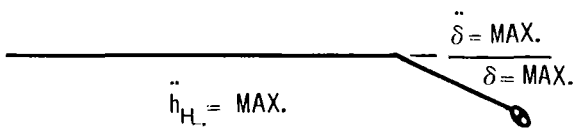


FIG 4-B

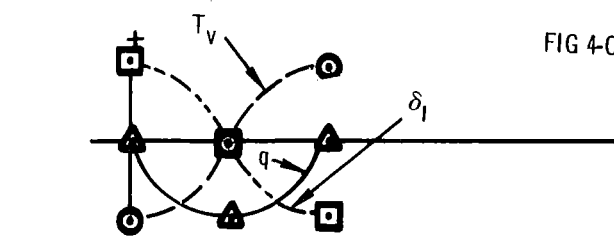
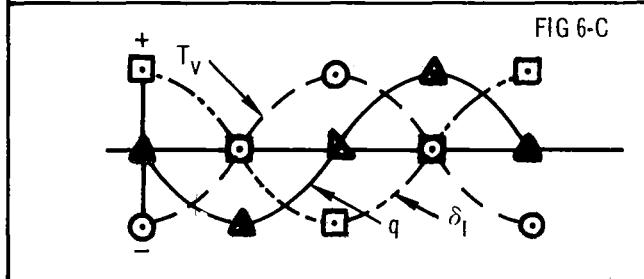
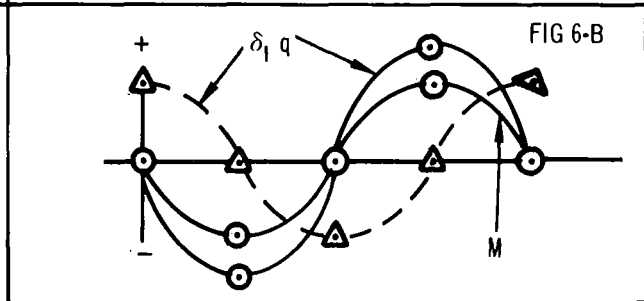
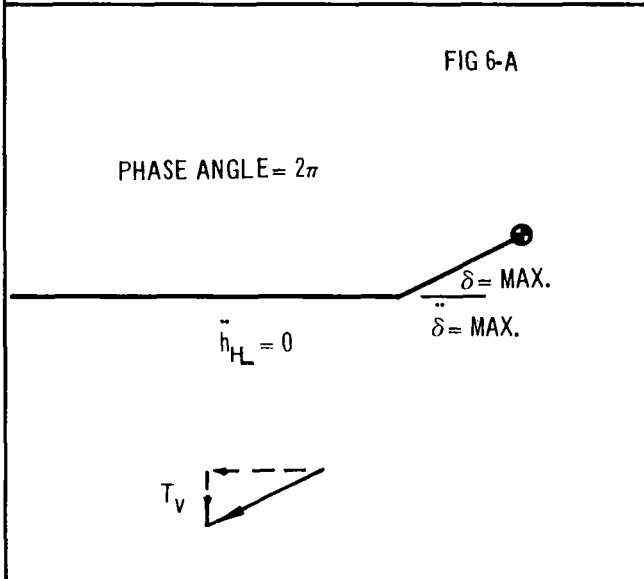
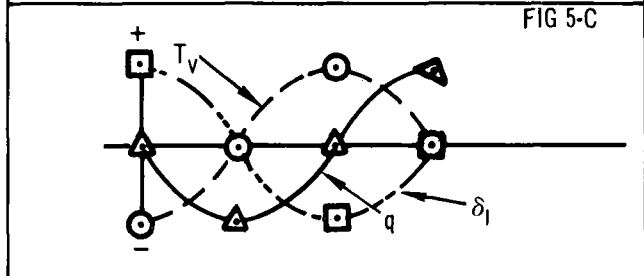
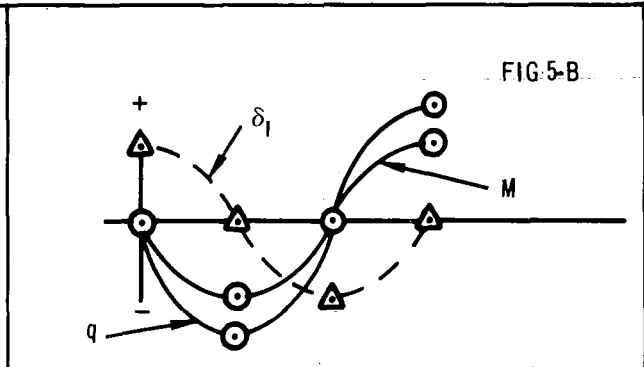
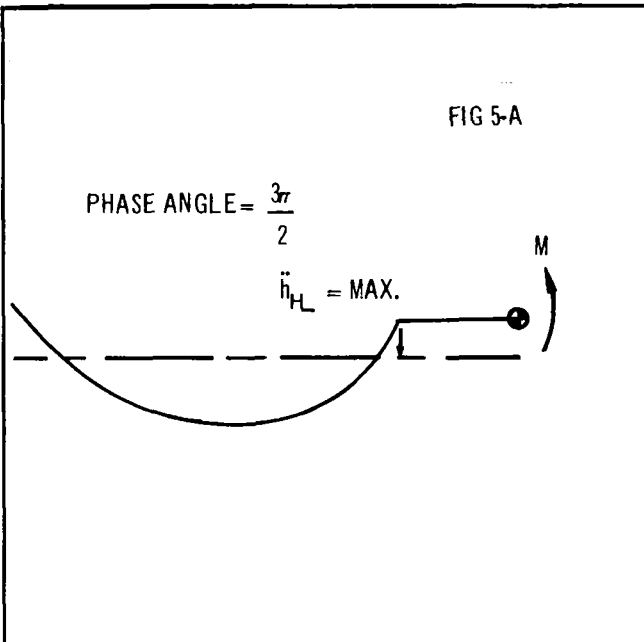


FIG 4-C



and will lead bending deflection by  $90^\circ$ . Since engine deflection is  $180^\circ$  removed from the vertical thrust component, the engine will lag the body by  $90^\circ$ . This phase relationship is the same as was realized in the first assumed system. The resulting engine position, body position and vertical thrust component time plots are presented in part C of figures 2 through 6.

Therefore, in the first assumed system the body drove the engine inertially and led the engine by  $90^\circ$ . In the second assumed system the engine drove body bending mode due to the vertical component of thrust and the body led the engine by  $90^\circ$ . Since the two modes are driving each other, the possibility of an instability is suggested. The assumed systems were fictitious as two coupled modes cannot possess the same frequency. However, two modes can be very close together in frequency, and produce motion similar to that discussed. The frequency for the resulting instability will be somewhere between the two natural frequencies of the natural free-free system.

If the engine were to be replaced by an airfoil and this airfoil subjected to a fairly high supersonic flow, a resulting flutter instability could be realized which would be very similar in nature to the garden hose instability. If the inertial effects of the airfoil were the same as the engine, the aerodynamic force change in the vertical direction for a change in  $\delta$  were the same as the vertical thrust component due to a change in  $\delta$ , and the aerodynamic center were on the hinge line, the resulting equations would be almost exactly the same. The only way the two would differ would lie in aerodynamic damping terms which would not be present in garden hose. However, the mechanism is primarily the same and the method of approach to the problem should not be foreign to one who is used to flutter solutions. This similarity is illustrated in figure 7.

For the system of figure 1, the equations of motion are presented in figure 8. The derivation of these equations is contained in the appendix to this presentation. The coordinates for writing the equations are chosen such that the system is mass coupled with no spring coupling.

Once the equations of motion have been written and the proper values inserted, the roots can be extracted and stability can be determined on the basis of whether the roots lie right or left of the complex plane. However, since

# GARDEN HOSE/FLUTTER SIMILARITY

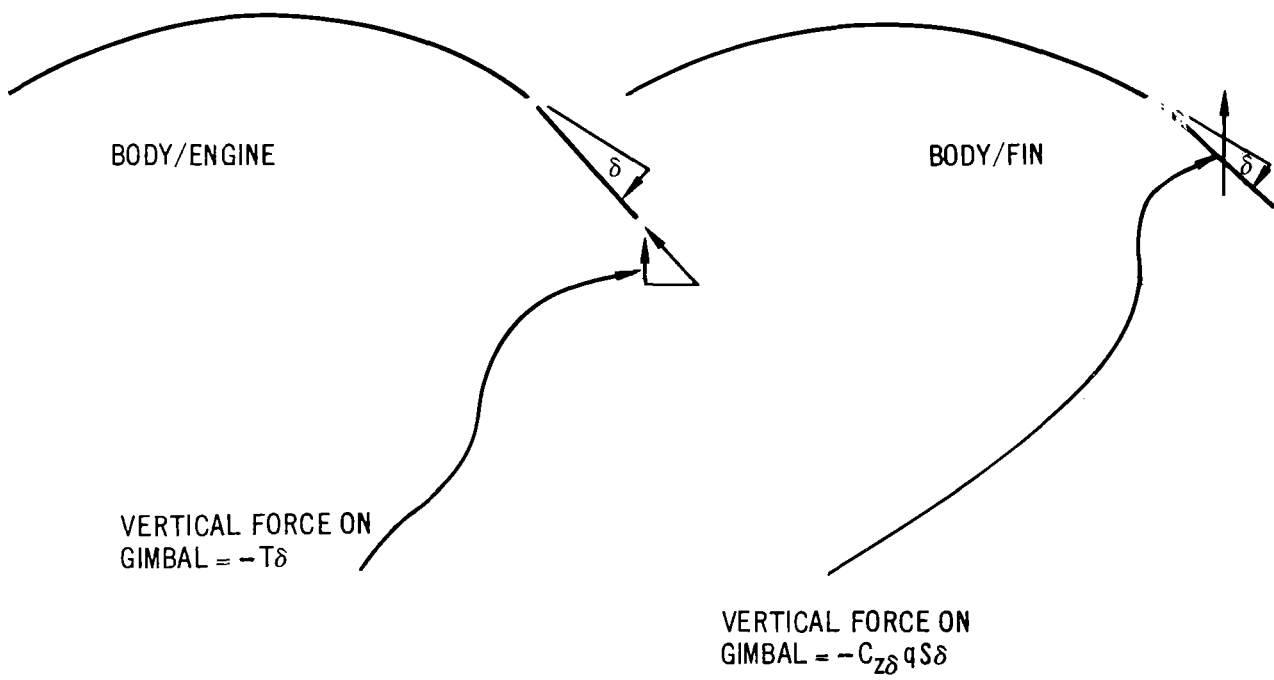


**FIGURE 7**

EQUATIONS OF MOTION

$$\left( \begin{array}{cc} M_{\xi} & P_{\xi\delta} \\ P_{\xi\delta} & I_H \end{array} \right) S^2 + \begin{array}{cc} D_{\xi} & 0 \\ 0 & D_{\delta} \end{array} S + \begin{array}{cc} K_{\xi} & 0 \\ 0 & K_{\delta} \end{array} \begin{array}{c} \xi \\ \delta \end{array} =$$

$$\begin{array}{ccc} -TA_{\delta} & A'_{\delta} & -TA_{\delta} \\ 0 & & 0 \end{array} \begin{array}{c} \xi \\ \delta \end{array}$$

FIGURE 8

an IBM solution is suggested and the use of IBM programs constitute a considerable time delay between set-up of the problem and the answer, an alternate method was used. If damping was disregarded and the equations of motion were expanded into a polynomial, the resultant polynomial would be fourth order, but with no odd powers (figure 9). The quadratic formula can be employed as a solution for  $S^2$ , and the resultant answer for  $S^2$  can simply be taken to the  $1/2$  power to find the root  $S$ . This relatively simple closed form solution was programmed onto the Bendix G-15 computer and the data for the trend study was obtained by this method. Another useful means was employed to determine the thrust that would be required for marginal stability or the onset of the instability. Since the characteristic equation has only even powers of  $S$  and all of the coefficients of the  $S$  operator are positive, it can be shown that the onset of instability occurs when the term inside the radical of the quadratic solution goes to zero. Making use of this fact, the G-15 computer was programmed to solve for the thrust required to cause an instability for any given set of input conditions. By these methods the thrust could then be varied and the roots extracted quite rapidly.

The results of the aforementioned trend study appear in figures 10 and 11 of the presentation. Figure 10 is a plot of thrust required versus engine spring rate. Three parametric sets of curves were generated for three body bending frequencies. As to be expected, the minimum thrust was required when the uncoupled engine frequency was set equal to be the uncoupled body bending frequency. This minimum thrust required situation corresponds to the low point of the parabola of each of the three curves. Figure 11 presents the damping ratios versus thrust for three conditions of uncoupled engine frequency.

Three uncoupled body frequencies were the same as used in figure 10, viz., 2.70 cps, 3.82 cps and 5.41 cps. Therefore, the boundary conditions of figure 11 correspond to the minimum point of each parabola of figure 10.

To determine the damping ratios that would result if damping had been included in the system, a very good approximation can be made by translating the curves in figure 2 down by the value of desired input damping. This approximation is given if the damping of both systems is assumed to be equal. If the damping of the two modes is assumed not to be equal, the two damping values would have to be weighed according to the magnitude of the resulting eigenvectors of the zero damped solution.

SOLUTION OF ZERO INPUT  
DAMPING EQUATIONS

$$\begin{vmatrix} M_{\xi} S^2 + K_{\xi} + T A_{HL} A'_{HL} & P_{\xi \delta} S^2 + T A_{HL} \\ P_{\xi \delta} S^2 & I_{HL} S^2 + K_{\delta} \end{vmatrix}$$

$$= a_4 S^4 + a_2 S^2 + a_0 = 0$$

$$S = \left( \frac{-a_2 \pm \sqrt{a_2^2 - 4a_4 a_0}}{2a_4} \right)^{1/2}$$

FIGURE 9

# THRUST VS. ENGINE ROTATIONAL SPRING ( $K_\delta$ )

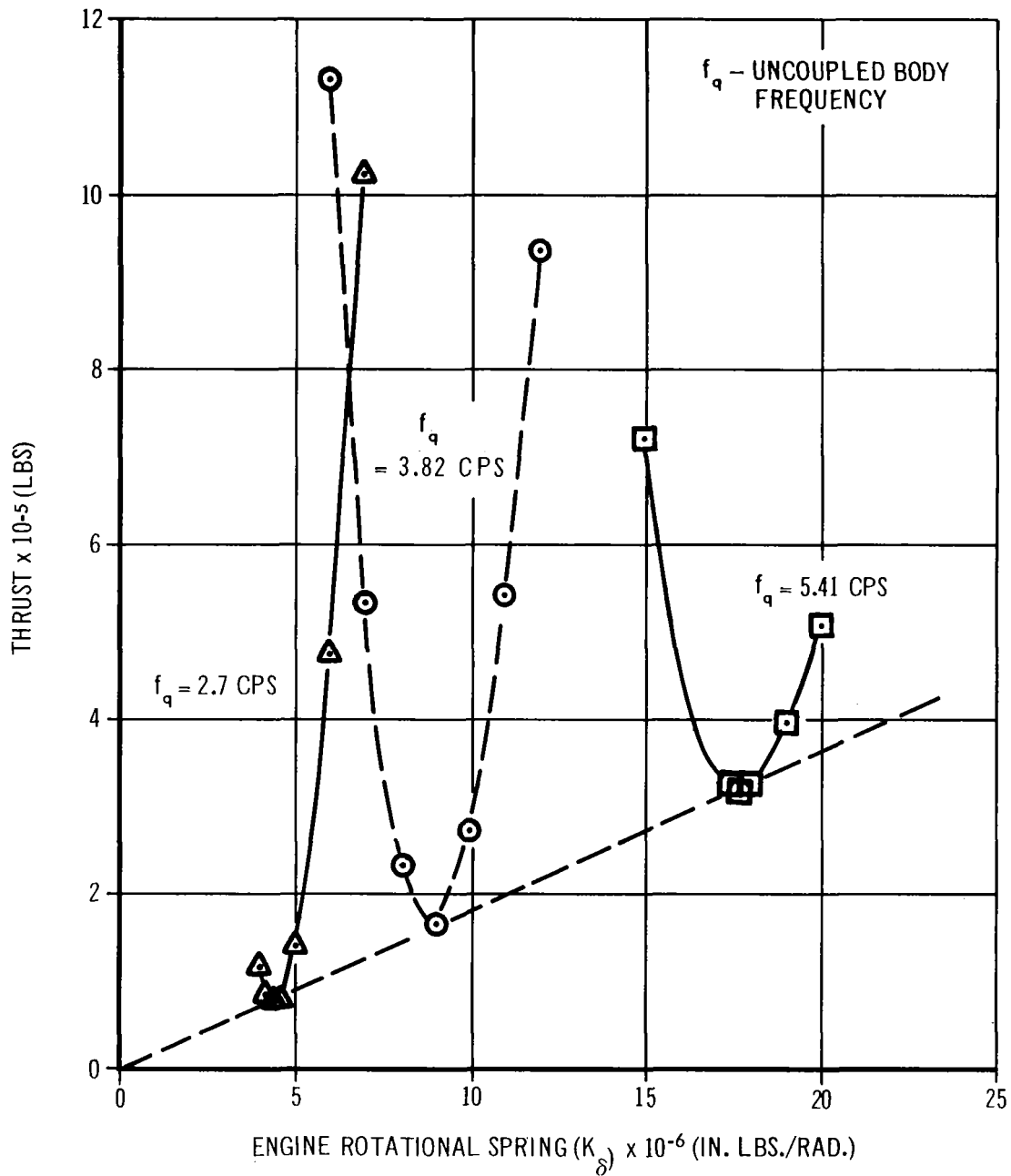
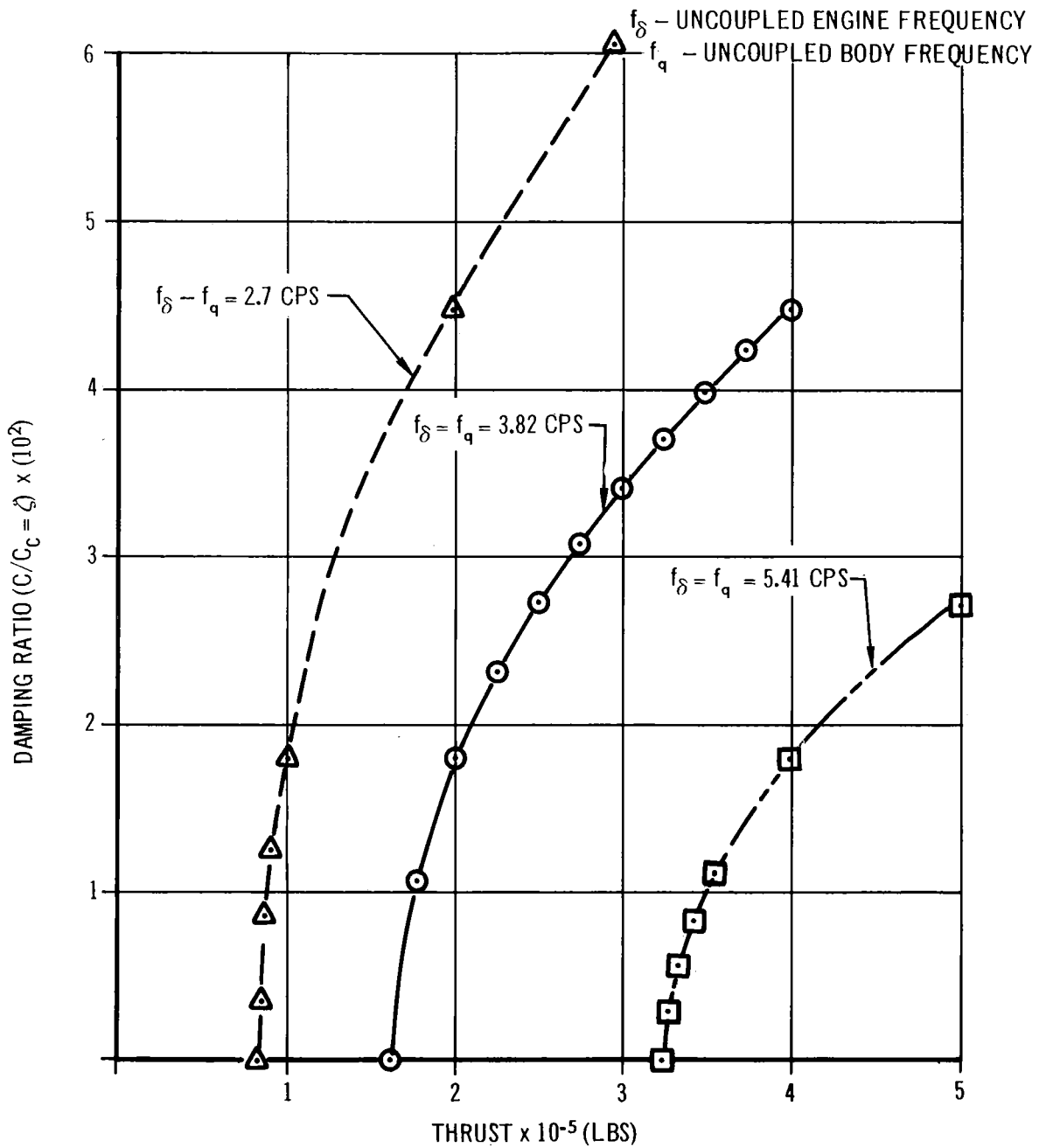


**FIGURE 10**

~~DAMPING RATIO ( $C/C_c$ ) VS THRUST~~  
FOR

EQUAL UNCOUPLED FREQUENCIES



$$K_\delta(f, 2.7) = 4.42 \times 10^6 \text{ IN LBS/RAD.}$$

$$K_\delta(f, 3.82) = 8.89 \times 10^6 \text{ IN LBS/RAD.}$$

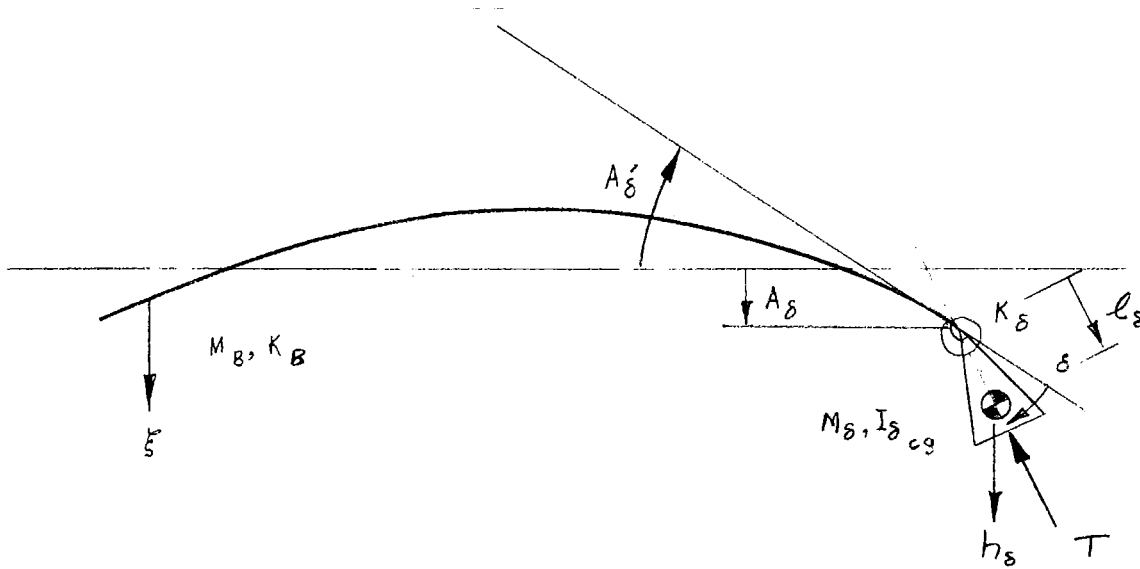
$$K_\delta(f, 5.41) = 5.24 \times 10^7 \text{ IN LBS/RAD.}$$

**FIGURE 11**

## CONCLUSIONS:

The impact of this analysis on the Saturn IB vehicle will probably be no more than one of close scrutiny and re-evaluation of the problem when the design is finally fixed. However, the solutions did show an instability of  $C/C_c = 0.0186$ . This negative damping should be easily overcome by hydraulic mechanism friction, or engine servo damping. However, until the engine gimbal friction and servo transfer functions are fully evaluated, the problem should be kept alive. If the problem did happen to manifest itself, the consequences could be quite catastrophic. The first bending mode of the Saturn IB vehicle during S-IVB powered flight is predicated upon the stiffness of the escape tower truss. Therefore, this truss would be one of the weak links in the system and might fracture first.

In conclusion, Douglas plans to keep a watchful eye on the garden hose problem and make sure all of the proper garden hose terms are included in the engine body bending transfer functions.



$$\mathcal{T} (\text{KINETIC ENERGY}) = \frac{1}{2} M_B \dot{\xi}^2 + \frac{1}{2} M_s h_s^2 + \frac{1}{2} I_{s_{cg}} (\dot{\delta} + A_s' \dot{\xi})^2$$

$$h_s = (A_s + l_s A_s') \xi + l_s \delta$$

$$\mathcal{T} = \frac{1}{2} M_B \dot{\xi}^2 + \frac{1}{2} M_s [(A_s + l_s A_s') \dot{\xi} + l_s \dot{\delta}]^2 + \frac{1}{2} I_{s_{cg}} (\dot{\delta} + A_s' \dot{\xi})^2$$

$$\frac{d}{dt} \left( \frac{\partial \mathcal{T}}{\partial \dot{\xi}} \right) = [M_B + M_s (A_s + l_s A_s')^2 + I_{s_{cg}} A_s'^2] \ddot{\xi} + [l_s M_s (A_s + l_s A_s') + A_s' I_{s_{cg}}] \ddot{\delta}$$

$$\frac{d}{dt} \left( \frac{\partial \mathcal{T}}{\partial \dot{\delta}} \right) = [l_s M_s A_s + l_s A_s' + A_s' I_{s_{cg}}] \ddot{\xi} + (l_s^2 M_s + I_{s_{cg}}) \ddot{\delta}$$

$$M_B + M_s (A_s + l_s A_s')^2 + I_{s_{cg}} A_s'^2 \quad - \text{BODY MODAL MASS } (M_{\xi})$$

$$l_s^2 M_s + I_{s_{cg}} \quad - \text{ENGINE MOMENT OF INERTIA ABOUT HINGE LINE } (I_{HL})$$

$$l_s M_s (A_s + l_s A_s') + A_s' I_{s_{cg}} \quad - \text{PRODUCT OF INERTIA BETWEEN BODY AND ENGINE } (P_{\xi\delta})$$

IN MATRIX FORM:

$$\begin{bmatrix} M_{\xi} \\ P_{\xi\delta} \end{bmatrix} \begin{bmatrix} \xi \\ \delta \end{bmatrix} S^2$$

$$U(\text{POTENTIAL ENERGY}) = \frac{1}{2} K_B \xi^2 + \frac{1}{2} K_S \delta^2$$

$$\frac{\partial U}{\partial \xi} = K_B \xi$$

$$\frac{\partial U}{\partial \delta} = K_S \delta$$

IN MATRIX FORM:

$$\begin{bmatrix} K_B & 0 \\ 0 & K_S \end{bmatrix} \begin{Bmatrix} \xi \\ \delta \end{Bmatrix}$$

SINCE DAMPERS ACT ACROSS SPRINGS:

$$\begin{bmatrix} D_B & 0 \\ 0 & D_S \end{bmatrix} \begin{Bmatrix} \xi \\ \delta \end{Bmatrix} S$$

FORCE TRANSFORMED TO LEFT SIDE OF EQUATION:

$$\begin{bmatrix} 0 & T A_S \\ 0 & 0 \end{bmatrix} \begin{Bmatrix} \xi \\ \delta_I \end{Bmatrix} = [F] \quad \text{NOTE: } \delta_I \text{ IS REFERENCED TO INERTIAL SPACE.}$$

$$\begin{Bmatrix} \xi \\ \delta_I \end{Bmatrix} = \begin{bmatrix} 1 & 0 \\ A'_S & 1 \end{bmatrix} \begin{Bmatrix} \xi \\ \delta \end{Bmatrix} = [A]$$

$$[A]^* [F] [A] = \begin{bmatrix} A_S A'_S T & A_S T \\ 0 & 0 \end{bmatrix} \begin{Bmatrix} \xi \\ \delta \end{Bmatrix}$$

## SECTION 8

### ROLL TORQUES GENERATED BY PROPELLANT SLOSHING

#### SUMMARY:

Since the S-IVB vehicle utilizes an auxiliary control system with a separate propellant supply to maintain roll control during powered flight, any effect of vehicle dynamics on the consumption of this propellant supply should be thoroughly understood. The purpose of this study is to determine the amount of propellant necessary to counter the roll moment generated by propellant sloshing. Knowing that the liquid hydrogen is unstable early in flight and very lightly damped during the remainder, it was suggested that this roll moment could be relatively severe. The results of this preliminary analysis indicate the propellant necessary to counter the worst case will be 0.6 lb. When this figure is compared to the 39 lb of fuel allotted for the suppression of roll moments or the total fuel in each module of 800 lb, it can be seen that the effect of this roll moment is very small. This study was made with a 2 degree of freedom vehicle rigid body representation (pitch and yaw). Consequently, yaw characteristics are independent of those in pitch and vice versa. This study is presently continuing with roll freedom, the roll autopilot, and Euler transformations included.

#### EXISTING ANALOG SIMULATION:

Figure 1 shows the model used and defines the parameters. The equations of motion of this model are:

$$M\ddot{\eta}_0 - m_1 \lambda_1 \dot{y}_1 - m_1 \omega_1^2 y_1 - m_2 \lambda_2 \dot{y}_2 - m_2 \omega_2^2 y_2 = -T\delta \quad (1)$$

$$I\ddot{\theta} - m_1 \ell_1 \lambda_1 \dot{y}_1 - m_1 \ell_1 \left( \omega_1^2 + \frac{T}{M_T} \right) y_1 - m_2 \ell_2 \lambda_2 \dot{y}_2 - m_2 \ell_2 \left( \omega_2^2 + \frac{T}{M_T} \right) y_2 = TL\delta \quad (2)$$

$$\eta_0 + \ell_1 \ddot{\theta} + \ddot{y}_1 + \lambda_1 \dot{y}_1 + \omega_1^2 y_1 = 0 \quad (3)$$

$$\eta_0 + \ell_2 \ddot{\theta} + \ddot{y}_2 + \lambda_2 \dot{y}_2 + \omega_2^2 y_2 = 0 \quad (4)$$

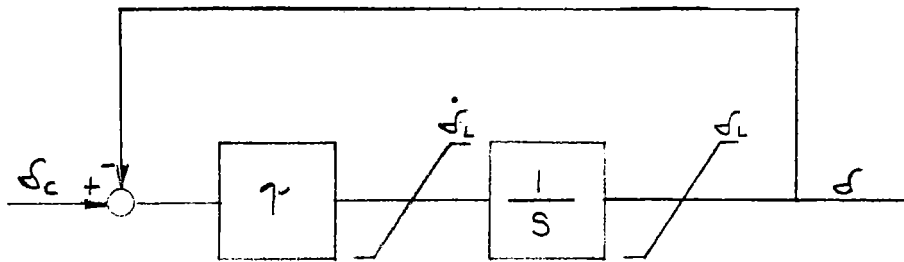
A simplified autopilot and engine loop were included in order to close the loop. The equation for the autopilot is:

$$\delta_c = K_{\theta} \Delta \theta + K_{\dot{\theta}} \Delta \dot{\theta} \quad (5)$$

Since commanded inputs are not being considered, equation (5) becomes

$$\delta_c = -K_{\theta} \theta - K_{\dot{\theta}} \dot{\theta} \quad (6)$$

The simplified engine loop may be best presented in block diagram form and is illustrated in sketch 1.



Sketch 1  
Simplified Engine Loop Model

Figure 2 shows the block diagram which results when the above equations are combined. Two of these block diagrams are used in the analog simulation to represent the pitch and yaw planes. The equation by which the roll moment is generated is found from figure 3 to be

$$M_{\phi} = \left[ m_1 y_{1\theta} + m_2 y_{2\theta} \right] \frac{T \delta_{\psi}}{M_T} - \left[ m_1 y_{1\psi} + m_2 y_{2\psi} \right] \frac{T \delta_{\theta}}{M_T} \quad (7)$$

It should be noted that the moment due to the damping forces action the walls of the tank has been assumed insignificant and therefore does not appear in equation (7). Preliminary runs using initial conditions of  $1^\circ$  and  $1^\circ/\text{sec}$  on vehicle attitude and vehicle rate respectively and assuming no thrust buildup indicated that the maximum fuel consumption occurred in the first 4 seconds of flight. Therefore, it was decided that a more realistic simulation of the separation conditions was warranted.

Since the slope of the thrust curve is very steep, it was felt that the thrust as a function of time could be approximated by a step at 4 seconds (the time at which the actual thrust is half of its maximum value). The other major consideration in the simulation of the vehicle's condition at separation is the initial position of the sloshing masses. The initial position and rate of the sloshing masses is determined by the moments applied to the vehicle by the separation mechanism, but, since the true nature of these moments is unknown, it was again necessary to resort to approximation. It was assumed that any combination of moments applied to the vehicle prior to separation which would result in a given set of initial conditions would have the same effect on the sloshing masses. For this reason, a constant moment was used to develop the various combinations of initial conditions used.

ANALOG RESULTS:

Using the following disturbances, a roll torque history (figure 4) was obtained.

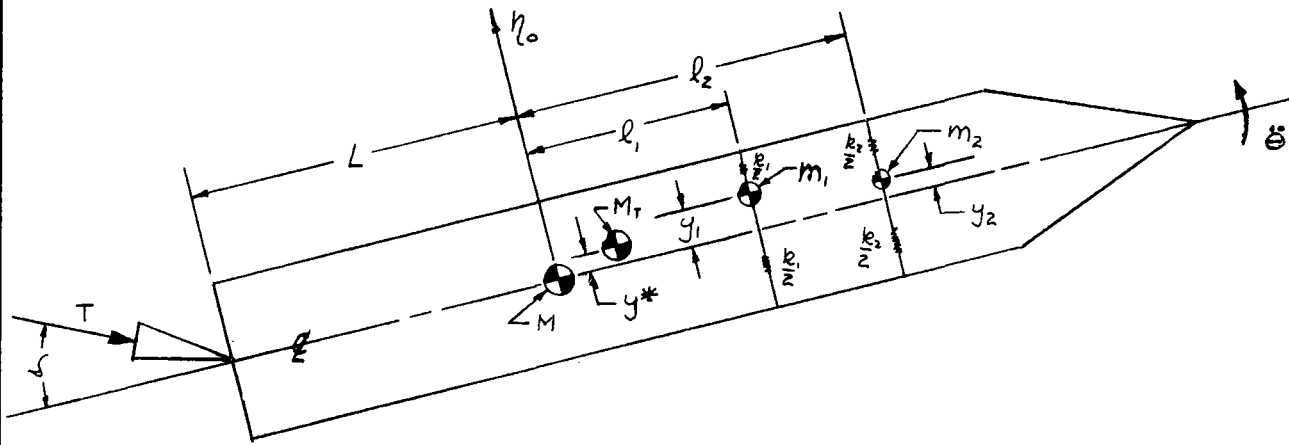
Disturbances at t (separation) - 2 sec.

Pitch attitude	=	0
Yaw	"	= +2°
Pitch acceleration	=	1/2°/sec <sup>2</sup> for 2 sec
Yaw	"	= -1/2°/sec <sup>2</sup> for 2 sec

These disturbances resulted in the following conditions at separation:

Pitch attitude	=	1°
Yaw	"	= 1°
Pitch rate	=	1 deg/sec
Yaw rate	=	-1 deg/sec

The resulting propellant consumption history is shown in figure 5. This curve indicated that 90 percent of the propellants are used in the first 10 seconds. Thus, the total amount used is largely a function of the initial disturbance encountered.



MISSILE MODEL

$T \sim$  THRUST

$L \sim$  GIMBALL STATION TO CG.

$l \sim$  CG TO SLOSH MASS

$m \sim$  SLOSH MASS

$y \sim$  MOTION OF SLOSH MASS FROM CENTER LINE

$k \sim$  SLOSH SPRING RATE

SUBSCRIPT 1 REFERS TO LOX

" 2 " " LH2

$y^*$  IS LATERAL CG SHIFT

$I \sim$  VEHICLE INERTIA LESS SLOSHING MASSES

$M \sim$  VEHICLE MASS LESS SLOSHING MASSES

$$M_T = m_1 + m_2 + M$$

$\delta \sim$  ENGINE DEFLECTION

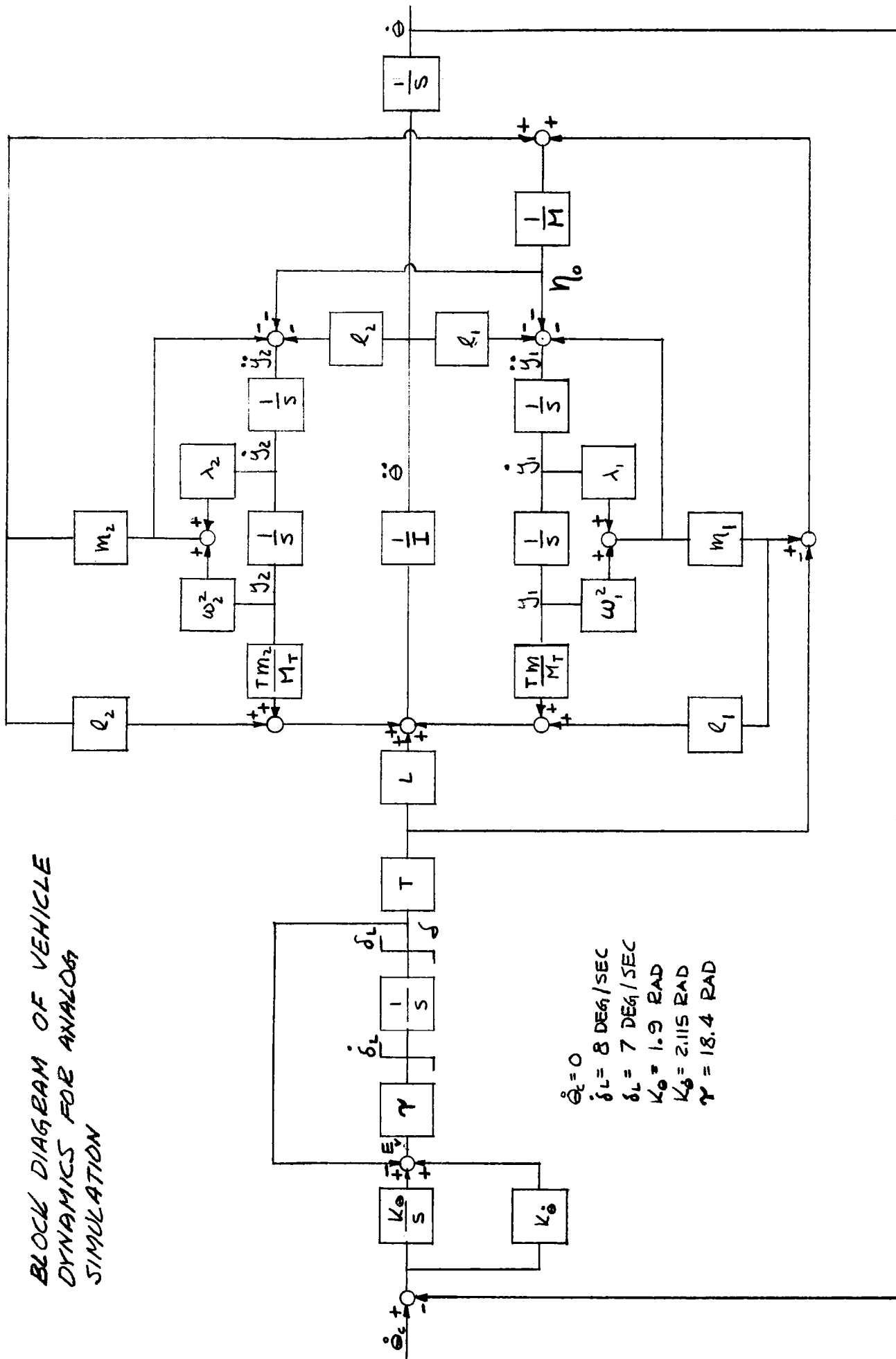
$\omega^2 \sim$  SLOSHING FREQUENCY SQUARED

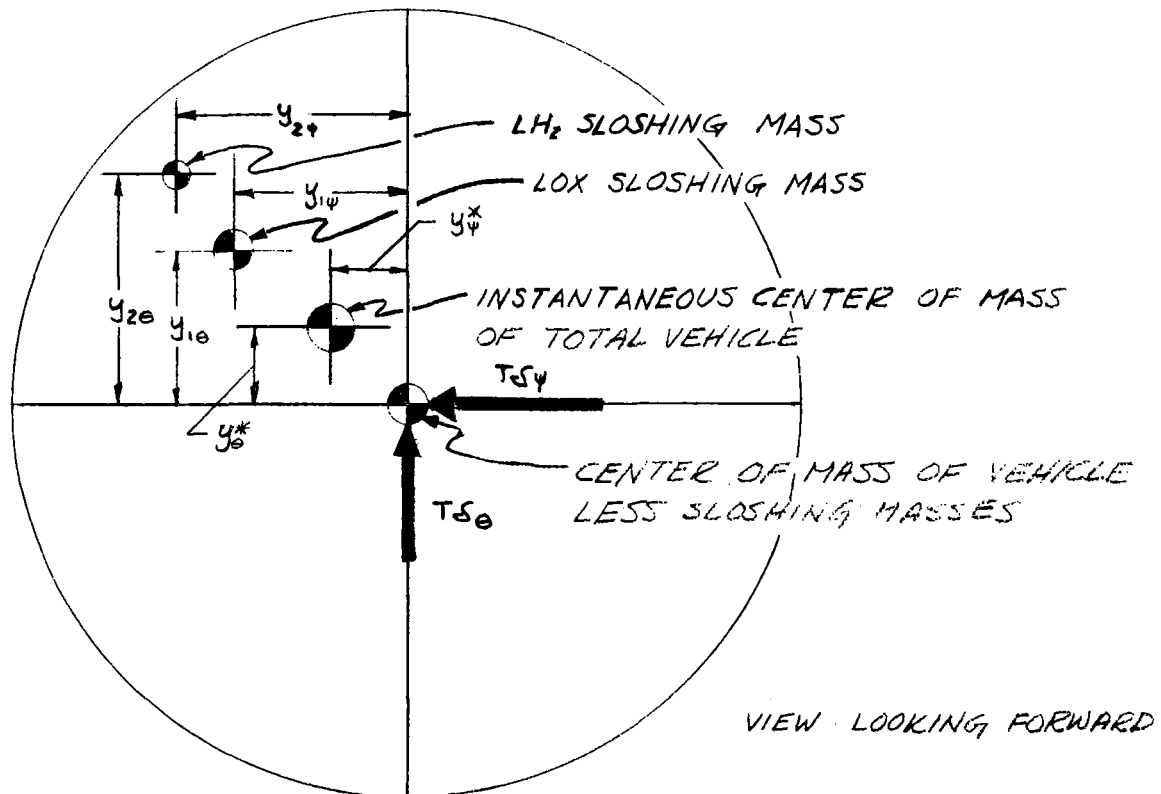
$\lambda \sim$  DAMPING CONSTANT

$$\omega^2 = \frac{k}{m} \quad \lambda = 2\gamma\omega$$

FIGURE 6

BLOCK DIAGRAM OF VEHICLE DYNAMICS FOR ANALOG SIMULATION





SUMMING MOMENTS :

$$M_T y_{\theta}^* = m_1 y_{1\theta} + m_2 y_{2\theta} \quad \text{OR} \quad y_{\theta}^* = \frac{m_1 y_{1\theta} + m_2 y_{2\theta}}{M_T}$$

$$M_T y_{\psi}^* = m_1 y_{1\psi} + m_2 y_{2\psi} \quad \text{OR} \quad y_{\psi}^* = \frac{m_1 y_{1\psi} + m_2 y_{2\psi}}{M_T}$$

FIGURE 3 SKETCH OF PHYSICAL CONDITIONS BY WHICH SLOSHING INDUCES ROLL MOMENTS

- NOTE :
- 1) SUBSCRIPT 1 REFERS TO LOX SUBSCRIPT 2 REFERS TO LH<sub>2</sub>
  - 2) SUBSCRIPT  $\theta$  REFERS TO PITCH,  $\psi$  TO YAW
  - 3)  $M_T$  IS TOTAL MASS OF VEHICLE INCLUDING SLOSHING MASSES
  - 4) THE SPRINGS & DAMPERS ON THE SLOSHING MASSES HAVE BEEN OMITTED FOR CLARITY.

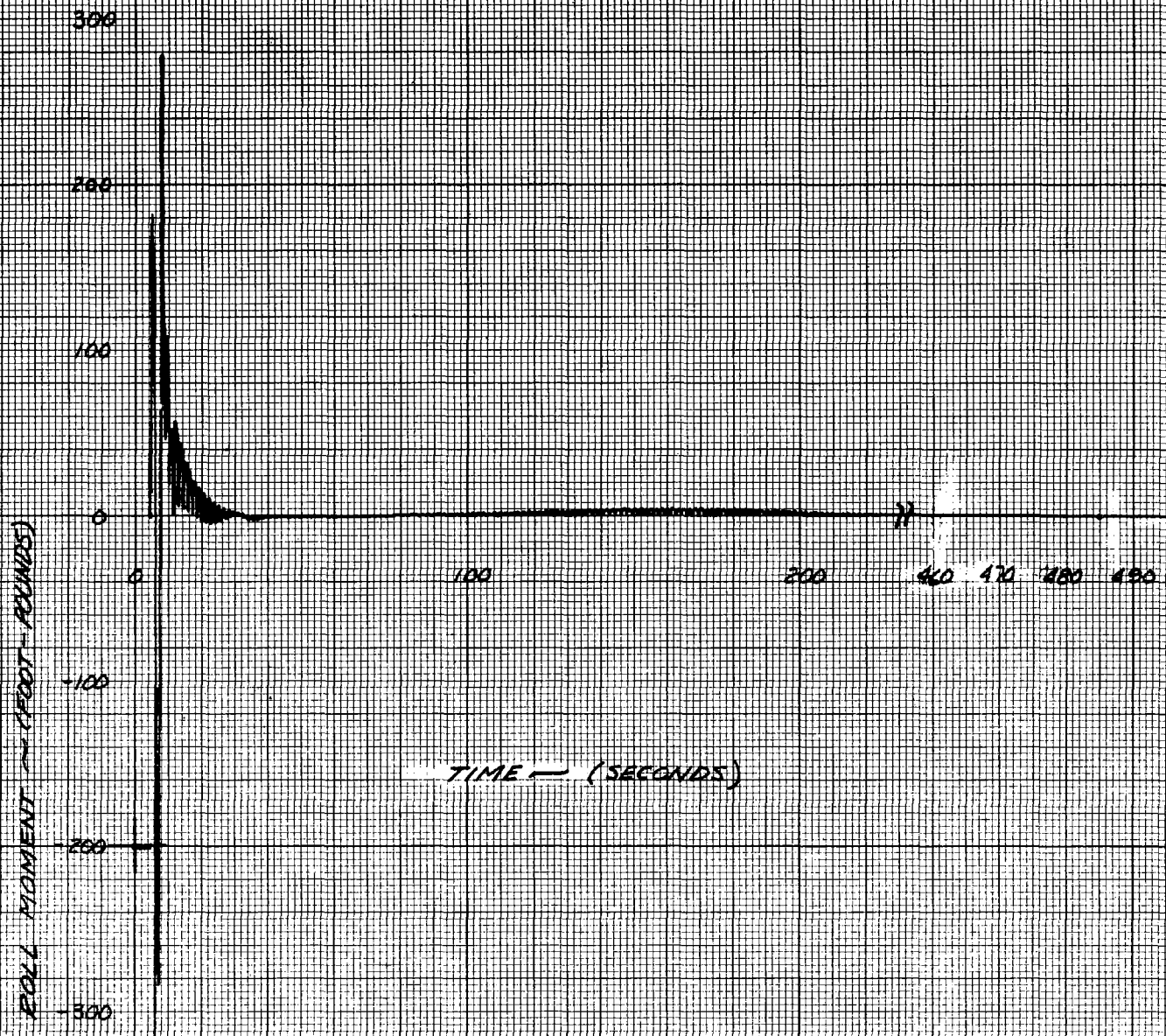


FIGURE A

DISTURBING MOMENT IN ROLL AS  
A FUNCTION OF TIME FOR THE  
FOLLOWING INITIAL CONDITIONS

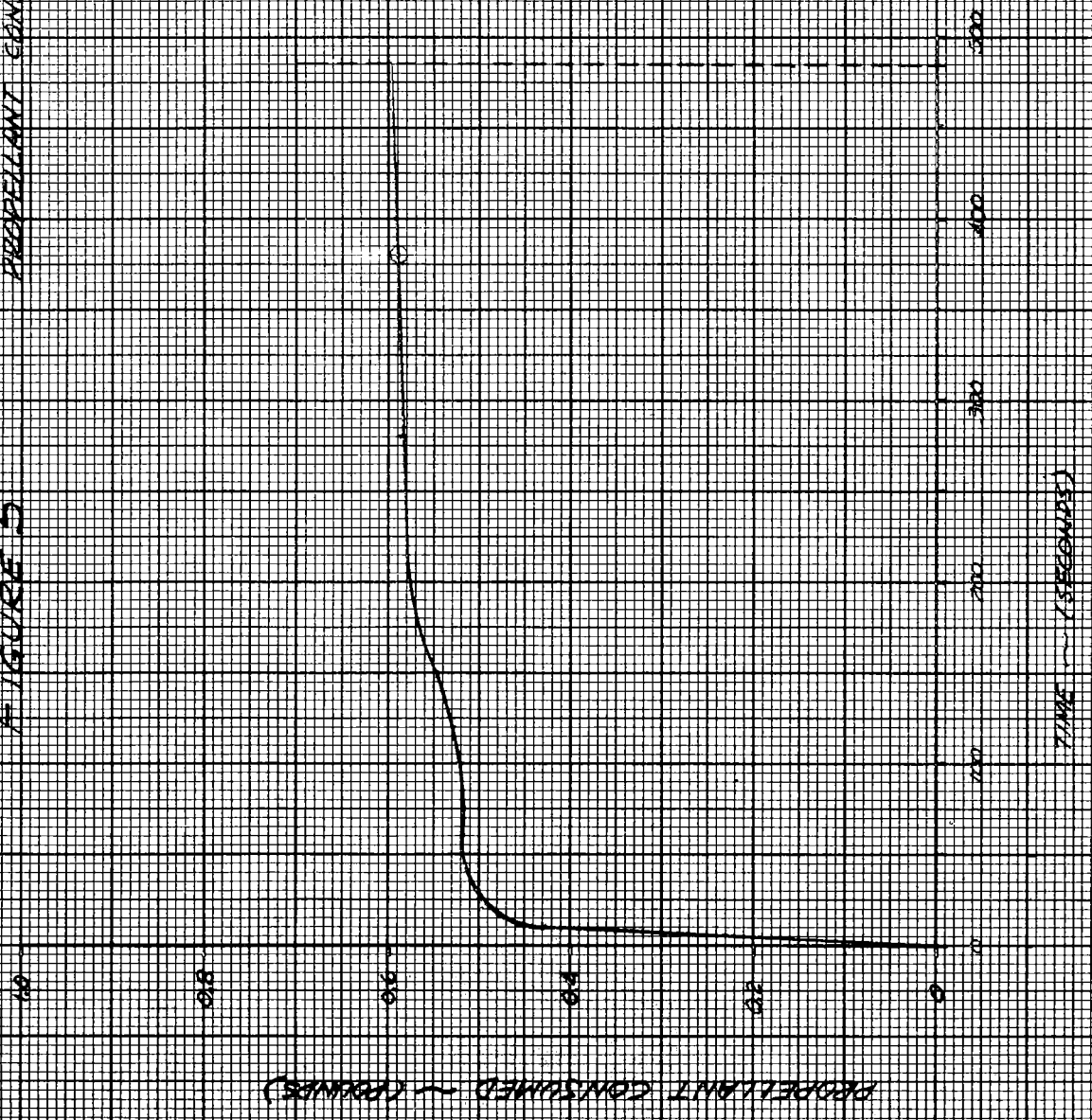
$\theta_0 = 0$  DEGREE

$\psi_0 = 1$  DEGREE

$\dot{\theta}_0 = 1$  DEGREE/SECOND

$\dot{\psi}_0 = 1$  DEGREE/SECOND

FIGURE 5 PROPELLANT CONSUMPTION HISTORY



## Section 9

### SATURN S-IVB GENERAL PROTUBERANCE WIND TUNNEL TEST PRELIMINARY REPORT

#### INTRODUCTION

A basic Saturn design requirement is the location of certain systems on the external surface of the vehicle. This is necessary in many cases for S-IVB application because the wall of the S-IVB liquid hydrogen tank including insulation is the skin of the vehicle. A number of protuberances in the form of external fairings and stiffeners are present to affect the aerodynamic flow field. These are totally or partially immersed within the thick turbulent boundary layer, including the external stringers which are small in comparison to the boundary layer thickness. The flow field caused by the protuberances within the boundary layer does not lend itself to analysis, and the interactions between stringers and protuberances create a very complex situation. It is necessary to perform wind tunnel tests to determine aerodynamic loads and heat flux rates for those cases in which these effects critically affect the design.

There are several effects which must be the subject of an effective test program to verify vehicle design. These include:

#### 1. Protuberance Loads and Pressure

The effects of protuberances on vehicle drag and the resulting payload penalties will be determined, also local structural and skin thickness requirements due to protuberance loads and induced pressures.

#### 2. Induced Flow Effects

Regions of unsteady flow and resulting effects will also be investigated. Wakes, separation regions, shock interactions, and unsteady pressure effects due to protuberances will be investigated.

### 3. Heat Transfer

Aerodynamic heating of protuberances and of regions affected by protuberances will be investigated. Heat transfer coefficients both on and around protuberances will be determined.

### 4. Body Shape Effects

Information regarding the effect of geometric shape as it influences the flow field surrounding the protuberances will be obtained.

### 5. Protuberance Combination

Information on effects of protuberances on each other will be obtained.

## ANALYTIC ANALYSIS

### Loads

The theoretical estimation of loads and pressures on protuberances is very complex. The protuberances are immersed within the thick turbulent boundary layer. The boundary layer must be determined before the various design parameters may be evaluated. The Saturn V dimensions assumed for the boundary layer analysis are shown in figure 1. Three solutions were used to determine the boundary layer thickness; two of which assumed incompressible flow, the other compressible flow. Figure 2 shows the results for both incompressible solutions as a function of time for the Saturn V design trajectory. Figure 3 gives the boundary layer thickness at  $M_{\infty} = 1.6$  (approximate maximum dynamic pressure) which is the critical condition for design loads. The Van Driest compressible solution does not vary greatly from the Van Driest incompressible solution

The protuberance drag coefficients were estimated assuming that the protuberances are attached to an infinite flat plate. The available literature was used to select the particular drag coefficient. The side loads were estimated by applying small aspect ratio wing theory in the presence of the upwash flow of the body. All side load analysis assumed 10 degrees angle of attack. Normal loads were evaluated from the estimated pressure distribution.

The list of protuberances, their location, geometry, and loads is being revised as soon as new information becomes available. Significant changes in protuberances are not anticipated.

### Heat Transfer

The analysis of aerodynamic heating in the vicinity of protuberances is complicated by the presence of the thick turbulent boundary layer. Available data shows that wide variations in heat transfer coefficients are experienced and that significant increases in the heat input to a vehicle skin in the vicinity of a protuberance will cause local hot spots. The formulation of a method of theoretical prediction of protuberance effects on the surrounding area would be very complex, and no known analytic method is available. The computation of heating of the protuberance itself is complicated by the variation of the boundary layer velocity along the height of the protuberance. Present design procedure for Saturn S-IVB application is to compute the boundary layer velocity that would occur at a certain protuberance height and determine the aerodynamic heat input at this height to the shape involved. The validity of thin boundary layer heat transfer theories becomes very questionable in the vicinity of objects whose dimensions are less than the boundary layer thickness.

The external stringers located on the forward and aft skirt and aft flare sections have very small dimensions in comparison with the boundary layer thickness. The heat transfer coefficient over a very large portion of the vehicle skin is therefore uncertain and present design practice is to assume that the heat transfer coefficient is twice the flat plate value in the vicinity of the leading edge of the stringers. The heating to the aft flare is enough to cause consideration to be given to some type of low temperature ablative coating. The minimum thermolag thickness that could be attached to the aft skin is 0.02 inches. This would incur a weight penalty of 250 pounds. The attitude control rocket fairing is large enough to be only partly within the boundary layer. The functioning of the antenna is influenced by heating thus, heat transfer coefficient data are desirable on this protuberance.

## Wind Tunnel Test

A wind tunnel test program is required to validate and adjust the results of analytic analysis. In addition, the test program would supply data for areas affected by regions of complex flow for which no known analytic method is available. Both aerodynamic load and heat transfer data, for the protuberances and the vehicle surface in the proximity of the protuberances, are necessary.

The assumption is made that the wind tunnel floor simulates the Saturn vehicle, and that the wind tunnel boundary layer simulates the vehicle boundary layer.

## Facility

All facilities and equipment needed to conduct this program are currently available within the Douglas Aircraft Company, Missile and Space Systems Division. These include the engineering facilities required for design of the models, a model shop capable of fabricating and instrumenting the models and support equipment, IBM 1620 and 7090 computing facilities required for data reduction and analysis, and the wind tunnel test facility.

The Douglas Aerophysics Laboratory Trisonic Four-Foot Tunnel located at El Segundo, California is a blowdown-to-atmosphere facility operating from a 525-psia storage reservoir with running times on the order of 30 to 60 seconds. Mach number range is continuously variable from 0.2 to 5.0. The four foot square test section provides for the development testing of large models.

A schematic of the design features of the tunnel is shown in figure 5. In addition to the tunnel itself, the facility contains or has directly available, associated equipment. A unique feature of the tunnel is the existing model protective and cooling shoe system used for heat transfer tests on sting mounted models. This system consists of two half-shoes which enclose a model on the tunnel center-line. When data are to be taken the shoes are retracted quickly into wells in the tunnel floor and ceiling. The shoes also incorporate a liquid nitrogen spray system so that heat transfer models can be cooled externally prior to a run. In their basic configuration when extended, the shoes

enclose a volume consisting approximately of a 40-degree included angle cone with a 15 inch diameter cylinder extending 7 inches from the cone base.

The experience provided by the design and operation of this shoe system greatly enhances the successful development of the proposed protective shoe system for floor mounted models.

Due to problems associated with the cooling shoe installation in the supersonic test section, it is proposed that the transonic test section be used for both transonic and supersonic testing. This would allow sufficient room in the test section plenum chamber to house the cooling shoe in the retracted position. The personnel at the Laboratory have tested the pilot tunnel in a similar configuration with excellent results. The use of the transonic test section would require only one model installation and allow a much easier access to the model mounting fixtures. Ease of access to the model mounting fixtures is necessary to facilitate protuberance changes and yaw angle changes. Approximately a saving of two (2) hours per model change can be realized by using the transonic test section for all testing. Preliminary testing will verify the desirability of this approach.

#### Model

The primary consideration for proper simulation is the relationship between the wind tunnel boundary layer and the vehicle boundary layer. Since the wind tunnel boundary layer will be utilized to simulate the boundary layer over the vehicle, the tunnel boundary layer will determine the model scale. Figure 6 shows the total boundary layer thickness versus Mach number for the aft skirt of the missile and for the wind tunnel test section. A 20 percent model would give good simulation at this point. Figure 7 compares the forward skirt boundary layer total thickness to the test section thickness. A 30 percent model gives good simulation in this region. A comparison of vehicle and wind tunnel boundary layer velocity profiles is shown in figure 8.

A preliminary analysis indicates that shock wave interaction and tunnel blockage are not problems but a limited tunnel verification is desired to provide information on any problem that may exist. This preliminary check will have

been performed for the auxiliary propulsion system test.

The protuberance models required for force testing will be designed for mounting on a six component strain gauge balance. Since it is not desirable to record pressure data simultaneously with force data, separate runs for the pressure data will be required. The same model will be modified so that both types of data can be obtained with a given model during different runs. These protuberances will be fabricated of aluminum or steel. Heating rates to protuberances will be measured on thin walled models instrumented with thermocouples. These will be electroformed shells. It does not appear desirable to measure pressure data on the models simultaneously with the heat transfer data as the model walls must be made thicker and the pressure tubes constitute heat sinks. The protuberance models utilized to measure pressure data required for the heat transfer tests will be force models instrumented with pressure taps. For details see figures 9, 10 and 11.

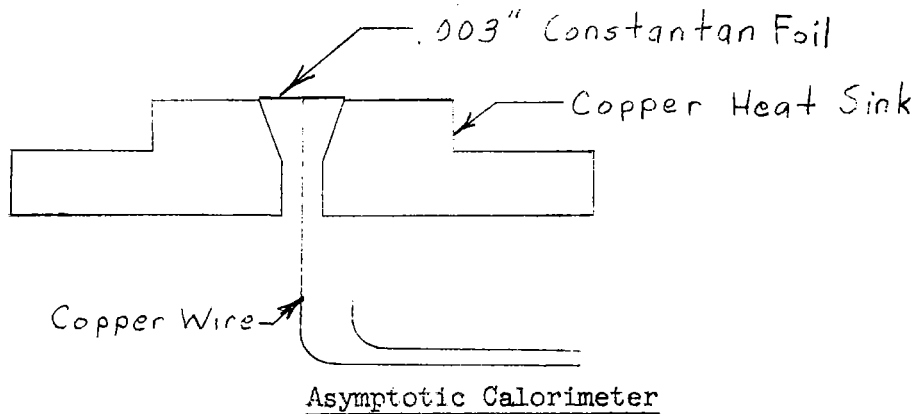
#### Test Technique

The floor mounted model will be cooled prior to the run with a fine mist of liquid nitrogen dispersed from the cooling shoe. When the model has reached the desired temperature (approximately  $-80^{\circ}\text{F}$ ) the tunnel flow will be initiated. After the tunnel flow is stabilized and the temperature of the air flow is essentially constant, the cooling shoe will be retracted into the tunnel ceiling. Just prior to the retraction of the cooling shoe, the data recording will begin. The data acquisition will last for approximately 10 seconds. When the data acquisition is complete the tunnel will be shut down. Pressure data runs will be conducted similarly except the cooling shoes will not be required. Heat transfer data will be acquired at Mach numbers from 2.0 to 5.0.

#### Instrumentation

The most accurate and reliable method of determining heat transfer coefficients is with asymptotic calorimeters. These instruments have a rapid response to

heat flux rates and may be calibrated to 3 percent accuracy. They appear as follows:



The junction of the constantan foil sensing disc and the copper heat sink forms a thermocouple. Another thermocouple junction is formed between the constantan foil and the copper wire attached to the center of the sensing surfaces. When a heat flux is applied over the sensing surface, the temperature of the constantan foil increases rapidly. The temperature of the copper heat sink responds very slowly to heat flux rates. The difference in the temperature at the two junctions is, therefore, a measure of the heat flux rate. The calorimeter is calibrated with a known heat source to obtain its calibration curve. Although radiant heat transfer should be very small over the range of temperatures encountered in the proposed wind tunnel test, the emissivity of the sensing surface is known and any corrections necessary will be made. The calorimeters will be calibrated over the test temperature range. The response time of the calorimeters for this application is 0.3 seconds. (Shorter response times occur with higher heat flux rates.) A thermocouple may be installed near the surface of the copper heat sink to measure heat sink temperature. The heat transfer coefficient is then determined.

The recovery temperature is determined by allowing the wind tunnel to run long enough to allow the temperature of the model (and calorimeter heat sinks) to reach an equilibrium temperature.

The limitations for use of the asymptotic calorimeters are their comparatively large size, and the necessity that they have flat sensing discs. They would distort curved model surfaces.

For the protuberances, since their size and shapes rule out the use of asymptotic calorimeters, the best method currently proven for determining heat transfer coefficients is making the measurements with a thin shell model (0.030 inches thick) instrumented with thermocouples. The wall is kept as thin as possible and the temperature history of the wall measured. The heat transfer coefficient is then determined. The limitations of this method are conduction and radiation losses, and the difficulty of forming a thin shell to very close tolerances.

The forces and moments acting on the protuberances will be measured with a strain gauge balance. The entire protuberance will be supported from the balance. A clearance gap large enough to allow sufficient clearance between the protuberance and the plate and stringers will be required. In addition it will be necessary to provide an interference circuit that will indicate when any grounding occurs. A special sealing technique will have to be provided for protuberances that are flush mounted on the vehicle. Probably a bleed and baffle system will be utilized. The pressure data can be applied to the force data. The load distribution on the protuberances will be determined with pressure measurements. The protuberance induced load distributions on the plate simulating the vehicle surfaces will also be determined with pressure measurements.

To measure fluctuating pressures at select locations a different pressure measuring system will be utilized. This pressure measuring system will be capable of measuring the pressure variations up to a frequency of 100 cps.

#### Items to be Tested

The items to be tested have been selected on the basis of their importance to the aerodynamic and thermodynamic design of the S-IVB. The aerodynamic

considerations are loads on protuberances themselves and protuberance induced pressures on critical skin areas. The thermal environment characteristics are protuberance heating and protuberance influenced skin heating. From these considerations it appears to be desirable to test the following. (This does not include the force testing necessary to design the attitude control rocket fairing.)

#### Force

1. hydrogen feed line
2. retro-rocket fairing
3. hydrogen fill line
4. S-II retro-rocket fairing
5. electrical tunnel

#### Pressure Induced on Structure

1. interstage aft of attitude control rocket fairing
2. interstage around S-II retro-rocket fairing
3. area under attitude control rocket fairing and on underside of the fairing

#### Heat Transfer (both to and around protuberance)

1. attitude control rocket fairing
2. stringers on aft flare
3. stringers on forward and aft skirt
4. antenna and pad
5. retro-rocket fairing
6. hydrogen feed line
7. ventilation system fairing

Experience has shown that where heat transfer is measured with thermocouples it is desirable to have the thinnest possible skin and to keep heat sinks away from the thermocouple to minimize conduction losses. It is, therefore, necessary to have separate pressure and heat transfer models. Heat transfer

measurements on the plate simulating the missile skin will be made with calorimeters which may be paired with pressure taps. Areas between calorimeters will be monitored with thermocouples. The number of models will be:

Force: Plate to mount force models and five force models of protuberances listed above.

Pressure and heat transfer: Plate and plate-flare combination to which stringer will be attached, instrumented with pressure taps, calorimeters, and thermocouples and models for both pressure and heat transfer of these protuberances:

1. attitude control rocket fairing
2. antenna and pad
3. retro-rocket fairing
4. hydrogen feed line
5. ventilation system

The same model will be used to measure forces and pressures, therefore, the total number is:

- 3 mounting plates
- 8 pressure-force protuberance models
- 5 thin walled heat transfer models

### Program Organization

Figure 12 is the organization chart for the general protuberance wind tunnel test program. The S-IVB Aeroballistics Section will provide program technical direction and management. In addition, this section will determine model design and test requirements. This information is supplied to the Model Test Group. The Model Test Group is responsible for coordination of model design and fabrication as well as wind tunnel scheduling and test conduction. The Model Design Group is responsible for satisfying the design requirements on all of the drawings which are subsequently delivered to the Model Shop for fabrication.

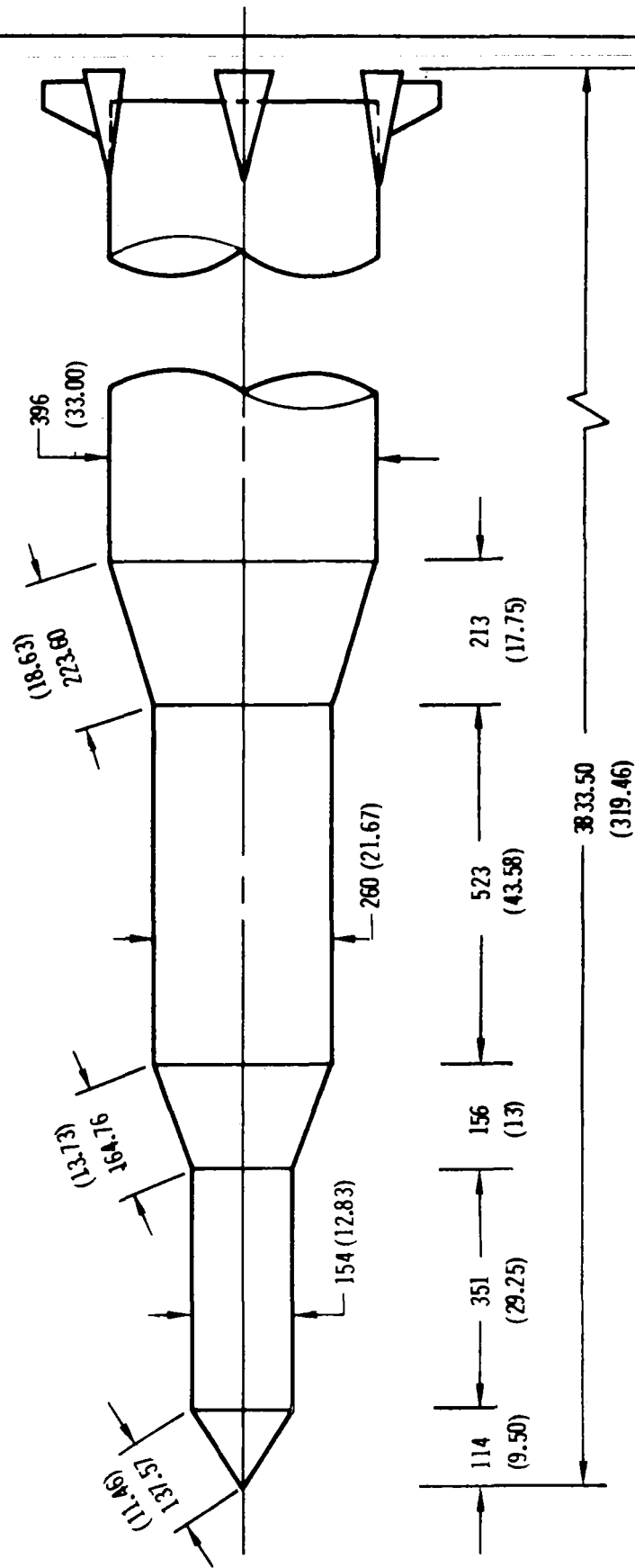
The Aerophysics Laboratory is responsible for test conduction and data gathering. The data will be analyzed by the Aeroballistics and Thermodynamics Sections. The Aeroballistics Section will be responsible for preparation of the final report.

### Program Schedule

The tentative schedule of the program, based on estimates of the Douglas Model Test Group and the Aerophysics Laboratory, is presented as figure 13. This schedule will be revised as better estimates becoming available. The schedule is based on the assumption that authority to proceed for the various phases will be available prior to the dates shown in the schedule.

SATURN V  
 VEHICLE CONFIGURATION  
 USED IN  
 BOUNDARY LAYER THICKNESS ANALYSIS

SCALE: 1 cm = 100 INCHES



NOTE:  
 DIMENSIONS OUTSIDE PARENTHESES = INCHES  
 DIMENSIONS IN PARENTHESES = FEET

FIGURE 1

SATURN V  
BOUNDARY LAYER THICKNESS PARAMETER VS TIME  
FOR INCOMPRESSIBLE FLOW

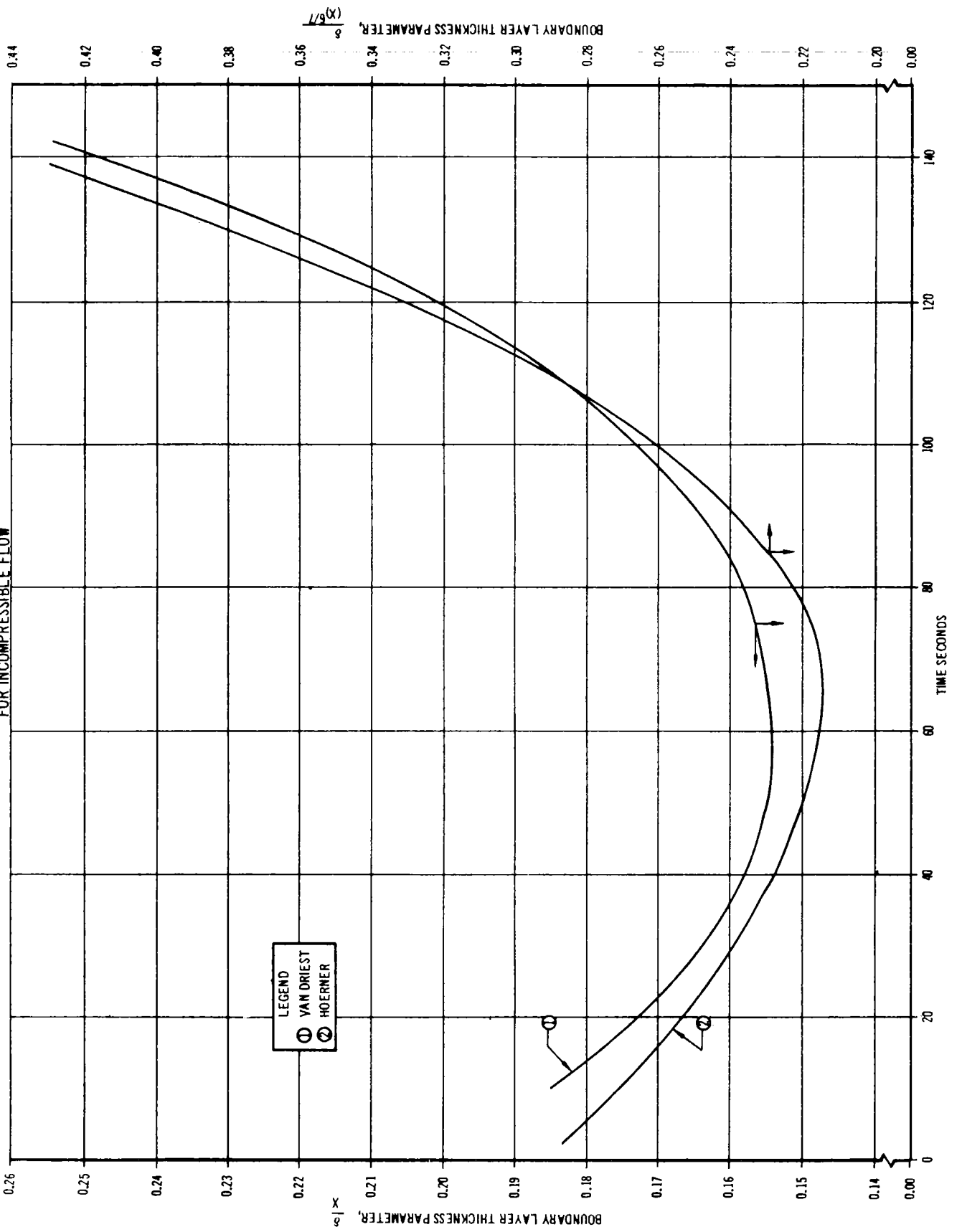


FIGURE 2

SATURN V  
BOUNDARY LAYER THICKNESS VS VEHICLE STATION

CONDITION:  $t = 77$  SECONDS,  $M = 1.60$   
ALTITUDE = 40,000 FT

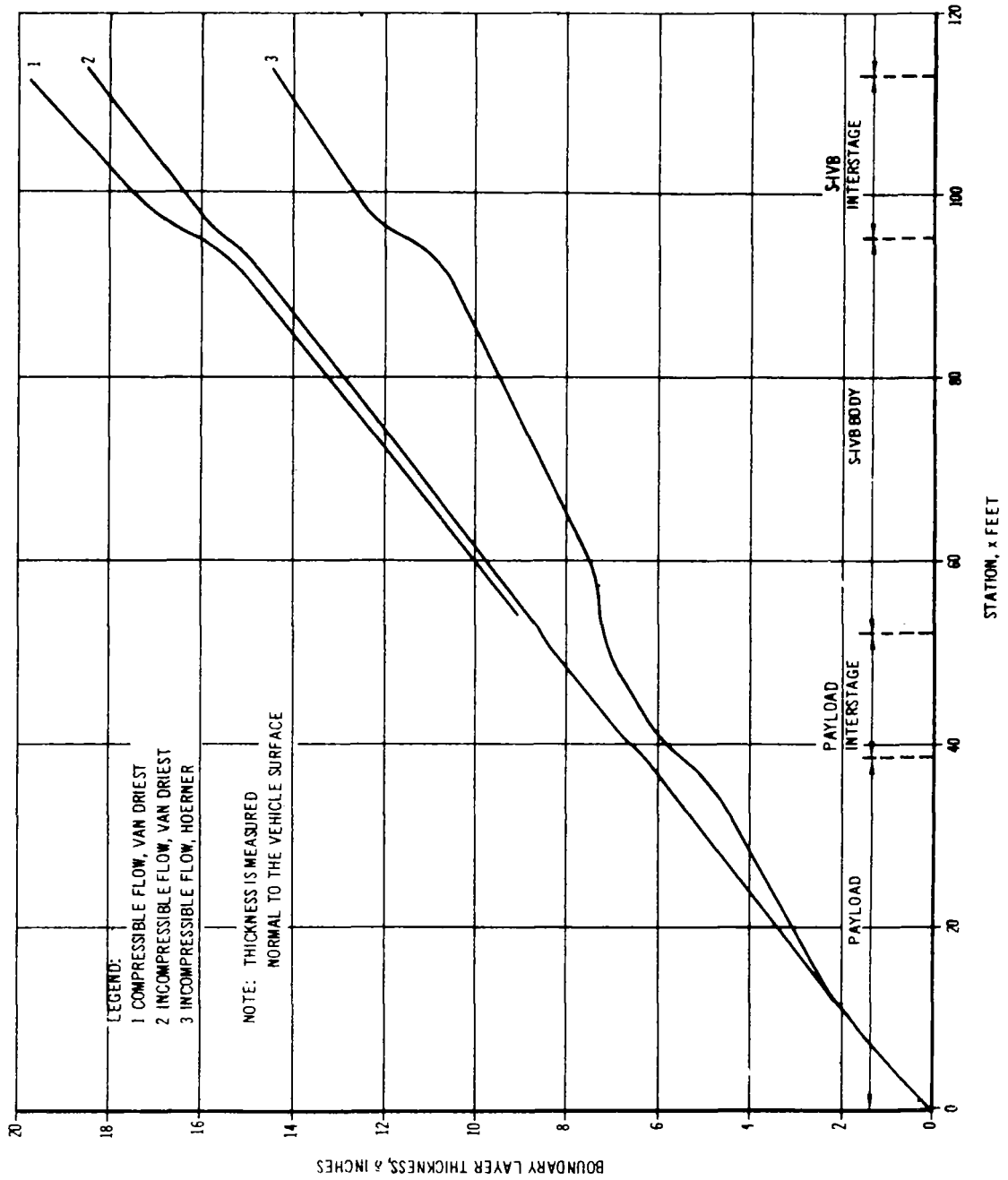
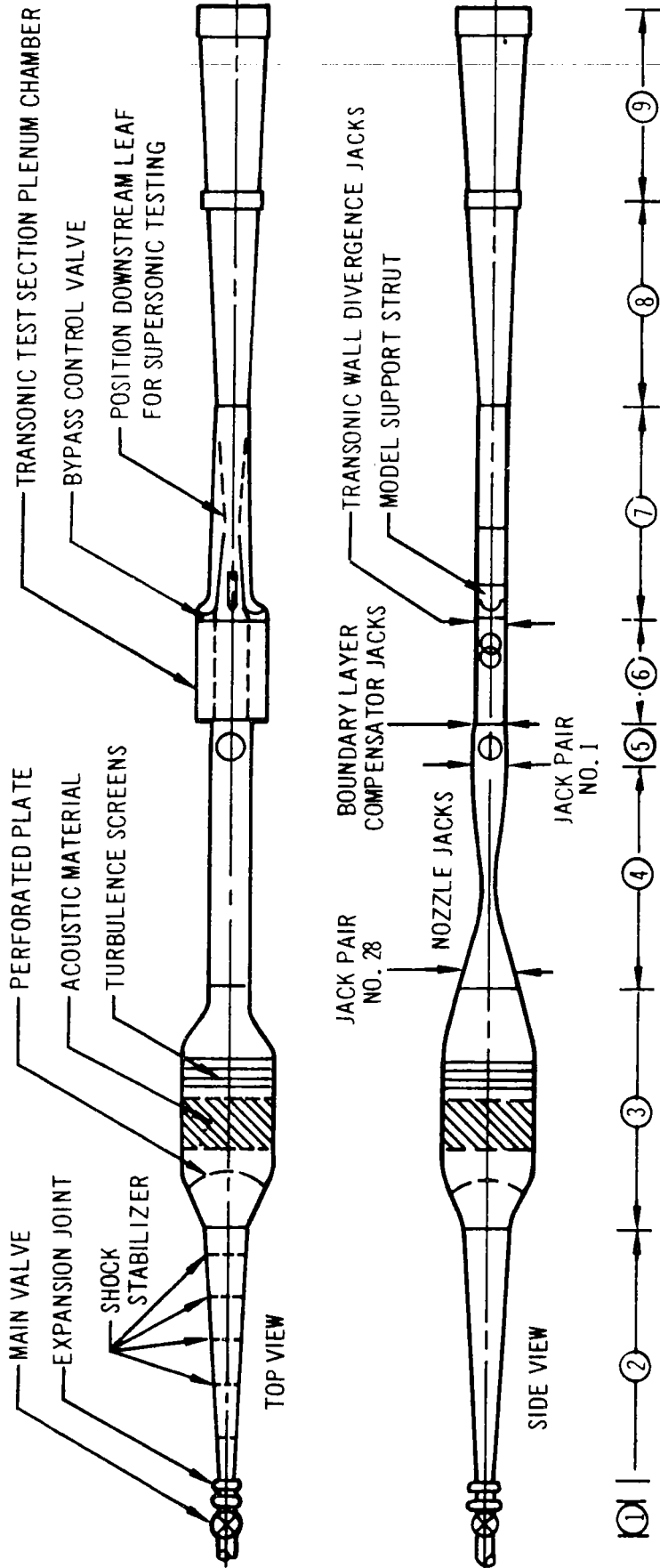


FIGURE 3

# DAL TRISONIC FOUR - FOOT TUNNEL DESIGN FEATURES



- ① CONTROL VALVE Valve regulated during run by electro-mechanical controller maintain constant pressure in still chamber.
- ② ENTRY DIFFUSER Entrance cone, 6° included angle; 4 shock stabilizer rings.
- ③ STILL CHAMBER Dished, 30% open-perforated plate; acoustic panels for 15-20 db acoustic energy attenuation; 4 turbulence screens.
- ④ NOZZLE 2-0.76" thick flexible plates, each controlled by 28 jacks; contours for Mach 1.0 to 5.0.
- ⑤ SUPERSONIC TEST SECTION 60" long 30" dia. windows in sidewalls; 24" openings top and bottom; boundary layer compensation by adjustable divergence on top and bottom walls, +0.13° To -0.50.
- ⑥ TRANSONIC TEST SECTION 144" long; 30" dia. windows at one of two positions; 4 walls perforated 22% open, holes normal to wall. Adjustable divergence on top and bottom walls, +0.29° to -2°. Section removable and downstream circuit moves up.
- ⑦ MODEL SUPPORT, BYPASS CONTROL VALVE & VARIABLE DIFFUSER Full height vertical struts with vertical motion and -1.9° to +2.9° pitch capability, 8" maximum strut width. Bypass valve controls Mach number. Downstream leaf of variable diffuser disconnected from upstream leaf for transonic testing. Variable throat allows extended run times at supersonic Mach numbers.
- ⑧ TELESCOPING DIFFUSER Telescopes into fixed diffuser, retracting model support-variable diffuser, opening tunnel for model installation and changes.
- ⑨ FIXED DIFFUSER Complete expansion to muffler tower.

FIGURE 5

COMPARISON OF FULL SCALE  
S-IVB AND DOUGLAS AEROPHYSICS LABORATORY TRISONIC  
TUNNEL BOUNDARY  
LAYER THICKNESS

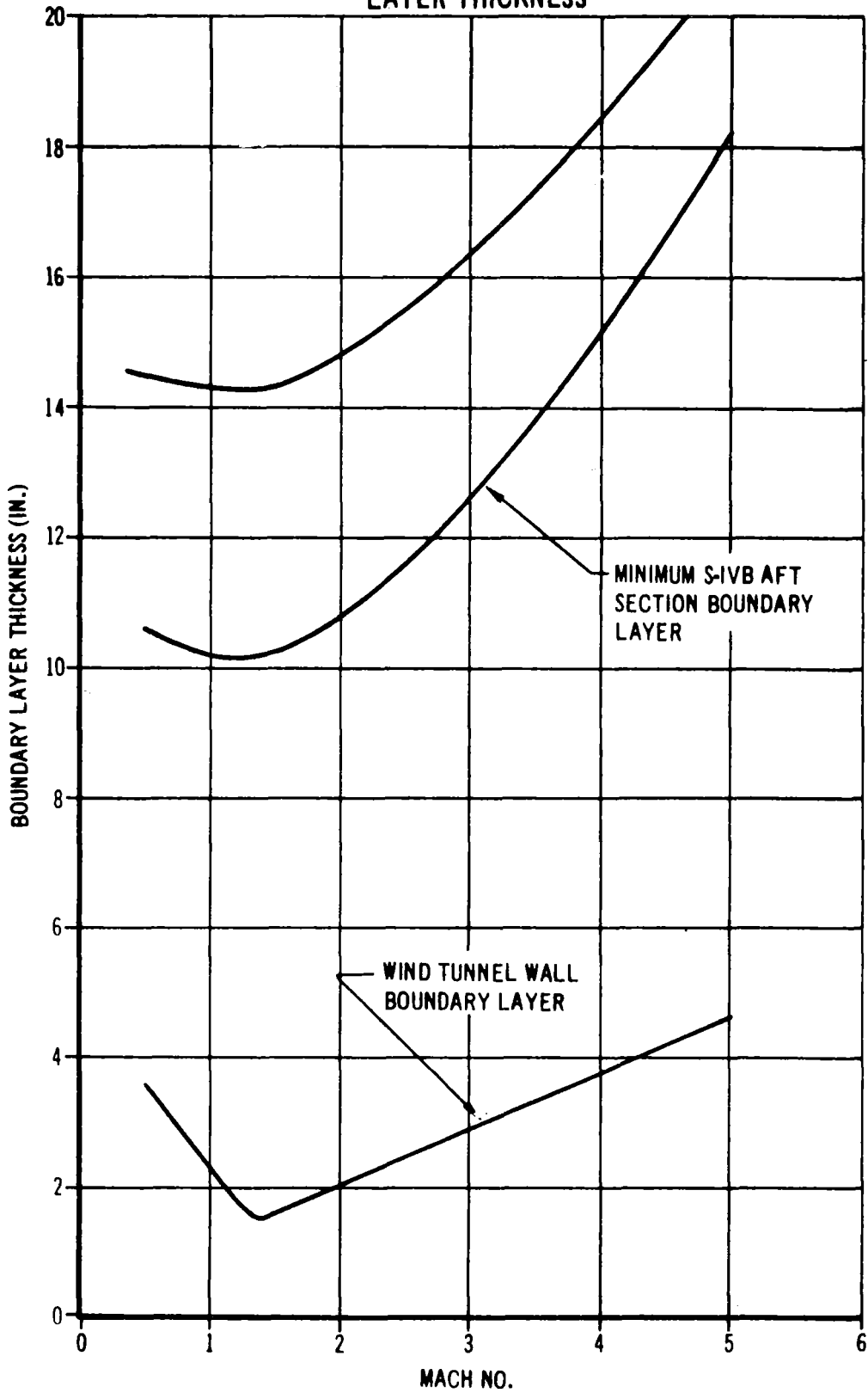


FIGURE 6

COMPARISON OF FULL SCALE S-IVB  
AND DAC AEROPHYSICS LABORATORY  
TRISONIC TUNNEL BOUNDARY LAYER THICKNESS

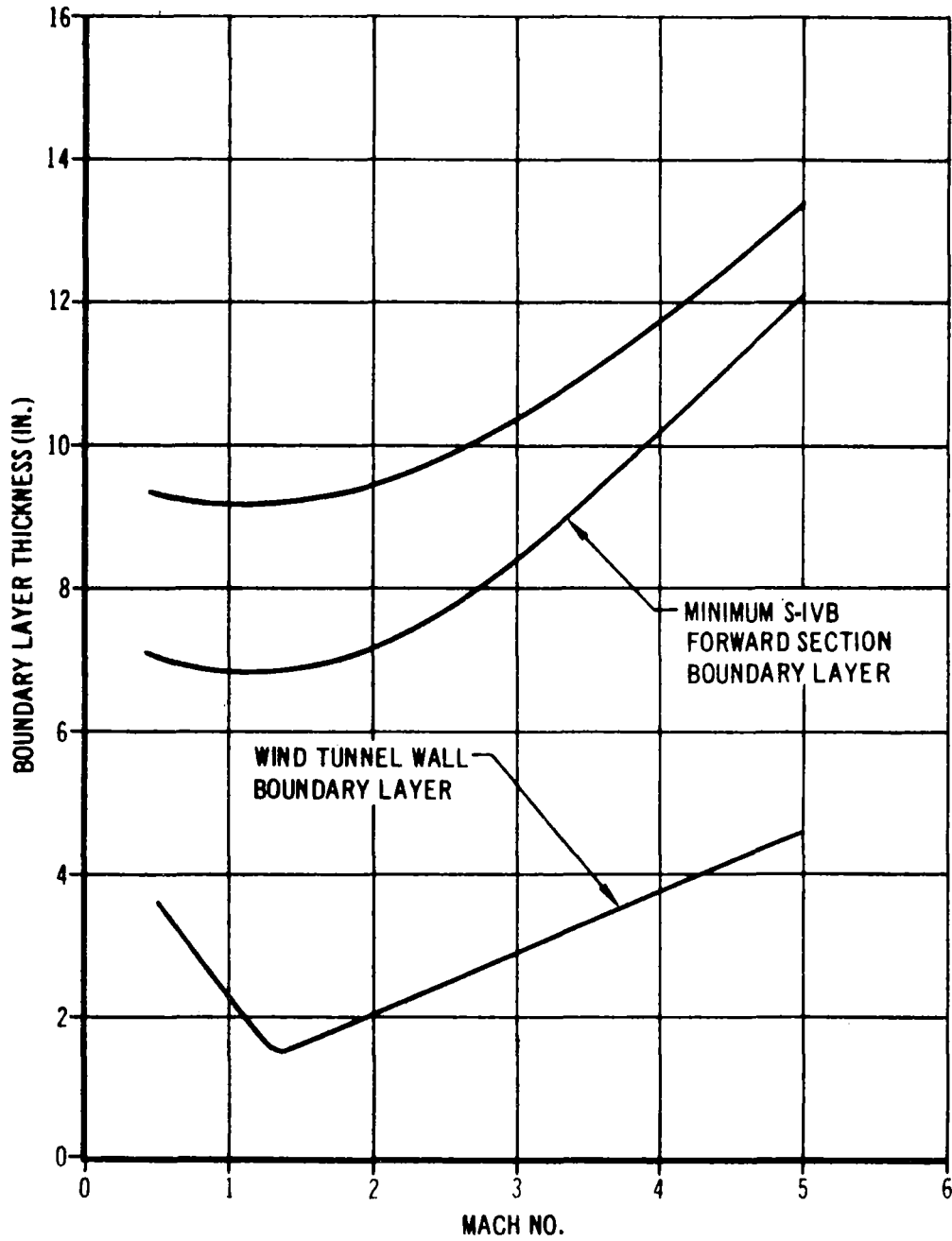


FIGURE 7

COMPARISON OF FULL SCALE  
S-IVB AND DOUGLAS AEROPHYSICS LABORATORY  
TRISONIC TUNNEL BOUNDARY  
LAYER PROFILES AT MACH 1.6

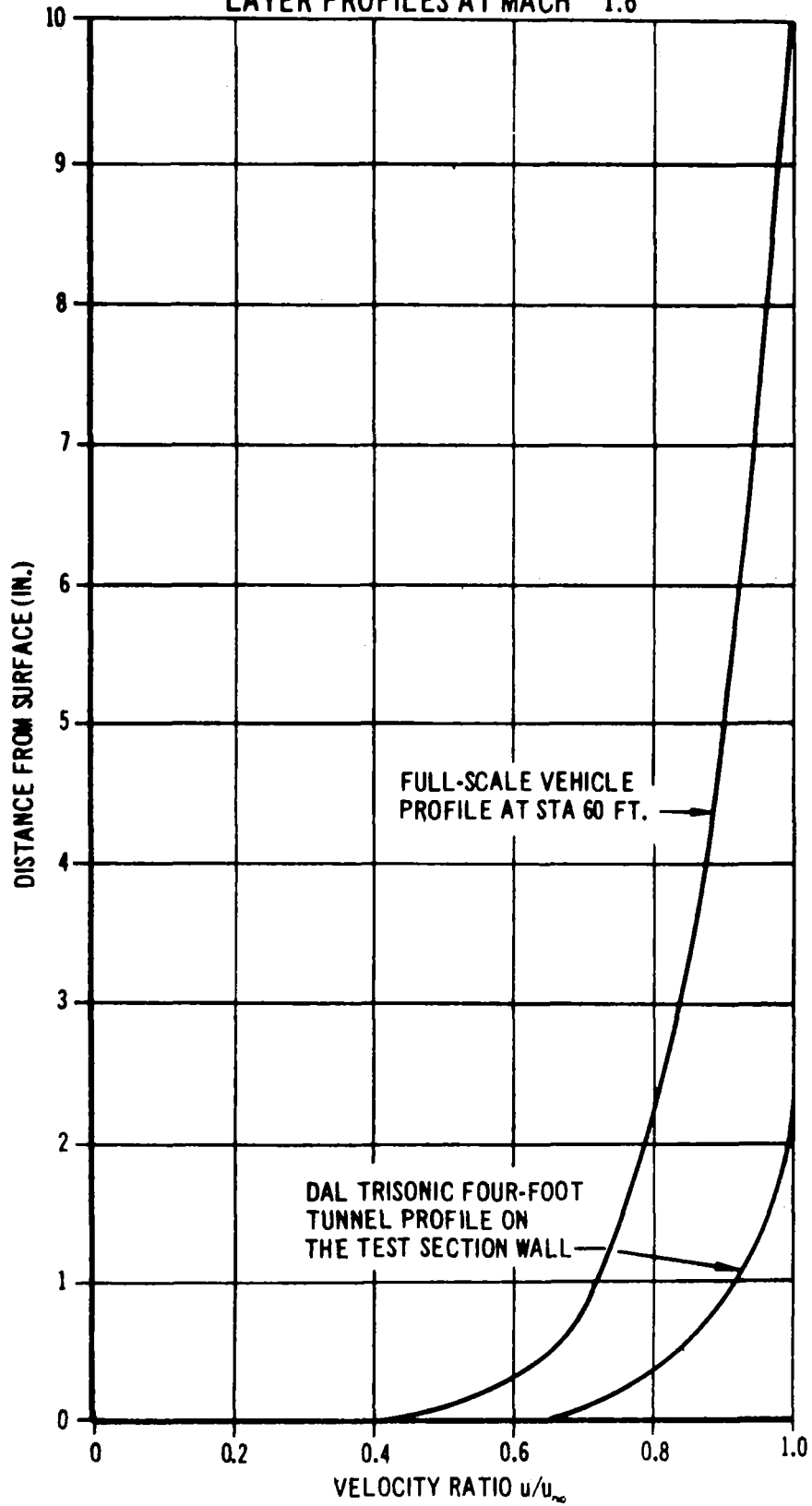


FIGURE 8

HEAT TRANSFER MODEL  
MOUNTING PLATE FOR AFT SECTION

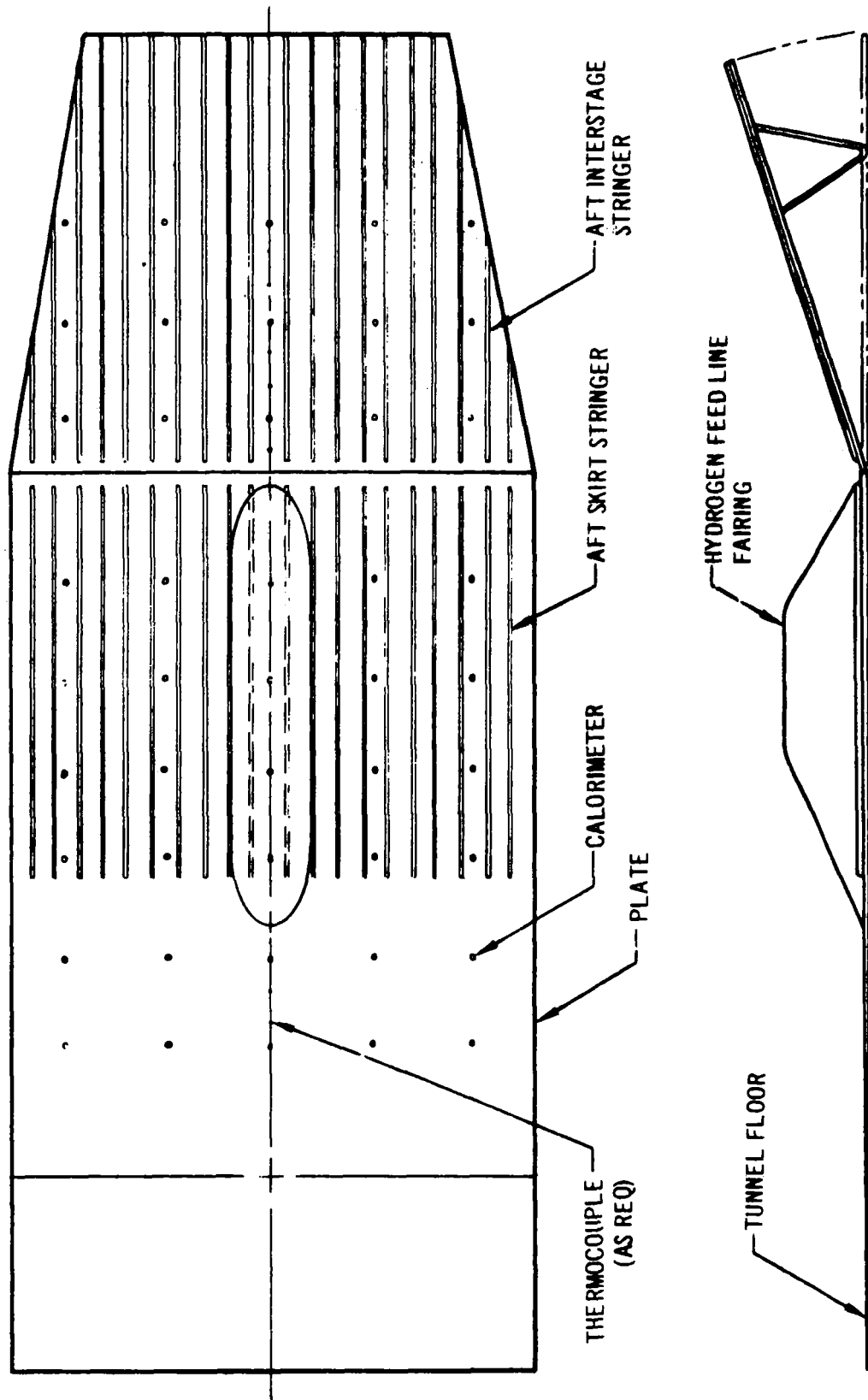


FIGURE 9

THIN WALLED PROTUBERANCE HEAT TRANSFER MODEL  
HYDROGEN FEED LINE FAIRING

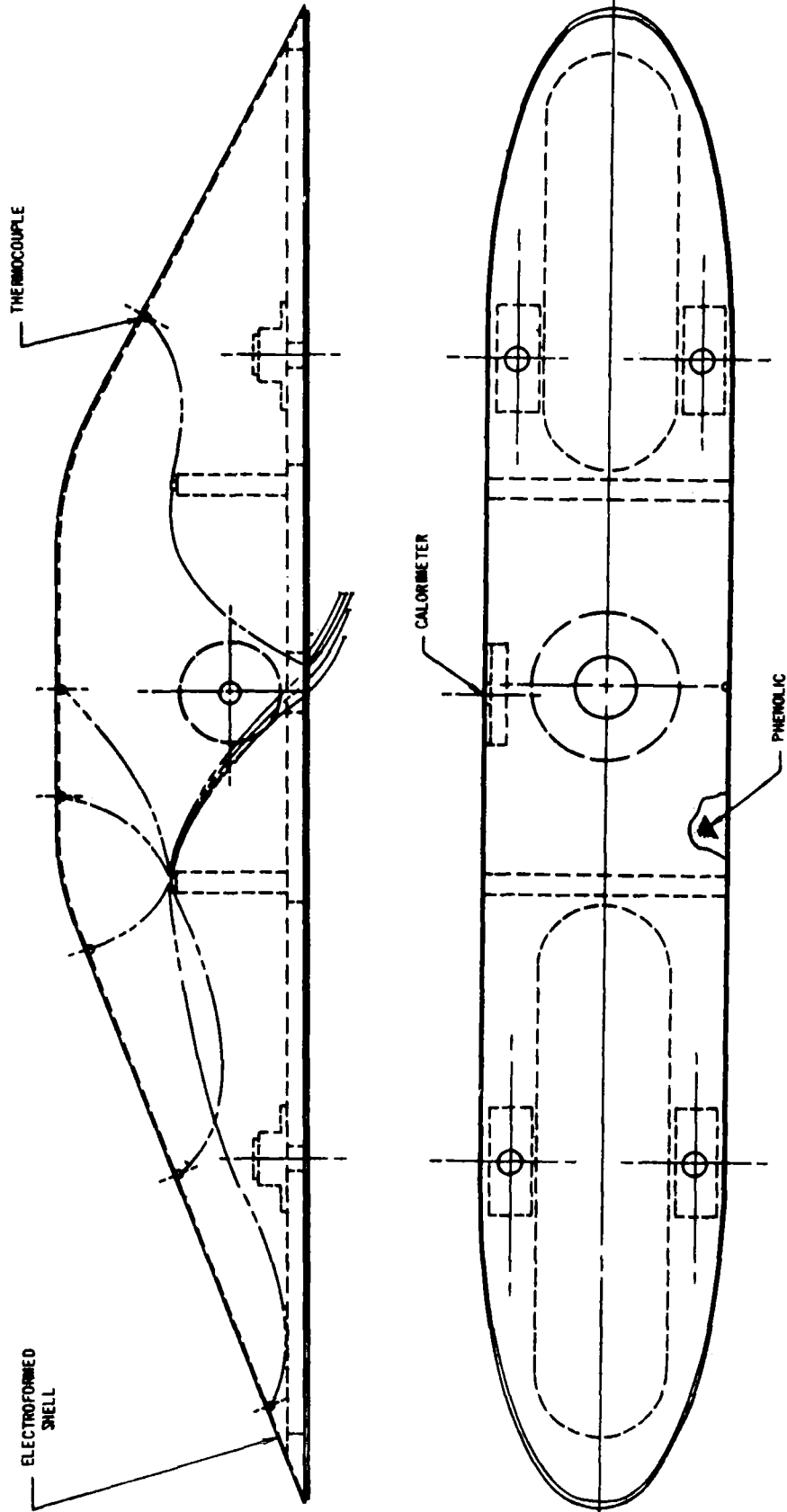


FIGURE 10

CALORIMETER & PRESSURE  
TUBE INSTALLATION

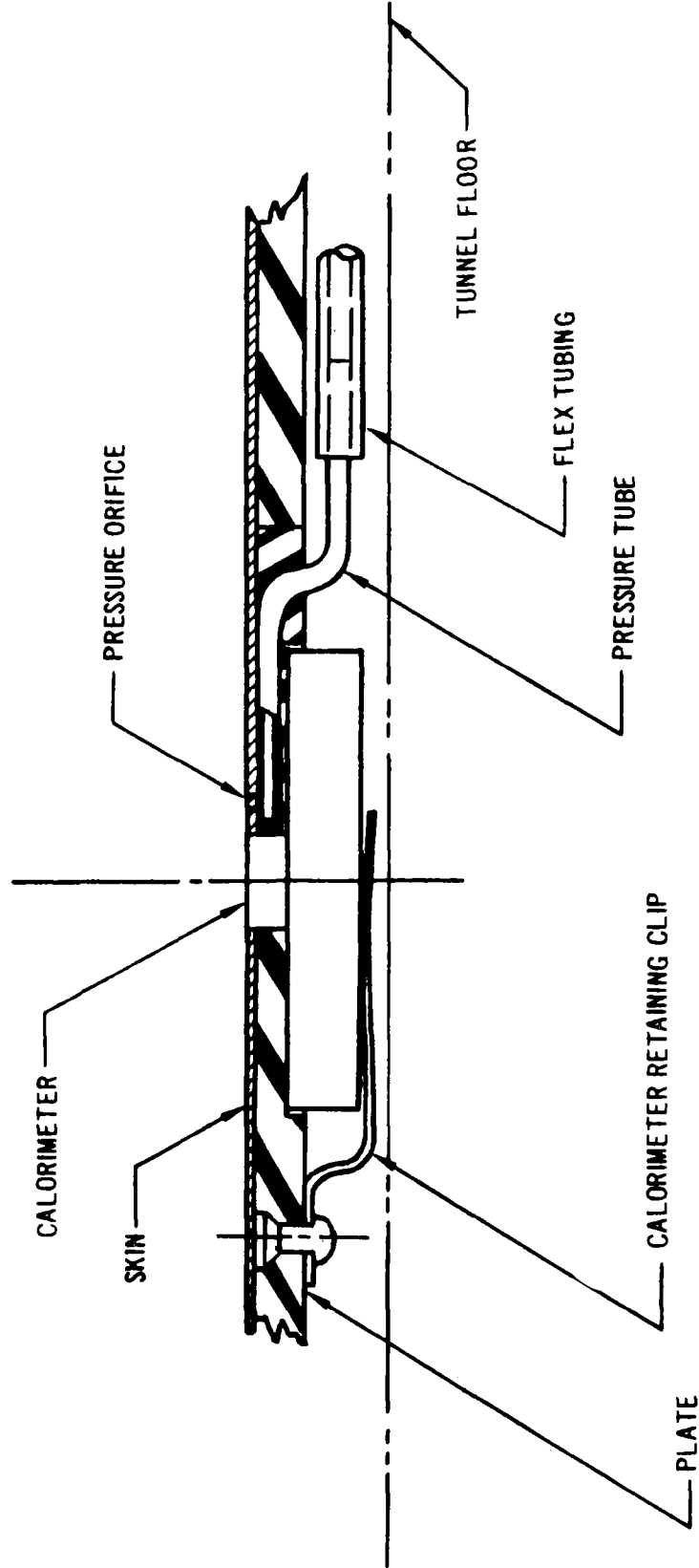
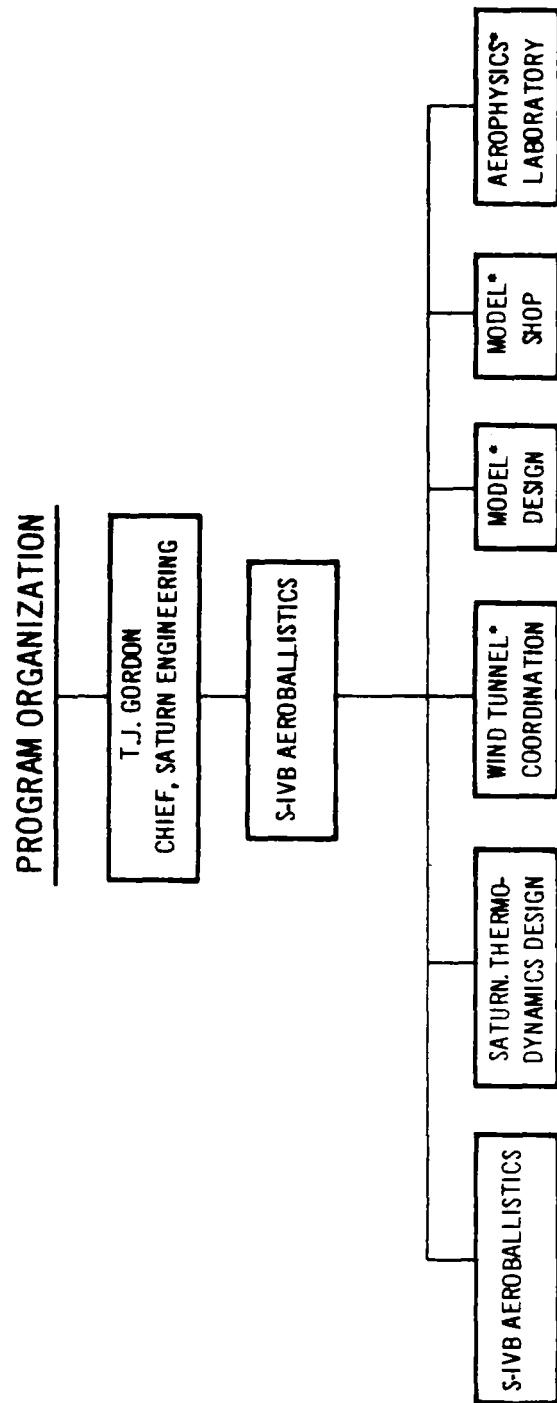


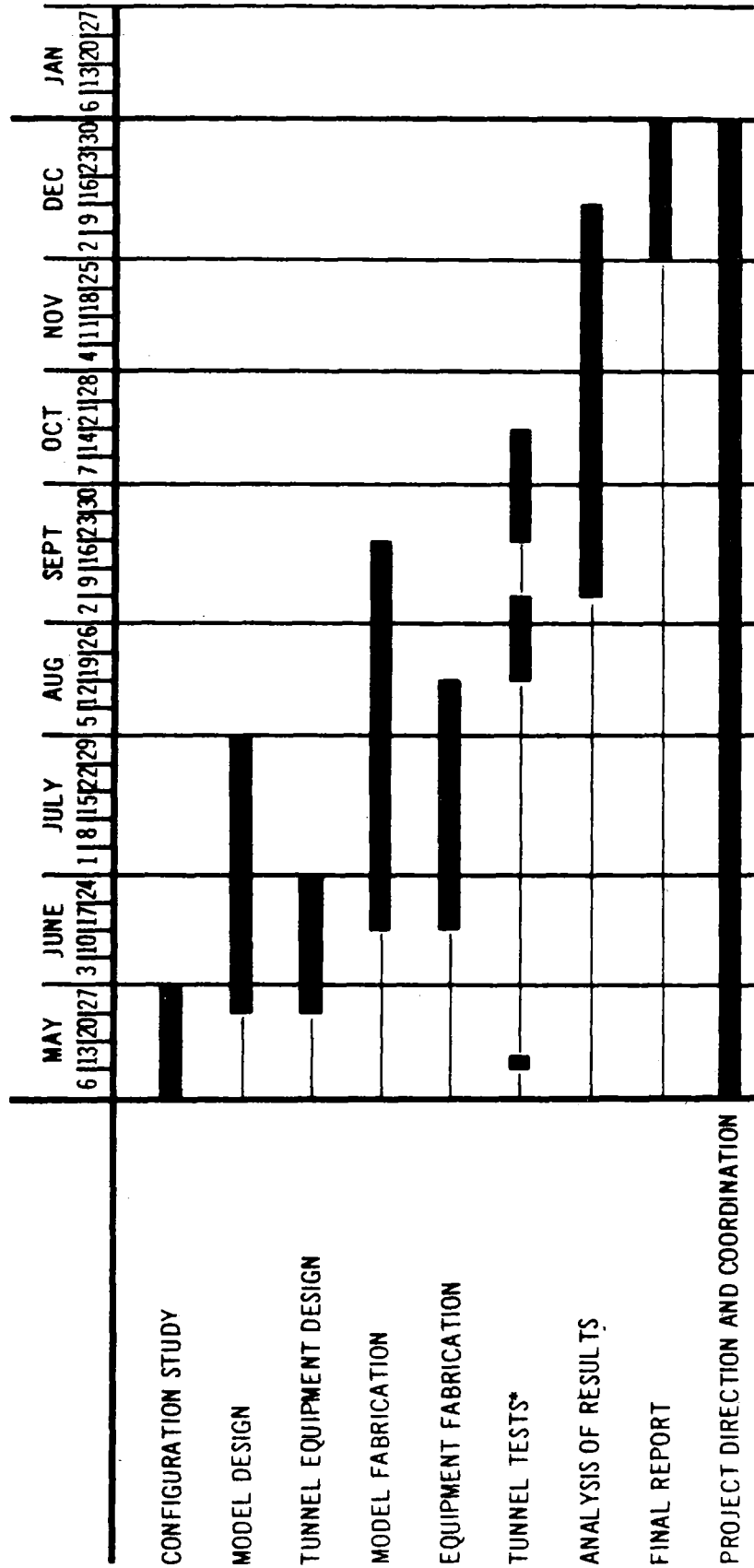
FIGURE 11



\* UNDER DIRECTION OF PRODUCT DEVELOPMENT ENGINEERING

FIGURE 12

# PROGRAM SCHEDULE

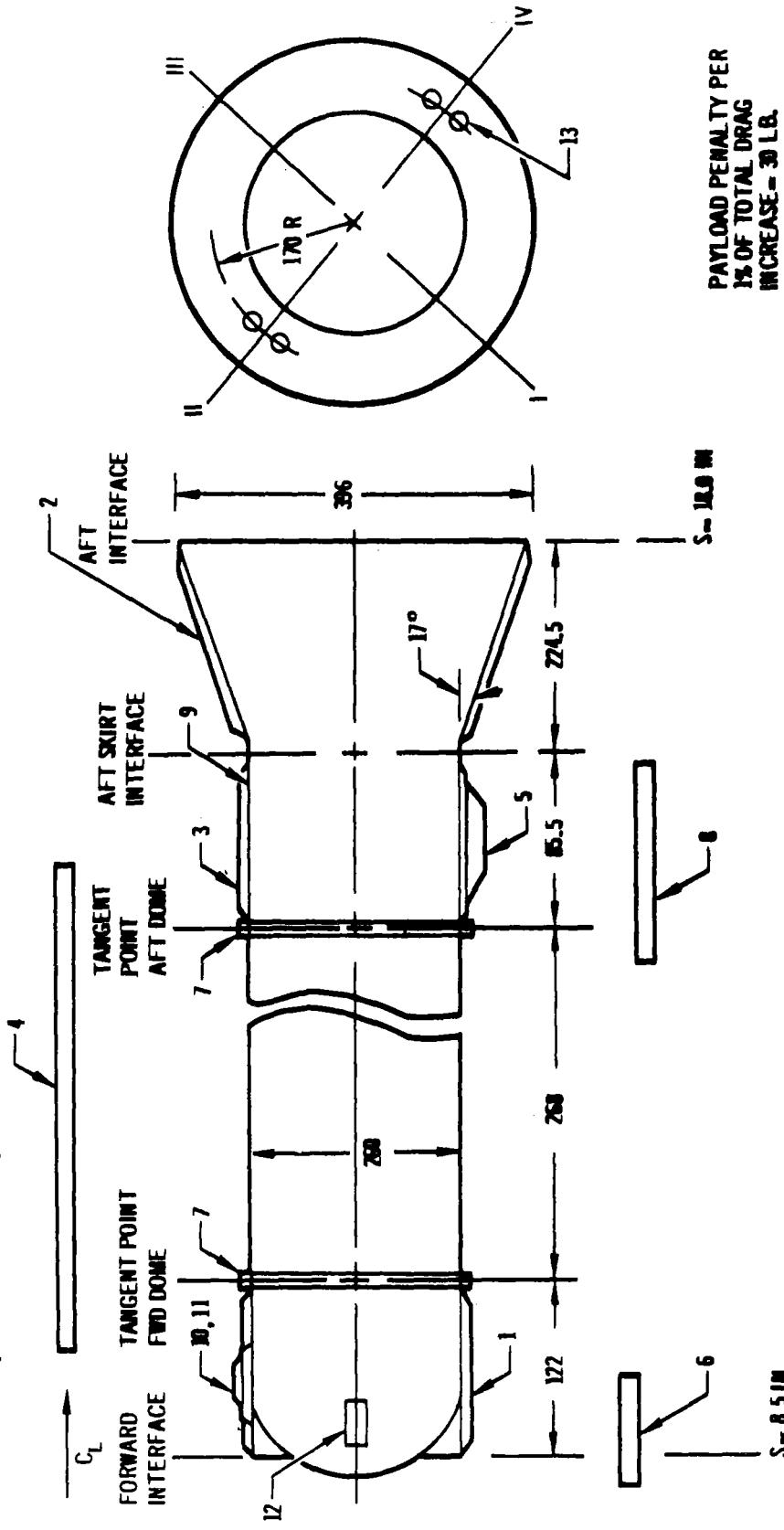


\* INCLUDES PRELIMINARY TESTING NECESSARY FOR EQUIP. DESIGN AND BOUNDARY LAYER CALIBRATION

FIGURE 13

S-IVB/ SATURN - V

$e M_{\infty} = 1.60$      $t = 77$  SEC  
 ALT. = 40,000 FT     $P_{\infty} = 393$  PSF  
 $q_{MAX} = 747$  PSF  
 $S = 8.5$  TO  $18.0$  IN (BOUND. LAY. THICK.)



PAYLOAD PENALTY PER  
 1% OF TOTAL DRAG  
 INCREASE = 30 L.B.

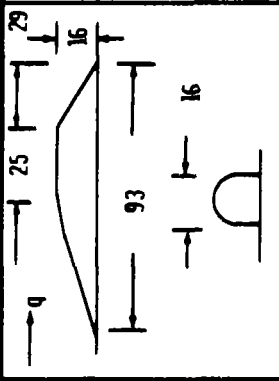
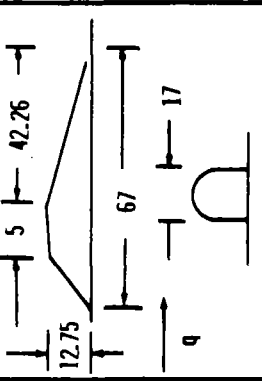
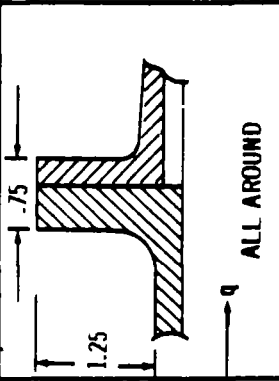
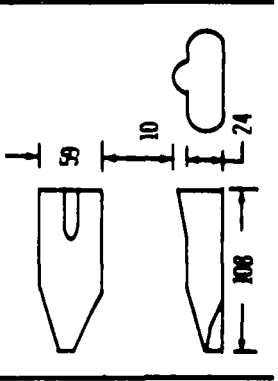
SATURN - V VEHICLE

LO-CA-TION	TITLE	SHAPE	h IN	w IN	l IN	A <sub>F</sub> FT <sup>2</sup>	A <sub>S</sub> FT <sup>2</sup>	A <sub>N</sub> FT <sup>2</sup>	C <sub>D</sub>	q PSF	D LB	% TOTAL LOAD PENAL- TY INCR- EASE	C <sub>L</sub>	N <sub>S</sub> LB	N <sub>N</sub> LB	C <sub>P</sub>
1	FORWARD STRINGER					.0071 PER STR				.8V .55q	4.1 PER STR.				306	
	108 REQ'D		1.25	.8175	120	A <sub>T</sub> = .77	1.04	.68	1.2	485	D <sub>T</sub> = 450		.6	300	210	-.125
2	AFT INTERSTAGE STRINGER					.009 PER STR				.8V .55q	5.3 PER STR.				673	
	144 REQ'D		1.30	1.0	235	A <sub>T</sub> = 1.30	2.12	1.63	1.2	485	D <sub>T</sub> = 770		.6	590	1,100	+ .40
3	AFT SKIRT STRINGER					.0093 PER STR				.8V .55q	5.5 PER STR.				376	
	144 REQ'D		1.375	.975	80	A <sub>T</sub> = 1.39	.76	.54	1.2	485	D <sub>T</sub> = 800		.6	250	210	-.025
4	TUNNEL														376	
	1 REQ'D		8	20	383	1.11	21.28	53.20	.8	747	700		.569	9500	20,000	-.025

NOTE: F = FRONT S = SIDE N = TOP T = TOTAL

ALL VALUES ARE FOR A SINGLE PROTRUSANCE UNLESS OTHERWISE NOTED.

SATURN-V/S-IVB

LO- CA- TION	TITLE	SHAPE	h IN	w IN	$\delta$ IN	$A_F$ FT <sup>2</sup>	$A_S$ FT <sup>2</sup>	$A_N$ FT <sup>2</sup>	$C_D$	q PSF	D LB	% TOTAL D INCR.	PAY LOAD PENAL- TY LB	$C_L$	$N_S$ LB	$N_N$ LB	$C_P$
5	HYDROGEN FEED LINE  1 REQ'D		16	16	93	1.14	6.55	10.0	.6	747	500	.10	3	.582	2900	4,500	-.025
6	RETRO- ROCKET FAIRING (FORWARD)  2 REQ'D		12.75	17	67	1.25	3.20	7.57	.6	747	590	1.1	2	.588	1400	2300	-.125
7	FLANGE  2 REQ'D		L.25	.75		7.15											
8	ALTITUDE CONTROL ROCKET FAIRING (SHAPE 3)  2 REQ'D		24 TO 34	59	108	9.80	17.6	44.3	.8 .33 .4	747	4250			.57	7000		

LO-CA-TION	TITLE	SHAPE	h	w	$\ell$	$A_F$	$A_S$	$A_N$	$C_D$	q	D	% TOTAL INCREASE	PAY-LOAD PENALTY LB	$C_L$	$N_S$ LB	$N_N$ LB	$C_P$
9	HYDROGEN GEN FILL LINE 1 REQ'D		10	8	54	.56	2.92	3.60	.8	747	400	.08	2	.588	1300	1,400	-.025
10	PAD 1 REQ'D		1.25	6.75	13	.059	.103	.61	1.2	485	40			.6	30	190	-.175
11	ANTENNA 1 REQ'D		1.625	4.5	9	.051	.085	.78	1.2	598	35			.6	25	90	-.125
12	VENTIL. SYSTEM 2 REQ'D		10	8	23	.556	1.01	1.78	.8	747	300	.05	2	.588	450	400	-.125

LO- CA- TION	TITLE	SHAPE	h IN	w IN	l IN	A <sub>F</sub> FT <sup>2</sup>	A <sub>S</sub> FT <sup>2</sup>	A <sub>N</sub> FT <sup>2</sup>	C <sub>D</sub>	q PSF	D LB	% TOTAL ID INCRE- ASE	PAY- LOAD PENAL- TY LB	C <sub>L</sub>	N <sub>S</sub> LB	N <sub>N</sub> LB	C <sub>P</sub>
13	S-II RETRO ROCKET		15		35	1.80				747				.588	800		
	4 REQ'D																

## Section 10

### AUXILIARY PROPULSION SYSTEM FAIRING WIND TUNNEL TEST

The Auxiliary Propulsion System (APS) fairing is a protuberance of the S-IVB stage of the Saturn V vehicle and is used for attitude control of the S-IVB after separation, for separation thrust and for propellant ullage control. This fairing covers the propellant tanks, the rocket engines and the associated equipment. It is a closed module attached to the stage at four attach points. The relative location and size of the APS, installed on the S-IVB, is illustrated in figure 1. Figure 2 details the attachment scheme. The two forward attach points are located on the forward ring. This ring absorbs the normal loading. The space available for the ring limits the method of strengthening the ring to widening it instead of deepening it, which would be much more efficient, structurally. Figure 3 presents the effect of normal load upon the weight of the ring. The weight is very sensitive to the load. By shaping the fairing properly, the reaction loads on the forward attach points may be minimized. However, any design load established must be known very accurately. Conservatism in the load would cause unnecessary weight penalties.

The location and relative size of the fairing results in the analytic statement of the aerodynamics being extremely complex. The boundary layer in that region is on the order of 10 to 15 inches which envelopes a large portion of the fairing. The pressure rise in the region of flare separates the boundary layer and causes turbulent flow over the aft portion of the fairing. These effects in combination with the three-dimensional character of the flow field around the fairing cause an accurate analytical solution to be practically impossible.

As a result of these problems, the only feasible method of determining the loads accurately is with proper simulation of the APS fairing environment in a wind tunnel. This approach requires a close estimation of the full-scale environment to establish wind tunnel conditions. The full-scale boundary layer thickness and velocity profile is presented in figure 4 and 5, respectively. Figure 6 shows the Reynolds number at this station as a function of Mach number.

Since the normal load is critical under the conditions described, an analytical investigation of various shapes were conducted in an effort to develop an

optimum fairing shape. The configurations are presented in figures 7(a) through 7(j). The loads based on the analysis are presented in table I. Configurations 6 and 7 were an attempt to use the flow to lower the normal load by creating a lift on the nose section by partially stagnating the flow beneath the nose. However, this region of stagnated flow would create problems in heat input to the hydrogen tank. For this reason, they were eliminated from further investigation. Configurations 8 through 10 were attempts to reduce the loading by reducing frontal area and planform area. As is shown by the loads in table I, other load limitations appeared in each configuration. Manufacturing complexity eliminated configuration 5 due to the compound curvature of the semi-ogive nose fairing.

The remaining configurations 1, 2, 3, and 4 are recommended as test configurations. Configuration 1 is recommended since it is the current design configuration. If it is satisfactory in reality, the design changes could be eliminated. Configurations 2, 3, and 4 are recommended as a result of the preliminary loads analysis. These three configurations are a spread of values of the nose incline angle ( $\theta$ ). These three values are expected to span the range necessary to define an optimum angle that would result in the lowest reaction loads on the forward ring.

All facilities and equipment needed to conduct this program are currently available within the Douglas Aircraft Company, Missile and Space Systems Division. These include the engineering facilities required for design of the models, modern model shops which are capable of fabricating and instrumenting the models and support equipment, IBM 1620 and 7090 computing facilities required for data reduction and analysis, and the wind tunnel test facility.

The Douglas Aerophysics Laboratory Trisonic Four-Foot Tunnel located at El Segundo, California is a blowdown-to-atmosphere facility operating from a 525 psia storage reservoir with running times on the order of 30 to 60 seconds. Mach number range is continuously variable from 0.2 to 5.0. Tabulated below are several of the pertinent operational characteristics.

Mach Number	Variable from 0.2 to 5.0
Run Time	30 to 60 seconds
Stagnation Pressure	20 to 350 psia depending on Mach Number
Stagnation Temperature	60° to 90°F at Mach 4.0 and below 120° to 200°F at Mach 4.5 and above
Dynamic Pressure	1,200 to 3,500 psf
Reynolds Number	$0.5 \times 10^6$ to $2 \times 10^6$ per inch
Boundary Layer Thickness	1.5 to 4.5 inches
Pump-up Time	10 to 20 minutes
Angle-of-Attack Range	-15° to 25° with straight sting
Storage Pressure	525 psia
Storage Volume	26,250 cubic feet
Thermal Mass	60 tons of galvanized steel tubing

A schematic of the design features of the tunnel is shown in figure 8. In addition to the tunnel itself, the facility contains or has directly available the following associated equipment:

- a) A shadowgraph system capable of producing shadowgraphs at 2 second intervals.
- b) A 16-channel digital system capable of recording data every 0.6 second on IBM punch cards.
- c) A pressure scanner which uses 16 pressure transducers and switches 10 pressures to each transducer enabling up to 160 pressures to be sensed every 8 seconds.
- d) A Benson-Lehner Electroplotter with a speed of approximately 1200 points per hour for as-run and summary plots.
- e) An auxiliary air supply system.
- f) A 12 channel Direct Writing Recorder with up to a 100 CPS response.

The entire model assembly will be mounted on the floor of the tunnel to simulate the surface of the S-IVB locally. As shown in figure 9 the model will incorporate simulation of the aft interstage flare which will establish the boundary layer effects at subsonic speeds and boundary layer shock-interaction at supersonic speeds.

A preliminary analysis indicates that shock wave interaction and tunnel blockage are not problems; but a limited tunnel verification is desired to provide information relative to the tunnel flow and the model.

The primary consideration for proper simulation is the relationship between the wind tunnel boundary layer and the vehicle boundary layer. Since the wind tunnel boundary layer will be utilized to simulate the boundary layer over the vehicle the tunnel boundary layer will determine the model scale. Figure 4 shows both wind tunnel and vehicle boundary layer thickness as a function of Mach number. It can be readily seen that the wind tunnel boundary layer is 20 percent of the vehicle boundary layer. A comparison of vehicle and wind tunnel boundary layer profiles is shown in figure 5. At supersonic velocities the tunnel and vehicle boundary layer velocity profiles are assumed to follow the turbulent power-law profiles of the form

$$\frac{u}{u_{\infty}} = \left( \frac{y}{\delta_0} \right)^{\frac{1}{n}}$$

where  $n$  increases from 6.8 at lower Mach numbers to 8.0 at higher Mach numbers for the tunnel and where  $n$  is 7.0 for the vehicle. If required, a boundary layer trip may be used to create a larger boundary layer.

The model will only be tested at zero angle of attack and up to 10 degrees in yaw. The Mach numbers tested will include 0.80, 1.2, 1.6 and 2.0. A test run summary is presented in table II.

Since pressure data are required for the vehicle surface a dummy tunnel floor will be required. This flat plate would house pressure instrumentation pick-ups and provide attachment fitting for the stringers. The dummy floor or plate would also have provisions for varying the angle of yaw. An additional plate is required to simulate the interstage section (for details, see figure 9). The APS fairing will be designed for mounting on a six component strain gauge balance. Since it is not desirable to record pressure data simultaneously with

force data due to the interference problems and since distributed loads on the fairing will be provided by subsequent tests pressures will be measured on the plate only. The three-dimensional effects resulting from the finite radius of the surface adjacent to the fairing and flare immediately behind the fairing are expected to be small. The data produced by this test will be directly applicable to the full scale vehicle. Only in the high Mach number range, above 3.0, will there be any problem in simulation; and this discrepancy will be small.

Aerodynamic forces and moments on the APS fairing will be measured with a six component balance and the data reduced to coefficient form. To establish the loads at the attachment points, the normal force, the axial force, the side force and the center of pressure must be established. The reference radius used for reduction of the force data will be the base radius of a Saturn V of the appropriate scale. In the case of the 20 percent model this radius would be 39.6 inches.

Around the APS fairing pressures are measured on the plate to establish the effect of the fairing on the local flow field. The locations of the taps are presented in figure 9. Pressures in the base region will be measured with probes as is illustrated in figure 9. The pressures measured beneath and behind the fairing will enable the assignment of the changes in loads to the proper cause. They aid the evaluation of the flow sealing, or blocking, directly below the nose fairing. This blocking is an attempt to eliminate large areas of stagnated flow to avoid heat influx to the cryogenic propellants.

The preliminary test, to determine if blockage problems exist and the size and quality of boundary layer on the tunnel floor, is to be conducted previous to any firm decision of scale. The larger the model the more severe will be the blockage problem. The smaller the boundary layer the smaller the scale must be to simulate full-scale effects. The effectiveness of tripping the boundary layer and varying Reynolds number to produce controlled thickness will also be studied. The boundary layer will be measured by one probe located on the plate as shown in figure 9. The boundary layer trip is also illustrated in 9.

TABLE I

ATTITUDE CONTROL SYSTEM FAIRING CONFIGURATION  
LOAD COMPARISON

<u>CONFIGURATION</u>	<u>AXIAL FORCE (POUNDS)</u>	<u>SIDE FORCE (POUNDS)</u>	<u>NORMAL FORCE (POUNDS)</u>
1	6,800	7,300	7,780
2	7,050	8,400	3,550
3	6,350	8,000	6,000
4	6,200	7,700	7,150
5	4,250	7,800	4,000
6	5,650	8,500	7,100
7	6,950	7,500	7,450
8	10,700	8,400	14,000
9	6,100	16,000	4,500
10	7,650	7,100	5,860

TABLE II

TUNNEL TIME BREAKDOWN

Configurations - 4

Test Mach Numbers - 0.80, 1.2, 1.6, 2.0, 3.0

Yaw Angles - 0, 5, 10°

Fifteen (15) Runs per Configuration (5 Mach Numbers, 3 Angles)

Ten (10) Boundary Layers Runs for Two Configurations, 0° Angle of Yaw

Total Number of Runs - 70 Runs = (4 Configurations x 15 Runs/Configuration +  
10 Boundary Layer Runs)

---

Available Testing Time - 40 Hours

Installation Time - 8 Hours

Useful Testing Time - 32 Hours

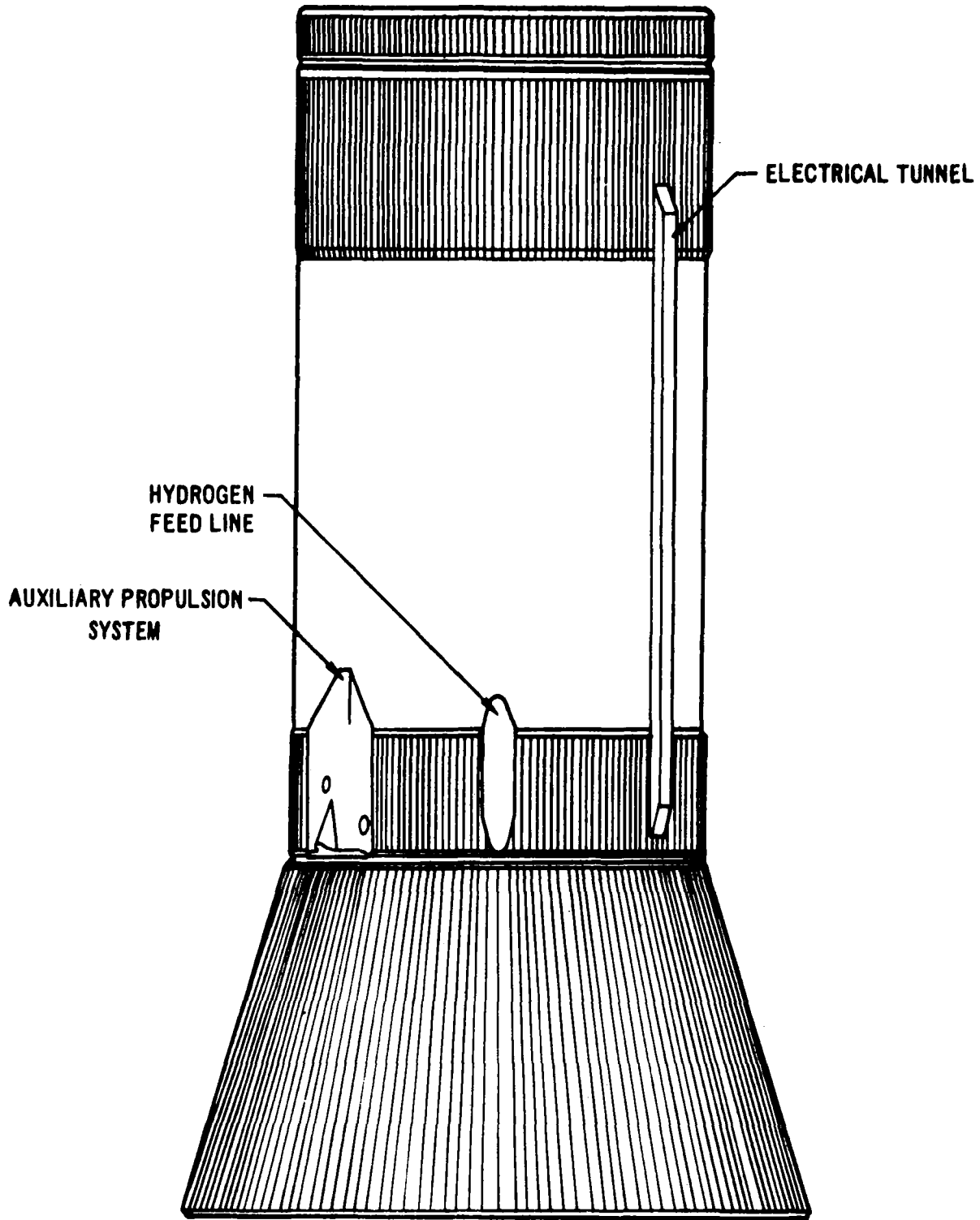
Average Runs Per Hour - 2 1/2

Available Runs - 80

---

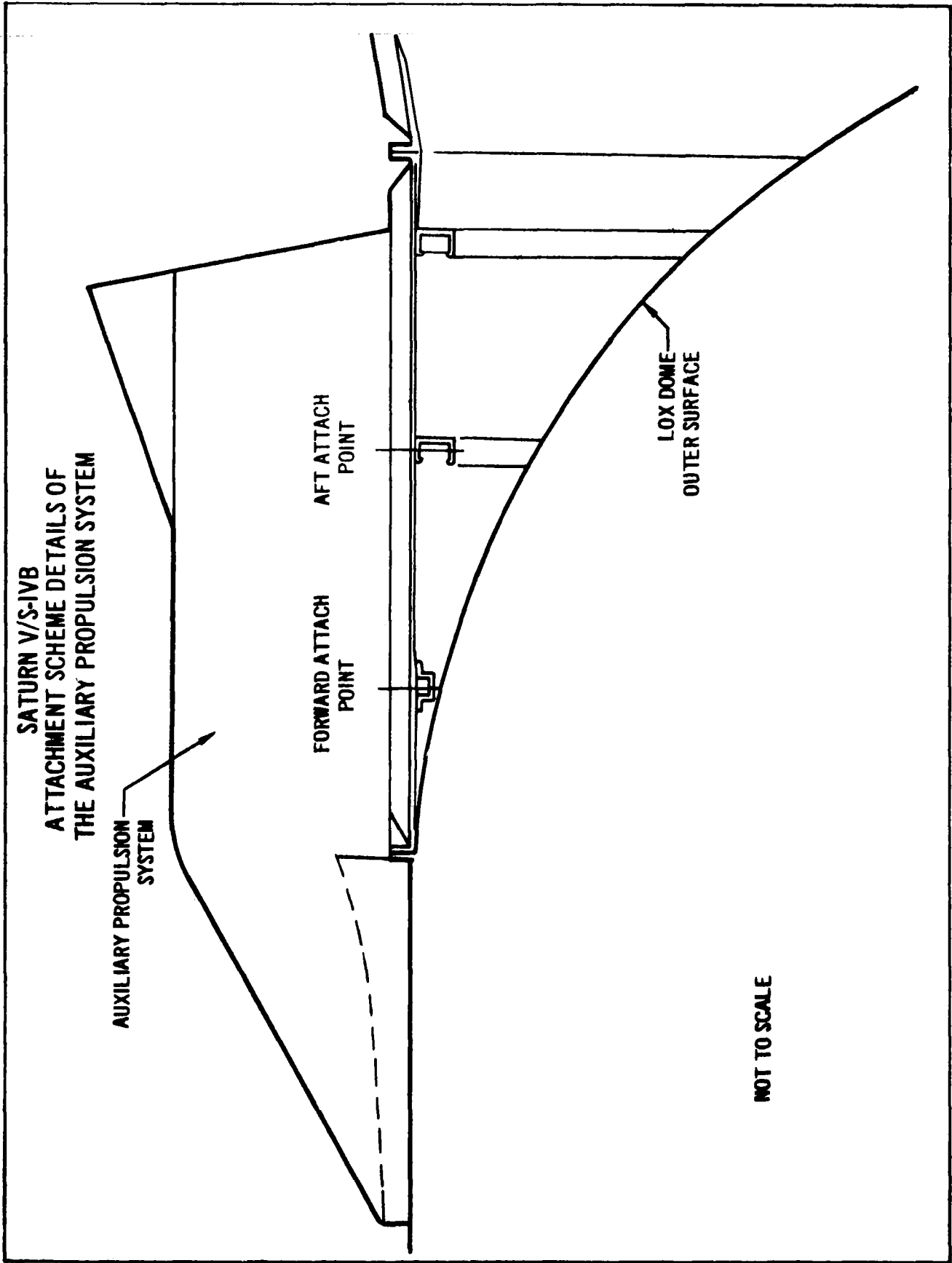
Runs Alloted for Data Repeatability and Further Boundary Layer Studies - 10 Runs =  
(80 Available Runs - 70 Total Scheduled Runs)

SATURN V/S-IVB



PROTUBURANCES SHOWN TO ILLUSTRATE RELATIVE SIZES.  
CIRCUMFERENTIAL LOCATIONS ARE NOT PROPERLY POSITIONED.

FIGURE 1



**SATURN V/S-IVB  
ATTACHMENT SCHEME DETAILS OF  
THE AUXILIARY PROPULSION SYSTEM**

**AUXILIARY PROPULSION  
SYSTEM**

**FORWARD ATTACH  
POINT**

**AFT ATTACH  
POINT**

**LOX DOME  
OUTER SURFACE**

**NOT TO SCALE**

**FIGURE 2**

SATURN V  
S-IVB STAGE  
FORWARD FRAME WEIGHT VS RADIAL  
LIMIT LOAD

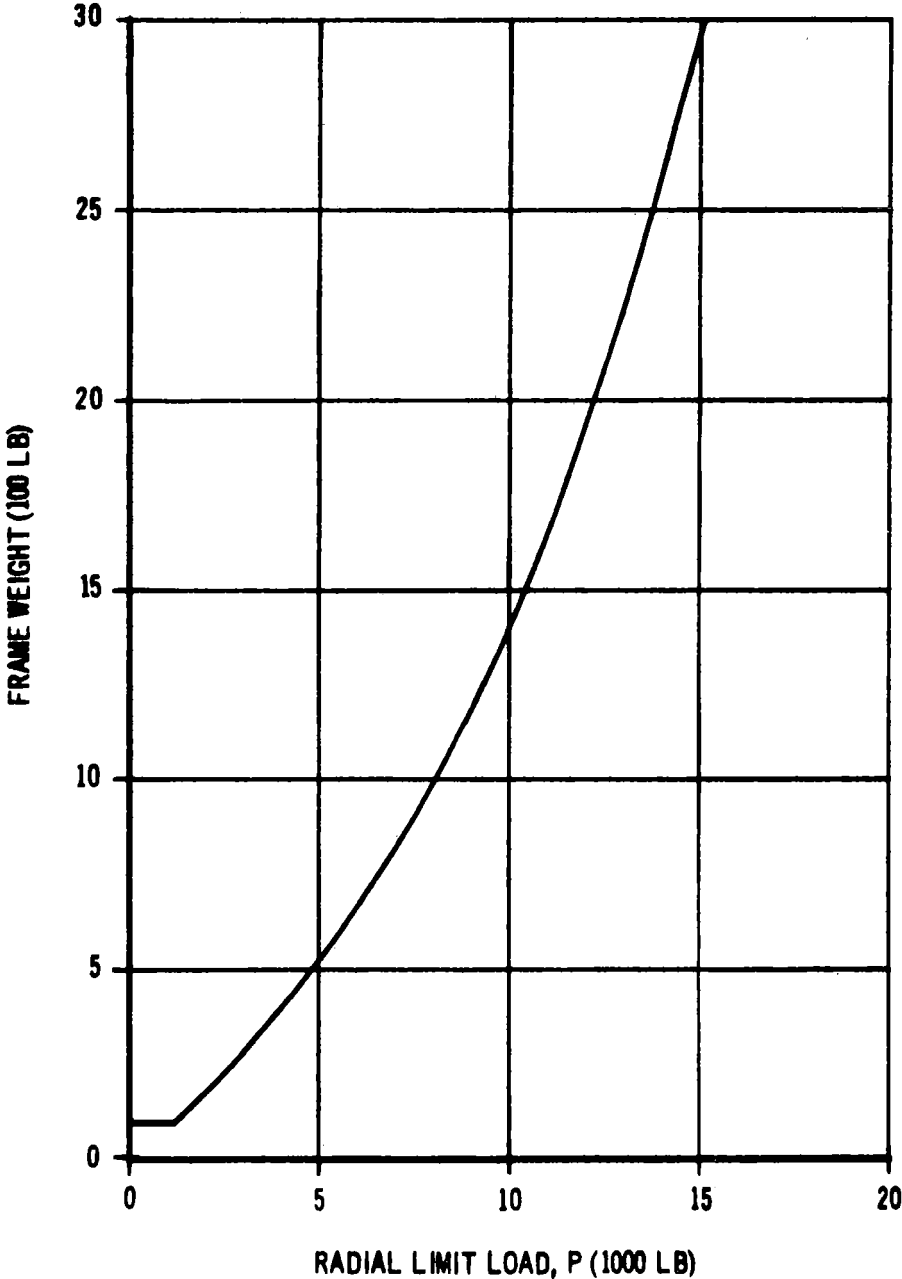


FIGURE 3

COMPARISON OF FULL-SCALE S-IVB AND DOUGLAS AEROPHYSIC LABORATORY  
FOUR-FOOT TUNNEL BOUNDARY  
LAYER THICKNESS

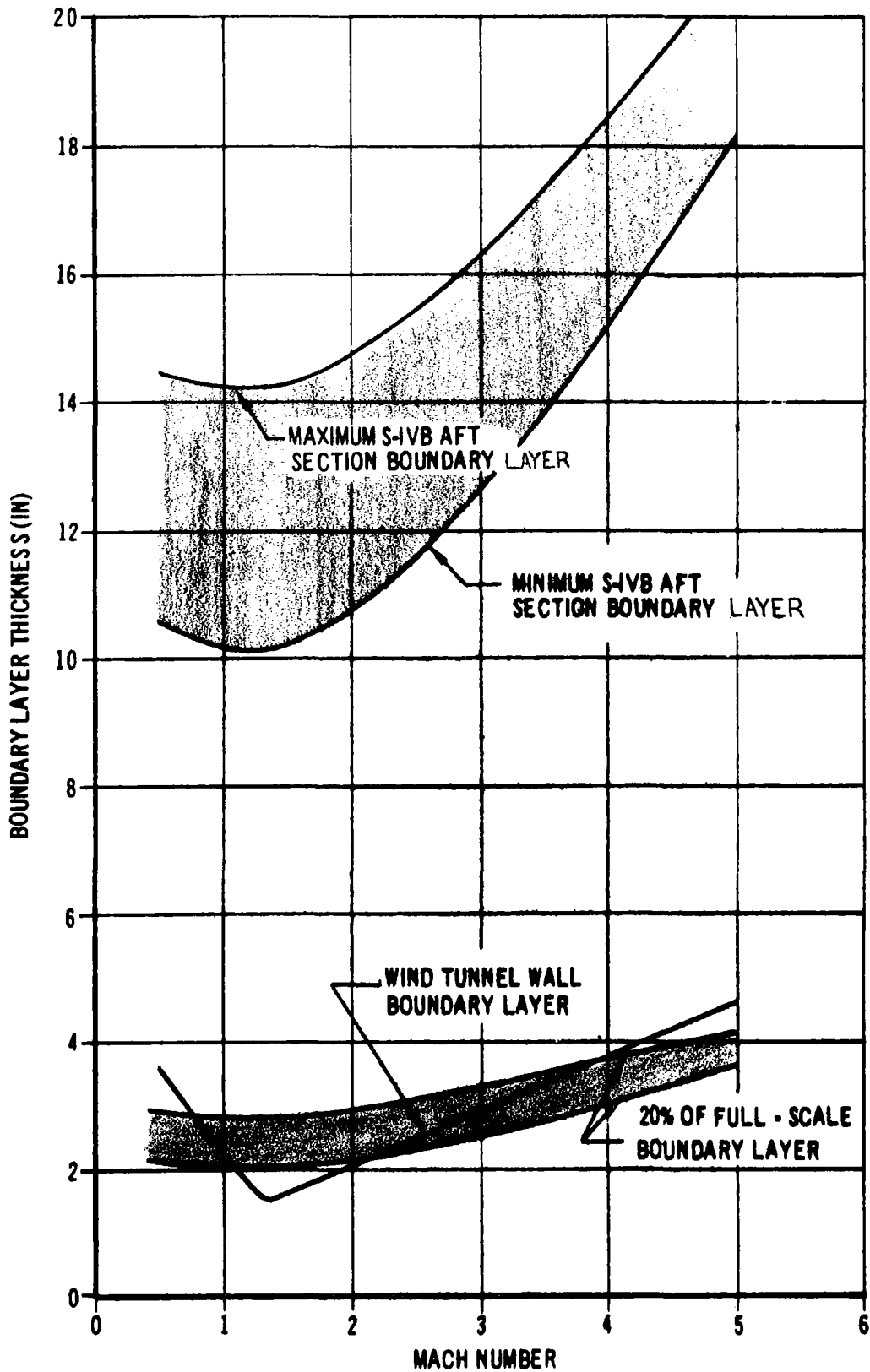


FIGURE 4

COMPARISON OF FULL-SCALE S-IVB AND DOUGLAS AEROPHYSICS LABORATORY  
FOUR-FOOT TUNNEL BOUNDARY  
LAYER PROFILES AT MACH - 1.6

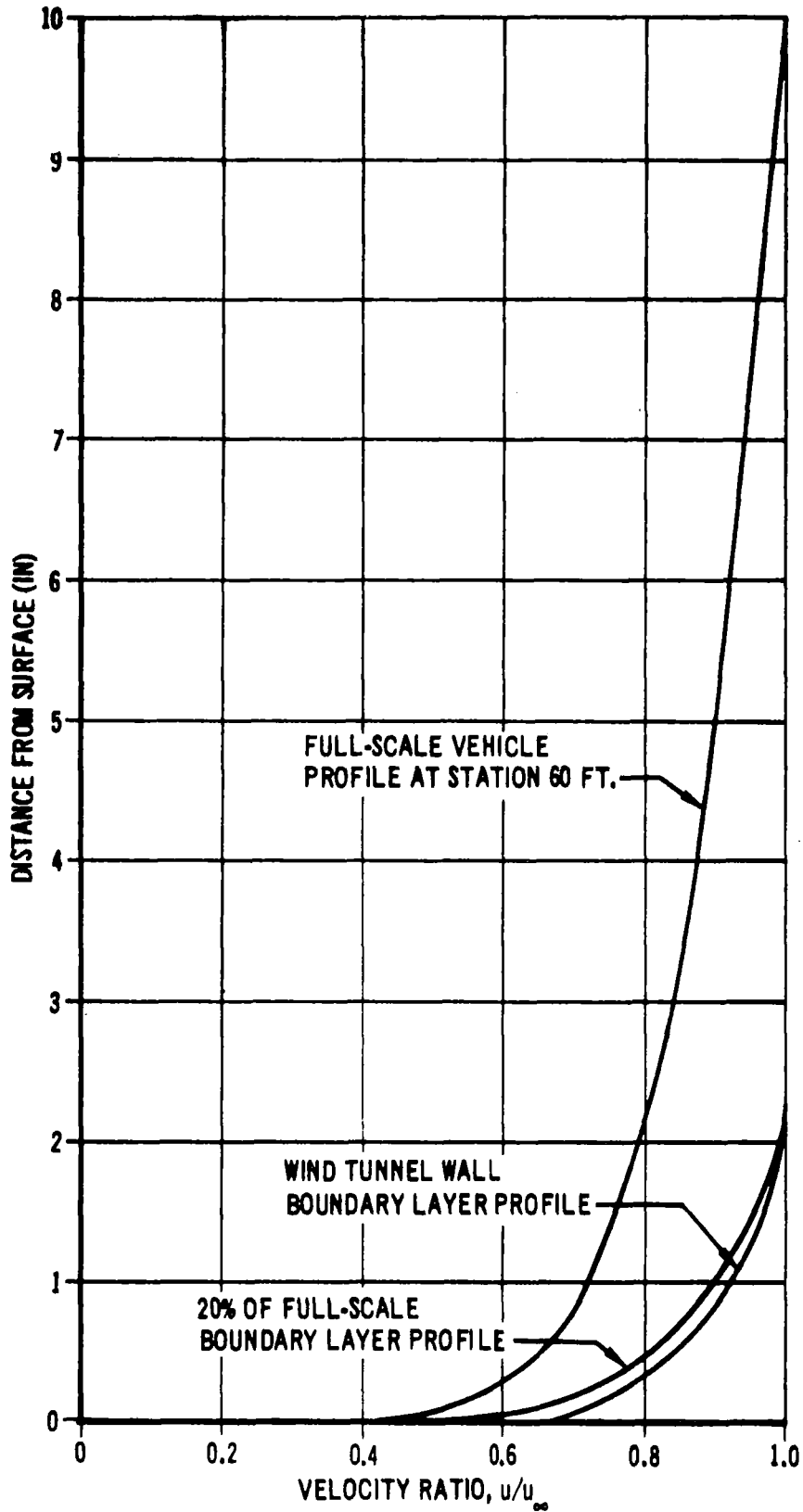
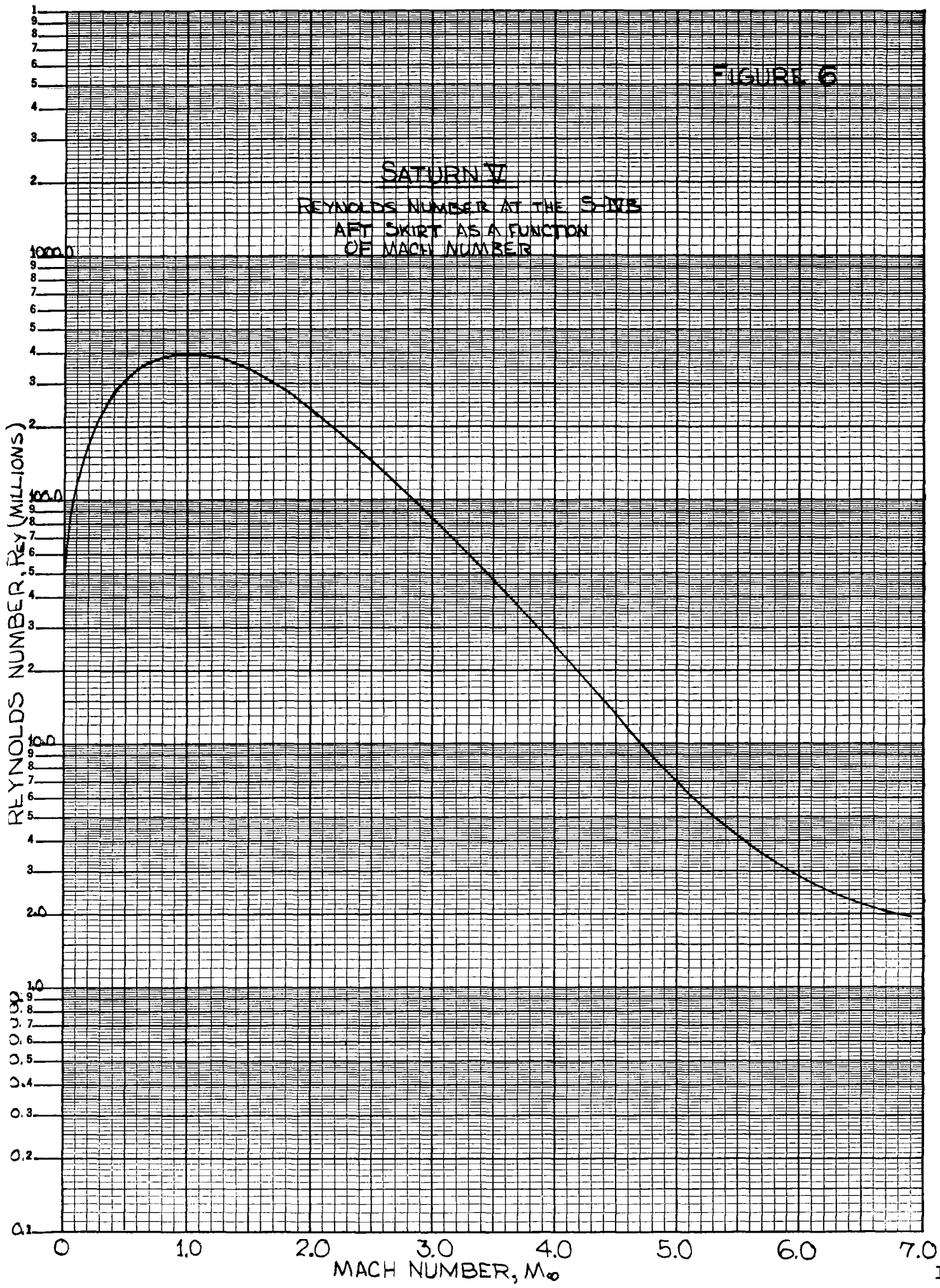


FIGURE 5

FIGURE 6

SATURN V  
REYNOLDS NUMBER AT THE S-IVB  
AFT SKIRT AS A FUNCTION  
OF MACH NUMBER



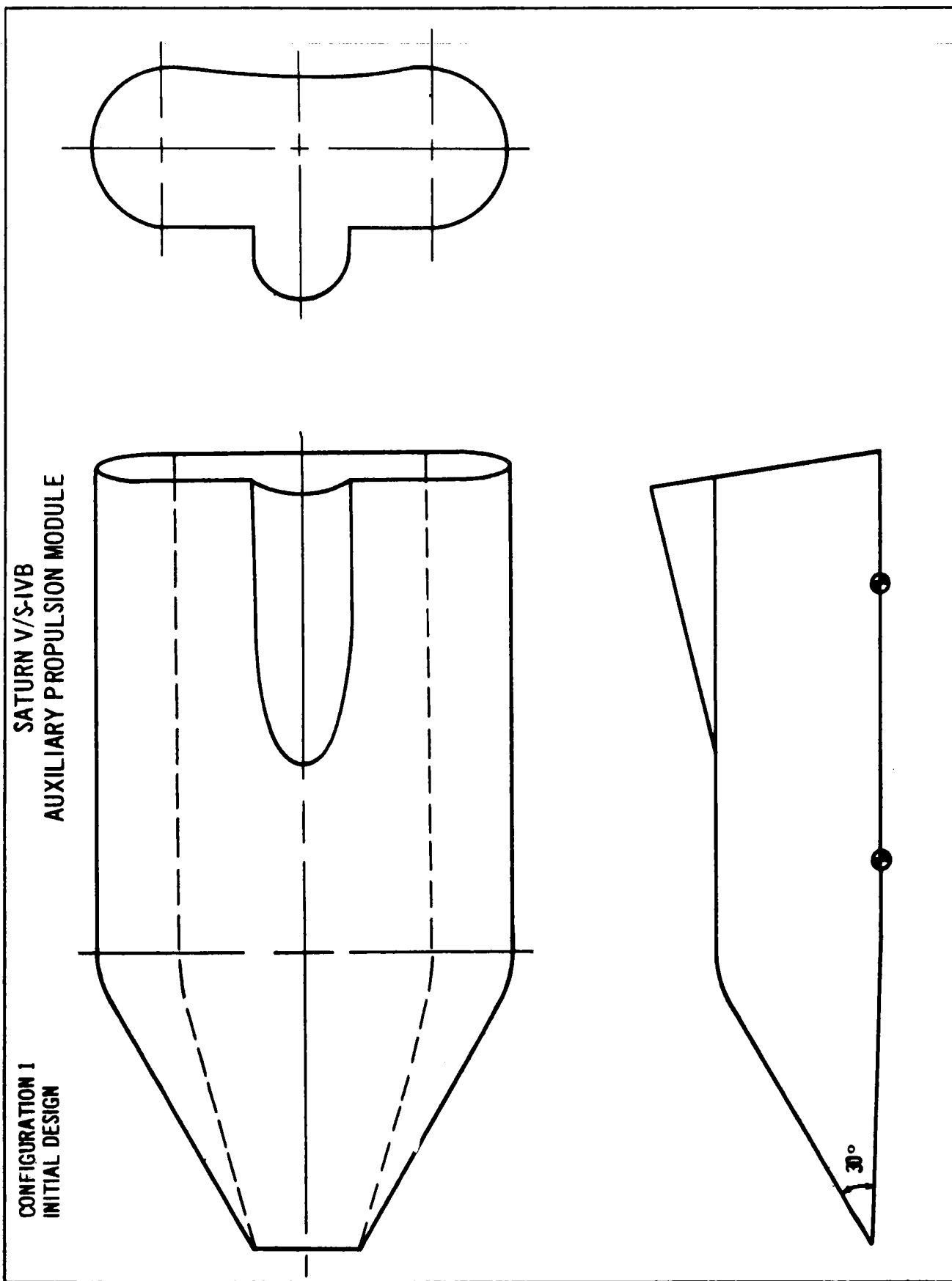


FIGURE 7 A

SATURN V/S-IVB  
AUXILIARY PROPULSION MODULE

CONFIGURATION 2

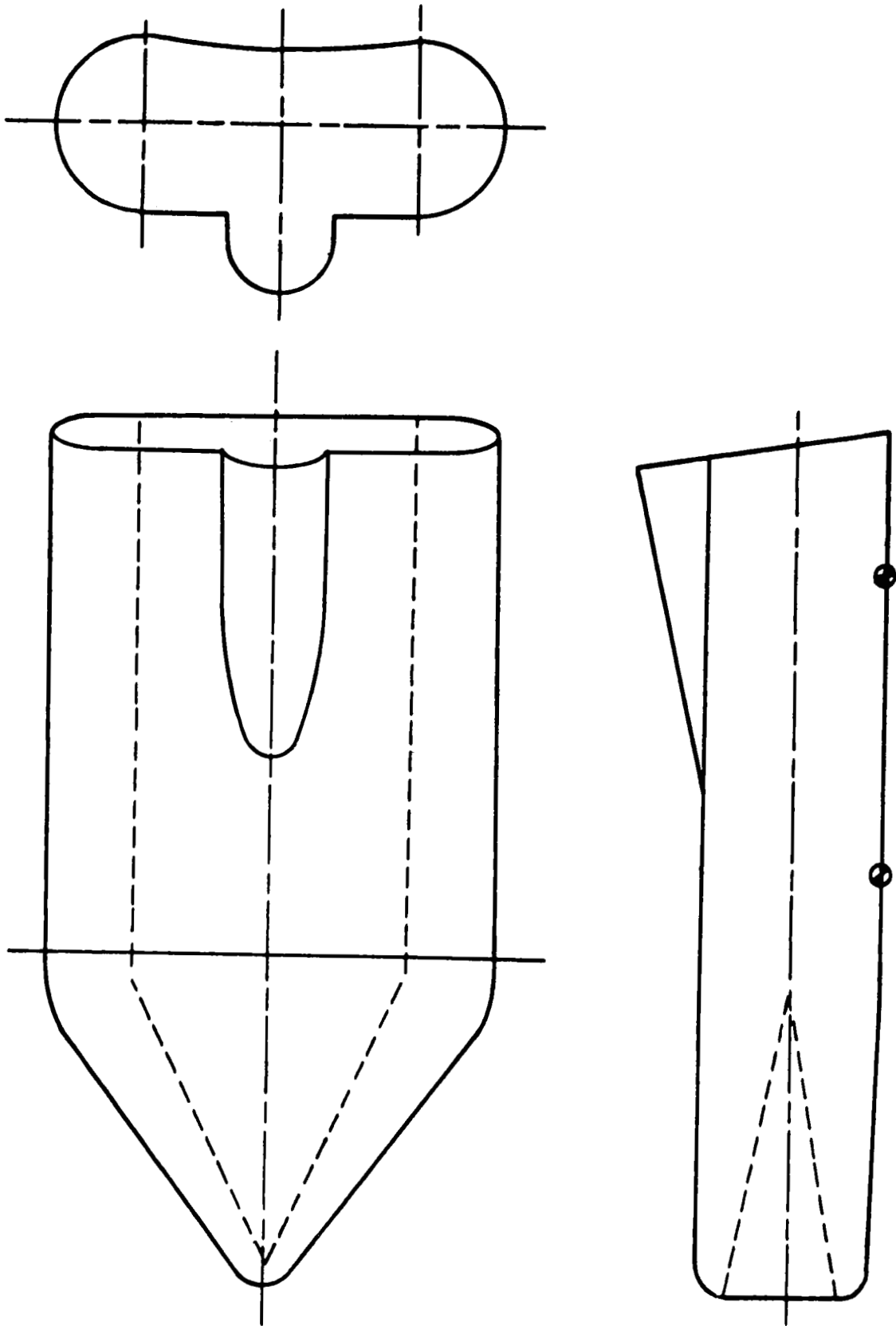


FIGURE 7 B

CONFIGURATION 3

SATURN V/S-IVB  
AUXILIARY PROPULSION MODULE

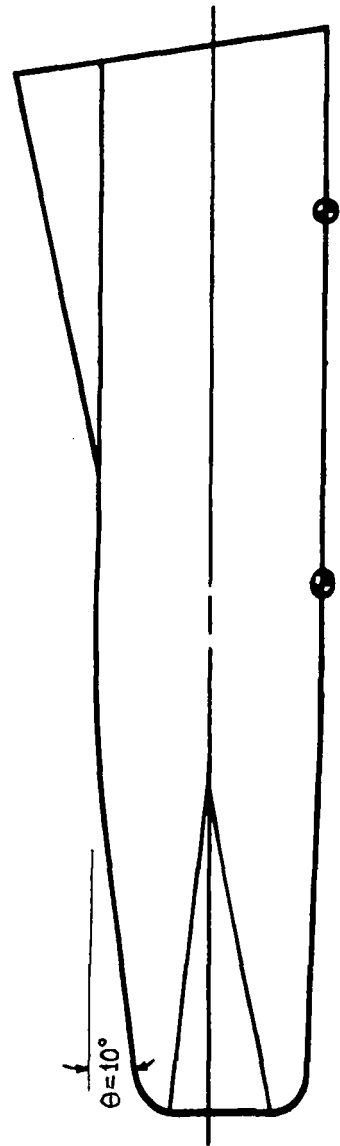
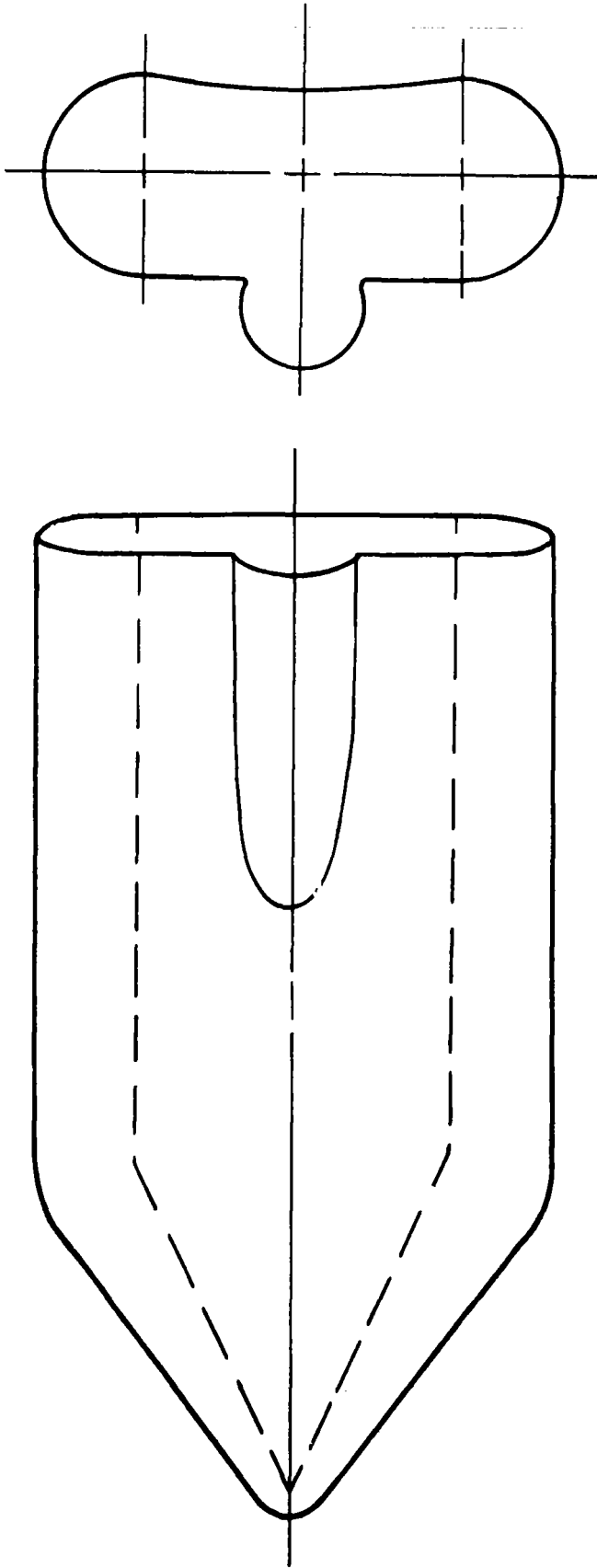


FIGURE 7C

SATURN V/S-IVB  
AUXILIARY PROPULSION MODULE

CONFIGURATION 4

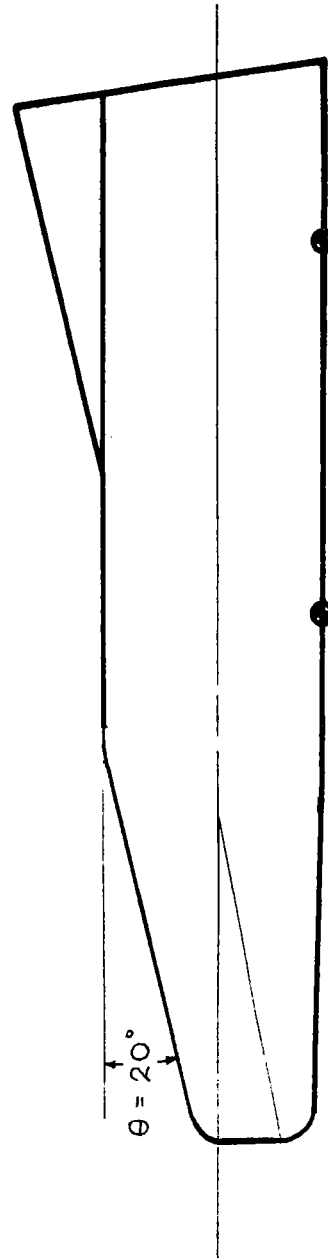
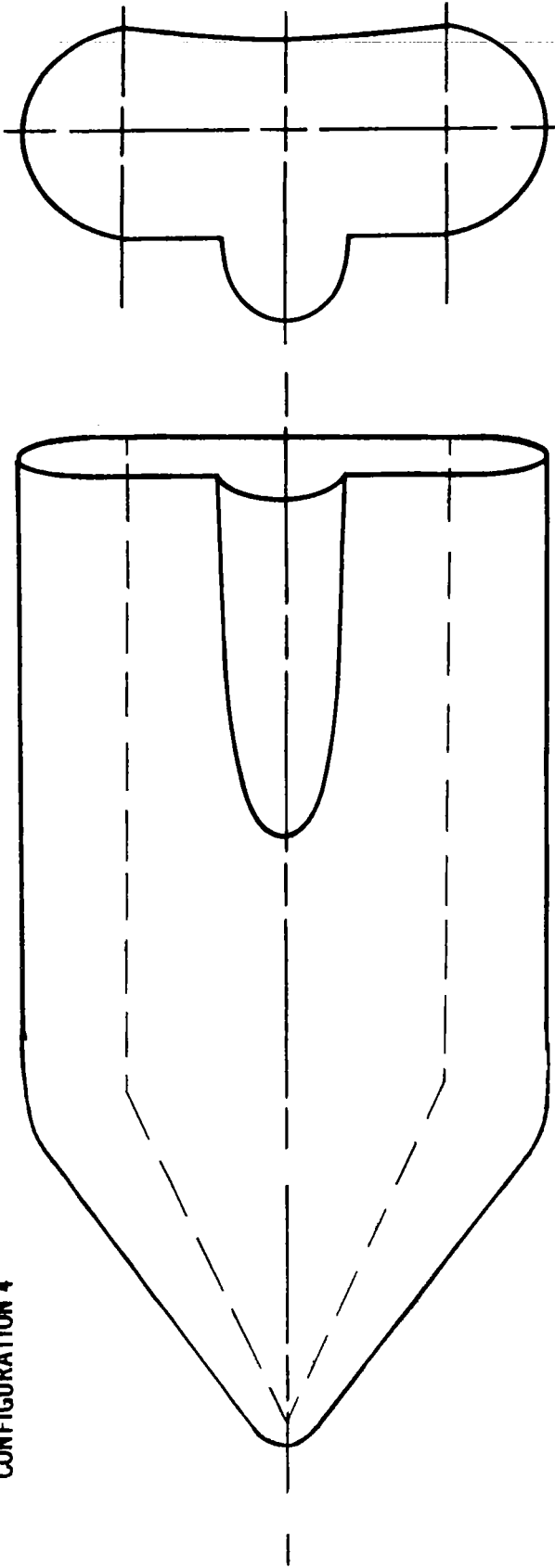


FIGURE 7 D

SATURN V/S-IVB  
AUXILIARY PROPULSION MODULE  
CONFIGURATION 5

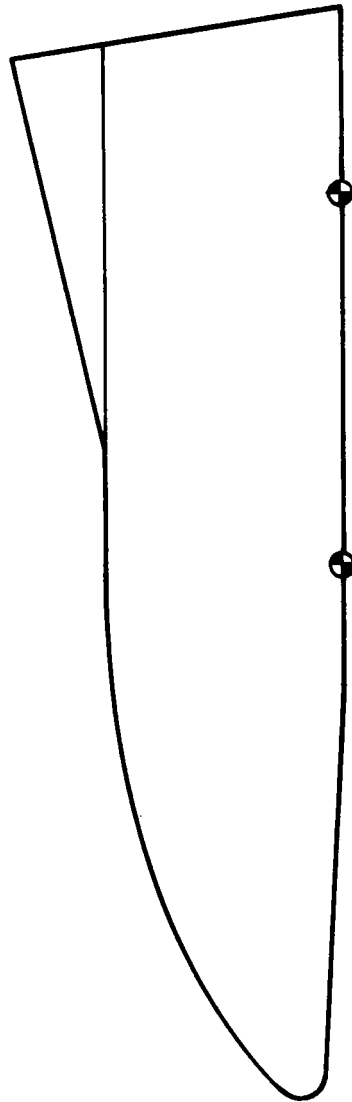
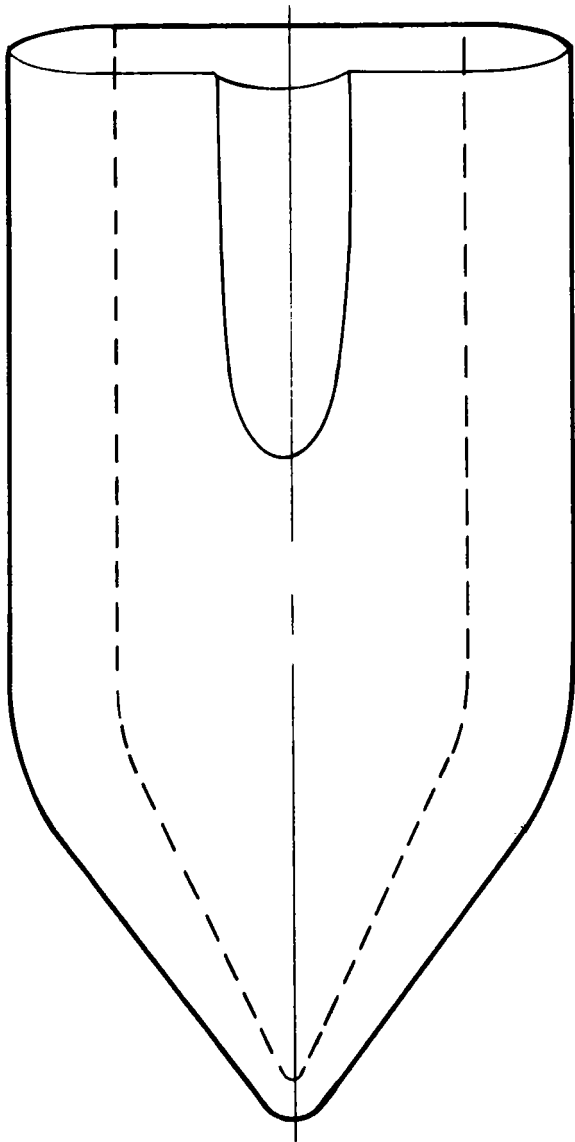
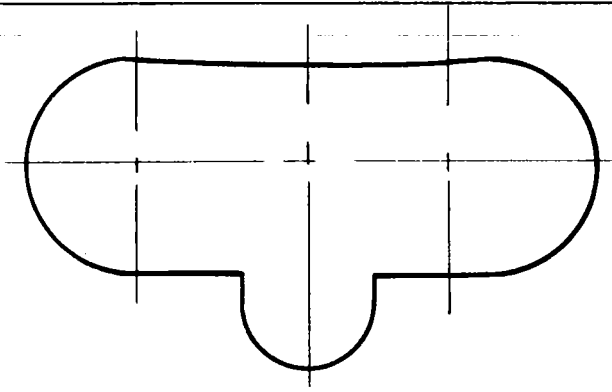


FIGURE 7 E

SATURN V/S-IVB  
AUXILIARY PROPULSION MODULE

CONFIGURATION 6

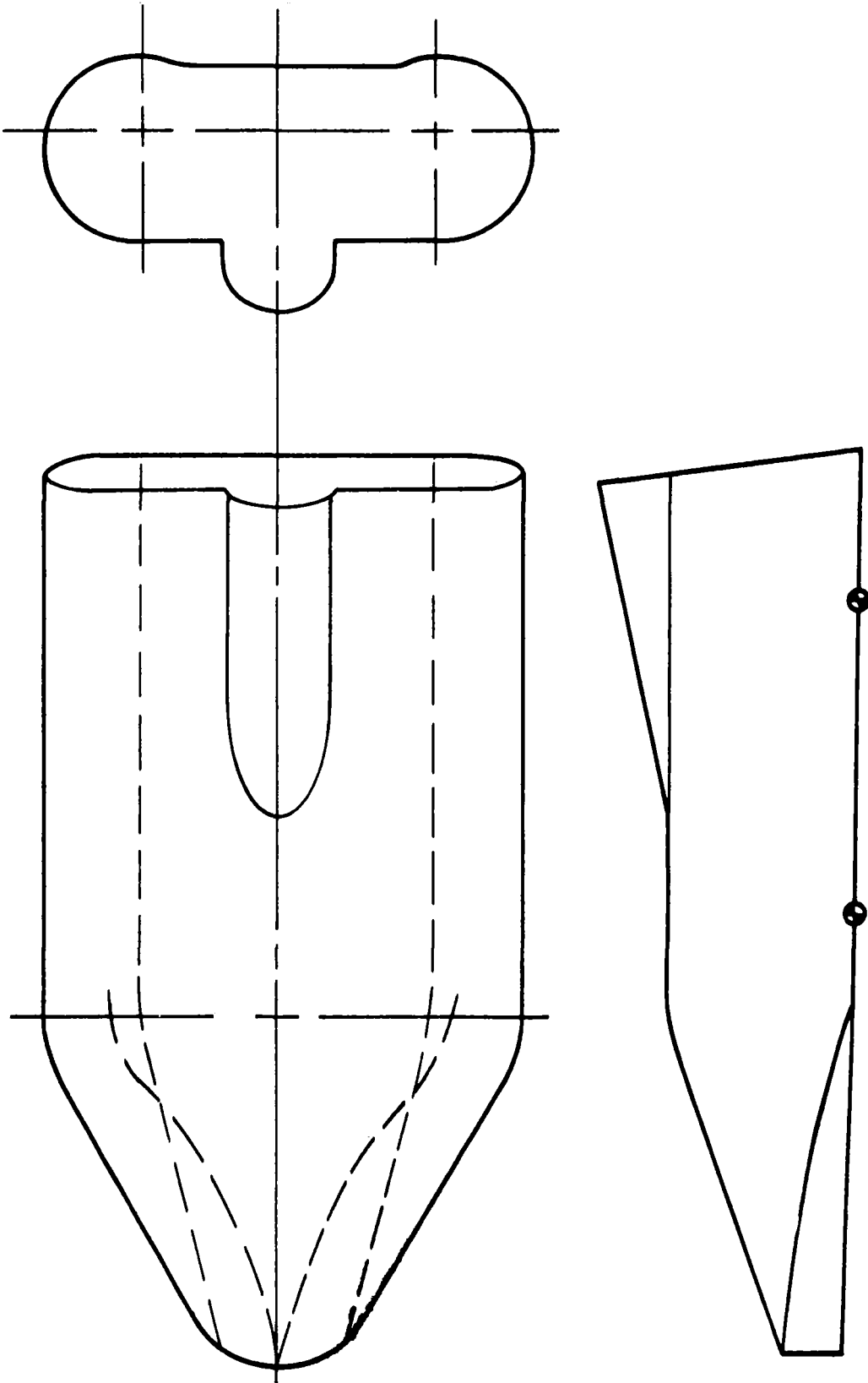


FIGURE 7 F

SATURN V/S-IVB  
AUXILIARY PROPULSION MODULE  
CONFIGURATION 7

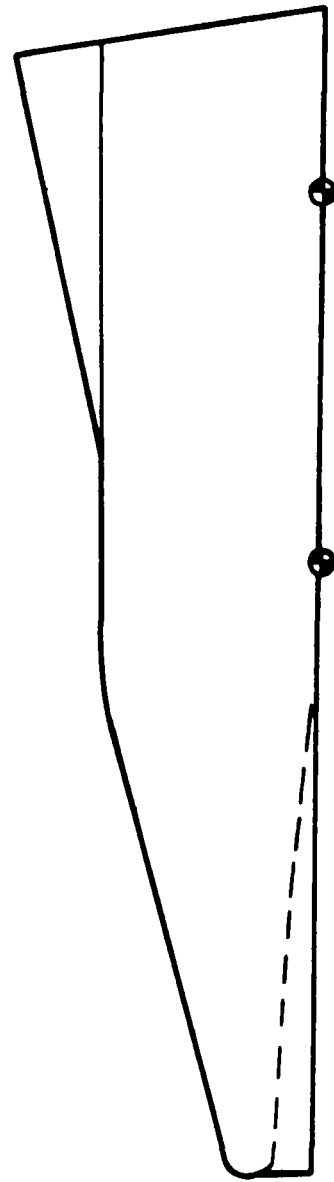
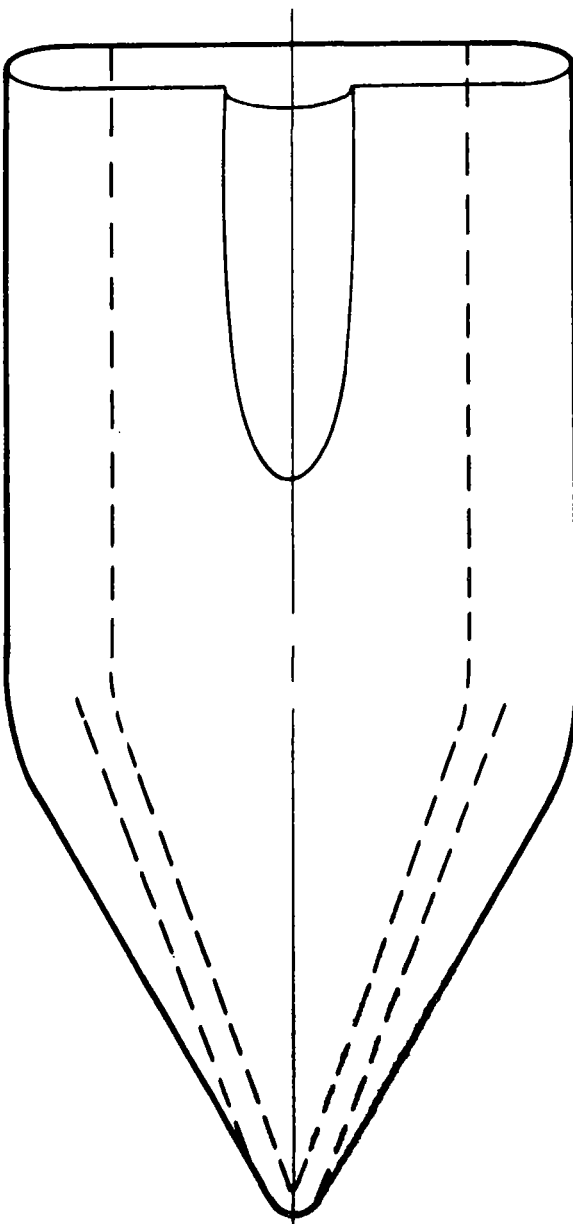
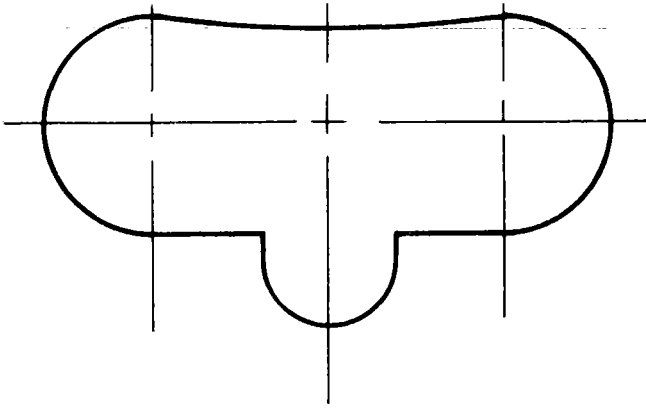


FIGURE 78

CONFIGURATION 8

SATURN V/S-IVB  
AUXILIARY PROPULSION MODULE

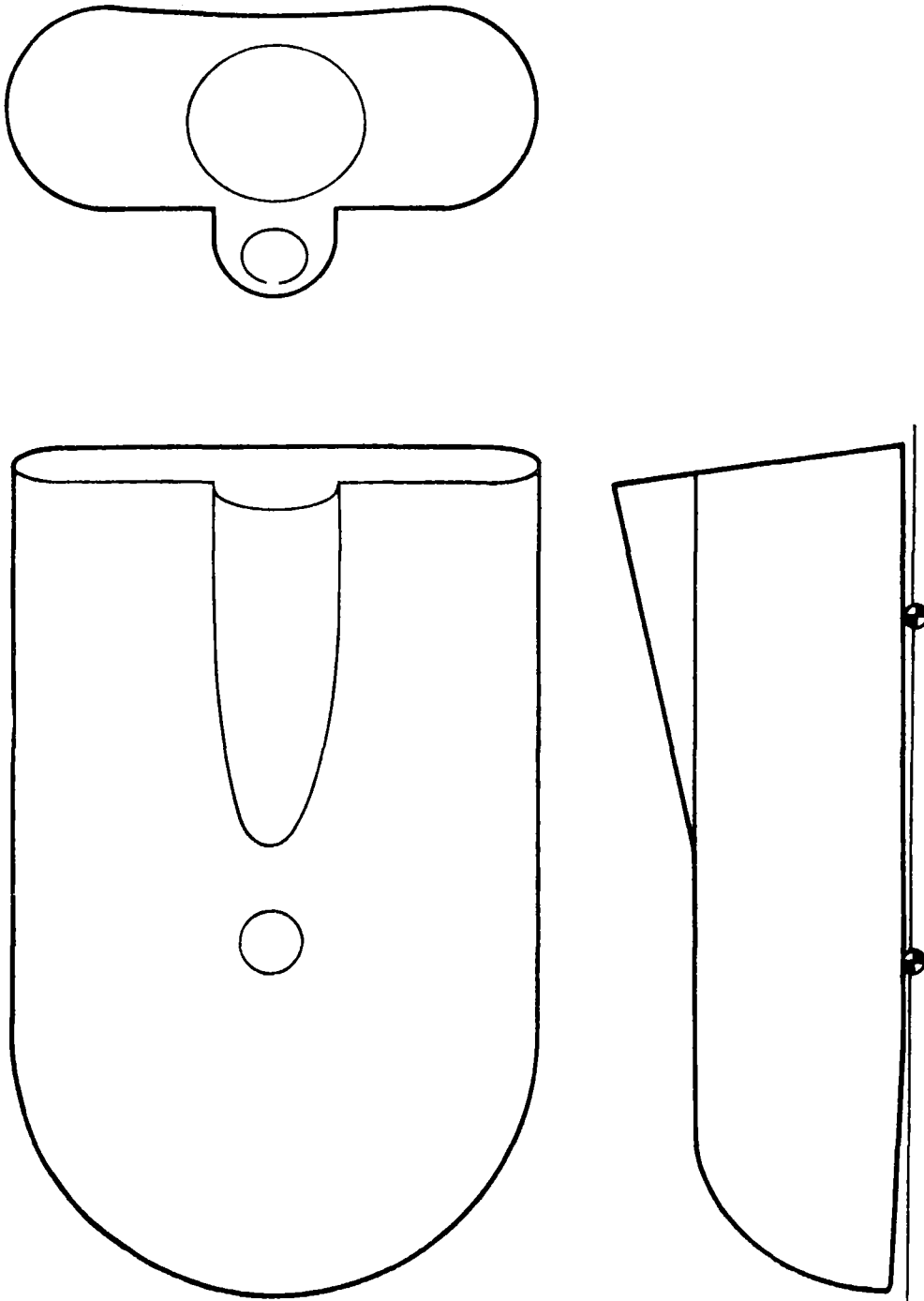


FIGURE 7H

SATURN V/S-IVB  
AUXILIARY PROPULSION MODULE

CONFIGURATION 9

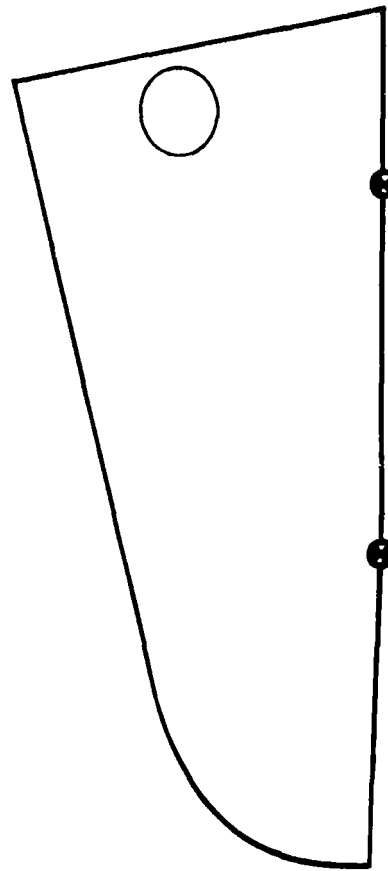
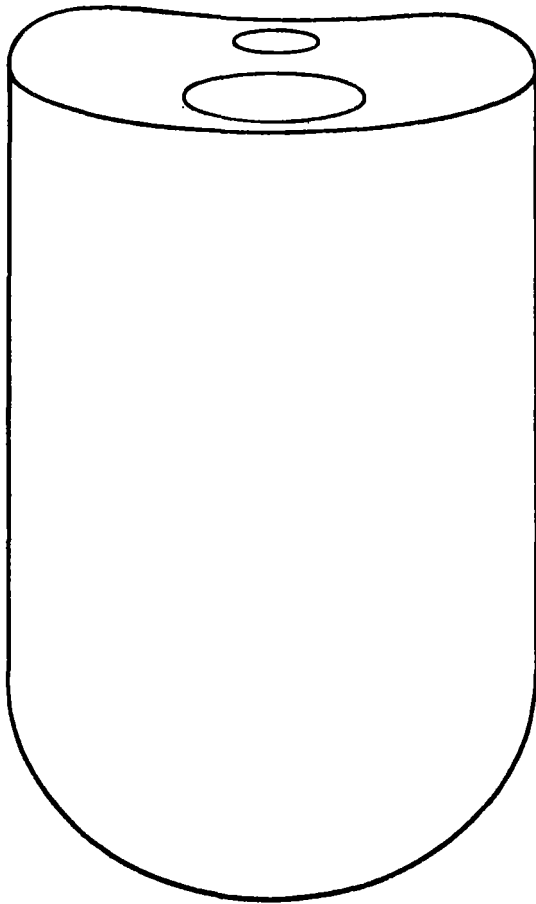
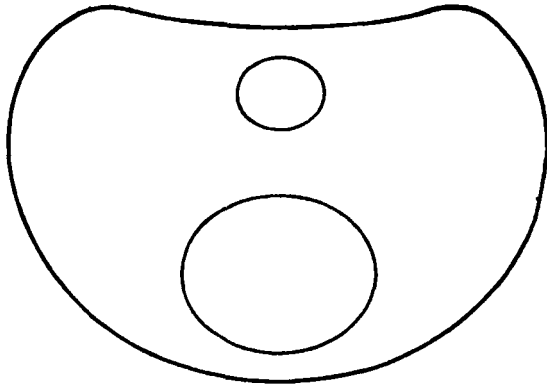


FIGURE 71

SATURN V/S-IVB  
AUXILIARY PROPULSION MODULE

CONFIGURATION 10

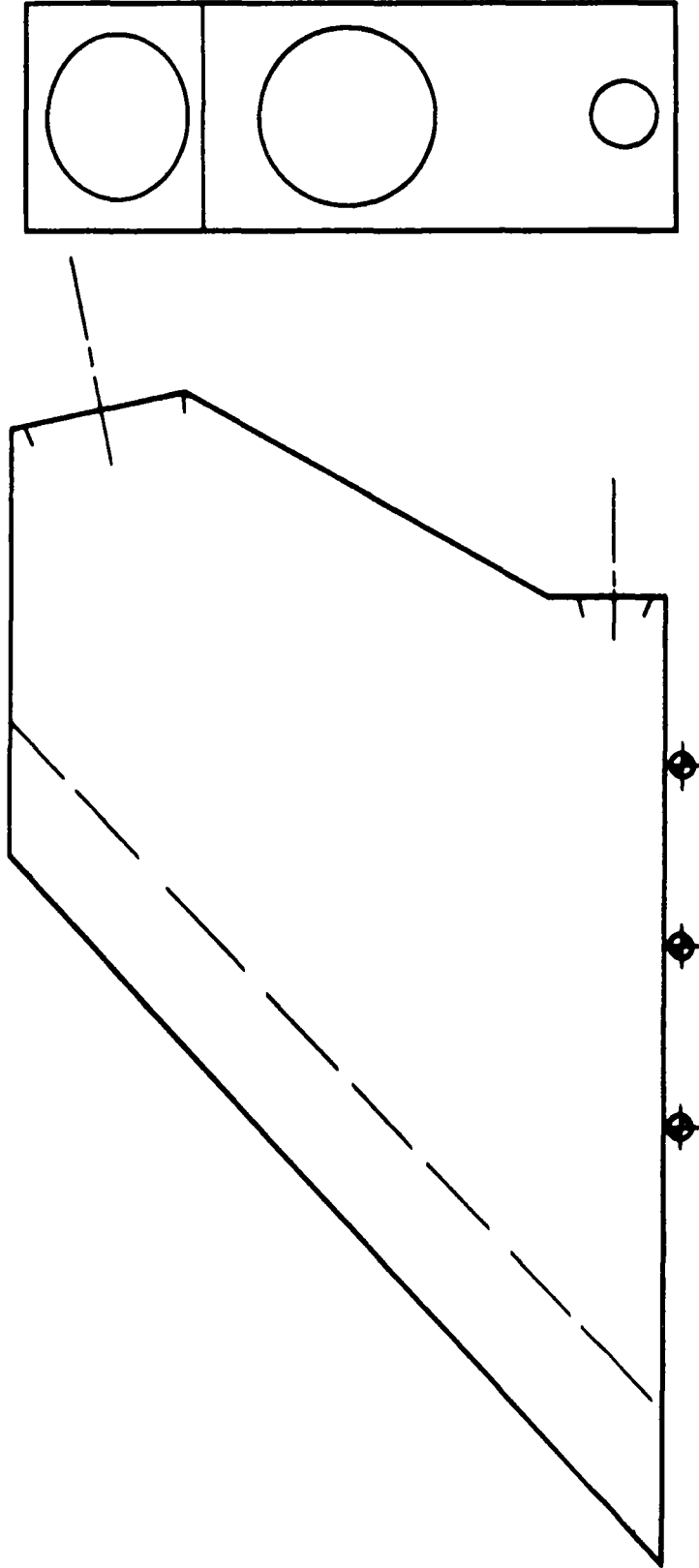
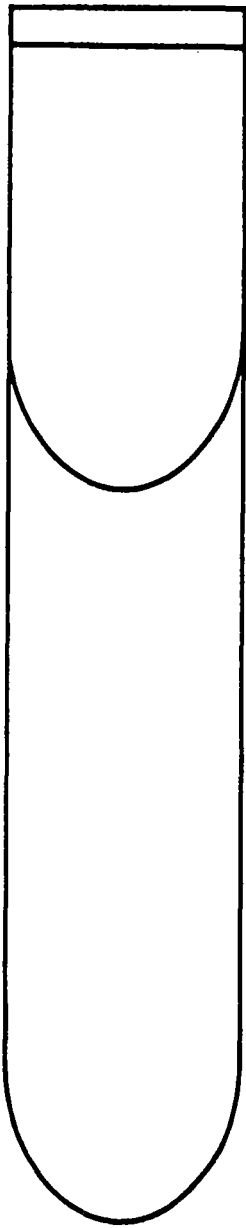
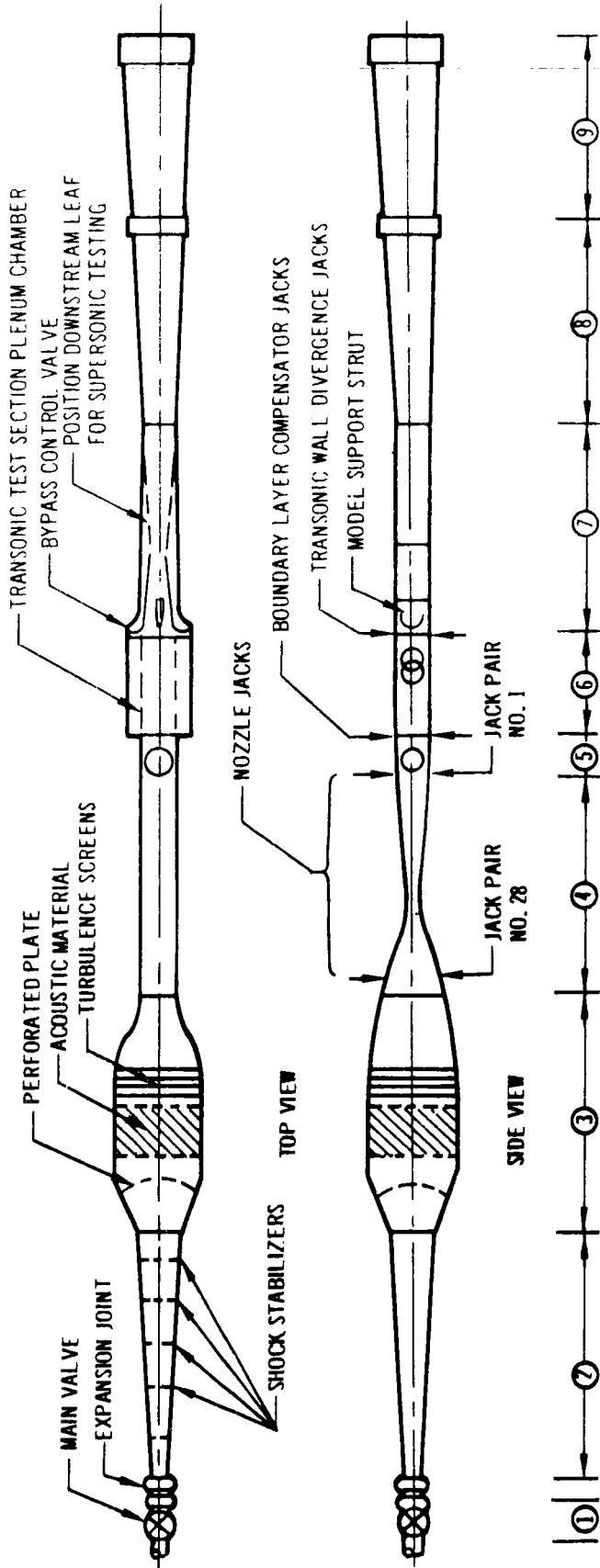


FIGURE 7J

# DAL TRISONIC FOUR-FOOT TUNNEL DESIGN FEATURES



- ① **CONTROL VALVE** VALVE REGULATED DURING RUN BY ELECTRO-MECHANICAL CONTROLLER TO MAINTAIN CONSTANT PRESSURE IN STILLING CHAMBER.
- ② **ENTRY DIFFUSER** ENTRANCE CONE 6° INCLUDED ANGLE; 4 SHOCK STABILIZER RINGS.
- ③ **STILL CHAMBER** DISHED 30% OPEN-PERFORATED PLATE; ACOUSTIC PANELS FOR 15-20 db ACOUSTIC ENERGY ATTENUATION; 4 TURBULENCE SCREENS.
- ④ **NOZZLE** 2-0.76" THICK FLEXIBLE PLATES, EACH CONTROLLED BY 28 JACKS; CONTOURS FOR MACH 1.0 TO 5.0.
- ⑤ **SUPERSONIC TEST SECTION** 60" LONG; 30" DIA. WINDOWS IN SIDEWALLS; 24" OPENINGS TOP AND BOTTOM; BOUNDARY LAYER COMPENSATION BY ADJUSTABLE DIVERGENCE ON TOP AND BOTTOM WALLS, +0.13° TO -0.5°
- ⑥ **TRANSONIC TEST SECTION** 144" LONG; 30" DIA. WINDOWS AT ONE OF TWO POSITIONS; 4 WALLS PERFORATED, 22% OPEN, HOLES NORMAL WALL. ADJUSTABLE DIVERGENCE ON TOP AND BOTTOM WALLS, +0.29° TO -2°. SECTION REMOVABLE AND DOWNSTREAM CIRCUIT MOVES UP.
- ⑦ **MODEL SUPPORT, BYPASS CONTROL VALVE & VARIABLE DIFFUSER** FULL HEIGHT VERTICAL STRUT WITH VERTICAL MOTION AND -19° TO +29° PITCH CAPABILITY, 8" MAXIMUM STRUT WIDTH. BYPASS VALVE CONTROLS MACH NUMBER. DOWNSTREAM LEAF OF VARIABLE DIFFUSER DISCONNECTED FROM UPSTREAM LEAF FOR TRANSONIC TESTING. VARIABLE THROAT ALLOWS EXTENDED RUN TIMES AT SUPERSONIC MACH NUMBERS.
- ⑧ **TELESCOPING DIFFUSER** TELESCOPES INTO FIXED DIFFUSER, RETRACTING MODEL SUPPORT-VARIABLE DIFFUSER, OPENING TUNNEL FOR MODEL INSTALLATION AND CHANGES.
- ⑨ **FIXED DIFFUSER** COMPLETES EXPANSION TO MUFFLER TOWER.

FIGURE 03

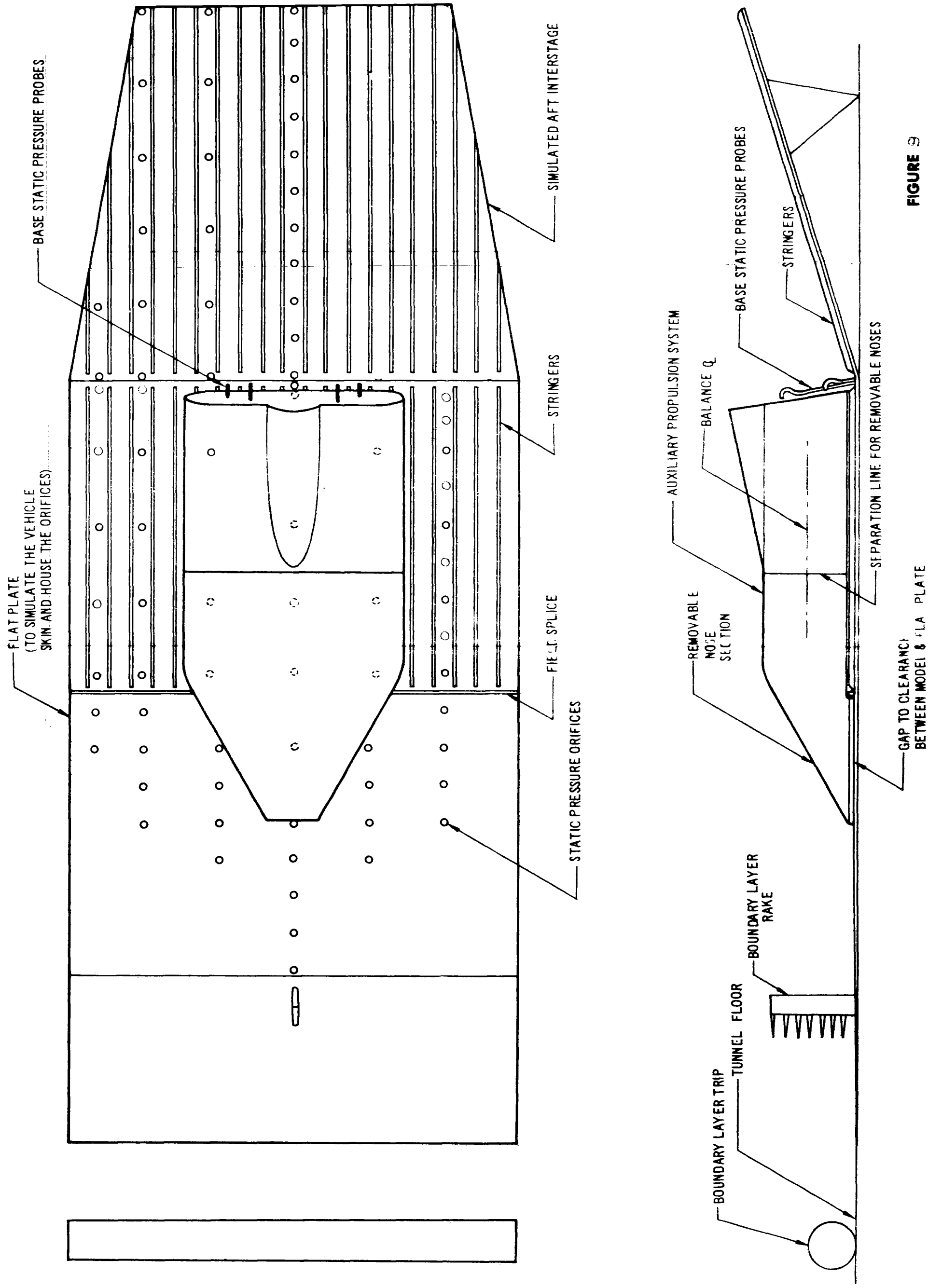


FIGURE 9

## Section 11

### SATURN-IB PROPELLANT RESERVE REQUIREMENT FOR A 105 NAUTICAL MILE CIRCULAR ORBIT MISSION

A study has been conducted to determine the propellant reserves required for the Saturn-IB vehicle, assuming a 72 degree launch azimuth from AMR to a 105 nautical mile circular orbit. The analysis was performed by statistically analyzing the magnitudes of three sigma variations of the nominal Saturn-IB stage and engine parameters and their effect on propellant requirements. The Saturn-IB consists of the S-IB as the boost stage, the S-IVB as the second stage, and the payload.

The maximum weight in orbit was determined for the Saturn-IB, assuming nominal weight and performance characteristics. Included in the gross weight in orbit is the payload, S-IVB structure, guidance equipment, and 2,973 pounds of contingency. Three sigma perturbations of the nominal characteristics were independently applied to determine their effect on propellant required to achieve orbit conditions.

The S-IVB stage is designed such that the guidance commands engine shutdown when velocity, altitude, and flight path direction, corresponding to the desired orbit, are achieved. This command occurs only if there is sufficient propellant available to reach these conditions. For a nominal vehicle, a small percentage of the propellant (reserves) is not used at engine shutdown. It is recognized, however, that on any actual vehicle the performance parameters will differ from their nominal values. These parameter deviations produce variations in the quantity of propellant required to achieve a set of shutdown trajectory conditions. It is possible for these variations to be of sufficient magnitude to cause propellant depletion before the required orbital conditions are reached. If the vehicle is required to achieve near maximum performance, such that the nominal propellant required approaches the amount of propellant loaded for combustion, the possibility of command shutdown not occurring becomes a significant design consideration. Deviations of the performance parameters about their nominal values occur randomly, therefore, the amount of propellant required to

achieve the mission must be statistically analyzed. Such an analysis has been applied to both stages to determine the S-IVB propellant reserve requirement. The equations used were developed by a statistical analysis of propellant utilization required (ratio of propellant weight required to propellant weight loaded.) The stage and engine three sigma deviations and their magnitudes affecting propellant reserves required are shown in table I. The values shown are derived from past experience and manufacturing tolerances and are believed to be reasonable estimates.

The necessary condition for command shutdown to occur is:

$$W_{P_r} < W_{P_a}$$

where

$W_{P_a}$  = Propellant available for combustion

$W_{P_r}$  = Propellant required to achieve vehicle shutdown conditions

The incremental propellant reserve required is defined:

$$\Delta W_{P_r} = \frac{(W_{P_{load}} - W_{P_{used}})}{W_{P_{load}}}$$

The propellant reserve required, is given by the following three sigma expression:

$$\begin{aligned} (3\sigma_{\Delta W_{P_r}})^2 &= \left(\frac{\partial W_{P_r}}{\partial F_1} 3\sigma_{F_1}\right)^2 + \left(\frac{\partial W_{P_r}}{\partial I_{SP_1}} 3\sigma_{I_{SP_1}}\right)^2 + \left(\frac{\partial W_{P_r}}{\partial W_{E_1}} 3\sigma_{W_{E_1}}\right)^2 \\ &+ \left(\frac{\partial W_{P_r}}{\partial W_{P_1}} 3\sigma_{W_{P_1}}\right)^2 + \left(\frac{\partial W_{P_r}}{\partial D} 3\sigma_D\right)^2 + \left(\frac{\partial W_{P_r}}{\partial P_{U,R_1}} 3\sigma_{P_{U,R_1}}\right)^2 \\ &+ \left(\frac{\partial W_{P_r}}{\partial Q_1} 3\sigma_{Q_1}\right)^2 + \left(\frac{\partial W_{P_r}}{\partial E_{R_1}} 3\sigma_{E_{R_1}}\right)^2 + \left(\frac{\partial W_{P_r}}{\partial E_{Q_1}} 3\sigma_{E_{Q_1}}\right)^2 \\ &+ \left(\frac{\partial W_{P_r}}{\partial E_{P_1}} 3\sigma_{E_{P_1}}\right)^2 + \left(\frac{\partial W_{P_r}}{\partial F_2} 3\sigma_{F_2}\right)^2 + \left(\frac{\partial W_{P_r}}{\partial I_{SP_2}} 3\sigma_{I_{SP_2}}\right)^2 \\ &+ \left(\frac{\partial W_{P_r}}{\partial W_{E_2}} 3\sigma_{W_{E_2}}\right)^2 + \left(\frac{\partial W_{P_r}}{\partial W_{P_2}} 3\sigma_{W_{P_2}}\right)^2 + \left(\frac{\partial W_{P_r}}{\partial E_{M,R}} 3\sigma_{E_{M,R}}\right)^2 \\ &+ \left(\frac{\partial W_{P_r}}{\partial P_{U,R_2}} 3\sigma_{P_{U,R_2}}\right)^2 \end{aligned}$$

where

$\Delta W_{P_r}$	=	Propellant Reserves Required
$\sigma$	=	Standard Deviation
$F_1$	=	S-IB Thrust
$I_{sp_1}$	=	S-IB Specific Impulse
$W_{E_1}$	=	S-IB Stage Weight
$W_{P_1}$	=	S-IB Propellant Loaded
D	=	Total Vehicle Drag
P.U. <sub>r<sub>1</sub></sub>	=	S-IB Propellant Utilization Residual
$Q_1$	=	S-IB Pitch Program Error
$E_{R_1}$	=	S-IB Yaw Gyro Drift
$E_{Q_1}$	=	S-IB Pitch Gyro Drift
$E_{P_1}$	=	S-IB Roll Gyro Drift
$F_2$	=	S-IVB Thrust
$I_{sp_2}$	=	S-IVB Specific Impulse
$W_{E_2}$	=	S-IVB Stage Weight
$W_{P_2}$	=	S-IVB Propellant Loaded
E.M.R.	=	S-IVB Engine Mixture Ratio
P.U. <sub>r<sub>2</sub></sub>	=	S-IVB Propellant Utilization Residual

All the quantities are expressed in percent of the nominal value.

Table II presents the change in propellant required for each three sigma variation of the stage and engine parameters, and the percentage of the nominal propellant burned. Obtaining the root-sum-square determines the three sigma deviation of propellant reserves required. The three sigma deviation is 0.900 percent, which is equivalent to 1,964 pounds of propellant reserves required. The value of propellant reserves required is within that available (2,973 pounds of contingency) for the nominal vehicle orbit weight.

TABLE I

ERROR SOURCES AFFECTING S-IVB PROPELLANT RESERVES REQUIRED

<u>SOURCE</u>	<u>THREE STANDARD DEVIATION</u>
<u>S-IB Stage</u>	
Thrust, $F_1$	2.0%/Engine . . . . 0.706%
Specific Impulse, $I_{sp1}$	1.5%/Engine . . . . 0.53%
Stage Weight, $W_{E1}$	2.5%
Propellant Loaded Weight, $W_{P1}$	0.5%
Vehicle Drag, D	10.0%
Propellant Utilization Residual, P.U. <sub>r1</sub>	5,000 lbs.
Pitch Program Error, $Q_1$	3.0%
Yaw Gyro Drift, $E_{R1}$	15°/hr.
Pitch Gyro Drift, $E_{Q1}$	15°/hr.
Roll Gyro Drift, $E_{P1}$	25°/hr.
<u>S-IVB Stage</u>	
Thrust, $F_2$	3.0%
Specific Impulse, $I_{sp2}$	1.0%
Stage Weight, $W_{E2}$	2.5%
Propellant Loaded Weight, $W_{P2}$	0.5%
Engine Mixture Ratio, E.M.R. (5.0:1)	2.0%
Propellant Utilization Residual, P.U. <sub>r2</sub>	0.25%

TABLE II

EFFECTS ON PROPELLANT RESERVES REQUIRED

<u>SOURCE (x)</u>	<u>PERTURBED EFFECT</u> (lbs/ $3\sigma_x$ )	$\frac{\Delta W_{P_r}}{3\sigma_x}$	$\frac{(3\sigma_x)(\text{PERTURBED EFFECT})}{W_{P_{\text{nominal}}}}$ (%)
<u>S-IB STAGE</u>			
Thrust	219 lb/ $3\sigma_x$		0.10038%
Specific Impulse	298 lb/ $3\sigma_x$		0.13659%
Stage Weight	250 lb/ $3\sigma_x$		0.11459%
Propellant Loaded Weight	125 lb/ $3\sigma_x$		0.05729%
Vehicle Drag	295 lb/ $3\sigma_x$		0.13521%
Propellant Utilization Residual	722 lb/ $3\sigma_x$ ←		0.33093%
Pitch Program Error	48 lb/ $3\sigma_x$		0.02200%
Yaw Gyro Drift	18 lb/ $3\sigma_x$		0.00820%
Pitch Gyro Drift	36 lb/ $3\sigma_x$		0.01650%
Roll Gyro Drift	18 lb/ $3\sigma_x$		0.00825%
<u>S-IVB STAGE</u>			
Thrust	650 lb/ $3\sigma_x$		0.29793%
Specific Impulse	844 lb/ $3\sigma_x$ ←		0.38685%
Stage Weight	539 lb/ $3\sigma_x$		0.24705%
Propellant Loaded Weight	1093 lb/ $3\sigma_x$ ←		0.50099%
Engine Mixture Ratio	336 lb/ $3\sigma_x$		0.15401%
Propellant Utilization Residual	545 lb/ $3\sigma_x$		0.24981%

$$(3\sigma_{\Delta W_{P_r}})^2 = \sum \left( \frac{\Delta W_{P_r} 3\sigma_x}{3\sigma_x} \right)^2$$

$3\sigma_{\Delta W_{P_r}} = 0.900\% = 1964$  pounds of propellant reserve required

## Section 12

### VENT CYCLE PERTURBATIONS TO EARTH WAITING ORBIT FOR APOLLO MISSION

#### SUMMARY

The error in the 100 nautical mile waiting orbit which gives maximum translunar trajectory errors are 9.1 ft/second in velocity, 1.2 n.mi. in altitude, and -0.04 degrees in flight path angle. These will result in a 1,825 nautical mile closest approach to the moon for a nominal 100 nautical mile closest approach transfer trajectory. If the closest approach is to be corrected to 100 nautical miles, at least one mid-course velocity correction will be required. If the venting perturbations are not known or are not relayed to the guidance computer, 34.4 ft/sec. of velocity will be required for the correction. But, since most of the perturbations to the waiting orbit will be known, and if they are relayed to the guidance computer, the maximum corrective velocity is of the order of 4 ft/sec.

It is possible to have no change in the waiting orbit velocity, altitude, and flight path angle if venting occurs perpendicular to the orbit plane. This can change the inclination 0.05 degree and will require no mid-course correction due to venting. The maximum auxiliary propellant required to orientate the vehicle is of the order of 100 pounds. If the Apollo vehicle is yawed only twice (entrance and exit from the waiting orbit), 20 pounds of auxiliary propellant would be required. But, since land sightings and star fixes are required, this constant attitude may not be feasible.

#### 1.0 INTRODUCTION

The basic lunar mission for the Apollo Saturn V configuration will utilize a preliminary low altitude earth waiting orbit prior to injection onto the translunar trajectory. At present, the waiting orbit has been fixed as circular at 100 nautical miles, offering a reasonable compromise between

payload considerations (which indicate the use of the lowest possible orbit) and orbit perturbations resulting from atmospheric drag. A waiting period of three complete orbits, or approximately 4.5 hours, is presently conceived.

Partial burning of the S-IVB stage propellants will place this stage and its Apollo-LEM payload into the circular parking orbit. During the boost exit, the S-IVB stage will experience external aerodynamic heating, and also, while in the waiting orbit, the stage will be heated by radiation from the earth-sun heat sources. Because the resulting pressure within the fuel tank will exceed the design load limitations, it will be necessary to relieve the tanks at several times during the waiting orbits. This will result in velocity additions to the circular orbit velocity and possible errors in the translunar transfer trajectory. The errors in the transfer trajectory result in not knowing the vent velocity vector. If the velocity addition is known and results in a correction in the guidance computer, no error in the trajectory will result due to venting. At the present, the acceleration level (0.001 g) associated with the venting velocity is too small to be determined by the present guidance system. But if an ephemeris is continuously computed and is relayed to the computer, no trajectory error will result due to venting. Currently, the astronauts in the Apollo vehicle will take two observations per orbit; consequently, many of the venting perturbations will be known.

It is the purpose of this study to determine the effects upon the translunar transfer trajectory due to venting in the waiting orbit. This results in observing the closest approach of the Apollo vehicle. Also considered in this study is an investigation into the mid-course correction required for a 100 nautical mile closest approach.

## 2.0 DISCUSSION

### 2.1 Fuel Tank Venting

The amount of fuel vented overboard in order to reduce the pressure within the fuel tank is dependent not only upon the thermal load transferred to the

fuel but also upon the utilization of the bulk heat capacity of liquid hydrogen. For this study the vehicle's longitudinal axis was assumed to be parallel to the velocity vector during the orbit. This resulted in a thermal load of 812,000 BTU. The bulk heat capacity of this fluid medium is in turn dependent upon the level of agitation of the liquid hydrogen within the fuel tank. Ullage rockets producing approximately 0.001 g will be used to settle the propellants prior to each pressure relief venting cycle. However, the uncertainty of the level of agitation throughout the venting cycle (because of lack of information regarding propellant behavior in a zero g environment) results in utilization of heat somewhere between complete agitation and complete stagnation. For the purpose of this analysis, the effects of both the complete stagnation and the total agitation cases will be investigated.

In order to realize a performance utilization from the vented propellant the venting orifices are designed to give a total average thrust of 220 pounds (for the vent relief valve pressure) oriented in the pitch plane parallel to the vehicle longitudinal axis. The accelerations produced by the venting nozzles are necessary to assure a reasonable level of propellant settling during the venting process.

Utilizing the heat input of approximately 812,000 BTU and a vent pressure cycle of 31-23 psia, indicates that 3 vents will be necessary for the case of complete agitation within the fuel tank, and 15 vents will be necessary to maintain the same pressure cycle when complete stagnation of the fuel is assumed. The propellant losses due to venting are approximately 3,305 pounds for the former case, and 3,808 in the latter case. The average vent duration for the three-vent cycles is 3 minutes at a frequency of approximately 80 minutes, while the duration for the 15-vent cycles is  $3/4$  of a minute at a frequency of 18 minutes.

## 2.2 Orbit Perturbations

Although somewhat unrealistic because the pressure within the fuel tanks is dropping during the vent cycle, producing a varying thrust history throughout the cycle, an average thrust of 110 pounds for each of the venting nozzles was

assumed and velocity increases due to venting computed on an impulse basis. The velocity increase after each of the three vents is approximately 4.81 <sup>sf</sup> feet per second and 1.1 <sup>sf</sup> feet per second after each of the 15 vents. A 30 second period of ullage for propellant settling prior to each vent provides an additional impulsive velocity of approximately 1.1 <sup>ullage</sup> feet per second. The total impulsive velocity gain after each of the three vents is approximately 5.91 <sup>sf</sup> feet per second and 2.2 <sup>sf</sup> feet per second after each of the 15 vents.

A two-body analysis was made to determine the orbital elements resulting from the venting cycle perturbations. For this purpose, the following mission profile was assumed:

- a. S-IC, S-II, and S-IVB to boost approximately 282,000 pounds into a 100 nautical mile parking orbit
- b. S-IVB, Apollo, and LEM remain in waiting orbit for a period of 4.5 hours (3 orbit passes)
- c. S-IVB reignited to inject Apollo and LEM onto 72 hour cis-lunar trajectory with a 100 nautical mile closest approach altitude at the moon.

The orbit prior to the venting perturbations was assumed to be circular at 100 nautical miles. The effects of the velocity additions attributed to each venting cycle were investigated in five vehicle orientations. The first two assumed a vehicle orientation tangential to the surface of the earth, one in the direction of the vehicle motion, and the other in opposition to the vehicle motion. Two additional cases oriented the vehicle along the radius vector from the central force field to the vehicle, one producing velocities outward from the center and the other toward the center of attraction. A fifth consideration was given to the vehicle oriented normal to the orbit plane of motion.

The variations from the nominal 100 nautical mile circular orbit parameters are presented in figures 1 through 4 as changes in the semi-major axes,  $\Delta a$ , changes in apogee altitudes,  $\Delta h_a$ , and eccentricity,  $e$ , of the perturbed orbit.

Changes in the initial conditions of altitude, velocity, and flight path angle at initiation of the next venting cycle are presented in tables I through III as variation above (+) and below (-) the nominal 100 nautical mile circular orbit conditions.

The change in the elements of the waiting orbit will probably be known up to a certain number of vents. This will then decrease the error in the unknown velocity, flight path angle, and altitude. It is possible to reduce the parking orbit inclination at those launch dates when the lunar orbit inclination is less than 28.5 degrees by venting normal to the parking orbit plane. If the vehicle is yawed so that it is perpendicular to the plane at entrance into the waiting orbit and yawed back at exit from the orbit, no midcourse velocity correction will be required due to venting. The amount of propellant required for the yaw maneuver is 20 pounds for the 3 and 15 vent cycles. It is not obvious that this method of reducing the effect of the venting perturbation is near optimum. Keeping the vehicle perpendicular to the waiting orbit may require many more maneuvers to accomplish navigation operations. Also, the heat input to the vehicle may be near maximum in the position.

### 2.3 Errors in Injection Parameters on Translunar Trajectory

To be able to determine the effect upon the translunar trajectory due to venting, a nominal trajectory must be generated. For this purpose a nominal, three-dimensional, 72 hour cislunar trajectory with a closest approach distance at the moon of 100 nautical miles was generated for a launch on January 12, 1967, at 18.4 GMT. This resulted in the following injection parameters:

Velocity	35,981.94 ft/sec.
Altitude	600,000.0 ft.
Flight Path Angle	7.98772 deg.
Azimuth	118.3 deg.
Latitude	-5.7 deg.
Longitude	169.7 deg. E

Perturbation trajectories at the injection point using the parameters defining the initial injection conditions were generated to indicate their effects upon the distance of closest approach at the moon. The perturbative effects of errors in the parameters upon the altitude of closest approach at the moon are presented in figures 5 through 11. It may be best to determine the effects of velocity at 100 nautical miles from the surface of the moon instead of the effect of distance itself, since maneuvers near the moon will depend mainly upon the velocity.

Although the Apollo vehicle will make up to three midcourse corrections on the translunar trajectory, this study considered only one correction. A time of 2 hours after injection was chosen to apply the midcourse correction in order to place the vehicle on a trajectory with a closest approach altitude at the moon of 100 nautical miles. Perturbations to the dynamical and position parameters at 2 hours after injection on the nominal trajectory were investigated to yield their partial effects on errors in closest approach altitude. The propagation of errors from the dynamical and position parameter perturbations at injection were determined for the 2 hour point on the perturbed trajectories. The perturbations from the nominal conditions at 2 hours resulting from perturbations in the injection parameters were determined from the trajectories utilized to generate the errors in lunar altitude due to the individual injection errors. These injection errors are the unknown errors and not the total error from a circular waiting orbit.

The partial effect of an error in velocity on the nominal trajectory at 2 hours was used with the total error in altitude resulting from the error in an injection parameter to determine an approximate correction (colinear to the velocity vector) to the velocity at the 2 hour point on the perturbed trajectory. A hunting procedure internal to the 3-D trajectory program was used to determine the actual velocity correction (colinear) required for a closest approach altitude of 100 nautical miles at the moon.

The effect of changing the flight path angle at 2 hours after injection to correct perturbations from the nominal trajectory at the 2 hour point resulting from errors in the various injection parameters was investigated for purposes of comparison with the midcourse colinear velocity corrections. The magnitude of the perturbed velocity at 2 hours was not changed while a change in the

flight path angle only was effected by the velocity change. It was found that a saving in velocity occurred for colinear velocity additions. As a result of perturbations in injection conditions, an error in the arrival time at the closest approach point to the moon will be experienced. Although the variations in the closest approach altitude due to injection parameter errors can be eliminated with velocity corrections in the plane of motion at some midcourse point, some errors will still exist in the time of arrival.

## .0 RESULTS

If rejection from the parking orbit occurs at 4.5 hours after injection and there is no knowledge of the waiting orbit errors, the largest perturbations in the translunar trajectory are observed for initial errors (table I for tangential velocity perturbation) are approximately  $\pm 9.1$  feet per second in velocity,  $\pm 1.2$  nautical miles in altitude, and  $\pm 0.04$  degree in flight path angle. Assuming that these errors are preserved throughout the burn phase of injection onto the translunar trajectory, an error of closest approach altitude of approximately  $\pm 1,725$  nautical miles will result. Again using the corrections for velocity perturbations in the same direction as the perturbed velocity at the 2 hour point in the translunar trajectory the necessary midcourse correction will be approximately  $34$  feet per second. The 15 vent cycle perturbation for a tangential vehicle orientation results in an error from the 100 nautical mile closest approach altitude of approximately 1,660 nautical miles from the desired altitude. A midcourse correction (colinear velocity addition) at 2 hours of approximately 27 feet per second is required to correct the perturbed trajectory for the errors presented in table III.

If the errors in the waiting orbit elements are known, and are relayed to the guidance computer, a reduction in midcourse velocity will result. At the present, the astronauts in the Apollo capsule will make two ephemerides per orbit revolution. This will reduce the unknown error in velocity, altitude, and flight path angle. If the perturbations due to the last and the next to the last vent are not known, the maximum velocity required for midcourse correction (colinear velocity addition) is of the order of 4 ft/second.

If the vehicle is oriented so that ullage and venting thrust is normal to the waiting orbit, essentially no change in waiting orbit velocity, altitude, and flight path angle will exist. This will result in zero error in the initial conditions for the translunar transfer trajectory. The inclination of the waiting orbit can be decreased by 0.005 degree, but approximately 100 pounds of propellant would be required. If the vehicle is yawed only twice (entrance and exit from the waiting orbit) only 20 pounds of propellant would be required. This would result in no change in inclination; but since land sightings and star fixes are required, this constant attitude may not be feasible.

The transfer time is changed due to errors in the waiting orbit. But for the maximum perturbation in the waiting orbit, the transfer time is increased approximately 6 hours. This may result in some serious problems in communication and lunar landing, but the error can be decreased by using more than one mid-course correction.

TABLE I  
WAITING ORBIT PERTURBATIONS  
COMPLETE AGITATION  
RADIAL AND TANGENTIAL VELOCITY ADDITIONS

LH <sub>2</sub> STATE	VENT NUMBER	VENT THRUST DIRECTION	CHANGE IN INITIAL CONDITIONS FROM CIRCULAR ORBIT AT NEXT PERTURBATION		
			$\Delta V$ (FT./SEC)	$\Delta H$ (FEET)	$\Delta \delta$ (DEG.)
COMPLETE AGITATION	1	TANGENTIAL	5.6	220	-0.00553
	2	"	3.1	7249	-0.0404
	3	"	9.1	7154	-0.0399
COMPLETE AGITATION	1	(-) TANGENTIAL	-5.7	-206	0.0053
	2	"	-3.6	-6920	0.0397
	3	"	-9.7	-6832	0.0393
COMPLETE AGITATION	1	RADIAL	1.1	-1023	0.0129
	2	"	8.9	-7529	0.0170
	3	"	8.8	-7461	0.0303
COMPLETE AGITATION	1	(-) RADIAL	-1.3	1017	-0.0129
	2	"	-9.0	7525	-0.0170
	3	"	-8.9	7458	-0.0303
COMPLETE AGITATION	1	NORMAL TO PLANE	0	0	0
	2	OF MOTION	0	0	0
	3		0	0	0

NOTE: VENT NUMBER DESIGNATES PERTURBATION  
JUST BEFORE NEXT VENT

TABLE II  
WAITING ORBIT PERTURBATIONS  
TOTAL STAGNATION  
RADIAL VELOCITY ADDITION

LH <sub>2</sub> STATE	VENT THRUST DIRECTION	VENT NUMBER	CHANGE IN INITIAL CONDITIONS FROM CIRCULAR ORBIT AT NEXT PERTURB.		
			$\Delta V$ (FT/SEC)	$\Delta h$ (FEET)	$\Delta \delta$ (DEGREES)
TOTAL STAGNATION	RADIAL	1	-2.0	1612	0.00235
		2	-3.7	3062	-0.00206
		3	-2.0	1649	-0.00742
		4	1.2	-1043	-0.00424
		5	-0.2	117	0.00283
		6	-3.5	2899	0.000252
		7	-3.9	2364	-0.0068
		8	0.3	-340	-0.00652
		9	0.2	-685	0.0004
		10	-1.9	1540	0.00379
		11	-4.4	3609	0.000160
		12	-4.0	3297	-0.00638
		13	-0.7	537	-0.0088
		14	0.0	-53	0.00416
		15	0.0	-52	0.00722
TOTAL STAGNATION	(-) RADIAL	1	1.9	-1608	0.00234
		2	3.6	-3059	0.00206
		3	1.9	-1649	0.00742
		4	-1.3	1041	0.00425
		5	0.1	-118	-0.00282
		6	3.4	-2896	-0.00025
		7	2.8	-2361	0.00681
		8	-0.4	339	0.00651
		9	-0.8	682	0.00040
		10	1.8	-1542	-0.00379
		11	4.3	-3605	-0.00015
		12	3.9	-3290	0.00638
		13	0.6	-532	0.00878
		14	-0.1	56	0.00414
		15	-0.1	54	0.0074

NOTE : VENT NUMBER DESIGNATES PERTURBATION JUST BEFORE NEXT VENT

TABLE III  
WAITING ORBIT PERTURBATIONS  
TOTAL STAGNATION  
TANGENTIAL VELOCITY ADDITION

LH <sub>2</sub> STATE	VENT THRUST DIRECTION	VENT NUMBER	CHANGE IN INITIAL CONDITIONS FROM CIRCULAR ORBIT AT NEXT PERTURB.		
			$\Delta v$ (FT/SEC)	$\Delta h$ (FEET)	$\Delta \delta$ (DEGREES)
TOTAL STAGNATION	TANGENTIAL	1	- 0.2	1908	0.00858
		2	- 6.3	8883	0.00163
		3	- 13.2	17,579	0.00883
		4	- 12.6	17,889	-0.00551
		5	- 8.5	16,239	0.00578
		6	- 12.9	21,806	0.0153
		7	- 21.4	30,790	0.01265
		8	- 23.4	34,318	0.00166
		9	- 19.4	32,815	- 0.00369
		10	- 18.5	33,868	0.0080
		11	- 23.8	40,194	0.0191
		12	- 31.8	48,800	0.0178
		13	- 36.3	54,432	0.00324
		14	- 34.4	54,672	0.0000344
		15	- 32.2	54,672	0.00004
TOTAL STAGNATION	(-)TANGENTIAL	1	0.1	- 1906	- 0.00856
		2	6.2	- 8885	- 0.01630
		3	13.3	- 16,573	- 0.00876
		4	12.5	- 17,840	0.00558
		5	8.3	- 16,197	- 0.00066
		6	12.9	- 21,828	- 0.01547
		7	21.3	- 30,789	- 0.01249
		8	23.2	- 33,169	0.00194
		9	19.2	- 32,613	0.00359
		10	18.4	- 33,789	- 0.00839
		11	23.9	- 40,261	- 0.01928
		12	32.9	- 48,824	- 0.01732
		13	36.1	- 53,144	- 0.00245
		14	34.1	- 54,279	0.00062
		15	31.9	- 54,277	0.00061

NOTE: VENT NUMBER DESIGNATES PERTURBATION JUST BEFORE NEXT VENT

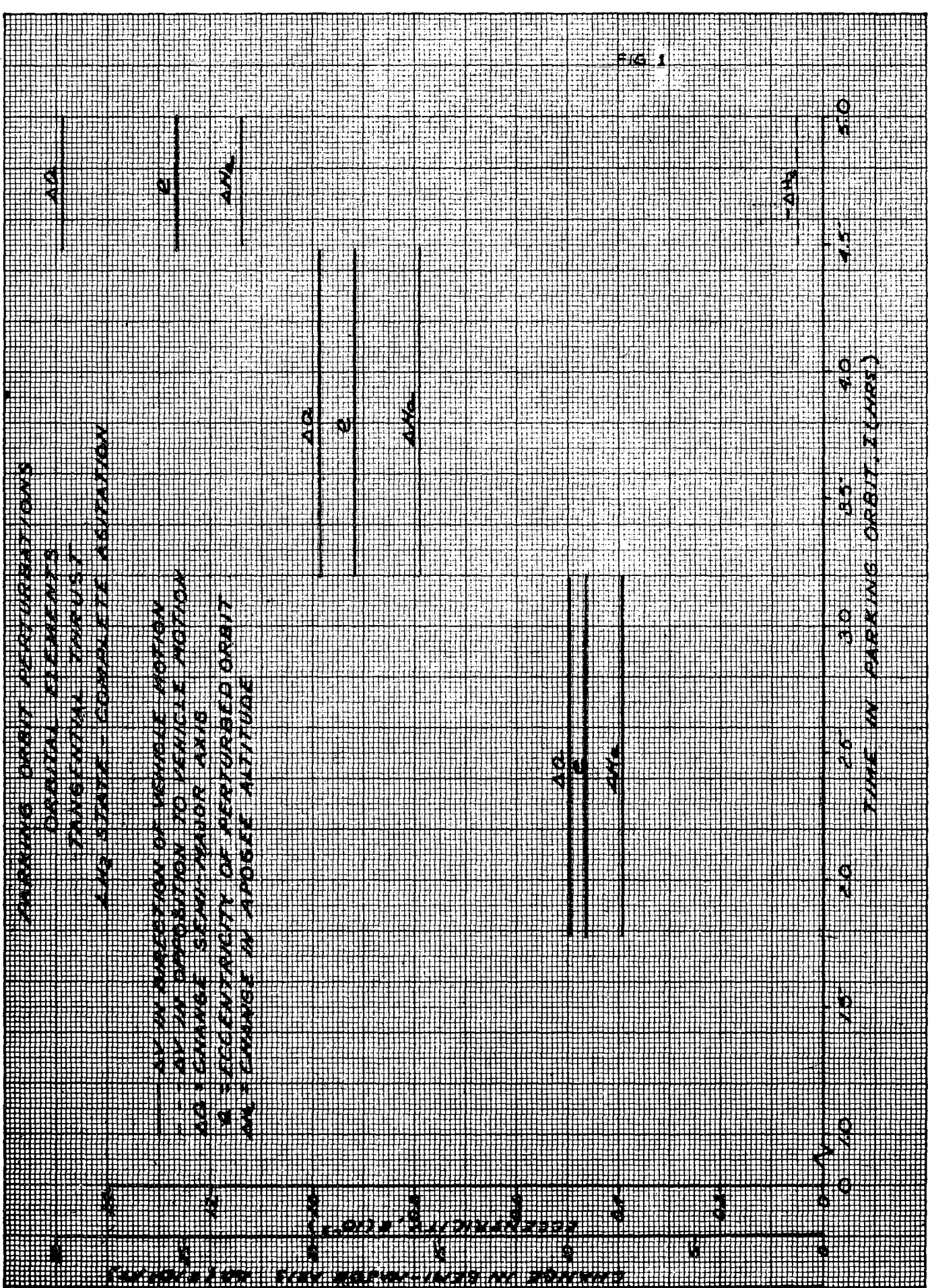
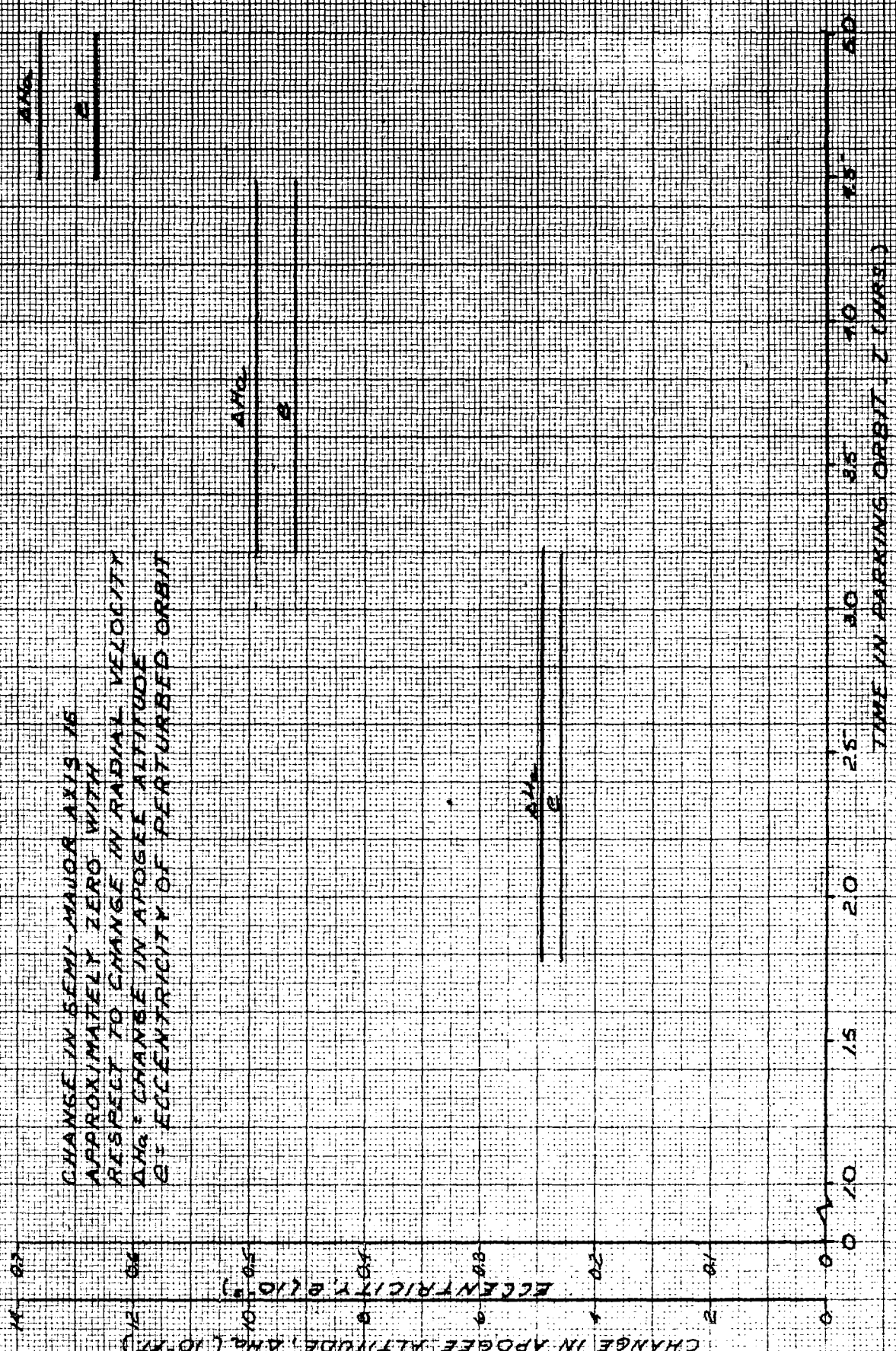


FIG. 1

PARKING ORBIT VENTING PERTURBATIONS  
 ORBITAL ELEMENTS  
 RADIAL THRUST  
 1/2 STATE - COMPLETE AGITATION



CHANGE IN SEMI-MAJOR AXIS IS  
 APPROXIMATELY ZERO WITH  
 RESPECT TO CHANGE IN RADIAL VELOCITY  
 $\Delta A_0$  = CHANGE IN APOGEE ALTITUDE  
 $E_0$  = ECCENTRICITY OF PERTURBED ORBIT

FIG. 2

# PARKING ORBIT VENTING PERTURBATIONS

ORBITAL ELEMENTS

TANGENTIAL THRUST

LP, STATE TOTAL STAGNATION

AV IN DIRECTION OF VEHICLE MOTION

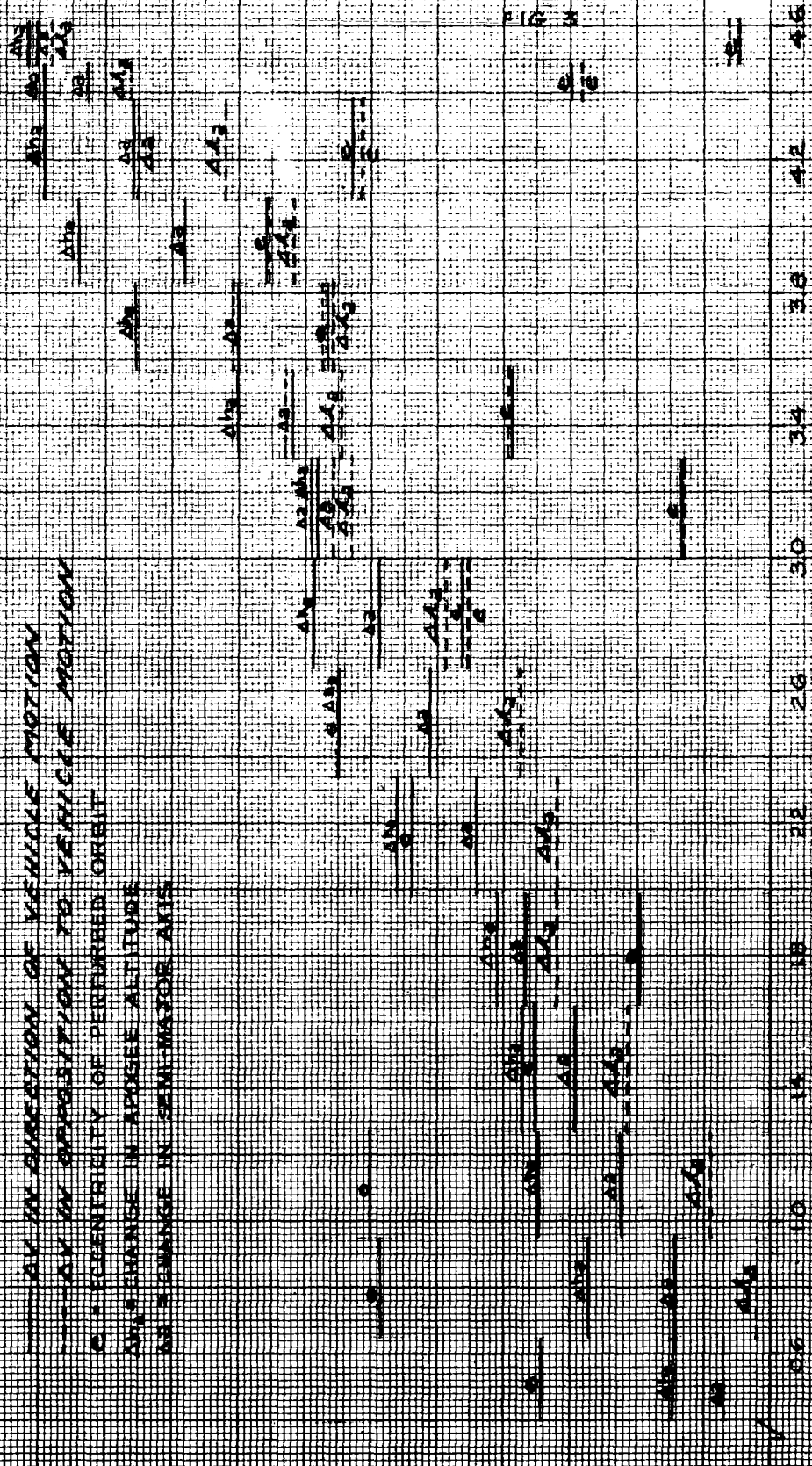
AV IN OPPOSITION TO VEHICLE MOTION

CELESTRIETY OF PERFORMED ORBIT

APL CHANGE IN APSEEE ALTITUDE

AS CHANGE IN SEMI-MAJOR AXIS

CHANGE IN SEMI-MAJOR AXIS AND APSEEE ALTITUDE  
 CELESTRIETY OF PERFORMED ORBIT  
 AV IN OPPOSITION TO VEHICLE MOTION  
 AV IN DIRECTION OF VEHICLE MOTION  
 TANGENTIAL THRUST  
 ORBITAL ELEMENTS  
 LP, STATE TOTAL STAGNATION  
 TIME IN PARKING ORBIT 1 (HOURS)



PARKING ORBIT VENTING PERTURBATIONS  
ORBITAL ELEMENTS

RADIAL THRUST VENTING  
LP STATE - TOTAL STAGNATION

CHANGE IN SEMI-MAJOR AXIS IS APPROXIMATELY

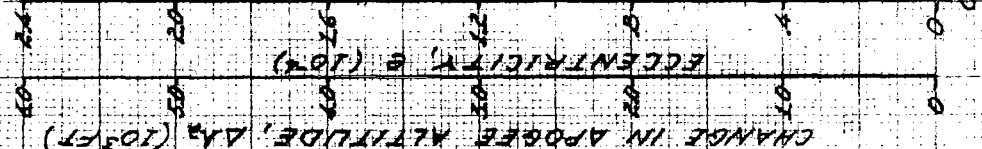
ZERO WITH RESPECT TO CHANGE IN RADIAL VELOCITY.

$e$  = ECCENTRICITY OF PERTURBED ORBIT

$\Delta A_2$  = CHANGE IN APOGEE ALTITUDE

---  $\Delta v$  IN DIRECTION OF VEHICLE MOTION

---  $\Delta v$  IN OPPOSITION TO VEHICLE MOTION



# SATURN 5

## LUNAR ORBIT SENSITIVITIES

### VARIATION IN ALTITUDE OF CLOSEST APPROACH TO INJECTION VELOCITY

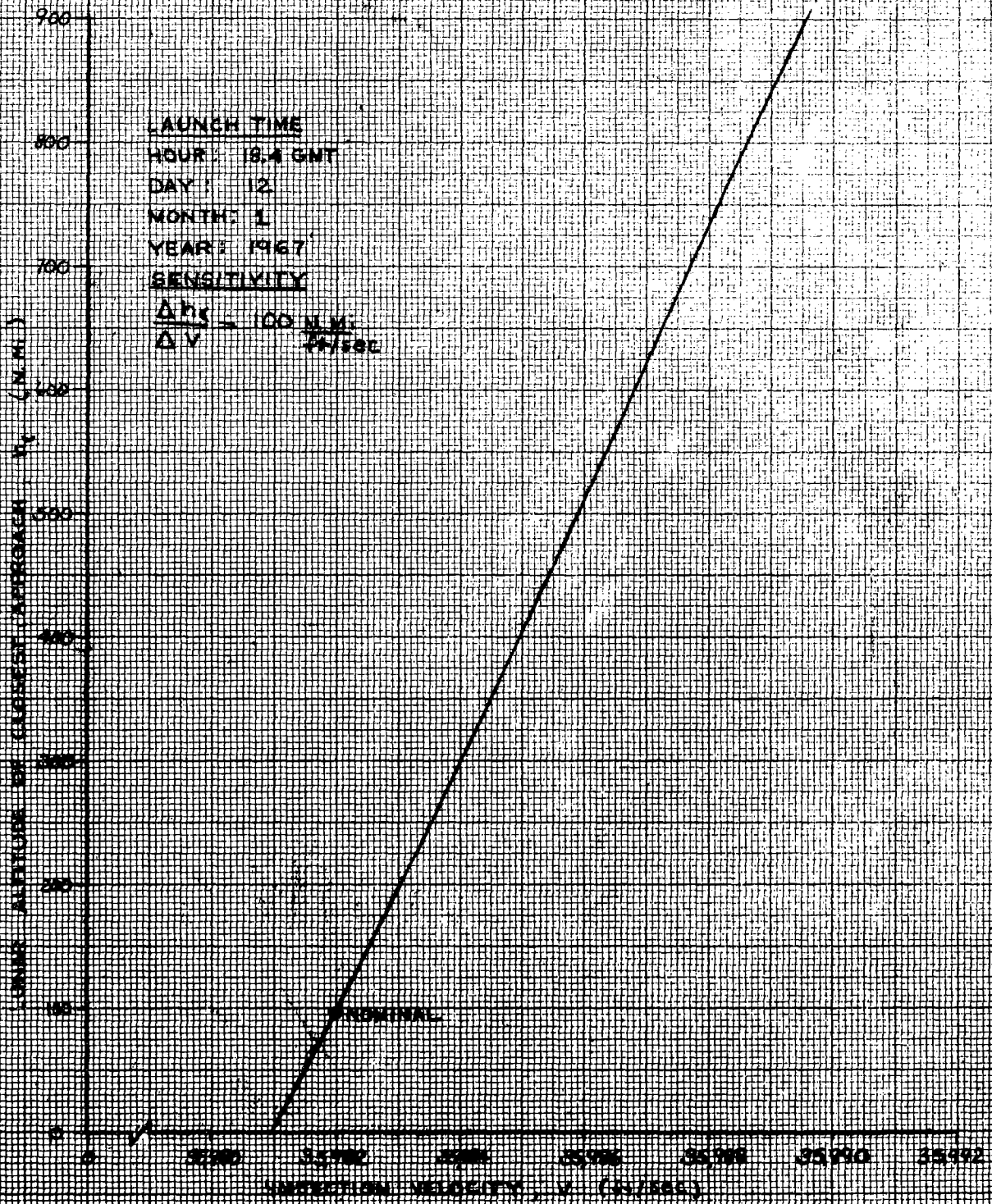
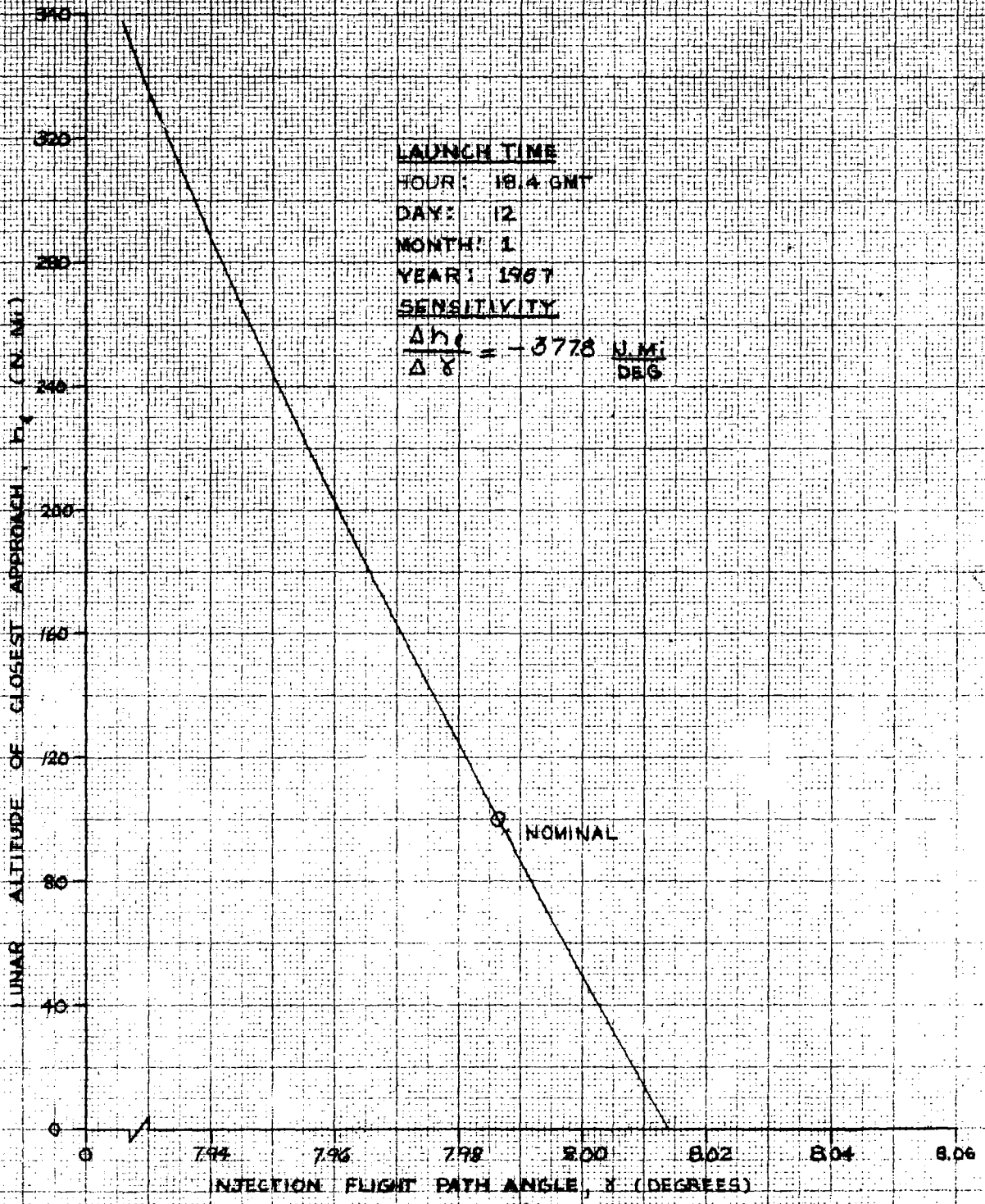
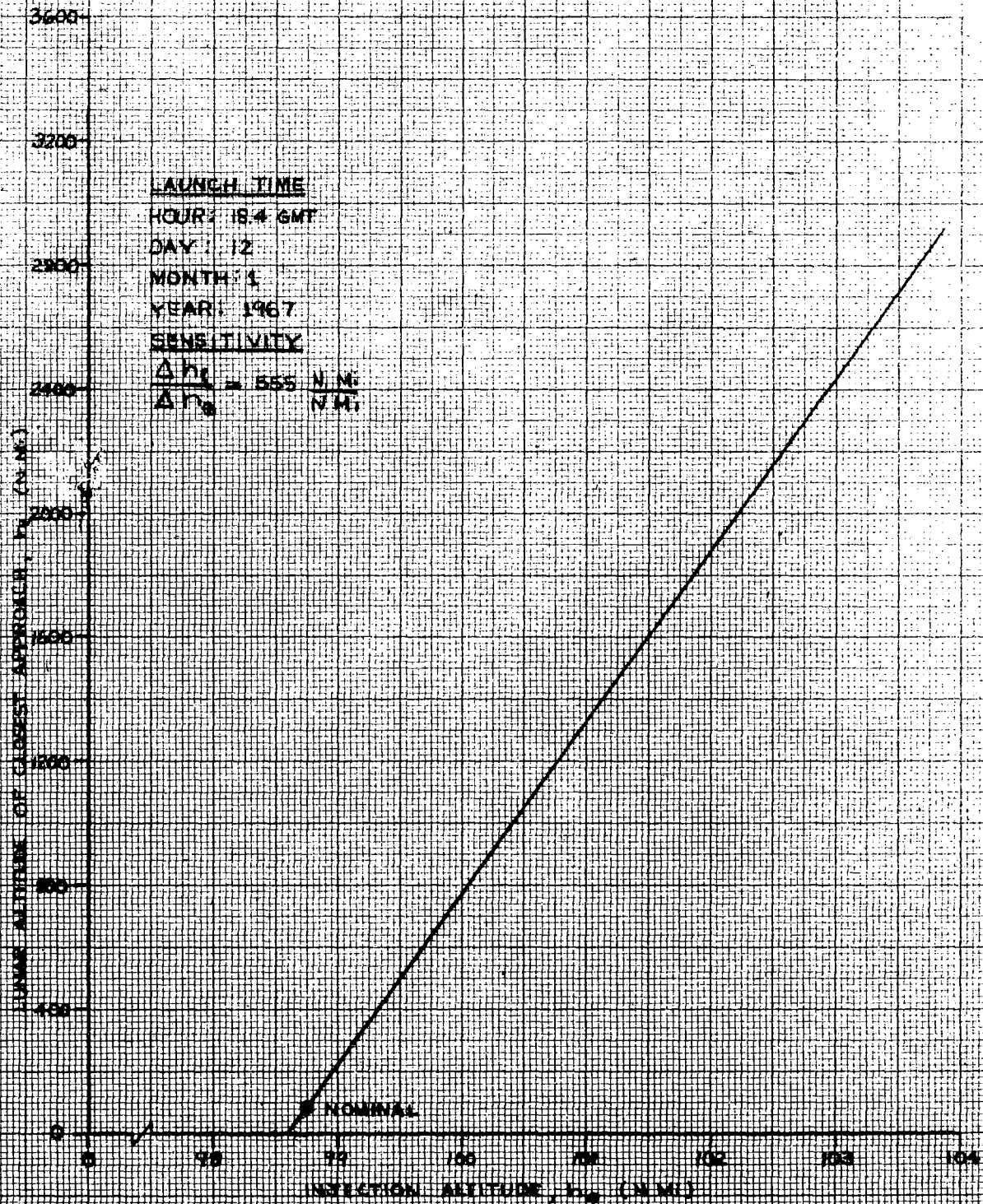


FIG 10

**SATURN 5**  
**LUNAR ORBIT SENSITIVITIES**  
**VARIATION IN ALTITUDE OF CLOSEST**  
**APPROACH TO INJECTION FLIGHT**  
**PATH ANGLE**

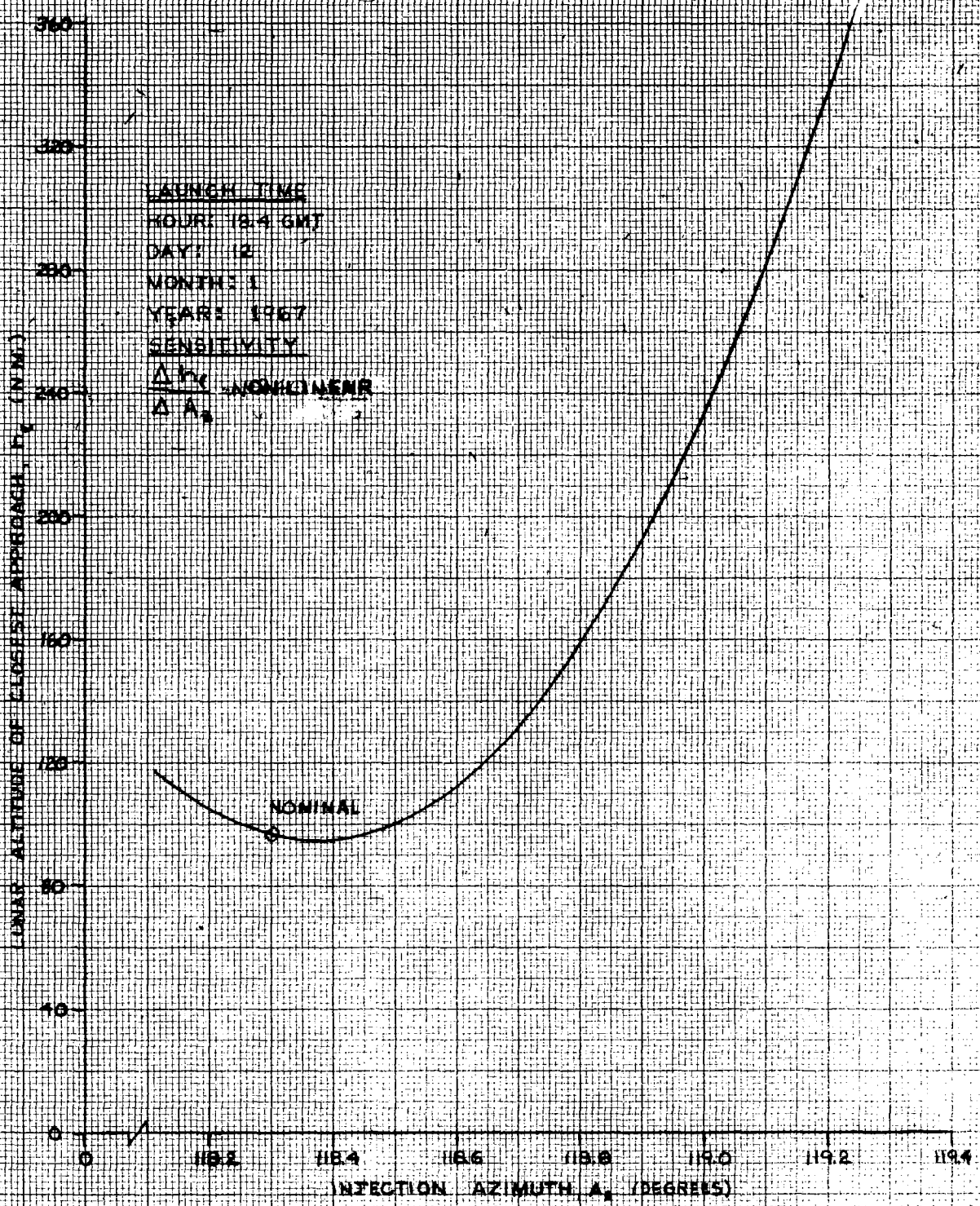


**SATURN 5**  
**LUNAR ORBIT SENSITIVITIES**  
**VARIATION IN ALTITUDE OF CLOSEST**  
**APPROACH TO INJECTION ALTITUDE**



### SATURN 13

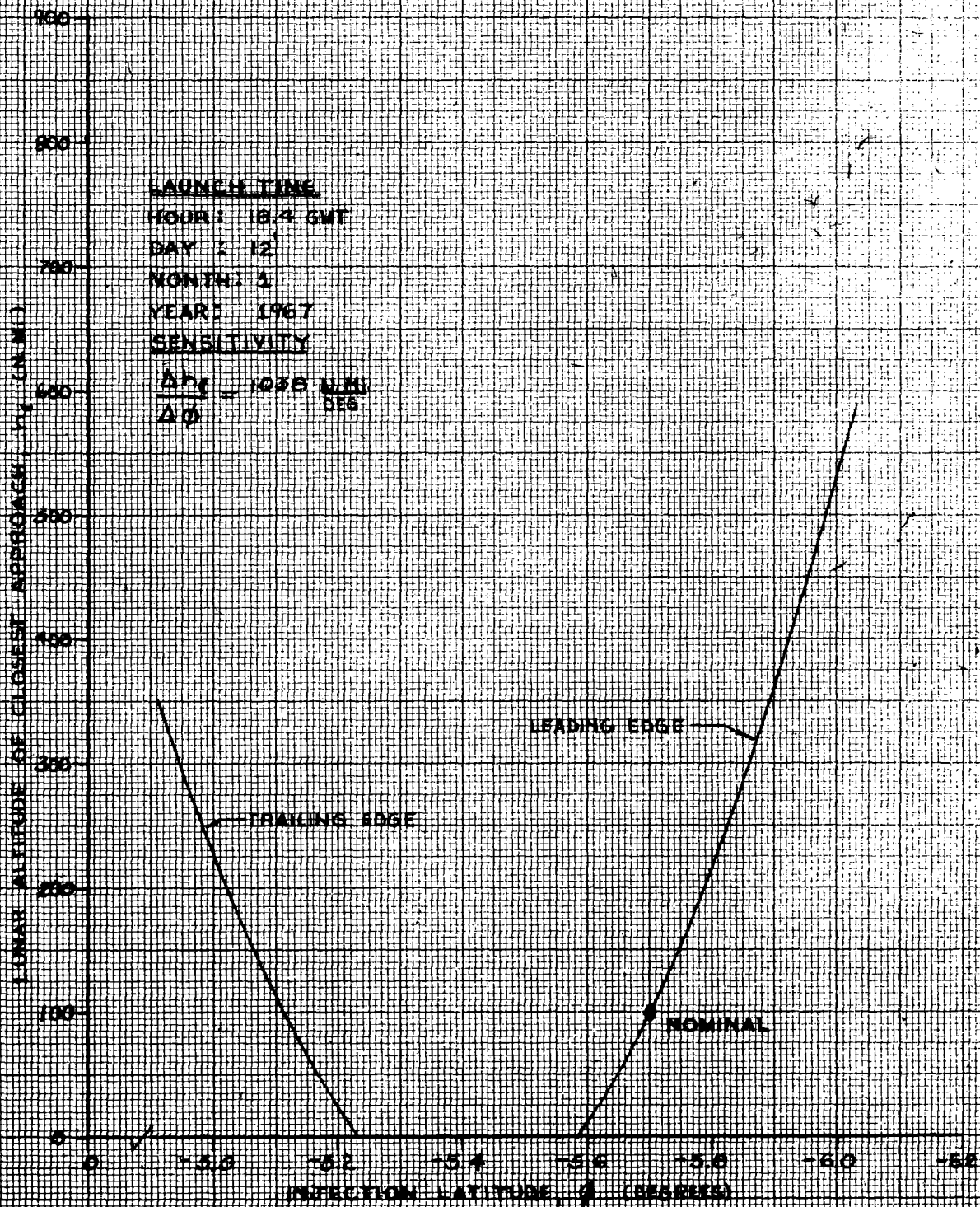
LUNAR ORBIT SENSITIVITIES  
VARIATION IN ALTITUDE OF CLOSEST  
APPROACH TO INJECTION AZIMUTH



# SATURN C-5

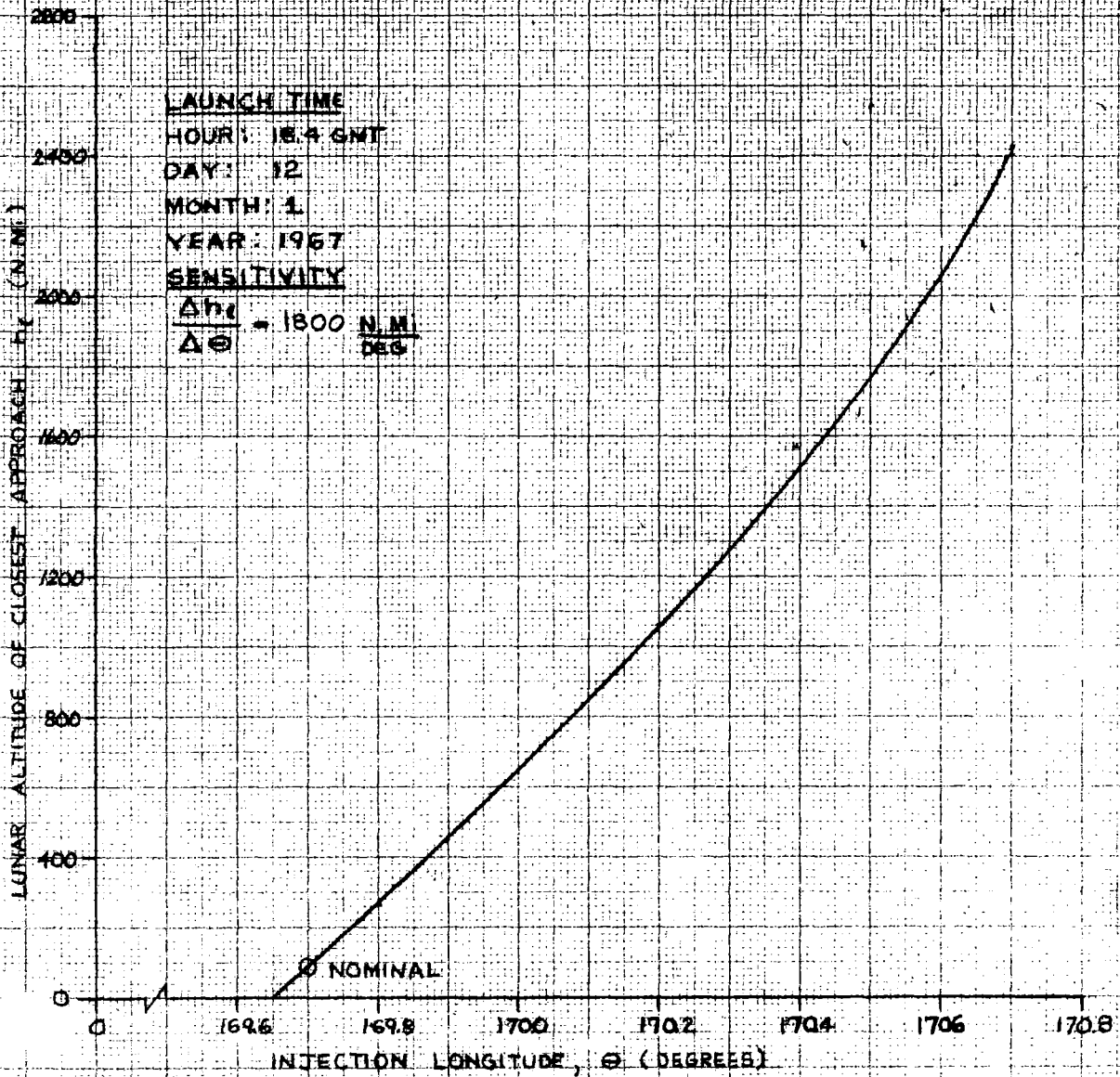
## LUNAR ORBIT SENSITIVITIES

### VARIATION IN ALTITUDE OF CLOSEST APPROACH TO INJECTION LATITUDE

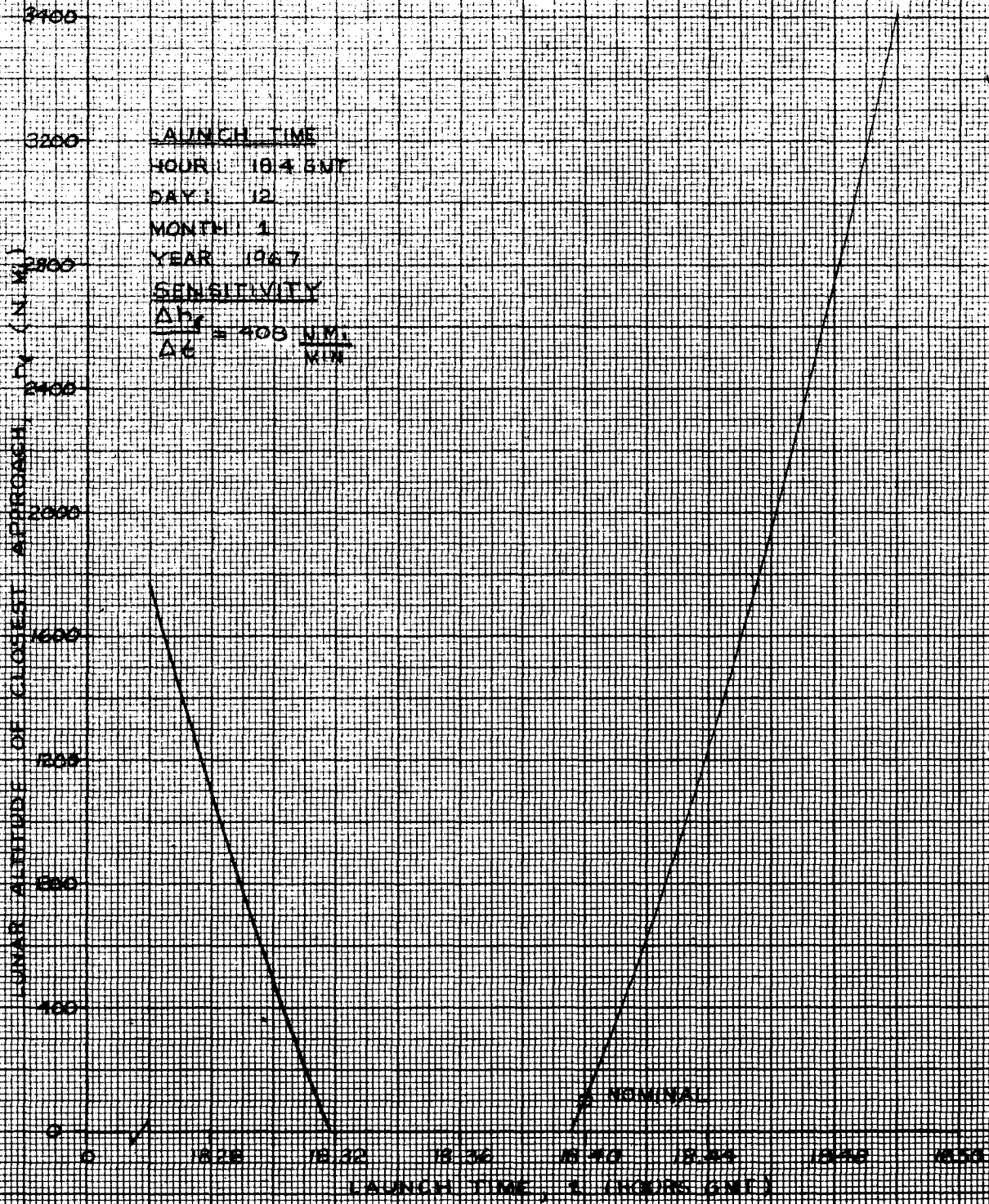


# SATURN 2B

## LUNAR ORBIT SENSITIVITIES VARIATION IN ALTITUDE OF CLOSEST APPROACH TO INJECTION LONGITUDE



SATURN - 5  
LUNAR ORBIT SENSITIVITIES  
VARIATION IN ALTITUDE OF CLOSEST  
APPROACH TO LAUNCH TIME



## Section 13

### INFLIGHT VENTING OF THE S-IVB/S-II INTERSTAGE

#### INTRODUCTION

At the Mechanical Design Integration Working Group Splinter Meeting, 27 March 1963, the interstage venting design criteria was established. The vent system will have 160 square inches of vent area and will be located as far aft as practical on the S-IVB interstage. The maximum allowable leak area on the S-IVB aft skirt and S-II forward skirt will be 15 and 30 square inches respectively. The S-IVB aft skirt and interstage will be designed to withstand an internal pressure of free stream ambient. S&ID agreed to improve the strength of the S-II forward skirt to allow a 5 psi pressure differential, internal greater than external.

#### DISCUSSION

Interstage internal pressures are being established using a mathematical model computed upon an IBM 7090 computer. The analysis is based on an energy balance approach and includes the following effects: heat transfer, multiple mass outlets, multiple mass inputs, variation of discharge coefficient with pressure ratio, varying gas mixtures and a check valve system.

A recapitulation of the data presented at the Mechanical Design Integration Working Group Splinter Meeting, 27 March 1963, is presented in figures 1 through 4. The only heat transfer effect considered was heat transfer from the interstage skin to the internal gas mixture. The multiple mass outlets considered were: a design vent area at point 3 (see figure 1) plus leak areas at points 2 and 4 singularly and in various combinations. Nominal liftoff conditions have been established as follows:

Initial Temperature	400°R - 520°R
Initial Pressure (max)	14.9 psi
Volume	14,100 ft <sup>3</sup> - 14,500 ft <sup>3</sup>
Initial Mass Fraction of Helium	0.05708
Initial mass Fraction of Nitrogen	0.94292

The initial conditions were combined to give maximum and minimum pressure during boost. The lower temperature and higher volume results in a maximum pressure in the interstage, while the combination of high temperature and low volume results in minimum internal pressure.

The design point, difference between ambient pressure and maximum value at point 2, was established by figure 2 to be approximately 70 seconds. Figure 3 presents the effects of leak area and initial conditions upon the internal pressure at the design point. The ordinate is the pressure increase above point 4. The data presented for leak area at point 4 include the initial condition combination that results in a minimum internal pressure while the data for leak area at point 2 are for the maximum internal pressure combination.

Maximum leak areas at point 2 and 4 were established at 15 square inches and 30 square inches, respectively. Figure 4 presents time histories of internal pressure for the design vent area of 160 square inches. The shaded region in figure 4 represents the region bounded by the maximum and minimum internal pressure time histories due to variations in initial conditions and external pressure variations due to angle of attack.

#### CONCLUSIONS

At the present time the computer program is being revised to facilitate its operation and use. The mass outlet capacity of the program is being expanded from three mass outlets to five mass outlets.

The present program does not consider the effect of external cross-flow velocity on the orifice discharge coefficient. This effect may be appreciable for conditions of high external velocity and pressure ratios close to 1.0, external pressure to internal pressure. The effect of external cross-flow on discharge coefficient will be included in the revised program.

The external pressure history is also being revised and will be included in the revised program. A discussion of the external pressure history is given in a later section.

DEFINITION OF POINTS

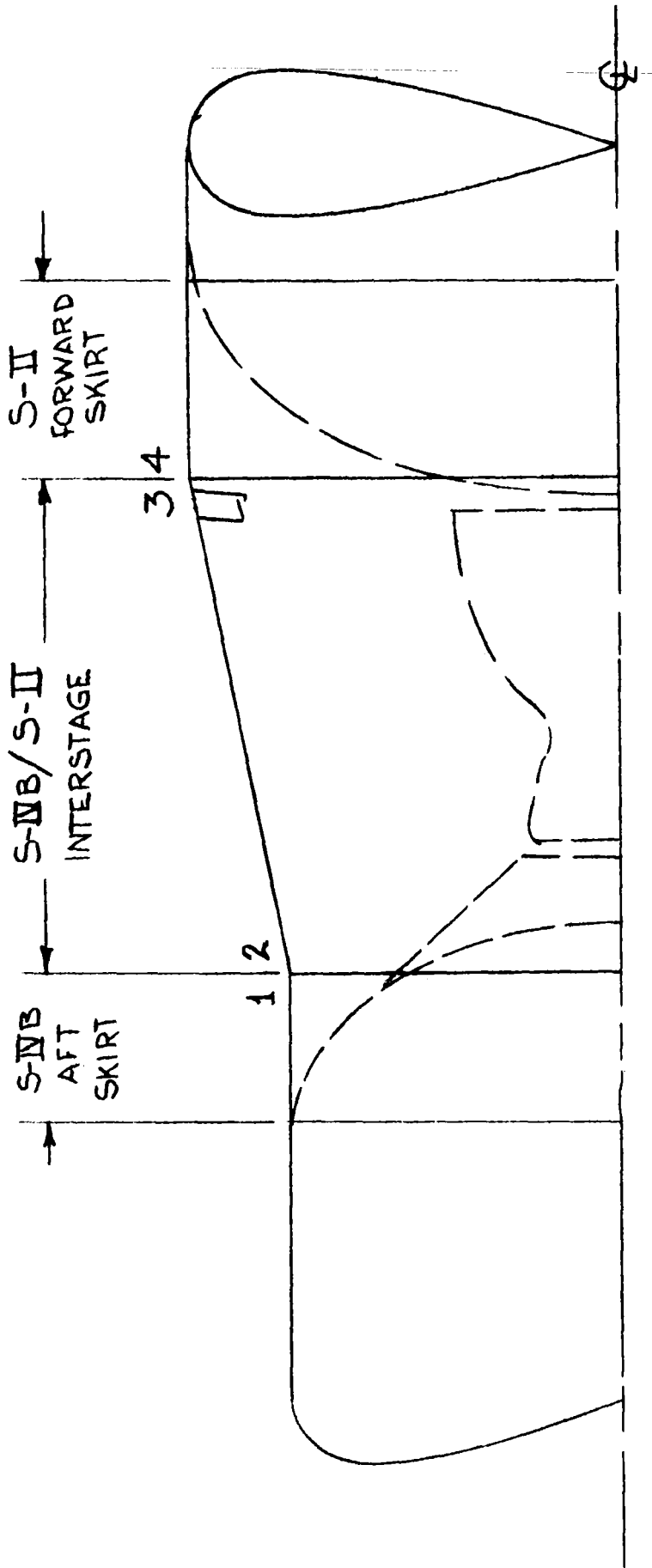
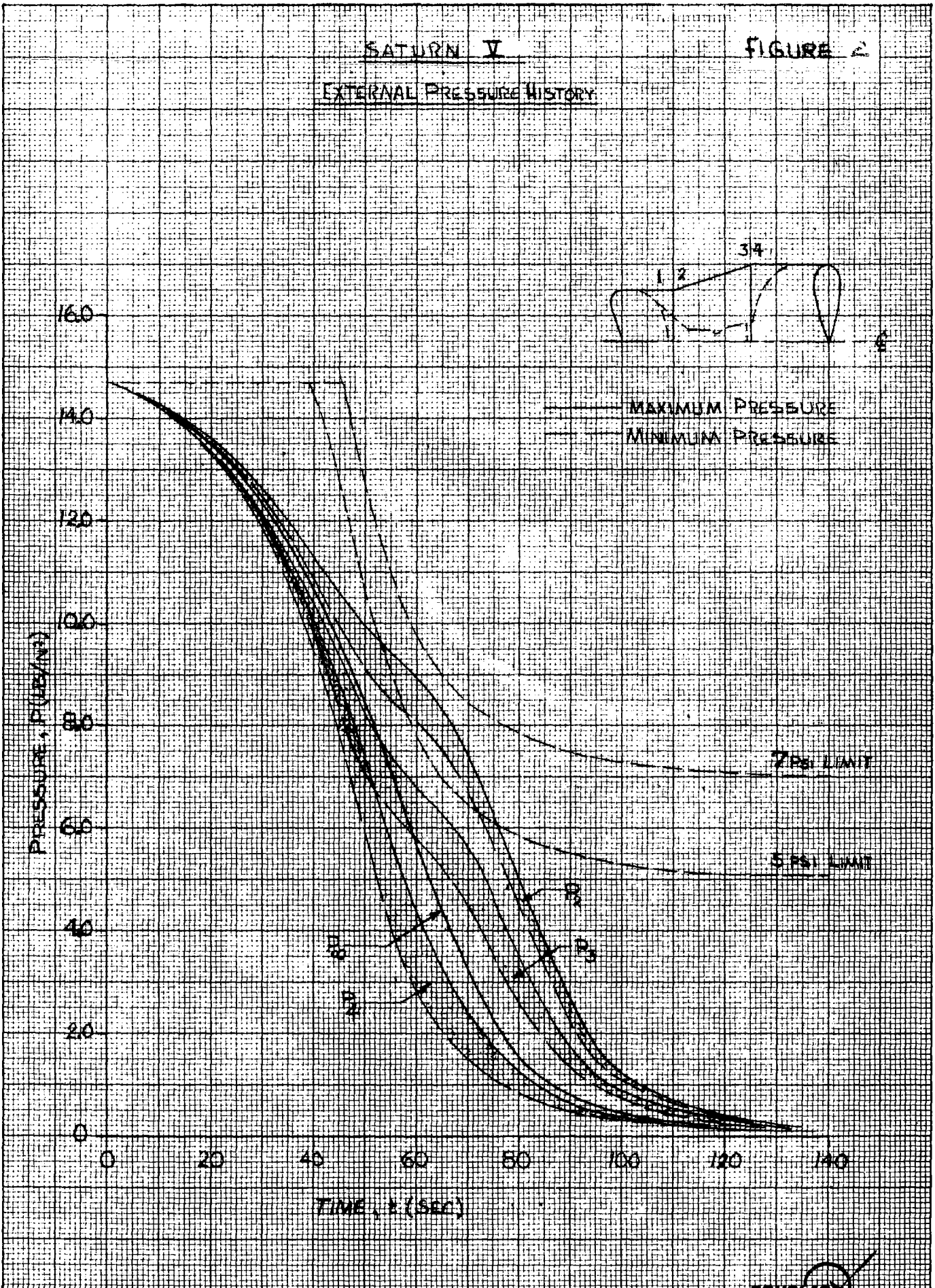


FIGURE 1

NOT TO SCALE

EXTERNAL PRESSURE HISTORY



# SATURN V

EFFECT OF LEAK AREA UPON  
INTERNAL PRESSURE AT THE  
DESIGN POINT  
(70 SEC)

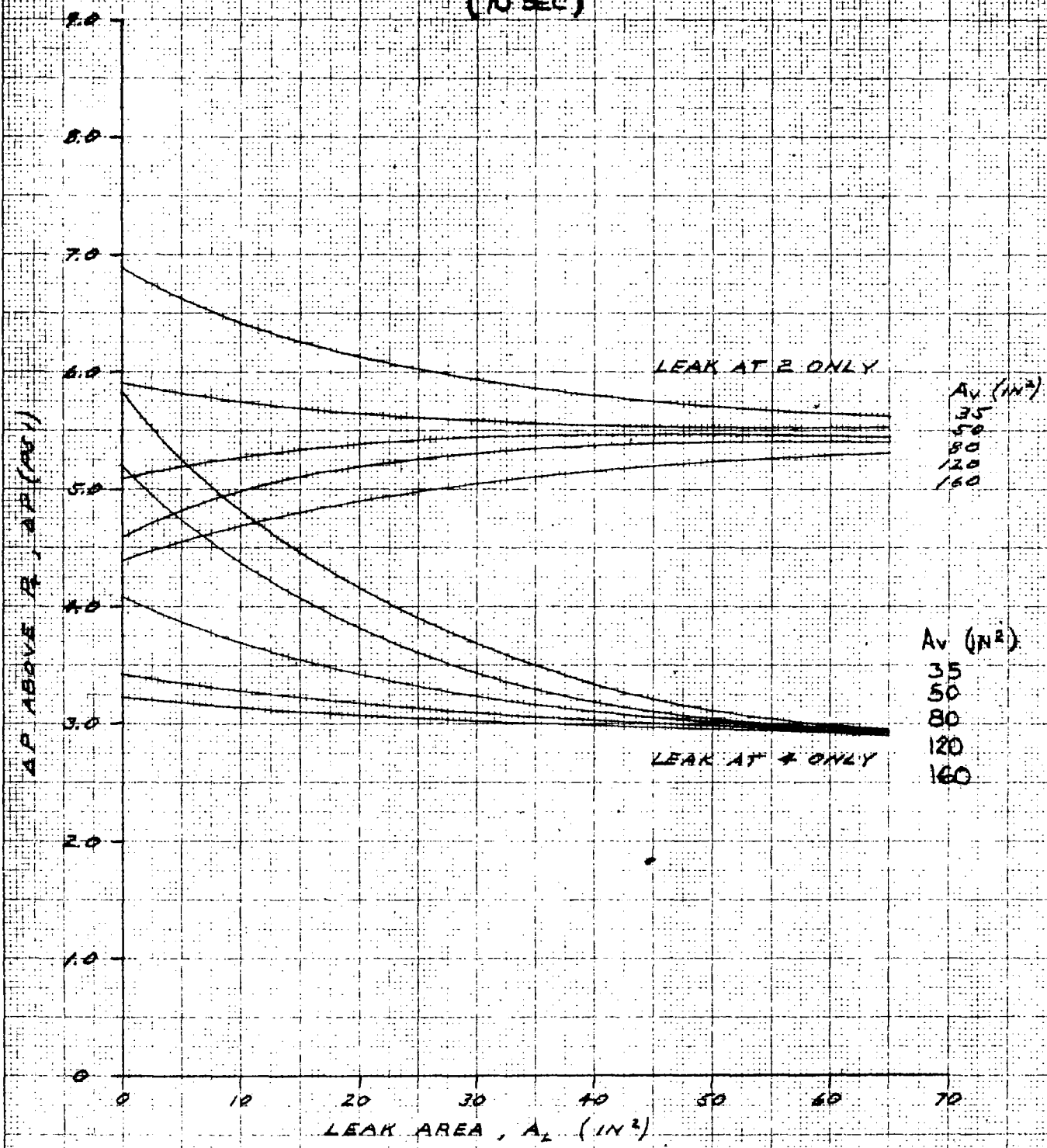


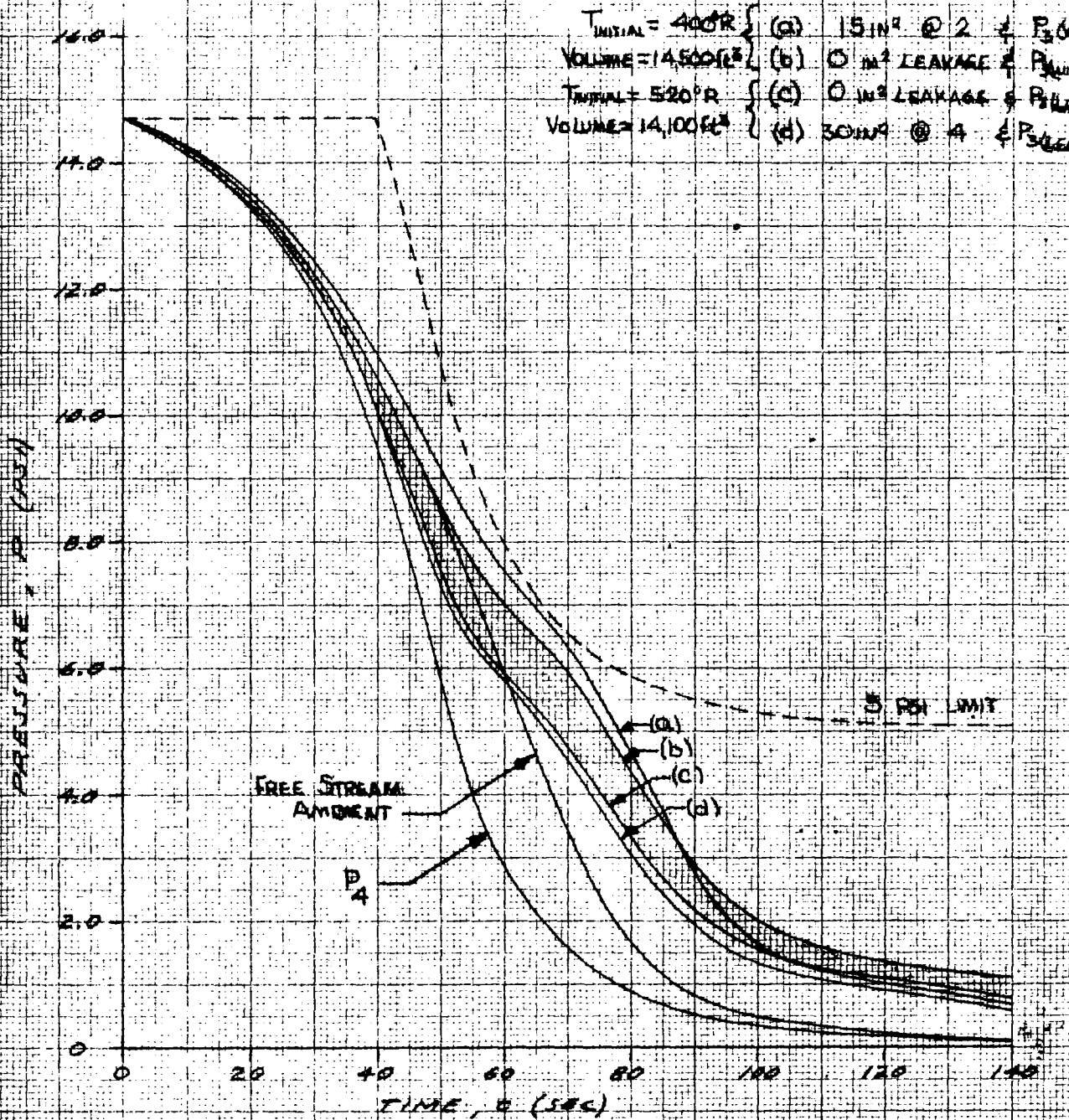
FIGURE 4

SATURN V

INTERNAL PRESSURE TIME HISTORY

$A_{N3} = 160 \text{ IN}^2$

- |  |   |
|--|---|
| $T_{\text{INITIAL}} = 400^{\circ}\text{R}$ | } (a) $15 \text{ IN}^2 @ 2 \frac{1}{2} \frac{1}{2} P_2 (\text{wind})$ |
| $\text{VOLUME} = 14,500 \text{ FT}^3$      |   |
| $T_{\text{INITIAL}} = 520^{\circ}\text{R}$ | } (c) $0 \text{ IN}^2 \text{ LEAKAGE } \frac{1}{2} P_2 (\text{wind})$ |
| $\text{VOLUME} = 14,100 \text{ FT}^3$      |   |



## Section 14

### EXTERNAL PRESSURE TIME HISTORIES

External pressure time histories presented in figure 2 were calculated for three points as shown in figure 1, the points are as follows:

Point 2 - on the front of the conical frustrum interstage.

Point 3 - in front of the corner of the frustrum and the S-II forward skirt.

Point 4 - on the S-II forward skirt immediately following the corner of the interstage.

A combination of analytical and wind tunnel test data (reference 1 and 2) were used in the analysis in conjunction with the necessary parameters taken from trajectory H (reference 3).

The angle of attack time history is presented in figure 3. This time history is taken from data presented to DAC as design angles-of-attack (reference 4). The subsonic portion of the curve was omitted, therefore, it was necessary to fair the curve from 0 to 60 seconds. The curve was faired to 90 degrees angle of attack due to the 75 ft/sec. ground wind.

Analytical data were obtained from three sources. The Neumann Potential Theory (subsonic), Van Dyke second order Potential Theory (low supersonic), and second order Shock Expansion Method (high supersonic), were employed.

The wind tunnel data show that the peak values predicted from inviscid theory are not realistic. This is due to boundary layer separation at these points. From boundary layers computed for the Saturn V (reference 5), an approximate pressure rise for incipient separation indicated that on the full scale vehicle these peak values might be higher than manifested in the wind tunnel tests. The values presented in figure 2 for point 2 are based on this analysis.

### REFERENCES

- 1) C-5 Wind Tunnel Pressure Test No. P-43, Boeing Document No. D5-11230,  
D. Lagler, dated 12/11/62
- 2) Preliminary Data Release, Wind Tunnel Test P-41, Parts 1, 2, and 3,  
Aero-H-053, 061, 078
- 3) MSFC Branch Working Paper 62/3, dated July 15, 1962
- 4) Rigid Body Control Data for the Saturn C-5 LOR Vehicle, M-AERO-DE-11,  
dated 12/12/62
- 5) Boundary Layer Thickness on the S-IVB/C-5 Vehicle, A2-860-S-IVB-K320-M-9,  
dated 2/1/63

DEFINITION OF POINTS

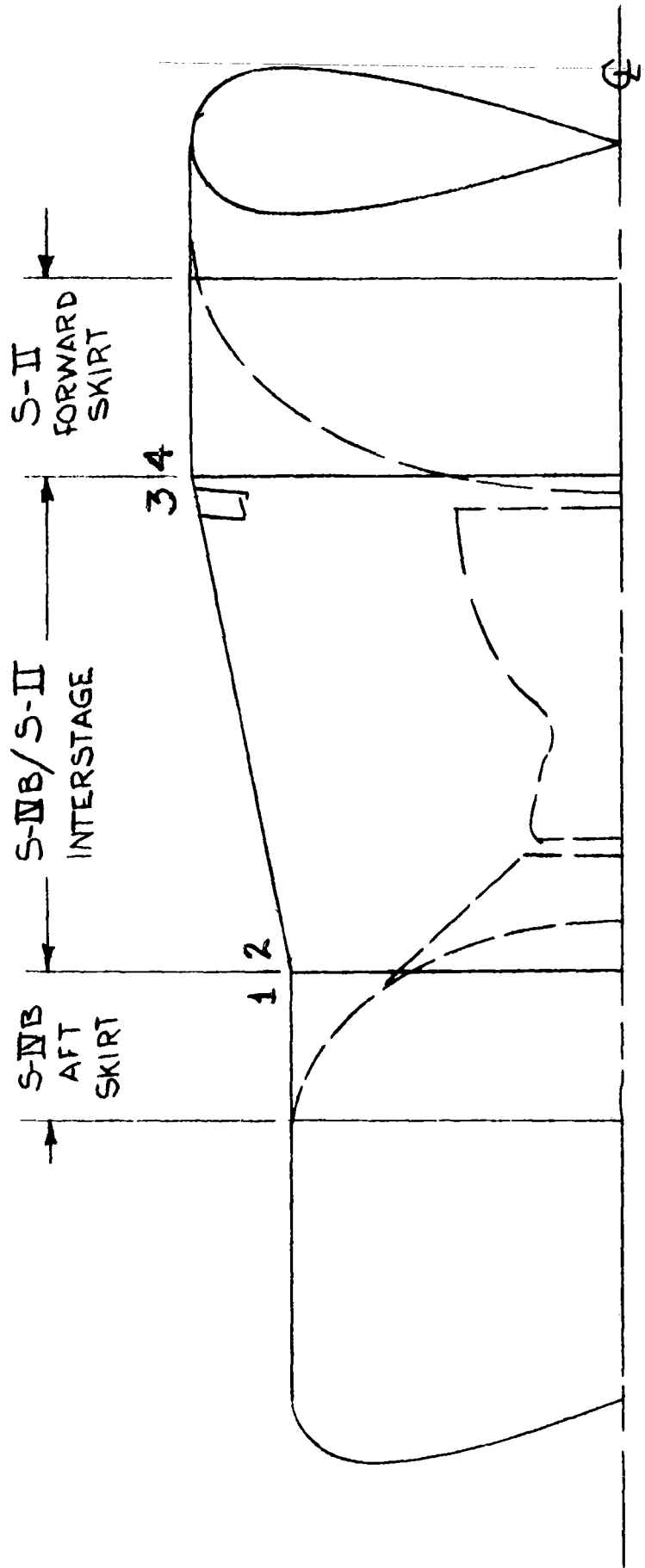


FIGURE 1

NOT TO SCALE

# SATURN V

FIGURE 2

## EXTERNAL PRESSURE TIME HISTORY

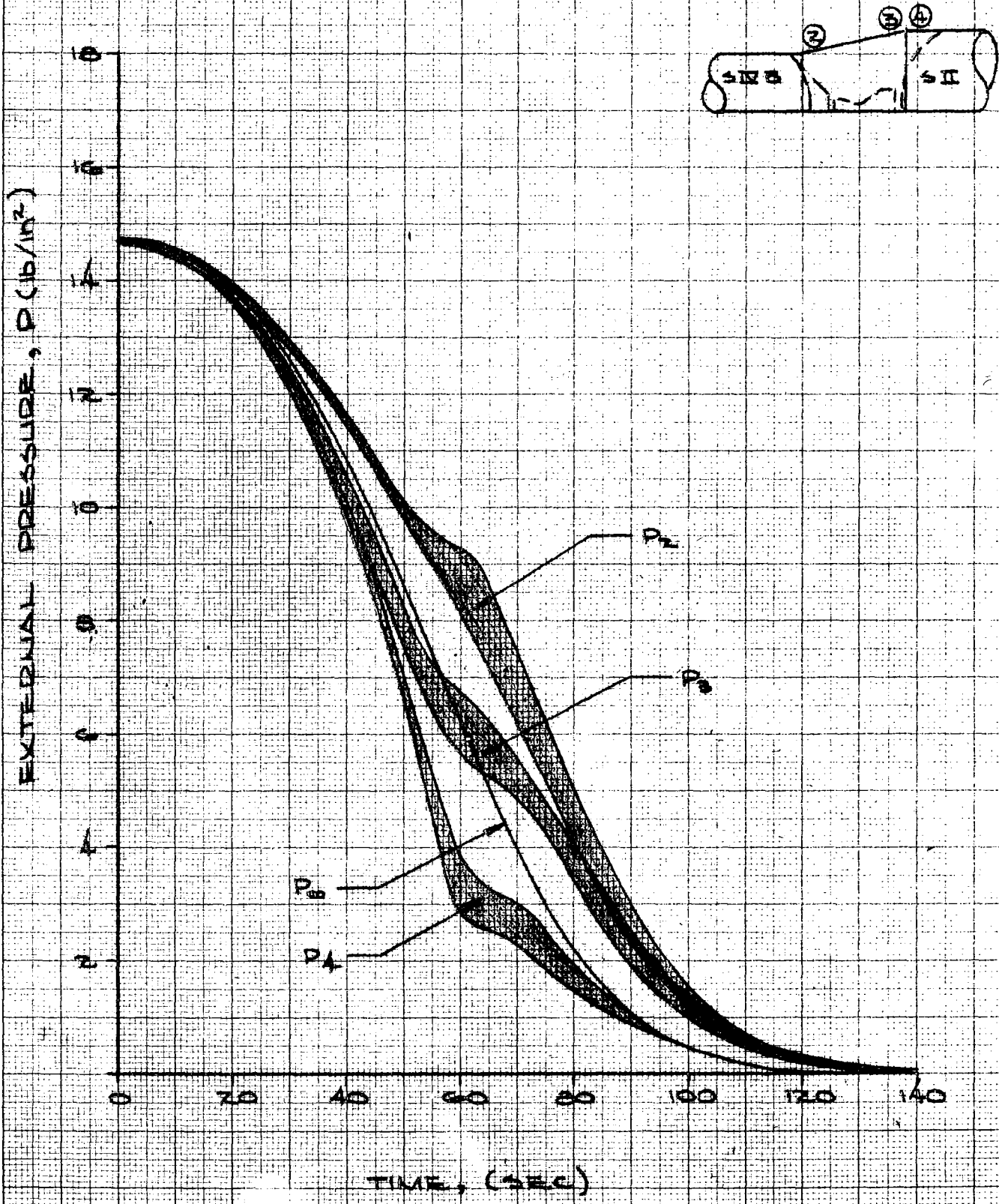
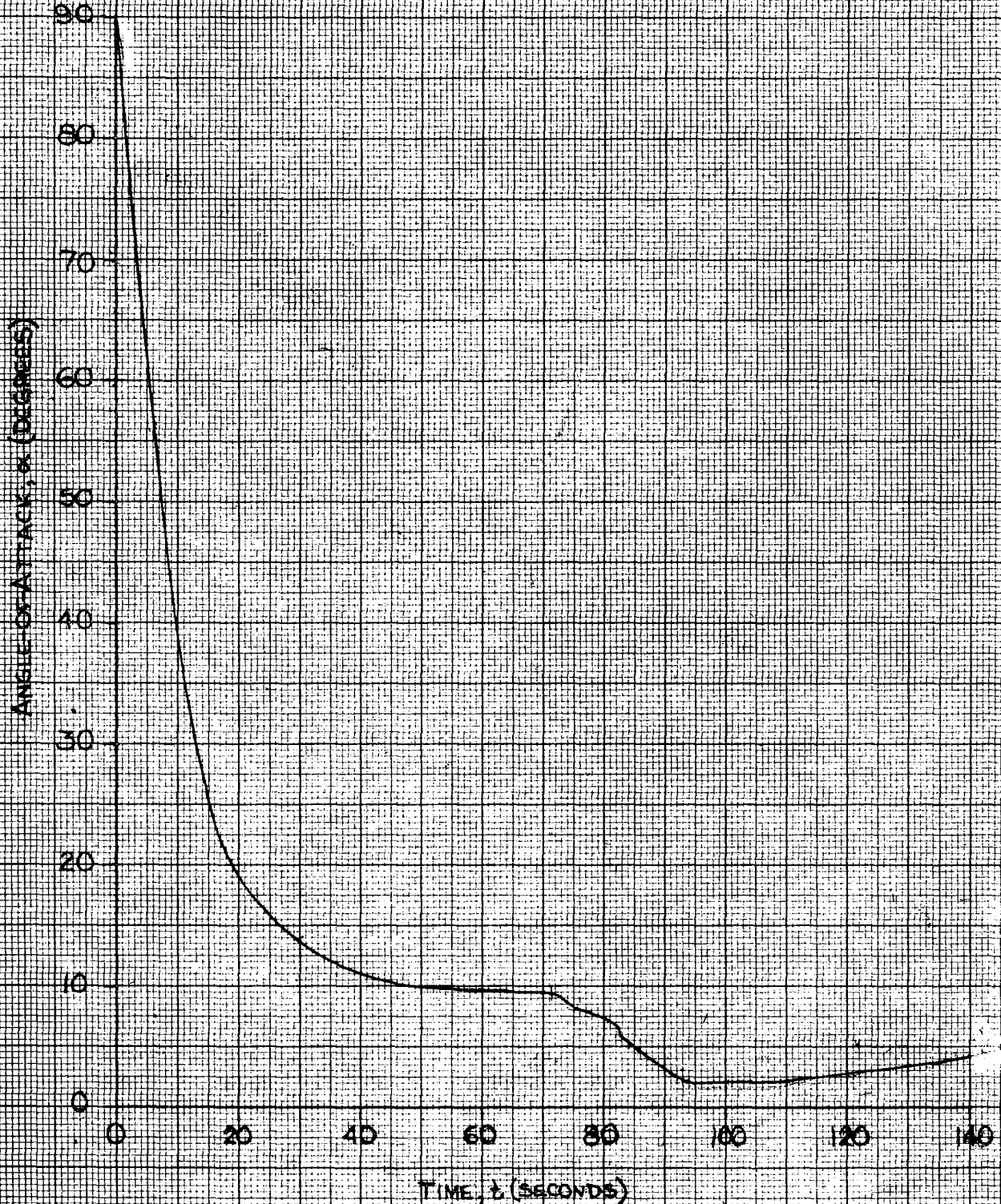


FIGURE 3

SATURN V

MAXIMUM ANGLE OF ATTACK  
HISTORY



## SECTION 15

### SERVO ACTUATOR RESPONSE TO LOAD INPUTS

#### INTRODUCTION

On 2-27-63 representative of NASA, Rocketdyne, S & I. D. and DACo met at NASA Huntsville to discuss the dynamics aspects of the J-2 engine side loads experienced during sea level testing. As a result of the discussion DACo was directed to investigate the response of the S-IV B engine positioning servo system to step, impulse and sinusoidal external load perturbations.

#### REFERENCE DOCUMENTS

- a. Rocketdyne Preliminary J-2 Engine Test Report, dated 3-18-63 (Confidential)
- b. Memo: M-P&VE-VJ-57-63-Section N (Confidential)

#### DISCUSSION

The mathematical model used in this analysis was that shown in figure I. Figure II defines the terms used. The model was based upon the following assumptions.

1. The load disturbance or driving force was assumed to be unaffected by small engine deflections.
2. For simplicity, the system distributed mass and compliance effects were treated as equivalent lumped parameters.
3. The disturbance load was assumed to be directly coupled with the lumped mass.
4. Servo valve flow gain was assumed to be essentially independent of load effects.

Digital computer programs were written based on the mathematical model of figure I, to facilitate evaluating the effects of changes in E.P.S.S. variables. Using the presently planned E.P.S.S., figures III, IV, and V show the predicted amplitude ratio of the induced actuator force to sinusoidal, step and impulse engine load disturbances, respectively.

The phantom curve of figure III shows that further reduction of dynamically generated loads could be achieved by the introduction of supplemental negative load acceleration feedback and/or piston position feedback. Naturally any supplemental feedback would be used only during static firing and even then would have to be removed (probably through electrical switching) after subsidence of starting transients, to permit evaluation of normal system characteristics.

While the purpose of this analysis was to investigate only dynamic aspects of the engine side load problem, it seems appropriate here to note that the force disturbance histories associated with several of the J-2 engine firings (notably tests 316-098A and 316-061A) reveal essentially static load disturbances which in themselves exceed the maximum allowable actuator loads.

### CONCLUSIONS

If it is found that SIV B engines (Block III) exhibit excessive steady state load disturbances such as those observed in tests 316-098A and 316-061A, then the side load problem will not be amenable to solution through the use of dynamic compensation in the E.P.S.S. If, however, the essentially steady state component of the engine side loads can be kept to an acceptable minimum, it appears that the residual dynamic side loads should be susceptible to reduction through the use of the presently planned SIV B E.P.S.S. dynamic compensation with possible further load reduction through the use of augmentative negative load acceleration feedback and/or positive piston position feedback. The effectiveness of this approach naturally is dependent upon the actual wave-form of the load disturbing force (to be determined by Rocketdyne).

The preceding conclusions are predicated upon the validity of the assumptions previously stated. However at this time it appears desirable to question the validity of the assumption that the load disturbance or driving force is necessarily independent of engine deflection; for if it should be found that the load disturbance force can be predictably and significantly reduced through controlled movement of the engine chamber, then it may be possible to use load force feedback to reduce static as well as dynamic engine side loads.

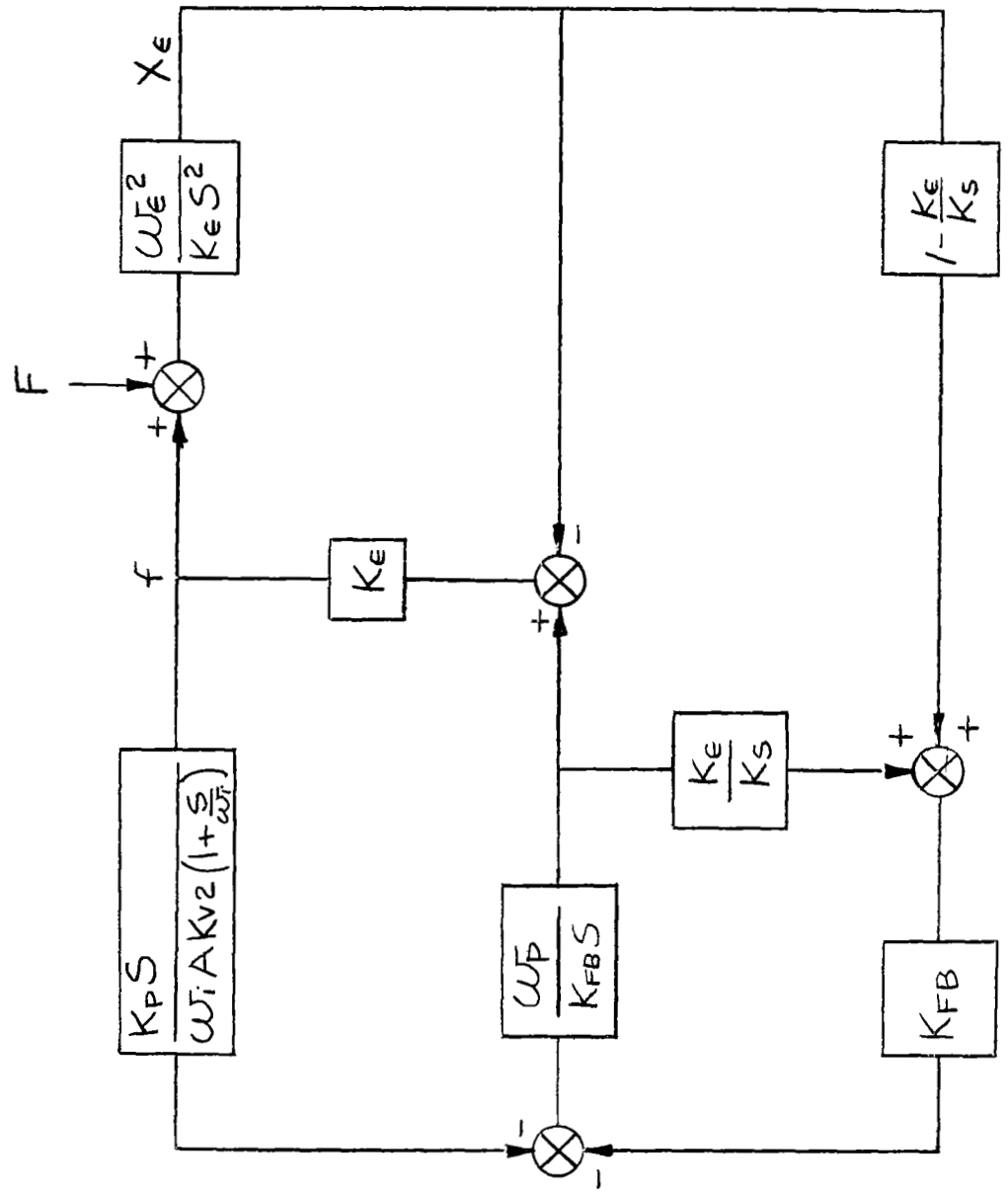
### RECOMMENDATIONS

It is recommended that Rocketdyne investigate whether a significant reduction in the load driving force can be predictably achieved through movement of the engine chamber. This might possibly be accomplished by holding the engine at the main fuel manifold outrigger attach points using position feedback actuators incorporating electrical feedback of a signal proportional to the output of an actuator load sensing device such as a load cell or actuator cylinder differential pressure transducer. Gains of the position feedback and load feedback loops would need to be adjustable remotely to permit optimization of compensation during engine firing.

Should this approach prove feasible, the compensation could be incorporated through switching during starting and shut-down transients and eliminated during the interim to permit hot gimbaling with the normal engine positioning servo system configuration.

REFERENCE: SM-43671

FIGURE I



SERVO SYSTEM MODEL

DEFINITION OF TERMS

A	Actuator piston area - $\text{in}^2$
F	External load disturbance force referred to plane of actuation - #
f	Resultant force exerted on actuator attach points - #
$K_e$	Net load spring rate - $\text{in}/\#$
$K_{fb}$	Piston position feedback gain - $\text{in}-\#/\text{in}$
$K_p$	Pressure feedback gain - $\text{c.i.s.}/\text{p.s.i.}$
$K_s$	Net structural spring rate - $\#/\text{in}$
$K_{v2}$	Valve second stage gain - $\text{c.i.s.}/\text{in}$
$W_a$	Acceleration loop break frequency
$W_e$	Natural frequency of mass and net load spring system - $\text{RAD}/\text{SEC}$
$W_i$	Break frequency of pressure feedback isolation network - $\text{RAD}/\text{SEC}$
$W_p$	Break frequency of actuator position loop - $\text{RAD}/\text{SEC}$

FIGURE III

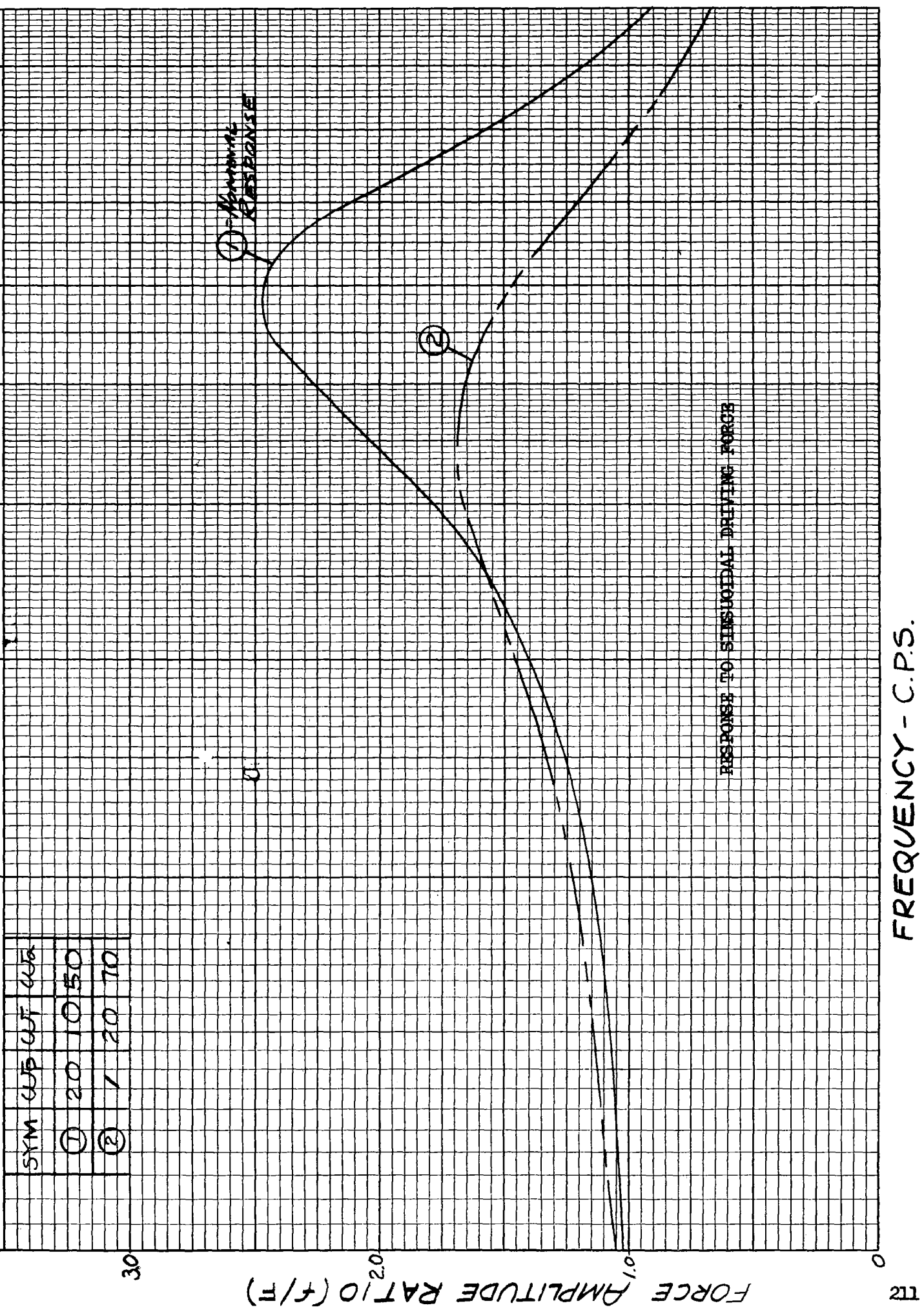
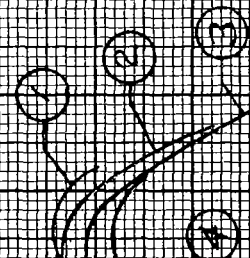


FIGURE IV

SYMBOL	ω <sub>p</sub>	ω <sub>n</sub>	ζ
①	20	50	15
②	22	42	10
③	22	42	5
④	20	50	5

FORCE AMPLITUDE RATIO (F/F)



RESPONSE TO UNIT STEP DRIVING FORCE

TIME - SEC.

0.4

0.3

0.2

0.1

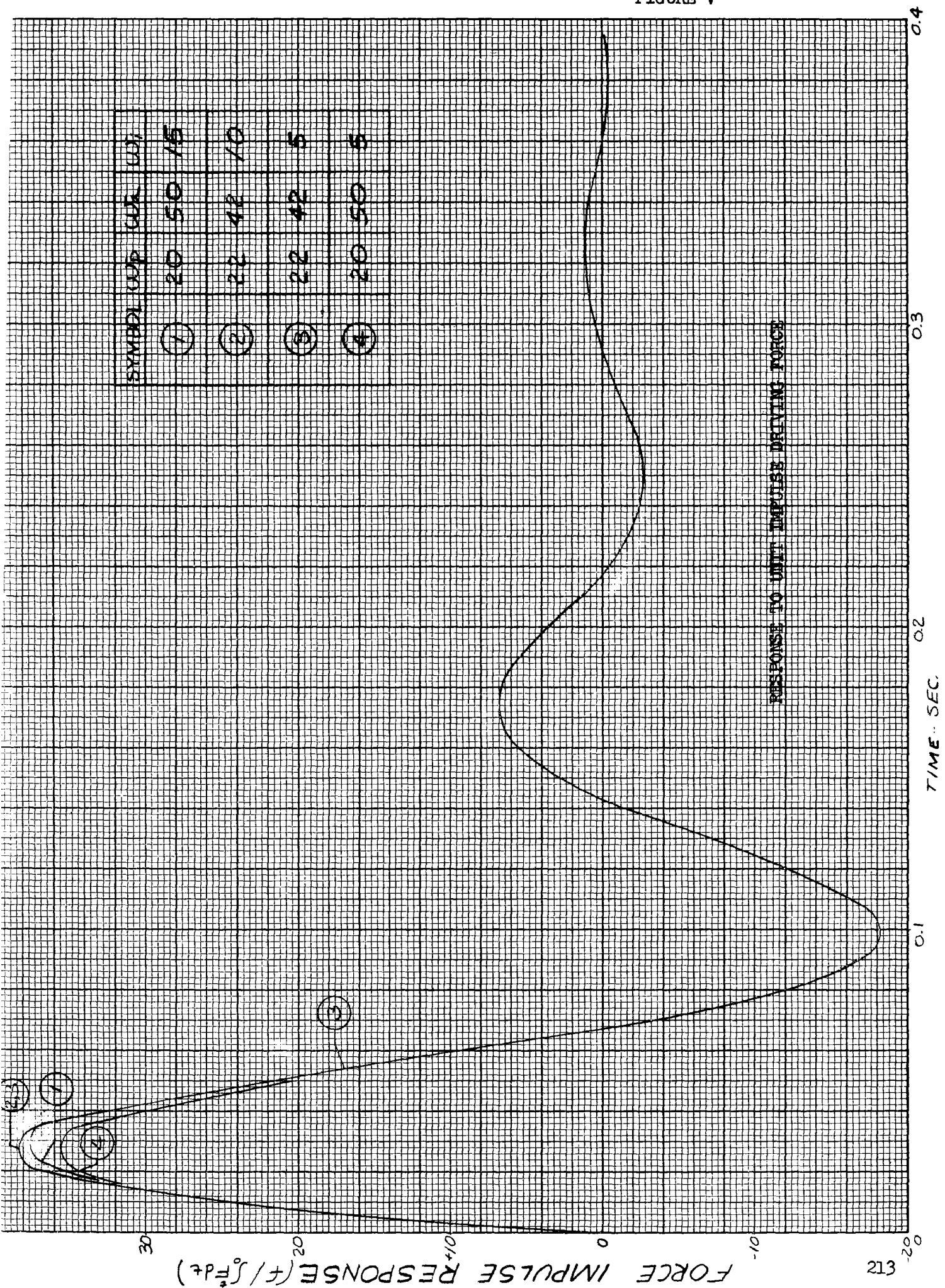
0

0.2

0.1

0

FIGURE V



RESPONSE TO UNIT IMPULSE DRIVING FORCE

## Section 16

### STATUS REPORT OF ACTUATION SYSTEM

#### INTRODUCTION

In discussion between NASA and DACo in November of 1962, it was decided that Saturn S-IVB E.P.S.S.\* design requirements were significantly different from those of the SII E.P.S.S., making the use of existing SII actuators on S-IV undesirable. DACo was therefore, authorized by C.C.N. #6, dated 12-12-62 to generate specification control drawing number 1A66248 for procurement of the requisite S-IVB actuators. The following is a discussion of the various steps involved in establishing the dynamics-related design characteristics reflected in that specification control drawing.

#### PROCEDURE

##### I. Establishment of Position Loop Break Frequency "Wp"

NASA specified that the theoretical closed loop E.P.S.S. phase lag should not be allowed to exceed  $20^\circ$  at 1 C.P.S. to insure adequate vehicle altitude control system phase and gain margins. At frequencies significantly below engine load resonance the following approximate relationship obtains between E.P.S.S. closed loop phase lag " $\phi$ " and actuator position loop break frequency "Wp".

$$1. \quad W_p \approx \frac{W(\text{ref.})}{\text{TAN } \phi}$$

Substitution of 1 C.P.S. for "W (ref.)" and  $20^\circ$  for  $\phi$  in 1 above, the corresponding value of 'Wp' is 17.3 radians/sec. A nominal value of  $W_p = 20$  (15% higher) was selected to allow for tolerance variations and minor additional low frequency phase lag attributed to artificial engine load damping.

It should be emphasized that the above selected value of 'Wp' can be expected to satisfy the low frequency closed loop phase requirement for command signals of significant amplitude but that the phase lag can be expected to increase catastrophically as the signal amplitude becomes very small. This is discussed in more detail in reference a.

##### II. Establishment of Artificial Engine Load Damping Criteria

In an E.P.S.S. such as that of SIV B the engine mass is coupled to the vehicle structure through several compliant members (including the structure itself).

\*Engine Position Servo System

The resulting spring-mass system contains almost no natural damping and if no artificial damping were provided the E.P.S.S. would be unstable for the value of 'Wp' selected. As a result of previous discussions with NASA it was decided that mechanical rather than electrical artificial damping should be specified. Artificial damping resulting from mechanical load acceleration feedback was selected as a logical, proven approach.

A study was made to determine whether a "high pass" filter should be incorporated in the load acceleration feedback path (D.P.Q.) or whether unfiltered load acceleration feedback would be acceptable (P.Q.). The two primary disadvantages of the P.Q. approach are listed below.

1. E.P.S.S. null shift and dead band resulting from uni-directional and bi-directional loads would be much greater with a P.Q. valve than with a D.P.Q. valve.
2. A "P.Q." valve would necessitate using lower piston position feedback gain to insure full engine deflection capability under load.

It was, therefore, decided to specify the use of the 'D.P.Q.' approach.

Optimization of the D.P.Q. acceleration loop break frequency 'Wa' and high pass isolation network break frequency 'Wi' was accomplished by computer analysis as described in Figures II and III.

### III. Incorporation of Mechanical Piston Position Feedback

DACo was directed verbally and by copy of internal memorandum NAV507/62 to utilize mechanical rather than the more conventional electrical actuator piston position feedback. DACo therefore set out to become better informed on the peculiarities of mechanical feedback.

In December of 1962 an analytical study of the advantages and disadvantages of actuator mechanical piston position feedback was initiated. Throughout January of 1963 similar analyses, obtained from several valve-actuator manufacturers were collated.

In mid January NASA, S & I.D. and DACo representatives met with personnel of the Martin Company at their facility in Denver, Colorado and were briefed on Martin's experiences to date, with mechanical piston position feedback actuators on the Titan missile.

In February of 1963 a typical mechanical feedback actuator was obtained from the Moog Manufacturing Company. The actuator was subjected to extensive static and dynamic testing in an attempt to bring to light any significant inherent mechanical feedback peculiarities. Reference documents the results of that study.

The following discussion is based on the information obtained from the above described activities.

Figure IA shows the block diagram of a typical engine positioning servo system with actuator piston position feedback accomplished electrically. (For clarity

no other dynamic compensation or load effects are shown.) Figure IB shows the block diagram of an equivalent engine positioning servo system with actuator piston position feedback accomplished mechanically. The two figures demonstrate that the basic difference in using mechanical rather than electrical piston position feedback is that the valve first stage or torque motor and the vehicle amplifier are outside of the piston position loop. Thus, any non linearities in the torque motor and amplifier will result in corresponding un-diminished non-linearities in the E.P.S.S. closed loop characteristics.

The relationship between piston position "Xp" and input current "Ic" for Figure IA is seen to be:

$$1. \frac{X_p}{I_c} = \frac{K_{act}}{1 + s \frac{1}{W_p}} \quad \text{Where } W_p \triangleq \frac{K_a K_{vt} K_{v2} K_{fb}}{A}$$

$$K_{act} = \frac{1}{K_{fb}}$$

For Figure IB:

$$2. \frac{X_p}{I_c} = \frac{K_{act}'}{1 + s \frac{1}{W_p'}} \quad \text{Where } W_p' \triangleq \frac{K_{v2}' K_{fb}'}{A} \quad \text{and}$$

$$K_{act}' = \frac{K_{vt}'}{K_{fb}'}$$

In order that the electrical and mechanical feedback systems respond identically, it is apparent that the following two relationships must obtain:

$$3. K_{act} = K_{act}'$$

$$4. W_p = W_p'$$

Thus, specification of "Kact" and "Wp" can be used to completely delineate the E.P.S.S. linear response characteristics attributable to piston position feedback.

Substitution of equivalent mechanical feedback parameters in 3. and 4. yields:

$$5. \frac{K_{vt}'}{K_{fb}'} = K_{act}$$

$$6. K_{v2}' K_{fb}' = W_p A$$

By combining equations 5. and 6. it can be shown that specification of servo valve static flow gain "Kv" in lieu of "Wp" in a system employing mechanical piston position feedback, would serve equally well in delineating linear response characteristics.

Thus:

$$7. K_v = W_p \sqrt{A} K_{act} \quad \text{Where: } K_v \triangleq \frac{K_{vt}}{K_{v2}}$$

As the piston area "A" is sized on the basis of load factors and the actuator static gain  $K_{act}$  is specified as one of the two independent variables determining piston position loop characteristics, it is seen that the value of  $K_v$  will determine 'Wp'.

In sizing the Saturn SIV-B E.P.S.S. the value for 'Kact' was not critical because of the flexibility of other parameters in the vehicle attitude control system. It was therefore, possible to minimize 'Kact' to minimize non-linearities in the mechanical feedback mechanism. The minimum practical value for  $K_{act}$  is limited by the fact that the feedback torque at maximum piston stroke must not exceed rated torque motor output; otherwise it would be impossible for the actuator to be extended fully. This limitation can be expressed as:

$$8. K_{act} \geq \frac{X_p \text{ (Max)}}{I_t \text{ (rated)}}$$

Substitution of actual SIV B valves in equation 8. yields:

$$K_{act} \geq \frac{1.45 \text{ in.}}{50 \text{ ma}} = .029 \text{ in/ma}$$

Selecting a value slightly greater than the above to ensure maximum stroke capability, we used:

$$\underline{K_{act} = .031 \text{ in/ma}}$$

The actual value of  $W_p$  used for SIV-B was 20 radians/sec. so that the corresponding value of "Kv" (from equation 7) was:

$$K_v = \frac{20 \times 11.5 \text{ in.}^2}{\text{sec.}} \times \frac{.031 \text{ in.}}{\text{ma}}$$

$$K_v = \underline{7.2 \text{ cis/ma}}$$

#### IV Establishing Valve Minimum and Maximum Flow Requirements

The SIV-B Actuator Load Analysis (reference c) established a piston area of 11.5 in.<sup>2</sup> and a critical valve flow requirement corresponding to 80/sec. engine deflection rate with a valve differential pressure of 643 psi. Thus the minimum acceptable servo valve no load flow with 3000 psi supply pressure is given by:

$$1. Q_v \text{ (min.)} = \frac{\dot{B} \text{ (min.)}}{K_d} \frac{A}{643 \text{ psi}} = \frac{3000 \text{ psi}}{643 \text{ psi}} = 10.7 \text{ gpm}$$

The actuator load analysis also specifies a maximum allowable engine deflection rate of 310/sec. based upon maximum allowable acceleration loads encountered during actuator piston bottoming. The corresponding maximum allowable servo valve no-load flow is:

$$Q_v \text{ (max.)} = \frac{\dot{B}}{K_d} \frac{A}{643 \text{ psi}} = 19.2 \text{ gpm}$$

It was therefore specified that the servo valve must be designed to limit no-load flow to  $12 \pm 2$  gpm.

FIG. I A

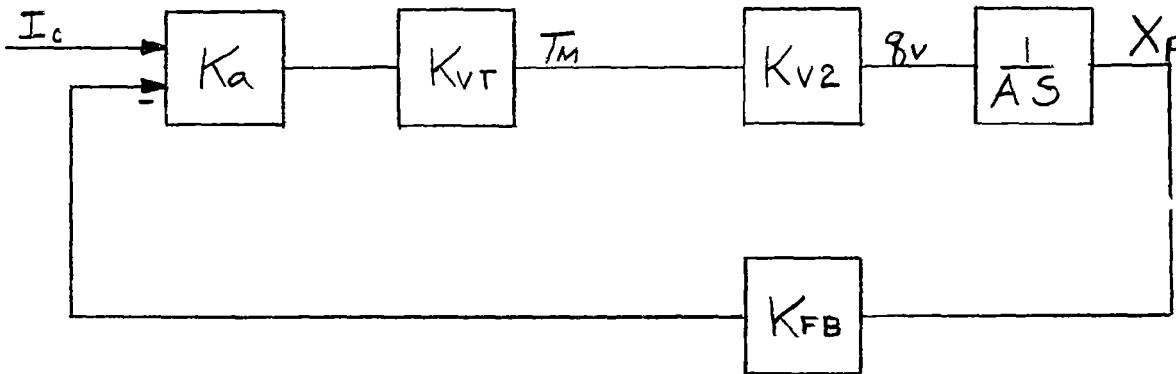


FIG I B

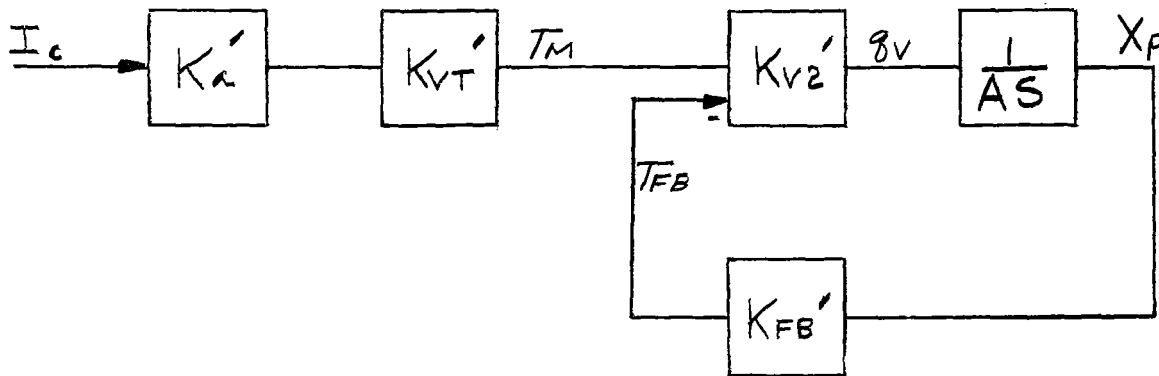
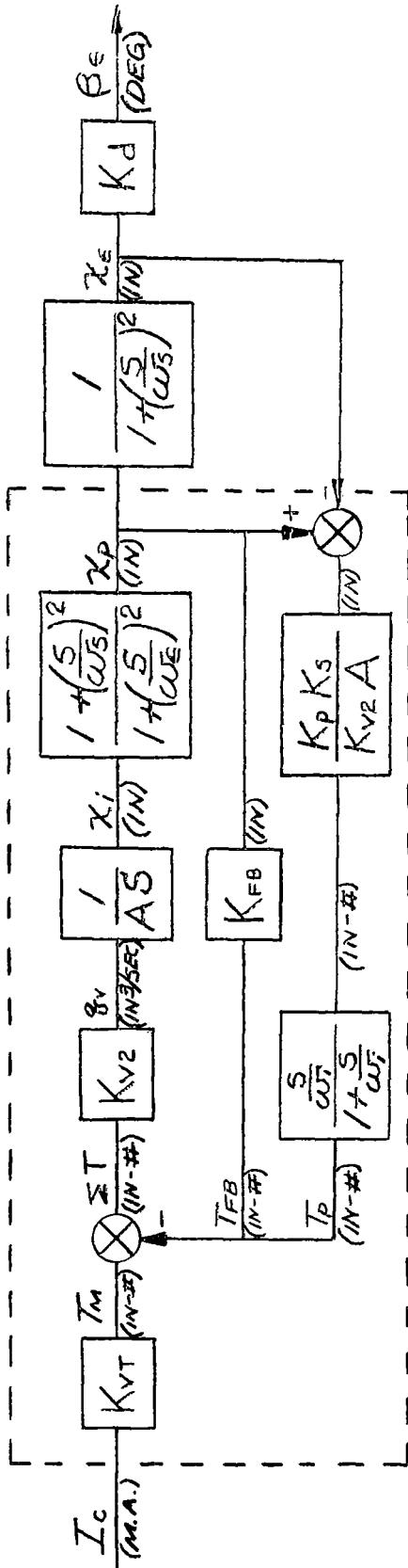


Figure IB

- A : Actuator Piston Area ( $\text{in}^2$ )
- $I_c$  : Command Signal (ma)
- $K_a$  : Amplifier Static Gain (ma/ma)
- $K_{vT}$  : Valve Torque Motor Gain ( $\text{in-}\#/\mu\text{a}$ )
- $K_{v2}$  : Valve Second Stage Gain ( $\text{c.i.s.}/\text{in-}\#$ )
- $q_v$  : Flow of ideal fluid from valve to cylinder (c.i.s.)
- s : Laplace Operator
- $T_{FS}$  : Mechanical Piston Position Feedback Torque (in-#)
- $T_M$  : Torque Motor Output (in-#)
- $X_p$  : Piston Position (inches)

# ACTUATOR ASSEMBLY



- A = Actuator piston area (11.5 in.<sup>2</sup>)
- I<sub>c</sub> = Command signal (m.a.)
- K<sub>d</sub> = Conversion factor between degrees and inches (4.83 deg./inch)
- K<sub>fb</sub> = Mechanical piston position feedback gain (in./in.); K<sub>fb</sub>/K<sub>vt</sub> = 32 m.a./in.
- K<sub>s</sub> = Structural spring rate (391,000 #/in.)
- K<sub>p</sub> = D.P.F. servo valve feedback gain (.0169 c.i.s./p.s.i.)
- K<sub>vt</sub> = Valve torque motor gain (in./m.a.)
- K<sub>v2</sub> = Valve second stage gain (c.i.s./in.-#) } K<sub>vt</sub> K<sub>v2</sub> = 7.20 c.i.s./m.a.
- q<sub>v</sub> = Flow of ideal fluid from valve to cylinder (c.i.s.)
- S = Laplace operator
- T<sub>fb</sub> = Mechanical piston position feedback torque (in.-#)
- T<sub>m</sub> = Torque motor output (in.-#)
- T<sub>p</sub> = D.P.F. servo valve feedback torque (in.-#)
- X<sub>e</sub> = Effective engine load position (inches)
- X<sub>i</sub> = Ideal piston position (inches)
- X<sub>p</sub> = Actual piston position (inches)
- β<sub>e</sub> = Engine position (degrees)
- ω<sub>Δ</sub> = Acceleration loop break frequency (50 radians/sec.) ≙ K<sub>p</sub>K<sub>s</sub>/A<sup>2</sup>
- ω<sub>ΔE</sub> = Natural frequency of mass and effective oil-structure spring (54.8 radians/sec.)
- ω<sub>ΔI</sub> = Natural frequency of mass and structure spring (60 radians/sec.)
- ω<sub>ΔF</sub> = Isolation network break frequency (20 radians/sec.) ≙ K<sub>v2</sub> K<sub>fb</sub>/A
- ω<sub>ΔS</sub> = Position loop break frequency (60 radians/sec.)

FIG. II - SERVO SYSTEM MODEL

PHASE LAG - DEGREES

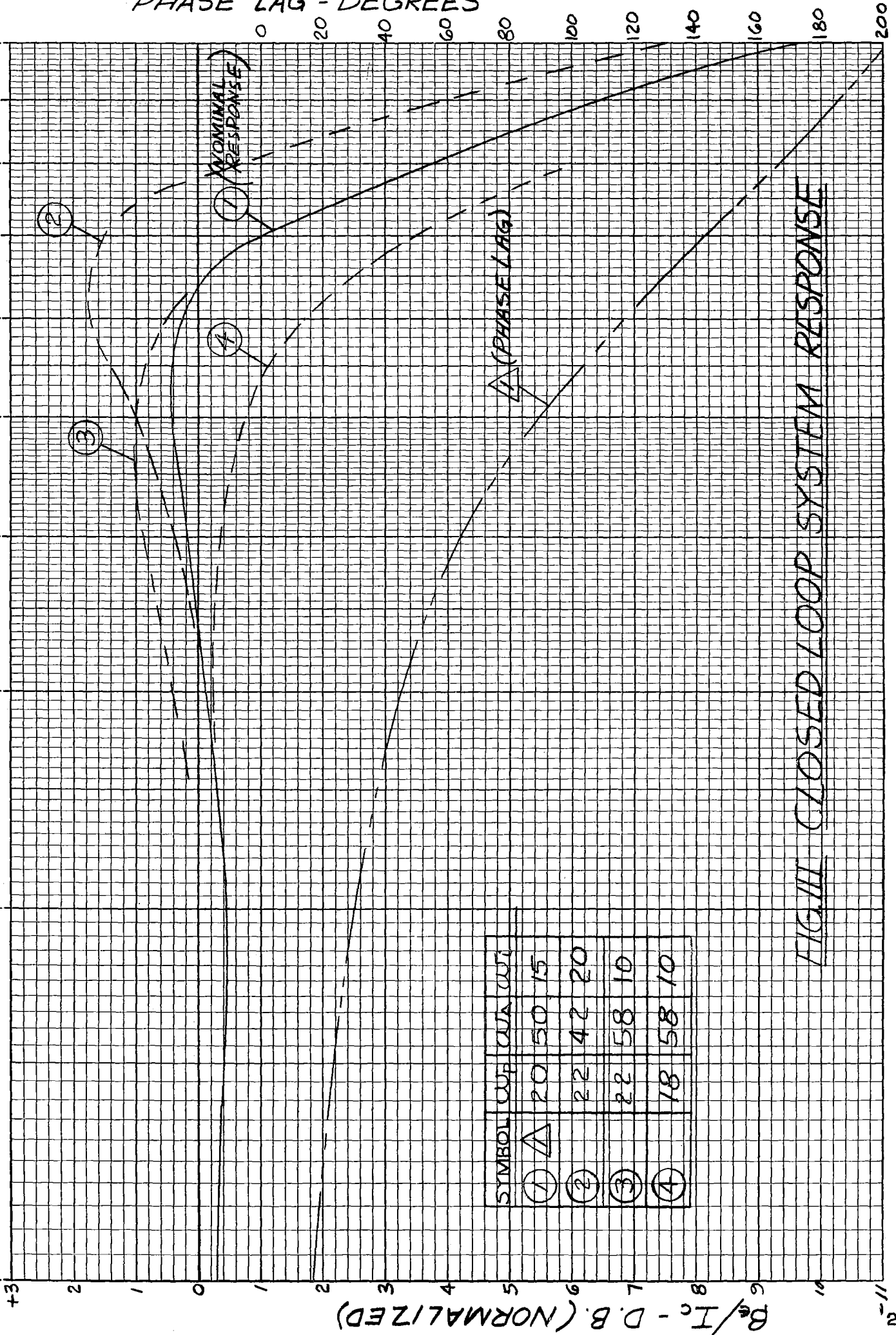


FIG. III CLOSED LOOP SYSTEM RESPONSE



MISSILE & SPACE SYSTEMS DIVISION  
DOUGLAS AIRCRAFT COMPANY, INC.  
SANTA MONICA, CALIFORNIA